Exploring the Capabilities of Metal-Organic Frameworks (MOFs) as Versatile Sensors for Diverse Sensing Applications: From Design to Practical Implementation

THESIS

Submitted in partial fulfilment

of the requirements for the degree of

DOCTOR OF PHILOSOPHY

by

LEELA SREE. T

ID No. 2019PHXF0054H

Under the Supervision of

Prof. Himanshu Aggarwal

BIRLA INSTITUTE OF TECHNOLOGY AND SCIENCE, PILANI

2024

BIRLA INSTITUTE OF TECHNOLOGY AND SCIENCE, PILANI

CERTIFICATE

This is to certify that the thesis entitled **Exploring the Capabilities of Metal-Organic Frameworks (MOFs) as Versatile Sensors for Diverse Sensing Applications: From Design to Practical Implementation** submitted by **LEELA SREE. T,** ID. No. **2019PHXF0054H** for award of Ph.D. of the Institute embodies original work done by her under my supervision.

Signature of the Supervisor:

Name in capital letters: Prof. HIMANSHU AGGARWAL

Designation: Associate Professor

Department of Chemistry

Birla Institute of Technology and Science-Pilani, Hyderabad Campus.

Date: 08-07-2024

DECLARATION

This is to certify that the thesis titled "**Exploring the capabilities of Metal-Organic Frameworks (MOFs) as Versatile Sensors for Diverse Sensing Applications: From Design to Practical Implementation**" is based on my own research work and has been carried out under the guidance and supervision of Prof. Himanshu Aggarwal, Associate Professor, Department of Chemistry, BITS Pilani, Hyderabad Campus, Hyderabad, India. The data and information which I have used from various sources have been duly acknowledged. I declare that this work has not been previously submitted by me to any other university/institute for the award of any other degree or diploma.

Date: 08-07-2024 Name: **Leela Sree. T**

Place: Hyderabad ID No: **2019PHXF0054H**

ACKNOWLEDGEMENTS

First and foremost, I would like to express my sincere thanks to my supervisor **Prof. Himanshu Aggarwal** for his remarkable support and guidance throughout my PhD. I am always grateful for his patience, time, constructive feedback, critical suggestions and for infusing great research values. Honestly, it would have been impossible to achieve this goal without his unwavering support. I am extremely thankful to my supervisor for always encouraging new ideas, providing an excellent research environment and for all his contributions.

I express my sincere thanks to my Doctoral Committee members **Prof. Ramakrishnan Ganesan** and **Dr. Parikshit Sahatiya** for their valuable insights and support. I would like to extend my thanks to the **Central Analytical Laboratory (CAL), BITS Pilani Hyderabad Campus** for all the characterization facilities. I also extend my sincere thanks to all our collaborators for their facilities and support.

My sincere thanks to **Prof. Sounak Roy,** Head of the Department (HOD), Department of Chemistry, BITS Pilani, Hyderabad Campus, the DRC convener **Prof. Tanmay Chatterjee** and the entire faculty of department of chemistry for their valuable support. I also express my gratitude to **Prof. Soumyo Mukherji,** current Director and **Prof. G. Sundar,** former Director, BITS Pilani, Hyderabad Campus, **Prof. Alivelu Manga Parimi,** Associate Dean, and **Prof. V. V. Vamsi Krishna,** Dean, Academic-Graduate Studies and Research Division, for facilitating the research and support.

It is definitely a source of pride to express my gratification with sense of joy to all those who supported me during this incredible journey. Firstly, I would like to express my deep sense of gratitude to my family, especially my parents **Mrs. T. Manjula** and **Mr. T. Bhaskar** and my brother **Mr. T. Chetan** for believing in me. I am extremely grateful for their sacrifices, love and always being there for me as a constant support system over this journey.

I am also grateful to my friends **Mr. A. Kishore, Dr. Kavya Ramisetty** and **Mrs. A. Ravallika** for their invaluable support, care and love during this journey. Special thanks to **Dr. Priyanka Manchanda** for her encouragement and support and I would also like to thank my research group - **Govu Radha, Akhil Chandran. P, Sankho Subhra Samanta** and **Suchashrita Mitra** and my colleagues- **Dr. Kaja Sravani** and **M. Christina Nilavu** for their support and cooperation. Lastly, I thank the almighty for all the blessings.

ABSTRACT

Metal-Organic Frameworks (MOFs) are crystalline materials with well-defined and ordered structures. These structures are composed of continuous array of networks created by metal ions or metal clusters and multidentate organic ligands serving as linkers. MOFs are an interesting class of porous materials due to their unique structural characteristics, high surface areas, programmable functionalities and tunable pore sizes. Thus, making MOFs a desirable choice for diverse applications in the fields of science and technology. This thesis mainly focuses on designing new MOFs in addition to exploring existing MOFs for sensing applications. It also emphasizes on employing MOFs for real-world applications rather than restricting their use to conceptual and experimental aspects. Further, this thesis showcases the strategies employed in designing MOF-based chemical sensors for targeted applications. It also demonstrates the application of MOFs in device fabrication, enhancing their feasibility and operational capabilities for practical purposes.

The first chapter of the thesis provides a detailed introduction on porous materials, in particular, MOFs, its design, synthesis and applications. The second chapter describes the characterization techniques used for the studies carried out in this dissertation. The third chapter details the development of a MOF-based breath sensor to monitor the breathing patterns for sleep apnea diagnosis. It is important to highlight that this marks the first-ever report of a flexible MOF-based breath sensor for the obstructive sleep apnea disorders. Furthermore, a proof-of-concept has been demonstrated by developing a smartphone-based prototype utilizing the MOF sensor. In the fourth chapter of the thesis, the work is further extended to fabricate an ultra-low humidity sensor based on MOFs for the detection of trace moisture in ppm levels for glove-box related applications. This section also highlights the potential of MOFs to function as a dual sensor capable of monitoring trace moisture and distinguishing between polar and non-polar solvents. The fifth chapter of the thesis focuses on synthesizing two novel mixed linker MOFs namely **BITSH-1** and **BITSH-2** (Birla Institute of Technology and Science, Hyderabad). The properties of these frameworks are investigated using a wide range of characterization techniques. Further, **BITSH-1** and **BITSH-2** were explored for sensing food spoilage indicators such as putrescine and cadaverine (categorized as biogenic amines) in protein rich foods. This section also elaborates on the design strategies employed in preparing MOF membranes, and assessing their feasibility and practical usage as sensors in food packets for detecting the release of food spoilage indicators released from spoiled fish and cheese samples.

In the sixth chapter of the thesis, the work is further extended to explore **BITSH-1** and **BITSH-2** for the detection of pervasive and harmful compounds such as amines. This section emphasizes on developing multifunctional chemical sensors for the detection of ammonia and discriminative sensing of aliphatic and aromatic amines. It highlights the potential of these frameworks to distinguish chemically similar substances such as aliphatic and aromatic amines possessing the same functionality. Density functional theory (DFT) studies reveal that aliphatic and aromatic amines interact with the MOF systems in distinct manners, resulting in "turn-off" and "turn-on" fluorescence behaviors, respectively. Additionally, mixed-matrix membranes were prepared and examined for on-site detection of ammonia liberated using a lab-scale chemical reaction setup. The seventh chapter of the thesis highlights the significance of developing MOF-based dual sensor for the detection of nicotine, a highly carcinogenic chemical using fluorescence and electrochemical methods. This section also discusses in detail the sensing capability of the MOF sensor for the detection of nicotine in actual cigarette and urine samples. The last chapter of the thesis discusses the conclusions drawn from the aforementioned studies and also provides a concise overview of the future prospects and potential directions for further research.

TABLE OF CONTENTS

CERTIFICATE.....I
DECLARATION.....II
ACKNOWLEDGEMENTS.....III
ABSTRACT…….....IV
TABLE OF CONTENTS…….....VI
LIST OF TABLES.....X
LIST OF FIGURES.....XI
ABBREVIATIONS.....XXIII
CHAPTER 1 Study of metal-organic frameworks (MOFs) for sensing applications.....24
1.1. Introduction.....24
1.2. Design of MOFs…….....25
1.3. Porous structures……..….....27
1.3.1. Zero-dimensional cavities…….....28
1.3.2. One-dimensional channels (1-D) …….....28
1.3.3. Two-dimensional layers (2-D) 31
1.3.4. Three-dimensional motifs (3-D) …….....34
1.4. Classification of porous coordination polymers.....39
1.5. Synthesis of MOFs……..…….....40
1.5.1. Solvothermal methods…….……...41
1.5.2. Alternative methods……42
1.5.3. Electrochemical method…….……...……42
1.5.4. Microwave-assisted method……..……43
1.5.5. Sonochemical method……..……..……...44
1.5.6. Mechanochemical method…….……..…….……45
1.6. Applications of MOFs……..……45
1.6.1. Chemiresistive sensing…….…...…….…...…….…46
1.6.2. Capacitive sensing…….……...…….……...……49
1.6.3. Electrochemical sensing…….…...……...…….……...….51
1.6.4. Fluorescence sensing…….…...…….…...……53
1.7. Research Gaps/Thesis objectives.....58
1.8. Thesis outline.....59

CHAPTER 2 Characterization Techniques……62
2.1. Single crystal X-ray diffraction (SC-XRD) ……62
2.2. Powder X-ray Diffraction (PXRD) ……62
2.3. Thermo Gravimetric Analysis (TGA) ……62
2.4. Brunauer-Emmett-Teller (BET) ……63
2.5. X-ray Photoelectron Spectroscopy (XPS) ……63
2.6. Field Emission Scanning Electron Microscopy (FE-SEM) ……63
CHAPTER 3 MOF based flexible, low-cost chemiresistive device as a respiration sensor for sleep apnea diagnosis……64
3.1. Introduction.....64
3.2. Experimental Section.....66
3.2.1. Materials……66
3.2.2. Synthesis Procedure of HKUST-1……66
3.2.3. MOF-MoS_2 device preparation……67
3.2.4. Details of the Android Application……67
3.3. Results and Discussions.....68
3.4. Conclusions.....81
CHAPTER 4 Fabrication of a low-cost MOF-based sensing device enables detection of ultralow humidity and solvent polarity changes.....82
4.1. Introduction.....82
4.2. Experimental Section.....84
4.2.1. Materials……84
4.2.2. Synthesis of [Eu(BTC)]-MOF……84
4.2.3. Designing Inter-digitated electrodes (IDE)……84
4.2.4. Fabrication of MOF-coated IDE device……85
4.2.5. Details of the custom-built volatile organic compound (VOC) sensing setup……85
4.3. Results and Discussions.....85
4.3.1. Structural details and characterization of the MOF……85
4.3.2. Water adsorption properties……89
4.3.3. Ultra-low humidity sensing studies……90
4.3.4. Sensing mechanism……92
4.3.5. Reliability and stability studies of MOF-coated IDE sensor……93
4.3.6. [Eu(BTC)]- MOF as a polarity sensor……95
4.3.7. MOF-coated IDE as a real-time humidity device……98

4.4. Conclusions.....99
CHAPTER 5 MOF sensors for food safety: ultralow detection of putrescine and cadaverine in protein rich foods.....100
5.1. Introduction.....100
5.2. Experimental Section.....102
5.2.1. Materials……...102
5.2.2. Synthesis of **BITSH-1** and **BITSH-2**……...…102
5.2.3. MOF + PVDF membrane strip synthesis……...103
5.2.4. Photoluminescence (PL) Measurements……...103
5.2.5. Electrochemical measurements……103
5.3. Results and Discussions 104
5.3.1. Structural details and characterization of the MOF…….……...…...…104
5.3.2. Turn-off fluorescence sensing of biogenic amines by **BITSH-1** and **BITSH-2**……...109
5.3.3. Quenching mechanism for the sensing of biogenic amines.…….…….……...110
5.3.4. Studies to support dynamic quenching mechanism…….…….…….……...117
5.3.5. HOMO-LUMO studies…...……...…….……..…120
5.3.6. X-Ray photoelectron spectroscopy (XPS) analysis for biogenic amines detection.....123
5.3.7. Visual evidence for the detection of biogenic amines…….…….……127
5.4. Conclusions.....128
CHAPTER 6 Cobalt Metal-Organic Frameworks and its Mixed-Matrix Membranes for Discriminative Sensing of Amines and On-site Detection of Ammonia.....129
6.1. Introduction.....129
6.2. Experimental Section.....131
6.2.1. Materials……...131
6.2.2. Synthesis of **BITSH-1** and **BITSH-2**……...……131
6.2.3. Photoluminescence (PL) Measurements……...131
6.2.4. Preparation of MOF-based mixed matrix membranes……...131
6.2.5. Electrochemical measurements……132
6.2.6. Computational Methods……132
6.3. Results and Discussions 132
6.3.1. Structural details and characterization of the MOF…..…….……...……132
6.3.2. Photoluminescence Studies…….……136
6.3.3. Studies to support dynamic quenching mechanism…….…….……140
6.3.4. Turn-on fluorescence studies and Limits of Detection (LOD) calculations…….…….…144

6.3.5. X-Ray photoelectron spectroscopy (XPS) studies for the detection of amines……148
6.3.6. Vapochromic sensing……152
6.3.7. Computational investigations and HOMO-LUMO studies……153
6.3.8. On-site detection of ammonia……157
6.4. Conclusions.....160
CHAPTER 7 MOF-based Dual Sensor for Electrochemical and Fluorescence Detection of Nicotine.....161
7.1. Introduction.....161
7.2. Experimental Section.....163
7.2.1. Materials……163
7.2.2. Synthesis of **BITSH-1** and **BITSH-2**……163
7.2.3. Photoluminescence (PL) Measurements……163
7.2.4. Electrochemical measurements……163
7.2.5. Preparation of cigarette and urine samples……164
7.3. Results and Discussions 164
7.3.1. Structural details and characterization of the MOF……164
7.3.2. Fluorescence sensing studies……167
7.3.3. Selectivity and recyclability studies……169
7.3.4. Studies to support dynamic quenching mechanism……171
7.3.5. HOMO-LUMO studies to analyze the sensing mechanism……174
7.3.6. X-Ray photoelectron spectroscopy (XPS) studies for the detection of nicotine……175
7.3.7. Electrochemical sensing studies……176
7.3.8. Real-time sensing studies……180
7.4. Conclusions.....182
Conclusions and Future perspectives.....183
Bibliography.....185
List of Publications and Conferences……204
Awards, Recognitions and Patents……206
Biography of the Candidate……207
Biography of the Supervisor……208

LIST OF TABLES

Table 3.1. A comparison of the response time and support used for various breath sensor materials reported in the literature with the MOF sensor in the present study.....77

Table 4.1. Relative solvent polarity index of the solvents analyzed for the study……...95

Table 4.2. A comparative analysis of MOF-based sensors for the detection of humidity and polarity…….....97

Table 5.1. Crystallographic data for **BITSH-1** and **BITSH-2**……...…….105

Table 5.2. K_D values of **BITSH-1** and **BITSH-2** obtained on incremental additions of PUT (1 mM) at different temperatures…….……...118

Table 5.3. Comparison of different probes, techniques and detection limits for sensing biogenic amines…….122

Table 6.1. Quenching efficiency (QE) of aliphatic amines analyzed for the study……...…...140

Table 6.2. Dynamic constant (K_D) values of **BITSH-1** and **BITSH-2** that were obtained upon the addition of NH_3 solution (10^{-1}M) at different temperatures ranging from 288 K to 308 K…….142

Table 6.3. State of the art of discriminative sensing of amines……...145

Table 6.4. Detection limit (LOD) of aliphatic and aromatic amines analyzed……...……146

Table 6.5. Comparison of fluorescence response and their detection limits of different MOFs used for sensing ammonia…….…….…….147

Table 6.6. HOMO and LUMO energy levels (in eV) of amines obtained from the computational studies…….…….……...…156

Table 7.1. K_D values of **BITSH-1** and **BITSH-2** in response to NIC at different temperatures……...174

Table 7.2. Comparison of electrochemical sensors for nicotine determination….....….179

Table 7.3. Determination of nicotine levels in cigarette and urine samples……....182

LIST OF FIGURES

Figure 1.1. Design of MOF-5 Framework…….....25

Figure 1.2. Varying orientations of linkers and connectors in MOFs……...……26

Figure 1.3. Classification of porous structures according to spatial dimensions……...…27

Figure 1.4. a) A part of one single infinite 3D network, b) Two independent, identical and interpenetrated frameworks. These frameworks are differentiated by "full" and "open" lines. The chemical formula of the compound is $\{[Zn(CN)(NO_3)(tpt)_{2/3}]\cdot 3/4C_2H_2Cl_4\cdot 3/4CH_3OH\}_n$. Tpt units are depicted as three spokes extending from a central point towards the triazine ligands. ZnCNZn units are represented by direct Zn-Zn bonds……28

Figure 1.5. Various motifs of 1D coordination polymers…….29

Figure 1.6. a) The coordination environment around Cu (II) ion and b) Structural view of two-dimensional layers of CPL-1……...…….30

Figure 1.7. Reaction scheme depicting the interaction between $Cd(ClO_4)_2$ and mnvp under varying conditions……....31

Figure 1.8. Various motifs of 2D coordination polymers……...…….…….32

Figure 1.9. (a) Representation of square grid network in $\{[Mn(N_3)_2(bix)_2]\}_n$, (b) coordination mode of the Cu (II) ion in $\{[Cu(bpy)_{2.5}(H_2O)](ClO_4)_2\cdot(H_2O)\cdot(CH_3OH)_{1.5}\}_n$ (water, perchlorate and methanol molecules are omitted for clarity, (c) bilayer architecture (terminal ligands are omitted, solid lines represent the “chain makers”, dashed lines represent the “linker between the chains” and black circles represent the Cu (II) centers)…….……..33

Figure 1.10. (a) Representation of brick wall motif in $\{[NdCl_3(dppeO_2)_{1.5}]\}_n$, (b) representation of parquet floor motif in $\{[Nd(NO_3)_3(dppeO_2)_{1.5}]\}_n$ and (c) depicting pseudo-honeycomb motif in $\{[Pr(NO_3)_3(dppeO_2)_{1.5}]\}_n$……...……...……34

Figure 1.11. Structural patterns of 3D- coordination polymers……...…….35

Figure 1.12. (a) Coordination arrangement in $\{[Cd(3,3\text{-azdb})_2](H_2NMe_2)(NH_4)\}n$ depicting large cavities and (b) schematic illustration of the diamondoid network in $\{[Cd(3,3\text{- azdb})_2](H_2NMe_2)(NH_4)\}_n$……...…….36

Figure 1.13. Representation of (a) cubical unit in $\{[Cu(SiF_6)(4,4\text{-bpy})_2]\cdot 8H_2O\}n$ and (b) cavities in $\{[Cu(SiF_6)(4,4\text{-bpy})_2]\cdot 8H_2O\}n$ (water molecules omitted for clarity) (Cu ions in blue, Si atom in green and nitrogen atoms in red)……..……...……..37

Figure 1.14. (a) Coordination arrangement of the cobalt binuclear unit in {[Co(terephthalate)(4,4-bpy)]}n (b) View of Co(terephthalate) sheet and (c) three-dimensional structural view……...37

Figure 1.15. MOF-5 based Iso-reticular MOFs (left) and functionalization of BDC struts (right) ……...38
Figure 1.16. Categorization of porous compounds into three generations: 1-st, 2nd, and 3rd....39
Figure 1.17. Schematic representation of solvothermal synthesis methods of MOFs……...42
Figure 1.18. Schematic representation of electrochemical synthesis methods…..……..….43
Figure 1.19. Schematic representation of the synthetic procedure using microwave-assisted method…….……44
Figure 1.20. Schematic representation of the synthetic procedure using sonochemical method…….……...…….….44
Figure 1.21. Schematic representation of the synthetic procedure using mechanochemical method…….….45
Figure 1.22. (a) ZIF-67 MOF structure and (b) response-recovery curve of the ZIF-67 sensor towards formaldehyde…….……...47
Figure 1.23. Schematic illustration of (a) the crystal structure of $Cu_3(HHTP)_2$ and b) the preparation of $Cu_3(HHTP)_2$ thin-film gas sensors (left). (Right) the gas-sensing performances of $Cu_3(HHTP)_2$-xC: a) the response and recovery curves for different concentrations of NH_3, b) the response-concentration relationship on a log-log scale, c) the response and recovery time curves for 100 ppm NH_3, d) bar graph representation of responses of $Cu_3(HHTP)_2$-10C to various reducing gases, e) Comparison of response-recovery time to 100 ppm NH_3 and f) Comparison of responses to NH_3 with varying concentrations……..…….....48
Figure 1.24. Sensing experiments of the MOF sensor towards different concentrations of H_2S (a) 100-1000 ppb with insets depicting the linear response for the corresponding range with inset depicting selectivity studies of the MOF sensor towards H_2S. (b) Capacitive responses of Mg-MOF-74-based capacitive gas sensor upon exposure to different concentrations of CO_2. (c) Illustration of the interactions between MOF and analyte before and after ethylenediamine functionalization. (d) Capacitive sensing experiments of MFM-300 MOF sensor towards the detection of SO_2 in the concentration range of 75 to 1000 ppb with inset depicting linear response for the corresponding range, (e) stability studies of the sensor SO_2 over a period of 24 days (f) selectivity of the MFM-300 MOF sensor towards SO_2 vs other gases at 1000 ppb…...50
Figure 1.25. (a) Electrochemical response of the NH_2-MIL-53(Cr) modified glassy carbon electrode (GCE) investigated at different concentrations of Pb^{2+}, SEM images of NH_2-MIL-53(Cr) MOF (inset), (b) DPV curves recorded for different concentrations of

2,4-DCP ranging from 0.04 to 1.0 μM in a 0.1 M PBS solution (pH 7.0), linear calibration curve of peak current and concentration of 2,4-DCP (inset)…….52
Figure 1.26. (a) Schematic representation of the various photophysical processes. (b) The illustration of the possible sensing mechanisms of luminescent MOF-based sensors……..……54
Figure 1.27. Schematic representation of a) PET, b) ICT, c) FRET mechanisms.…….55
Figure 1.28. (a) The ABAB packing mode of the Eu-MOF, (b) schematic representation of the MOF sensing behavior towards Cu^{2+} and UO_2^{2+} metal ions. Luminescence spectra of the MOF towards increasing additions of (c) Cu^{2+} and (d) UO_2^{2+} metal ions…….57
Figure 1.29. (a) Depiction of hydrogen-bonding interaction between the acetophenone molecule (shown in blue) and the host framework, (b, c) 3D representation of the framework after the introduction of acetophenone molecules along the a and c axial directions, (d) solvochromic behavior of the framework towards different solvents and solvochromic behavior of the MOF towards different ketones……..….58
Figure 3.1. Schematic illustration of HKUST-1 synthesis and its crystal structure…….…….69
Figure 3.2. (a) Comparison of the experimental and simulated XRPD patterns of HKUST-1, (b) TGA profile of as-synthesized HKUST-1 crystals, N2 sorption isotherm for the (c) pristine and (d) grinded HKUST-1 samples. N_2 adsorption isotherm of HKUST-1, (e) Pore size distribution of activated Cu-BTC MOF, and (f) the comparison of XRPD pattern of as-synthesized HKUST-1 crystals, HKUST-1 sample drop casted on MoS_2, and HKUST-1 sample after exposure to water for 24 h……..…70
Figure 3.3. Schematic illustration of growing MoS_2 on a cellulose paper substrate and drop casting of MOF powder on MoS_2 support for device fabrication…….……71
Figure 3.4. SEM images of (a) HKUST-1 single crystals, (b) MoS_2, (c) HKUST-1 grinded sample drop casted on MoS_2 support and XPS data of HKUST-1-MoS_2 sample (d) full XPS spectrum, (e) Cu 2p XPS spectrum and (f) Mo 3d S 2s XPS spectrum…….……72
Figure 3.5. EDX spectrum and elemental data of Cu-BTC MOF (top), XPS spectrum of HKUST-1 MOF on MoS_2 showing binding energies for a) S 2p, b) O 1-s and c) C 1-s (bottom)……73
Figure 3.6. HKUST-1-MoS_2 fabricated sensor for breath sensing (top), and breath sensing experiments showing variation in current in response to different types of breaths; normal breath, slow breath, fast breath and deep breath (bottom) ……74

Figure 3.7. (a) Breath cycles showing five breath cycles of three breaths each, (b) three breath iterative breathing pattern for around 1000 sec, breath sensing experiments for (c) hydrated, and (d) dehydrated breaths……75
Figure 3.8. Breath sensing experiments showing stability of HKUST-1-MoS_2 sensor over a period of 4 weeks…….……76
Figure 3.9. (a) Breath sensing experiments for pristine MoS_2, and (b) Response time of HKUST-1-MoS_2 breath sensor……..……77
Figure 3.10. Breath sensing mechanism in HKUST-1-MoS_2 integrated device. (a) adsorption and transfer of water molecules from MOF to MoS_2 layer and (b) mechanism of proton conduction in the MOF layer involving proton transfer from acidic water molecules coordinated to the metal cluster to the solvent molecules present in the channels. Only one cluster has been shown for clarity…….79
Figure 3.11. Schematic illustration of the face mask with the embedded HKUST-1-MoS_2 device showing real time operation using a smartphone device……80
Figure 3.12. Different types of signals shown by the android app; normal and abnormal (top) and alert (bottom)…….……81
Figure 4.1. (a) Coordination environment of [Eu(BTC)]- MOF. Packing diagrams of [Eu(BTC)]- MOF (b) along the c axis, (c) along the b axis and (d) along a axis. C, H, O, and Eu atoms have been shown in gray, white, red, and green, respectively.....86
Figure 4.2. (a) Comparison of simulated and as-synthesized PXRD patterns of [Eu(BTC)]- MOF to confirm the bulk phase purity, (b) SEM images of [Eu(BTC)]- MOF. (c) N_2 adsorption isotherm of the MOF at 77 K, and (d) thermogravimetric analysis (TGA) of as-synthesized and activated crystals of [Eu(BTC)]- MOF…….87
Figure 4.3. (a) Energy-dispersive X-ray spectroscopy (EDS) spectrum of the MOF, (b) EDS analysis of [Eu(BTC)]- MOF showing the atomic and weight % of the elements present in the MOF system, and (c) Elemental mapping of [Eu(BTC)]- MOF depicting the presence of (a) Eu, (b) C, and (c) O elements……....88
Figure 4.4. X-ray photoelectron spectroscopy (XPS) analysis of [Eu(BTC)]- MOF depicting (a) XPS survey spectra, (b) Eu 3d spectrum, (c) C 1-s spectrum, and (d) O 1-s spectrum……88
Figure 4.5. (a) PXRD analysis of as-synthesized with simulated patterns, water exchanged and activated crystals of [Eu(BTC)]- MOF. (b) Water sorption isotherm of [Eu(BTC)]- MOF…...89
Figure 4.6. (a) Schematic illustration of device fabrication. (b) Custom-built setup for VOC sensing with LCR meter…….……..……..……90

Figure 4.7. (a) MOF-coated IDE sensor response (a) towards ultra-low concentrations of water vapor at 23 ℃, (b) towards increased concentrations of water vapor measured at 23 ℃, (c) Linear response of the sensor towards the water in the concentration range of 10 - 100 ppm, (d) Linear response of the sensor towards the water in the concentration range of 100 - 400 ppm, (e) Response curves of the sensor towards increasing relative humidity levels (% RH) and (f) response time of the sensor towards water……..…..…92
Figure 4.8. (a) Capacitive response of the sensor showing recyclability towards 1500 ppm concentration of water (b) Stability cycles of the sensor towards water over a period of 4 weeks (c) Humidity hysteresis curve of the sensor…….……..…….94
Figure 4.9. Vapor adsorption isotherm of [Eu(BTC)]- MOF towards solvents……..…...…...96
Figure 4.10. (a) Capacitance response of the sensor towards water and other solvents (Ethanol, methanol, acetonitrile, acetone, toluene, and hexane) and (b) Illustration of an increasing trend of the capacitive response of the sensor in agreement with the polarities of the solvents……...97
Figure 4.11. Illustration of operation of real-time humidity sensor in response to humidity depicted with (a) LED OFF (in the presence of negligible humidity levels) and (b) LED ON (in the presence of humidity) …….…….…….……99
Figure 5.1. Chemical structures of the biogenic amines used in the present study…….……102
Figure 5.2. Synthesis procedure for **BITSH-1** and **BITSH-2** MOFs…….……....104
Figure 5.3. Comparison of the experimental and simulated PXRD patterns of (a) **BITSH-1** and (b) **BITSH-2**. TGA profile of as-synthesized and activated (c) **BITSH-1** and (d) **BITSH-2** crystals……106
Figure 5.4. N_2 adsorption isotherm of a) **BITSH-1** and b) **BITSH-2** and pore diameter of c) **BITSH-1** and d) **BITSH-2** samples. SEM images of (e, f) **BITSH-1** and (g, h) **BITSH-2** crystals……107
Figure 5.5. Packing diagrams of **BITSH-1** along the b and a *axis* (a and b) and **BITSH-2** along the c and a *axis* (c and d), respectively…….108
Figure 5.6. (a) UV absorption spectra and PL emission spectra of **BITSH-1** and **BITSH-2** systems. Decrease in the PL emission intensity of **BITSH-1** (excitation at 278 nm) and **BITSH-2** (excitation at 280 nm) upon incremental additions of putrescine (b and d) and cadaverine (c and e), respectively. (f) Quenching efficiency of biogenic amines on addition to **BITSH-1** and **BITSH-2** systems (incremental addition of 200 mL of each analyte in ethanol medium) 109
Figure 5.7. Quenching efficiencies of analytes in the concentration range of 0-10 μM on addition to (a) **BITSH-1** and (b) **BITSH-2**. Comparison of the PXRD patterns of as-synthesized (c) **BITSH-1** and (d) **BITSH-2** in the presence of biogenic amines (BA) obtained

by collecting the sample through centrifugation after fluorescence experiments and collected samples were dried at 100 °C……..……..…110
Figure 5.8. PL emission spectra of (a) **BITSH-1** and (e) **BITSH-2** against the incremental additions of 1 mM of putrescine (PUT) in ethanol, (λex = 278 nm). Detection limit (LOD) of PUT with respect to (b) **BITSH-1** and (f) **BITSH-2**. Linear fit of Stern-Volmer plot of (c) **BITSH-1** and (g) **BITSH-2** in response to PUT. Quenching efficiency of PUT with respect to (d) **BITSH-1** and (h) **BITSH-2**……...……111
Figure 5.9. PL emission spectra of (a) **BITSH-1** and (e) **BITSH-2** against the incremental additions of 1 mM of cadaverine (CAD) in ethanol, (λex = 278 nm). Detection limit (LOD) of CAD with respect to (b) **BITSH-1** and (f) **BITSH-2**. Linear fit of Stern-Volmer plot of (c) **BITSH-1** and (g) **BITSH-2** in response to CAD. Quenching efficiency of CAD with respect to (d) **BITSH-1** and (h) **BITSH-2**…….....112
Figure 5.10. PL emission spectra of (a) **BITSH-1** and (e) **BITSH-2** against the incremental additions of 1 mM of spermine (SPM) in ethanol, (λex = 278 nm). Detection limit (LOD) of SPM with respect to (b) **BITSH-1** and (f) **BITSH-2**. Linear fit of Stern-Volmer plot of (c) **BITSH-1** and (g) **BITSH-2** in response to SPM. Quenching efficiency of SPM with respect to (d) **BITSH-1** and (h) **BITSH-2**……...……113
Figure 5.11. PL emission spectra of (a) **BITSH-1** and (e) **BITSH-2** against the incremental additions of 1 mM of spermidine (SPD) in ethanol, (λex = 278 nm). Detection limit (LOD) of SPD with respect to (b) **BITSH-1** and (f) **BITSH-2**. Linear fit of Stern-Volmer plot of (c) **BITSH-1** and (g) **BITSH-2** in response to SPD. Quenching efficiency of SPD with respect to (d) **BITSH-1** and (h) **BITSH-2**……...……...……114
Figure 5.12. PL emission spectra of (a) **BITSH-1** and (e) **BITSH-2** against the incremental additions of 1 mM of tyramine (TYRM) in ethanol, (λex = 278 nm). Detection limit (LOD) of TYRM with respect to (b) **BITSH-1** and (f) **BITSH-2**. Linear fit of Stern-Volmer plot of (c) **BITSH-1** and (g) **BITSH-2** in response to TYRM. Quenching efficiency of TYRM with respect to (d) **BITSH-1** and (h) **BITSH-2**…...……...115
Figure 5.13. PL emission spectra of (a) **BITSH-1** and (e) **BITSH-2** against the incremental additions of 1 mM of tryptamine (TRYP) in ethanol, (λex = 278 nm). Detection limit (LOD) of TRYP with respect to (b) **BITSH-1** and (f) **BITSH-2**. Linear fit of Stern-Volmer plot of (c) **BITSH-1** and (g) **BITSH-2** in response to TRYP. Quenching efficiency of TRYP with respect to (d) **BITSH-1** and (h) **BITSH-2**……...……....116
Figure 5.14. Stern Volmer plot of a) **BITSH-1** and b) **BITSH-2** on incremental additions of PUT (1 mM) recorded at different temperatures…….117

Figure 5.15. Linear fit of Stern-Volmer plot of **BITSH-1** and **BITSH-2** in response to PUT at different temperatures (a, d) 288 K (b, e) 293 K and (c, f) 298 K respectively…….118
Figure 5.16. UV-vis spectra of **BITSH-1** on addition of (a) PUT (b) CAD (c) SPM (d) SPD (e) TYRM (f) TRYP in ethanol medium…….……119
Figure 5.17. UV-vis spectra of **BITSH-1** on addition of (a) PUT (b) CAD (c) SPM (d) SPD (e) TYRM (f) TRYP in ethanol medium…….……...…….119
Figure 5.18. Spectral overlap between absorption spectra of analytes and emission spectra of both the MOF systems……120
Figure 5.19. Cyclic Voltammogram (CV) of (a) **BITSH-1** and (b) **BITSH-2** recorded in acetonitrile medium……121
Figure 5.20. Schematic representation of the HOMO (π) and LUMO (π*) energy levels of **BITSH-1** and the HOMO energy levels of the biogenic amines analyzed….……121
Figure 5.21. XPS survey spectrum (a) and Co 2p XPS spectrum (b) of **BITSH-1** sample, XPS survey spectrum (c) and Co 2p XPS spectrum (d) of **BITSH-2** sample……...123
Figure 5.22. (a, e) N 1-s XPS spectrum of **BITSH-1** and **BITSH-2** on addition of PUT and (b, f) deconvoluted spectrum of **BITSH-1 + PUT** and **BITSH-1 + PUT**. (c, g) N 1-s XPS spectrum of **BITSH-1** and **BITSH-2** on addition of CAD and (d, h) deconvoluted spectrum of **BITSH-1 + CAD** and **BITSH-2 + CAD**…….……124
Figure 5.23. N 1-s XPS spectrum of **BITSH-1** and on addition of (a) SPM and (e) SPD. Deconvoluted spectrum of (b) **BITSH-1 + SPM** and (f) **BITSH-1 + SPD**. N 1-s XPS spectrum of **BITSH-2** on addition of (c) SPM and (g) SPD. Deconvoluted spectrum of (d) **BITSH-2 + SPM** and (h) **BITSH-2 + SPD**……...……125
Figure 5.24. N 1-s XPS spectrum of **BITSH-1** and on addition of (a) TYRM and (e) TRYP. Deconvoluted spectrum of (b) **BITSH-1 + TYRM** and (f) **BITSH-1 + TRYP**. N 1-s XPS spectrum of **BITSH-2** on addition of (c) TYRM and (g) TRYP. Deconvoluted spectrum of (d) **BITSH-2 + TYRM** and (h) **BITSH-2 + TRYP**…….…….……...……126
Figure 5.25. Visual detection of biogenic amines from the fish (top) and cheese (bottom) samples using MOF + polymer membrane strips as real-time sensors: (a) the **BITSH-1 + PVDF** strip, (b) the **BITSH-2 + PVDF** strip, and (c) only the PVDF strip before exposure and (d, e, and f) show the corresponding sensor strips after exposure to the food samples……127
Figure 6.1. Packing diagrams of (a) **BITSH-1** and (b) **BITSH-2** shown along the *c* axes, where cobalt, carbon, oxygen, nitrogen and hydrogen atoms are shown in yellow, dark grey, red, blue, and white colors, respectively. All the solvent molecules have been omitted for clarity. Green spheres represent the guest-accessible void space in both the MOFs. (c) comparison of

simulated and experimental PXRD patterns of **BITSH-1** and **BITSH-2**, and (d) UV-vis absorption and emission spectra for **BITSH-1** and **BITSH-2** MOF crystals in ethanol……133
Figure 6.2. SEM images of as-synthesized (a) **BITSH-1** crystals and (b) **BITSH-2** crystals. TGA analysis of as-synthesized (blue) and activated (pink) (c) **BITSH-1** crystals, (d) **BITSH-2** crystals……134
Figure 6.3. N_2 adsorption isotherm of activated crystals of (a) **BITSH-1** and (b) **BITSH-2** and corresponding pore diameter of (c) **BITSH-1** and (d) **BITSH-2** crystals collected at 77 K, (e) XPS survey spectrum of **BITSH-1** crystals and its corresponding (f) Co 2p XPS spectrum exhibiting the presence of Co^{2+} (g) XPS survey spectrum of **BITSH-2** crystals and its corresponding (h) Co 2p XPS spectrum exhibiting the presence of Co^{2+}……135
Figure 6.4. Emission spectra of (a) **BITSH-1** and (e) **BITSH-2** recorded upon the incremental additions of 10^{-1} M of Ammonia (NH_3) in ethanol medium. Quenching efficiency of (b) **BITSH-1** and (f) **BITSH-2** on addition of NH_3. Linear stern-Volmer plot of (c) **BITSH-1** and (g) **BITSH-2** fluorescence intensity against the addition of NH_3. Detection limit (LOD) obtained on addition of NH_3 to (d) **BITSH-1** and (h) **BITSH-2**……137
Figure 6.5. Emission spectra of (a) **BITSH-1** and (e) **BITSH-2** recorded upon the incremental additions of 10^{-1} M of Methylamine (MA) in ethanol medium. Quenching efficiency of (b) **BITSH-1** and (f) **BITSH-2** on addition of MA. Linear stern-Volmer plot of (c) **BITSH-1** and (g) **BITSH-2** fluorescence intensity against the addition of MA. Detection limit (LOD) obtained on addition of MA to (d) **BITSH-1** and (h) **BITSH-2**……138
Figure 6.6. Emission spectra of (a) **BITSH-1** and (e) **BITSH-2** recorded upon the incremental additions of 10^{-1} M of Triethylamine (TEA) in ethanol medium. Quenching efficiency of (b) **BITSH-1** and (f) **BITSH-2** on addition of TEA. Linear stern-Volmer plot of (c) **BITSH-1** and (g) **BITSH-2** fluorescence intensity against the addition of TEA. Detection limit (LOD) obtained on addition of TEA to (d) **BITSH-1** and (h) **BITSH-2**……139
Figure 6.7. Photoluminescence emission spectra of **BITSH-2** showing quenching upon the incremental additions of 10^{-1}M of (a) Ammonia (NH_3) (b) Methylamine (MA) and (c) Triethylamine (TEA) in ethanol medium……140
Figure 6.8. Stern-Volmer plots of **(a) BITSH-1** and **(b) BITSH-2** that were obtained upon the addition of NH_3 solution (10^{-1}M), recorded at 288 K, 298 K and 308 K temperatures……141
Figure 6.9. Linear fitting of Stern-Volmer plots in the concentration range of 0-0.25 mM upon addition of NH_3 solution (10^{-1}M) to **BITSH-1** and **BITSH-2** recorded at three different temperatures ranging from (a, d) 288 K, (b, e) 298 K and (c, f) 308 K respectively……141

Figure 6.10. UV-vis absorption spectra of **BITSH-1** and **BITSH-2** upon incremental additions of (a, d) Ammonia (NH_3) solution, (b, e) Methylamine (MA) and (c, f) Triethylamine (TEA) in ethanol medium respectively…….……142
Figure 6.11. UV-vis absorption spectra of **BITSH-1** and **BITSH-2** upon incremental additions of (a, c) Aniline (AN) solution and (b, d) N-methylaniline **(N-MA)** solution in ethanol medium respectively…….143
Figure 6.12. Spectral overlap between the absorption spectra of aliphatic and aromatic amines analyzed for the study and the emission spectra of **BITSH-1** and **BITSH-2**……...144
Figure 6.13. Fluorescence sensing experiments of **BITSH-1** MOF showing quenching of fluorescence intensity with aliphatic amines a) NH_3, b) methylamine, and c) triethylamine and enhancement of fluorescence intensity with aromatic amines, d) aniline, e) N-methylaniline, and f) bar graph showing quenching efficiencies of both the MOFs with aliphatic amines….144
Figure 6.14. Detection limit (LOD) obtained from the linear fit of Intensity Vs [Q] plot of **BITSH-1** (top) upon additions of (a) Aniline (AN) and (b) N-methylaniline (N-MA) and **BITSH-2** (bottom) upon additions of (c) Aniline (AN) and (d) N-methylaniline (N-MA) solutions in ethanol medium……...146
Figure 6.15. PXRD patterns of (a) **BITSH-1** and (b) **BITSH-2** in the presence of aliphatic amines and aromatic amines showing the structural integrity of the framework…….147
Figure 6.16. (a) N 1-s XPS spectral analysis of pristine **BITSH-1** and in the presence of Ammonia (NH_3) (b) Deconvoluted N 1-s spectrum of **BITSH-1 + NH_3**. (c) N 1-s XPS spectral analysis of pristine **BITSH-2** and in the presence of Ammonia (NH_3) (d) Deconvoluted N 1-s spectrum of **BITSH-2 + NH_3**…….……148
Figure 6.17. (a) N 1-s XPS spectral analysis of pristine **BITSH-1** and in the presence of Methylamine (MA) (b) Deconvoluted N 1-s spectrum of **BITSH-1 + MA**. (c) N 1-s XPS spectral analysis of pristine **BITSH-2** and in the presence of Methylamine (MA) (d) Deconvoluted N 1-s spectrum of **BITSH-2 + MA**…….……149
Figure 6.18. (a) N 1-s XPS spectral analysis of pristine **BITSH-1** and in the presence of Triethylamine (TEA) (b) Deconvoluted N 1-s spectrum of **BITSH-1 + TEA**. (c) N 1-s XPS spectral analysis of pristine **BITSH-2** and in the presence of Triethylamine (TEA) (d) Deconvoluted N 1-s spectrum of **BITSH-2 + TEA**…….……...……150
Figure 6.19. (a) N 1-s XPS spectral analysis of pristine **BITSH-1** and in the presence of Aniline (AN) (b) Deconvoluted N 1-s spectrum of **BITSH-1 + AN**. (c) N 1-s XPS spectral analysis of pristine **BITSH-2** and in the presence of Aniline (AN) (d) Deconvoluted N 1-s spectrum of **BITSH-2 + AN**……...151

Figure 6.20. (a) N 1-s XPS spectral analysis of pristine **BITSH-1** and in the presence of N-Methylaniline (N-MA) (b) Deconvoluted N 1-s spectrum of **BITSH-1 + N-MA**. (c) N 1-s XPS spectral analysis of pristine **BITSH-2** and in the presence of N-Methylaniline (N-MA) (d) Deconvoluted N 1-s spectrum of **BITSH-2 + N-MA**……..…...152
Figure 6.21. The visible change in the color of MOF pellets upon exposure to ammonia, methylamine (MA), and triethylamine (TEA)……....153
Figure 6.22. Cyclic Voltammetry plot of **(a) BITSH-1** and **(b) BITSH-2** obtained in acetonitrile medium with scan rate of 100 mV/s……154
Figure 6.23. Zoom-in view optimized structure of AN@**BITSH-1** displaying the interaction of (a) a hydrogen bonding between the nitrogen of aniline and hydrogen of an H_2O molecule coordinated to a Co site of **BITSH-1** (b) a hydrogen bonding between the hydrogen of aniline and oxygen of COO- group coordinated to a Co site of **BITSH-1**. (c) Optimized structure of NH_3@**BITSH-1**, displaying no hydrogen binding (only weak dispersive interactions are expected). Colour codes C- Black, Co- blue, H- white, O- red, C of analytes- maroon and N of analytes- cyan…….……....155
Figure 6.24. (a) The alignment of highest occupied molecular orbitals (HOMOs) and lowest unoccupied molecular orbitals (LUMOs) of adsorbates (Ammonia, methyl amine, triethylamine, aniline, and N-methyl aniline) computed at DZVP/PBE+D3 level of theory with experimentally obtained HOMO-LUMO of MOF. Optimized structures of (b) Aniline@**BITSH-1** and (c) NH_3@**BITSH-1**.....157
Figure 6.25. Flexible MOF membranes of **BITSH-2** (a) before and (b) after exposure to the vapors of ammonia. Illustration of experimental setup (c) before and (d) after the exposure of MOF membranes to ammonia vapors……158
Figure 6.26. Experimental setup for ammonia sensing from a chemical reaction using MOF membranes a) before the experiment and a') after the experiment; MOF membrane color b) before and b') after exposure to the vapors of ammonia and c-g depicts the flexibility of the MOF membranes before ammonia exposure and c'-g' depicts the MOF membranes flexibility after ammonia exposure…….……159
Figure 7.1. Chemical structure of nicotine (top). Synthesis and packing diagrams for **BITSH-1** and **BITSH-2** (bottom)……164
Figure 7.2. PXRD patterns of (a) **BITSH-1** and (b) **BITSH-2**. TGA plot of as-synthesized (c) **BITSH-1** and (d) **BITSH-2**. PXRD patterns of as-synthesized and activated (e) **BITSH-1** and (f) **BITSH-2**……165

Figure 7.3. N_2 adsorption isotherm of (a) **BITSH-1** and (b) **BITSH-2** and pore diameter of (c) **BITSH-1** and (d) **BITSH-2** MOF samples……166
Figure 7.4. SEM images of (a, b) **BITSH-1** and (c, d) **BITSH-2**. Energy-dispersive X-ray spectroscopy (EDAX) spectrum of (e) **BITSH-1** and (f) **BITSH-2**. EDAX analysis of (g) **BITSH-1** and (h) **BITSH-2**. Elemental mapping images of (i-l) **BITSH-1** and (m-p) **BITSH-2**……...…….…….……167
Figure 7.5. (a) UV-vis absorption spectra and PL emission spectra of **BITSH-1** and **BITSH-2**. PXRD patterns of (b) **BITSH-1** and (c) **BITSH-2** recorded after exposure to nicotine…...168
Figure 7.6. Photoluminescence (PL) emission spectra of **BITSH-1** (a) and **BITSH-2** (b) on incremental additions of 0.1 M NIC in ethanol medium…….……168
Figure 7.7. Quenching efficiency of nicotine (NIC) obtained from PL measurements of (a) **BITSH-1** and (b) **BITSH-2** on incremental additions of 0.1 M NIC. Detection limit (LOD) of NIC obtained from PL measurements of (a) **BITSH-1** and (b) **BITSH-2**. Linear fit of Stern-Volmer plot of (a) **BITSH-1** and (b) **BITSH-2** in response to NIC……169
Figure 7.8. Recyclability studies of **BITSH-1**……170
Figure 7.9. Selectivity studies of **BITSH-1** on addition of 0.1 M (a) sodium chloride (NaCl), (b) potassium chloride (KCl), (c) ammonium chloride (NH_4Cl), (d) glucose (Glu), (e) dopamine (DOP) and (f) uric acid (UA) ……..……171
Figure 7.10. Spectral overlap between absorption spectra of NIC and emission spectra of both the MOF systems……172
Figure 7.11. UV-vis spectra of (a) **BITSH-1** and (b) **BITSH-2** on addition of NIC in ethanol medium. Stern Volmer plot of (c) **BITSH-1** and (d) **BITSH-2** on incremental additions of NIC recorded at different temperatures…….……173
Figure 7.12. Linear fit of Stern-Volmer plot of **BITSH-1** and **BITSH-2** in response to NIC at different temperatures (a, d) 288 K (b, e) 293 K and (c, f) 298 K respectively…….174
Figure 7.13. Cyclic Voltammogram (CV) of (a) **BITSH-1** and (b) **BITSH-2** recorded in acetonitrile medium……175
Figure 7.14. Schematic representation of electron transfer between HOMO (π) energy levels of **BITSH-1** and HOMO energy levels of NIC……...175
Figure 7.15. N 1-s XPS spectrum of (a) **BITSH-1** and (c) **BITSH-2** on addition of NIC. Deconvoluted spectrum of (b) **BITSH-1 + NIC** and (d) **BITSH-2 + NIC**…….…….……176
Figure 7.16. Cyclic voltammetry response of MOF/GCE, bare GCE in the absence and presence of nicotine, recorded in 0.1 M PBS (pH 7.04) at a scan rate of 100 mV/s….……177

Figure 7.17. (a) Cyclic voltammetry response of MOF/GCE recorded in 0.1 M PBS (pH 7.04) in the presence of 10 µM NIC at different scan rates ranging from 20 mV/s to 200 mV/s, (b) linear relationship between peak current and scan rate……....178
Figure 7.18. (a) Square wave voltammetry response of MOF/GCE recorded in 0.1 M PBS (pH 7.04) on the addition of nicotine in the concentration range of 0.25 µM to 2.49 µM and (b) calibration plot of current response vs. concentration of nicotine……...179
Figure 7.19. (a) Square wave voltammetry response of MOF/GCE recorded in 0.1 M PBS (pH 7.04) on the addition of nicotine in the concentration range of 1.25 µM to 47.62 µM. (b) Amperometric response of MOF/GCE recorded in 0.1 M PBS buffer (pH 7.04) on the addition of nicotine (2 µM) and 100-fold excess concentration of interferents at an applied potential of +0.85 V. Calibration curve of nicotine used for calculating the recovery concentrations of nicotine in (c) cigarette and (d) urine samples…….....….181

ABBREVIATIONS

g	gram
mg	milligram
µg	microgram
M	molarity
mM	millimolar
µM	micromolar
nM	nanomolar
m	metre
cm	centimetre
mm	millimetre
µm	micrometre
nm	nanometre
ppm	parts per million
ppb	parts per billion
V	volts
eV	electron volt
P	pressure
v	volume
L	litre
ml	millilitre
µL	microlitre
s	seconds
min	minutes
h	hours
λ	wavelength (usually in nm)
θ	theta
K	kelvin
℃	degree Celsius
%	percentage
Å	angstrom

CHAPTER 1

Study of Metal-Organic Frameworks (MOFs) for Sensing Applications

1.1. Introduction

Porous solids are materials with well-defined pores that enables guest molecules to pass through in a reversible manner without altering the characteristics of the pores. Based on their pore sizes, porous materials are divided into three groups - microporous materials with pore size less than 20 Å, mesoporous solids with pore sizes in the range of 20-500 Å, and macroporous solids with large pore sizes (more than 500 Å).[1,2] Porous materials can be further categorized into three types on the basis of their composition: pure inorganic materials such as zeolites, organic materials like activated carbons, and inorganic-organic hybrid materials such as metal-organic frameworks (MOFs). Porous materials have garnered significant interest from material chemists due to their unique properties and their potential use for various applications such as gas storage, separation and catalysis.

Zeolites are inorganic microporous crystalline structures with a three-dimensional arrangement. They are made up of hydrated alkaline or alkaline-earth aluminosilicates, with the general formula $M^{n+}_{x/n}[(AlO_2)_x(SiO_2)_y]^{x-}.wH_2O$ (where, M = metal).[3-5] The framework is constructed using TO_4 tetrahedra (T= Al, Si) that share corners by establishing a network of interconnected tunnels or cages that can accommodate water molecules and M ions. A rigid porous framework is obtained by removing the water molecules from the channels. Due to their porous nature and high stability, zeolites have been used for numerous applications including gas separation and catalytic processes. However, a significant disadvantage of zeolites is their strong binding to the guest molecules, making the removal of guest molecules challenging.[6]

Activated carbons are a class of porous organic materials with substantial open porosity and a significant specific surface area. The fundamental structural characteristic is a twisted helical arrangement of defective hexagonal carbon layers, interconnected by aliphatic bridging units. Basic functional groups and hetero elements are integrated into the network and are attached to the outer edges of the carbon layers. However, the non-uniform porosity and structural disorderness of activated carbons limit their applicability as materials for the selective sorption and separation of guest molecules.

There have been advancements in the development of inorganic-organic hybrid porous coordination polymers with unique properties and ordered networks which are beyond the

scope of conventional porous materials like zeolites and activated carbons. Metal-organic frameworks (MOFs) is a burgeoning class of hybrid porous materials that exhibits fundamental characteristics such as strong bonding, robustness, high surface areas and ease of structural tunability.[7] Moreover, these solids also possess a high degree of crystallinity, which is a crucial for accurately establishing structure-property relationships. MOFs can be defined as a class of porous crystalline materials which are formed by the self-assembly of metal ions/clusters coordinated to multifunctional organic ligands. Owing to their high surface area, stability, design flexibility, high porosity, MOFs are desirable for various applications such as gas separation, storage, catalysis, sensing, drug delivery, etc.[8-13] The fine control over structure tunability and pore size makes MOFs better candidates than other conventional porous systems like zeolites and activated carbons. The idea of constructing hybrid materials with permanent porosity led to the synthesis of MOF-5 which is known as one of the very early MOF materials reported in literature. MOF-5 forms a regular Zn_4O tetrahedron with single O atom binding to four Zn atoms. Each Zn atom of a tetrahedron is further binded to CO_2 groups of BDC (benzene dicarboxylic acid) resulting in $Zn_4(O)(CO_2)_6$ cluster.[14] **(Figure 1.1)**.

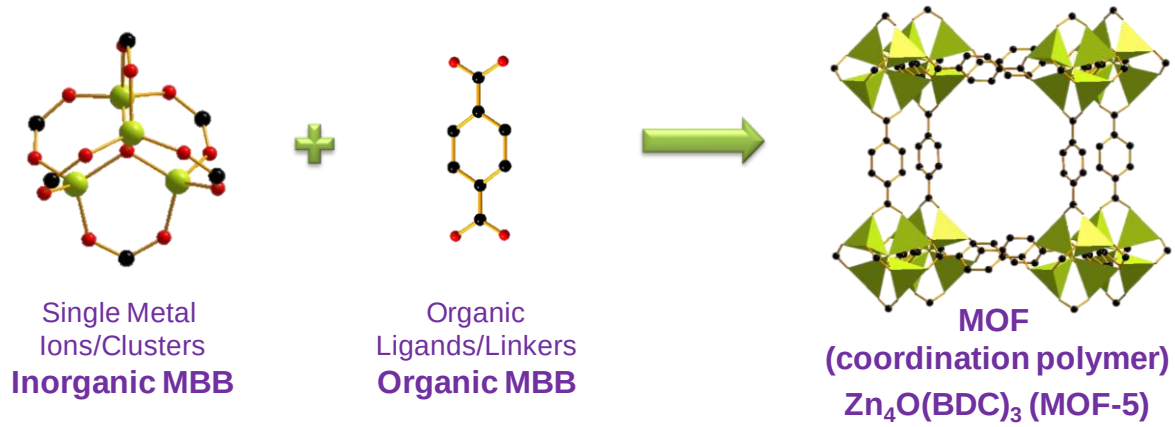

Figure 1.1. Design of MOF-5 framework.

1.2. Design of MOFs

MOFs consist of two primary constituents, namely connectors and linkers, where connector is often a metal node and linkers are generally carboxylate or pyridyl containing organic ligands. The salient attributes of connectors and linkers pertain to their binding sites, specifically their coordination numbers and coordination geometries. Depending on the metal and its oxidation state, coordination numbers can exhibit a range of values, from 2 to 7. This variability in coordination numbers leads to the formation of diverse geometries, including linear, tetrahedral, T- or Y-shaped, square-planar, square-pyramidal, trigonal-bipyramidal, trigonal-

prismatic, octahedral, pentagonal-bipyramidal, as well as their respective distorted forms **(Figure 1.2)**.[15,16]

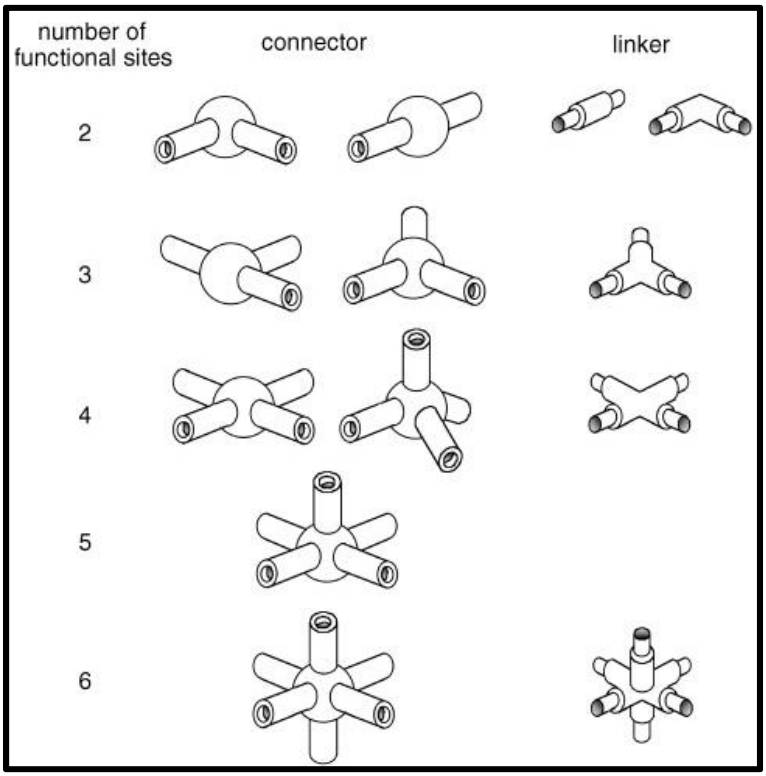

Figure 1.2. Varying orientations of linkers and connectors in MOFs.[15]

For example, the Ag (I)[17,18] and Cu (I)[19] ions, which possess a d-10 electron configuration, exhibit diverse coordination numbers and geometries that can be achieved through the modulation of reaction conditions, including solvents, counter anions, and ligands. The lanthanide ions exhibit polyhedral coordination geometries with coordination numbers ranging from 7 to 10. These large coordination numbers have proven to be valuable in the creation of novel and atypical network topologies. Furthermore, the generation of coordinatively unsaturated lanthanide ion centers can be achieved through the removal of solvent molecules that are coordinated to the ions. These available vacant sites could be effectively utilized in many applications such as chemical adsorption, heterogeneous catalysis, and sensing analytes.[20,21]

Linkers provide a diverse range of linking sites that have been adjusted to have certain binding strength and directionality to form a continuous and well-ordered framework. According to their coordinating groups, organic ligands can be classified into many categories, such as carboxylic acid-based linkers, nitrogen-containing heterocyclic linkers, sulfonyl linkers, phosphoryl, and cyano linkers, etc. Carboxylic acid-based linkers are commonly selected as

multifunctional organic linkers due to their numerous coordination nodes. This property enables the assembly of a diverse range of structural topologies in the formation of MOF structures. Similarly, heterocyclic linkers possessing a nitrogen atom exhibit unique coordination patterns that enhance the structural controllability of the resulting molecule.

1.3. Porous structures

As discussed above, MOFs with varying geometries can be synthesized based on the coordination number of the metal ion and the number of donor sites available in the linker. Based on spatial dimensions, porous structures are broadly divided into four types as depicted in **Figure 1.3**.[15] These include zero-dimensional cavities (0-D), also known as dots, channels in one dimension (1-D), layers in two dimensions (2-D), and intersecting channels in three dimensions (3-D). 0-D cavities are entirely enclosed by molecules forming the walls. Guest molecules can be either confined or distributed throughout the solid material within these cavities. However, 1-D channels, 2-D layers and 3-D structures are commonly used to accommodate or exchange guests.

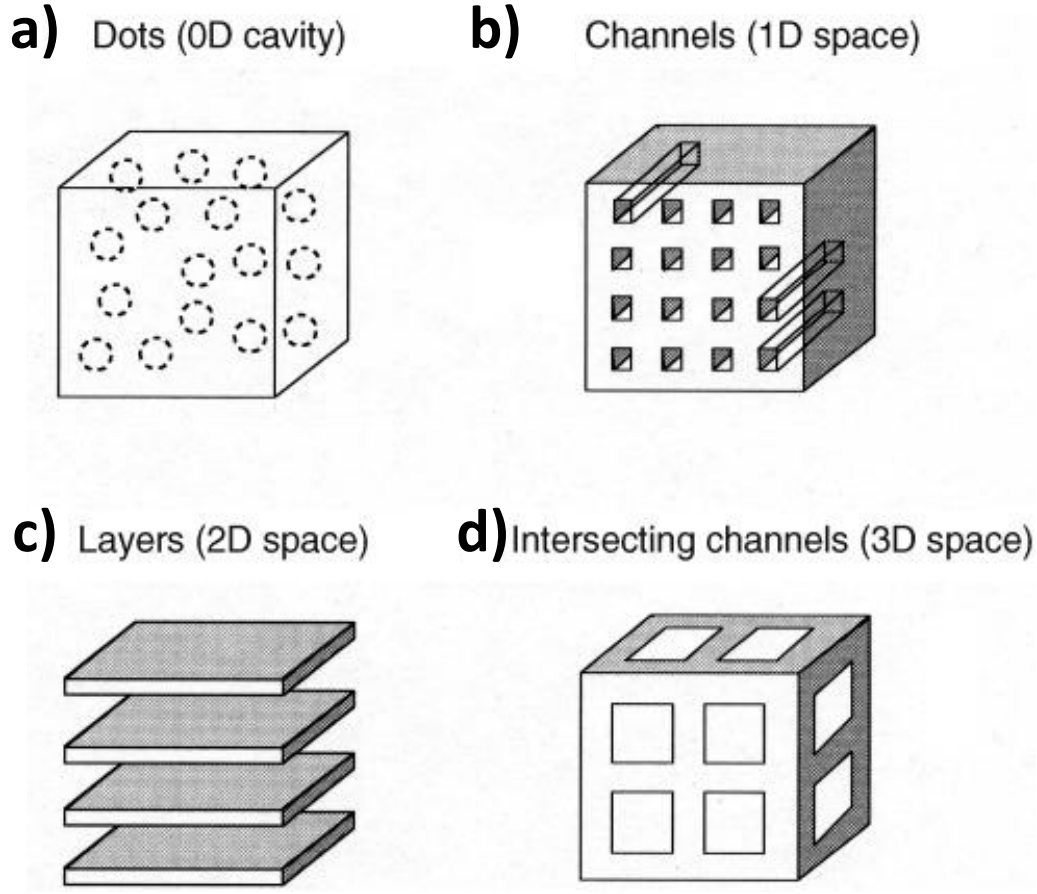

Figure 1.3. Classification of porous structures according to spatial dimensions.[15]

1.3.1. Zero-dimensional cavities (0-D)

Many coordination polymer compounds contain nanosized pores that are separate from one other and distributed throughout the solid. These pores can be classified into two categories- solids with very small windows where window size is smaller than the guest molecules and solids without windows. In both the cases, the guest molecules are incapable of exiting these cavities. This is clearly illustrated in an interpenetrated three dimensional network $\{[Zn(CN)(NO_3)(tpt)_{2/3}]\cdot 3/4C_2H_2Cl_4\cdot 3/4CH_3OH\}_n$. This network acts as a barrier by preventing the passage of any guest molecules with H_2 as the possible exception. Each cavity is effectively isolated from its neighboring cavities and from the external environment as shown in **Figure 1.4**.[22] The sealed cavities are remarkably spacious, with a unit cell length of 23.448(4) L, measured from one Zn_4 square to the parallel and opposite Zn_4 square within the inner shell. The cavity has the sufficient capacity to hold roughly nine molecules of 1,1,2,2 tetrachloroethane and nine molecules of methanol, all of which are in a highly disordered state and essentially liquid.

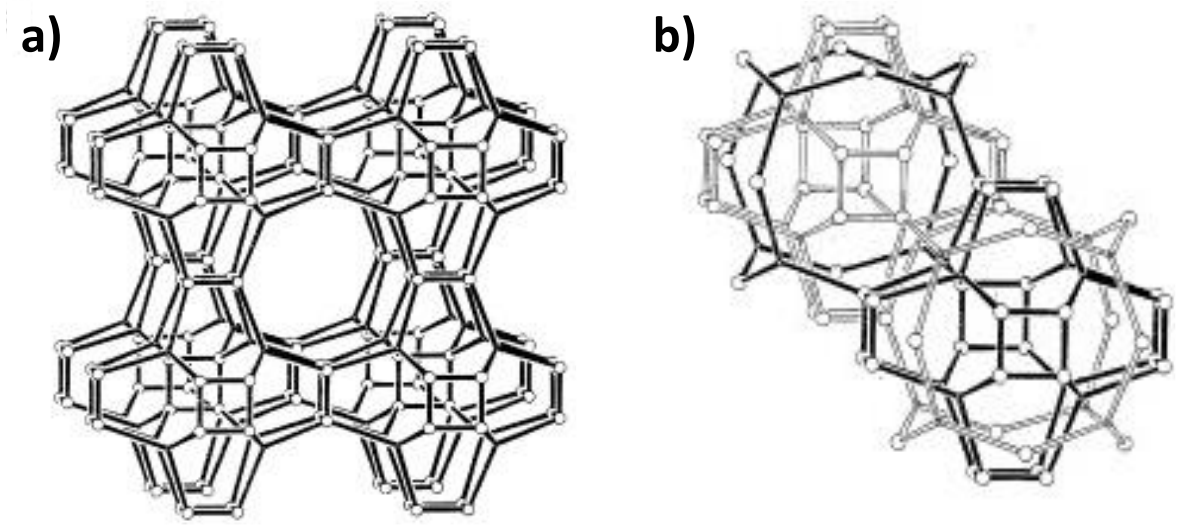

Figure 1.4. a) A part of one single infinite 3D network, b) Two independent, identical and interpenetrated frameworks. These frameworks are differentiated by "full" and "open" lines. The chemical formula of the compound is $\{[Zn(CN)(NO_3)(tpt)_{2/3}]\cdot 3/4C_2H_2Cl_4\cdot 3/4\ CH_3OH\}_n$. Tpt units are depicted as three spokes extending from a central point towards the triazine ligands. ZnCNZn units are represented by direct Zn–Zn bonds.[22]

1.3.2. One-dimensional channels (1-D)

Coordination polymers with well-defined one-dimensional channels have been synthesized and characterized using crystallography.[23-25] These structures possess simple topologies and

provide easy tunability to alter the functional characteristics of the framework. This is achieved by altering the functional characteristics of the metal center or the organic linker. 1D channels exhibit diverse architectural structures, including linear chains, pillared layer, ladders, zigzag chains, helix, ribbons, and more **(Figure 1.5)**.[23]

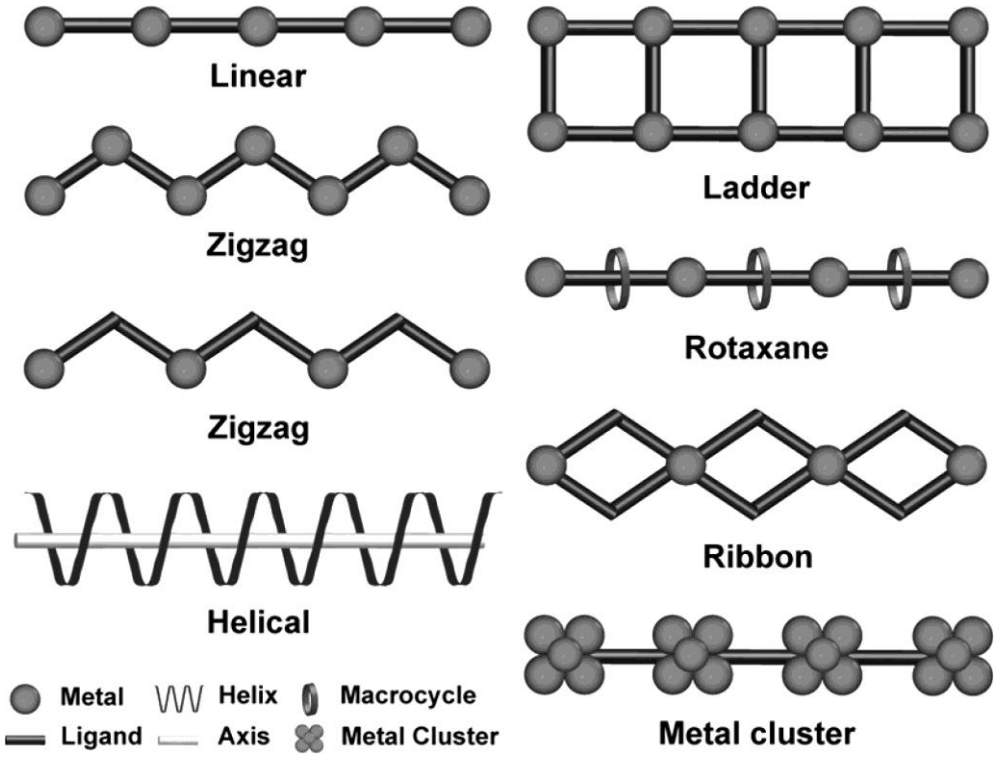

Figure 1.5. Various motifs of 1D coordination polymers. [23]

The pillared layer motif is highly advantageous in constructing diverse porous frameworks at the macroscopic and microscopic level. This is due to the ability to control the porous structures and properties by making slight modifications to the pillar module. [26] This is illustrated in the coordination polymer CPL-1. The coordination polymer CPL-1, consists of Cu (II) ions and ligands, exhibits a pillared layer structure. This unique structure makes CPL-1 an ideal candidate for creating porous structures with specific features. The Cu (II) center in CPL-1 exhibits a deformed square-pyramidal coordination, created by three carboxylate oxygen atoms, one nitrogen atom from pzdc, and one nitrogen atom from pyz **(Figure 1.6a)**. The 2D sheets made of Cu (II) and pzdc units are connected by pyz ligands to form a 3D porous pillared layer structure. [27] This structure, as shown in **Figure 1.6b**, does not contain any vacancies that are big enough for molecules to pass through. The system consists of 1D channels along a axis, which are located between the 2D sheets. Each of these channels contains one water molecule per Cu (II) ion. The channel diameters and surface features of this pillared layer coordination network can be manipulated by modifying the pillar ligands.

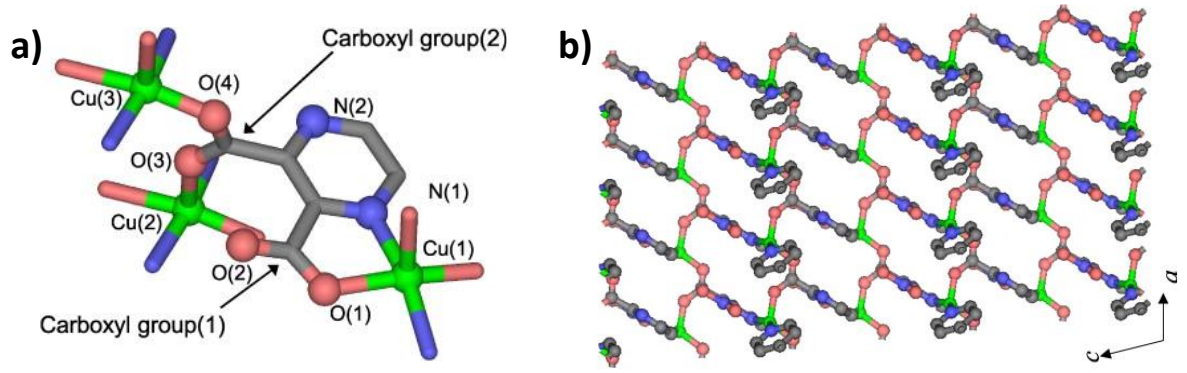

Figure 1.6. a) The coordination environment around Cu (II) ion and b) Structural view of two-dimensional layers of CPL-1. [28]

Wu and coworkers showed that various 1D structures can be synthesized when $Cd(ClO_4)_2$ reacts with (S)-2,2′-dimethoxy-1,1′-binaphthyl-3,3′-bis(4-vinylpyridine) (mnvp) under different conditions **(Figure 1.7)**.[29] The reaction in dimethylformamide (DMF), ortho-dichlorobenzene ($o\text{-}C_6H_4Cl_2$), and ethanol (EtOH) resulted in the formation of a zigzag polymer, $[Cd(mnvp)(DMF)_4](ClO_4)_2 \cdot EtOH \cdot 0.5H_2O$. This polymer has two mnvp ligands that are coupled to Cd(II) centers in cis positions. The adjacent chains are connected to one another through π-π stacking interactions (with a distance of 3.47 Å) resulting in a three-dimensional supramolecular structure that contains one-dimensional chiral channels. A ribbon-like polymer, $[Cd(mnvp)_2(ClO_4)_2].3EtOH \cdot H_2O$ was obtained under the same conditions at a temperature of 70 °C. The compound consists of 38-membered macrocycles composed of four mnvp ligands in the equatorial plane and two perchlorate anions in the axial locations. The introduction of a little quantity of water into the reaction mixture resulted in the formation of a comparable ribbon polymer, namely $[Cd(mnvp)_2(ClO_4)(H_2O)].1.5o\text{-}C_6H_4Cl_2.3EtOH.6H_2O$ with perchlorate anions located at the axial locations. It is observed that the ribbon-like crystalline polymers lose their crystalline structure when the solvent molecules are removed by heating under vacuum. However, their crystallinity can be regained by immersing the compounds in ethanol.

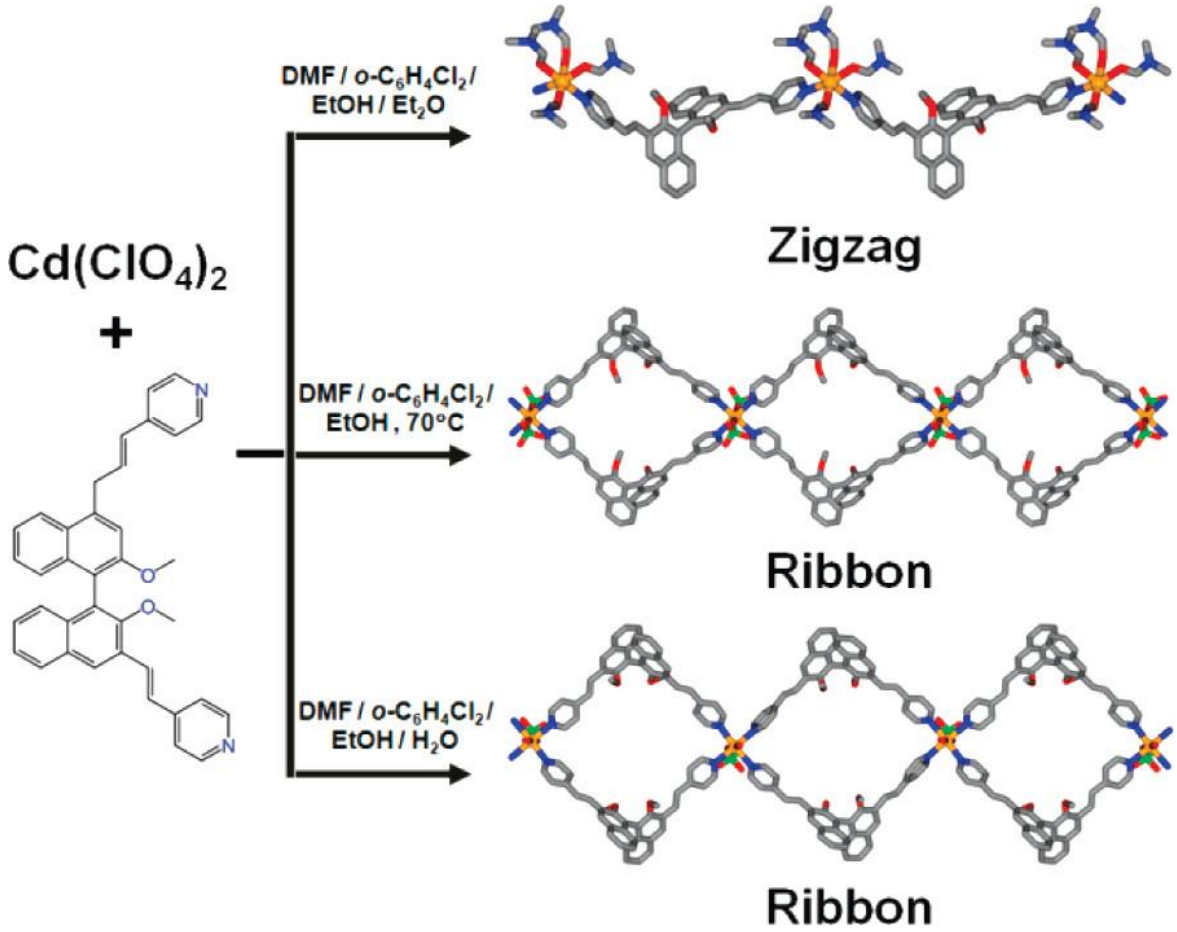

Figure 1.7. Reaction scheme depicting the interactions between $Cd(ClO_4)_2$ and mnvp under varying conditions. [29]

1.3.3. Two-dimensional layers (2-D)

Numerous 2D structures with diverse architectures were synthesized and reported in the literature by combining the known coordination geometries of metals and linear bifunctional ligands. Some well-known 2D structures are depicted in the **Figure 1.8** which include herringbone, brick wall, square grid, honeycomb, and bilayer. [30] The nature of coordination of the organic ligands and the relative proportions of metal and ligand significantly influences the overall structure of the framework. Square grid networks represent the most basic illustration of two-dimensional structures. The ratio of metal to ligand in these coordination polymers is typically 1:2.[31] The metal centers are bound to four ligand molecules, and further repetition of this unit enables the growth of the structure in two dimensions. Additionally, other variations of these motifs, such as rhombic or rectangular grids,[32-35] have also been extensively studied. Even in the case of rhombic or rectangular grids, the metal centers are connected to four ligand molecules.

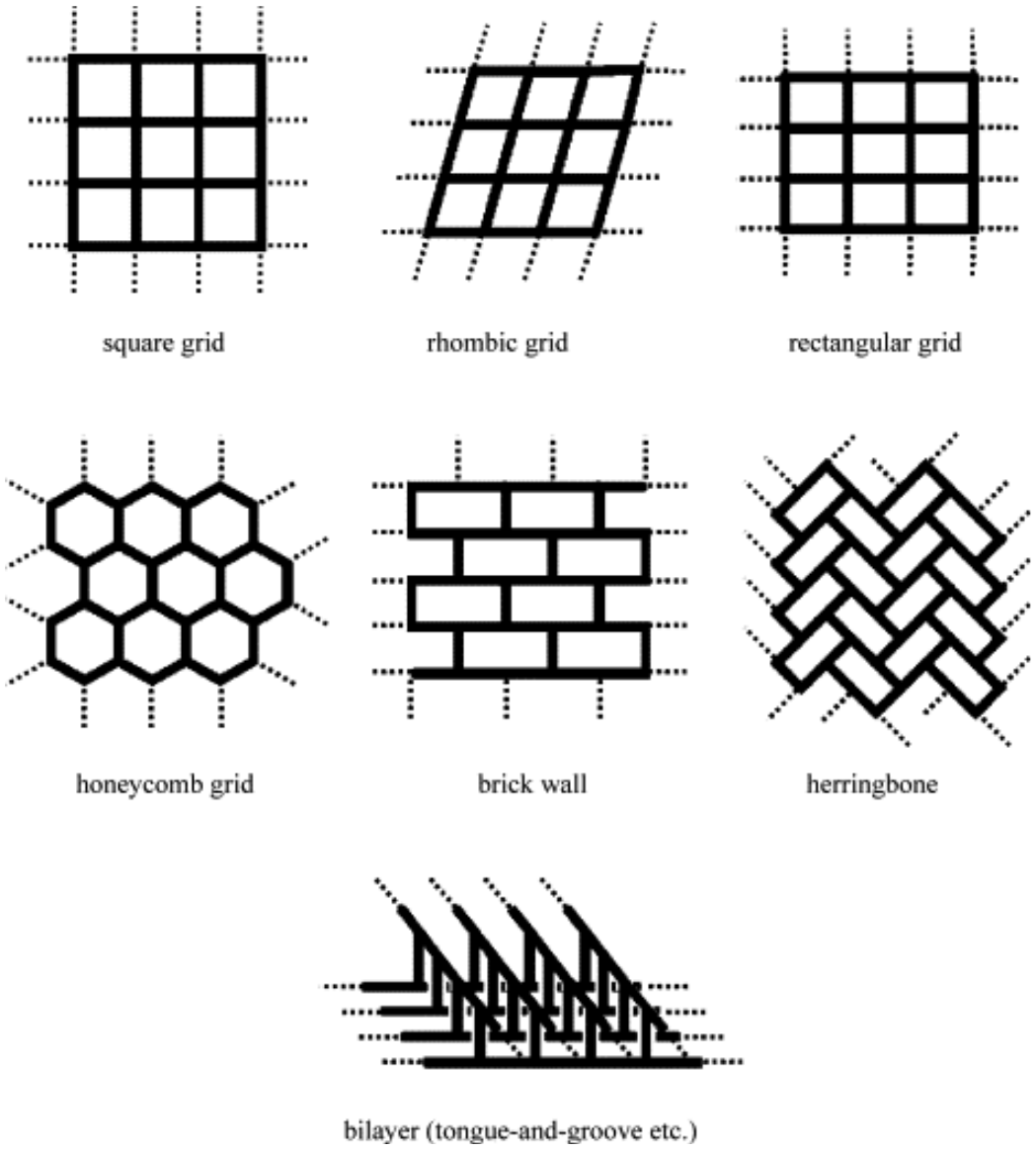

Figure 1.8. Various motifs of 2D coordination polymers. [30]

The compound 1,4-bis(imidazol-1-ylmethyl)benzene (bix) undergoes a chemical reaction with Mn (II) ions, resulting into a structure composed of perfectly arranged square grid layers, as shown in **Figure 1.9a**. [36] The metal ions in the structure are surrounded in an octahedral fashion. Specifically, the four nitrogen atoms of the ligand molecules occupy the equatorial positions, while the counter anions (azide or dicyanamide anions) occupy the apical positions. In some cases, a "T-shape" arrangement is created around the node when three ligand molecules are coordinated with the meatal ions. This arrangement leads to the formation of layers, which are referred to as honeycomb grid, brick wall, herringbone motifs, or other parquet floor architectures. An interesting bilayer motif with metal centers fashioned in "T-shape" is observed in the compound $\{[Cu(bpy)_{2.5}(H_2O)](ClO_4)_2 \cdot (H_2O) \cdot (CH_3OH)_{1.5}\}_n$.[37] The

metal to ligand ratio used in this case is 1:2.5. Each Cu (II) center exhibits a distorted square-planar arrangement, with four nitrogen atoms positioned equatorially. The four nitrogen atoms are from three bidentate bridging bipyridine molecules and one monodentate terminal ligand connector. The apical coordination sites are weakly coordinated by water molecules **(Figure 9b, c)**.

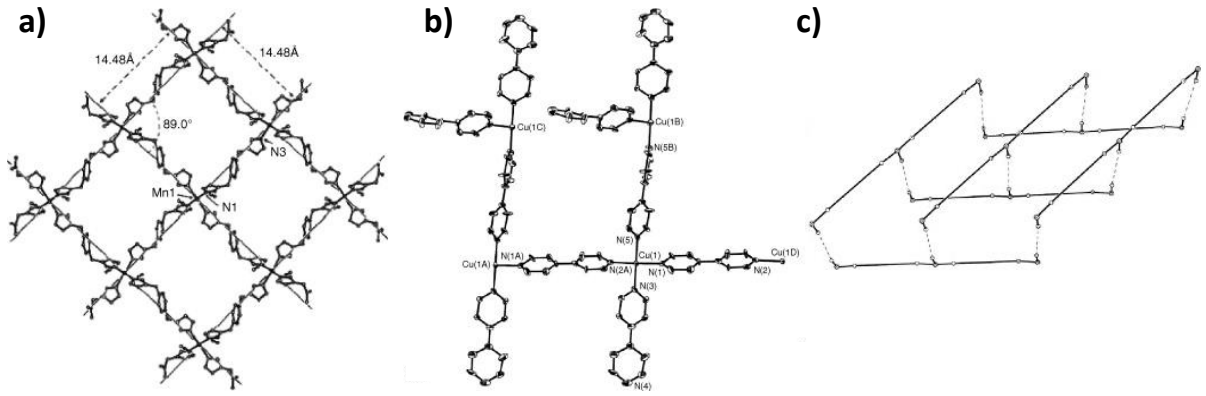

Figure 1.9. (a) Representation of square grid network in $\{[Mn(N_3)_2(bix)_2]\}_n$, (b) coordination mode of the Cu (II) ion in $\{[Cu(bpy)_{2.5}(H_2O)](ClO_4)_2 \cdot (H_2O) \cdot (CH_3OH)_{1.5}\}_n$ (water, perchlorate and methanol molecules are omitted for clarity, (c) bilayer architecture (terminal ligands are omitted, solid lines represent the "chain makers", dashed lines represent the "linker between the chains" and black circles represent the Cu (II) centers).[36,37]

Necas and co-workers demonstrated brick wall, parquet floor and pseudo-honeycomb motif in coordination polymers containing lanthanide metal ions and the dppeO_2 ligand (dppeO_2: $Ph_2P(O)$-CH_2CH_2-$P(O)Ph_2$ **(Figure 1.10)**. The metal to ligand ratio used here is 1:1.5.[38] Generally, in order to obtain "T-shape" connectors, some coordination sites of the metal center are blocked by strongly coordinating counter anions (halide anions, nitrate anions), or by terminal ligand molecules. Thus, the 2-D structures are obtained when three or four ligand molecules serve as connectors between the node centers. The remaining coordination sites of the centers are filled with other building components (such as counter-anions, solvent molecules, or other organic molecules). The metal to ligand ratios used to obtain 2-D structures are 1:1.5, 1:2, or 1:2.5 and is not limited to 1:1 as in the case of 1-D networks (excluding double chain motifs). These types of structures can exhibit cavities and this vacant space is typically occupied by guest molecules, such as counter ions or solvent molecules, by proper arrangement of the sheets or by interpenetration.

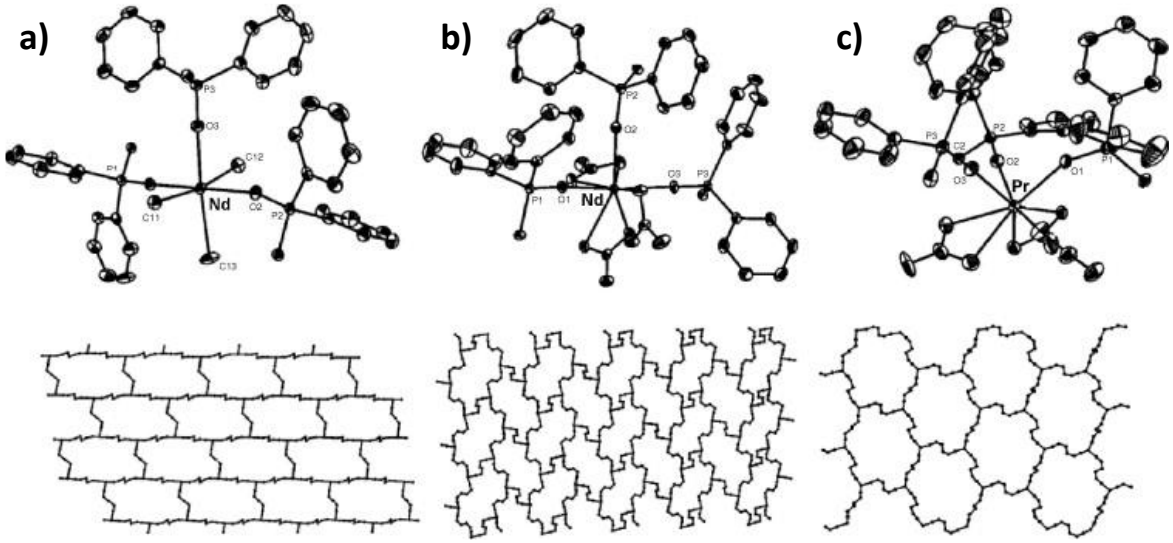

Figure 1.10. (a) Representation of brick wall motif in $\{[NdCl_3(dppeO_2)_{1.5}]\}_n$, (b) representation of parquet floor motif in $\{[Nd(NO_3)_3(dppeO_2)_{1.5}]\}_n$ and (c) depicting pseudo-honeycomb motif in $\{[Pr(NO_3)_3(dppeO_2)_{1.5}]\}_n$.[38]

1.3.4. Three-dimensional motifs (3-D)

A diverse array of connectors and linkers have enabled the creation of a broad spectrum of three-dimensional metal-organic frameworks (MOFs). 3D MOFs are formed when organic ligand connectors are extended in all three dimensions and form a continuous network. Framework stability issues were the common problems with the early MOFs where the MOF structures were not capable of maintaining permanent porosity and showed framework collapse when the guest molecules were extracted. This difficulty was resolved by employing multidentate linkers, such as carboxylates, which facilitate the creation of more stable three-dimensional frameworks. The 3D-coordination polymer motifs such as diamondoid net, octahedral net, NbO net, $ThSi_2$ net, PtS net and $CdSO_4$ net depicted in **Figure 1.11** are quite prevalent.[30] Among these motifs, diamondoid and octahedral net patterns stand out.

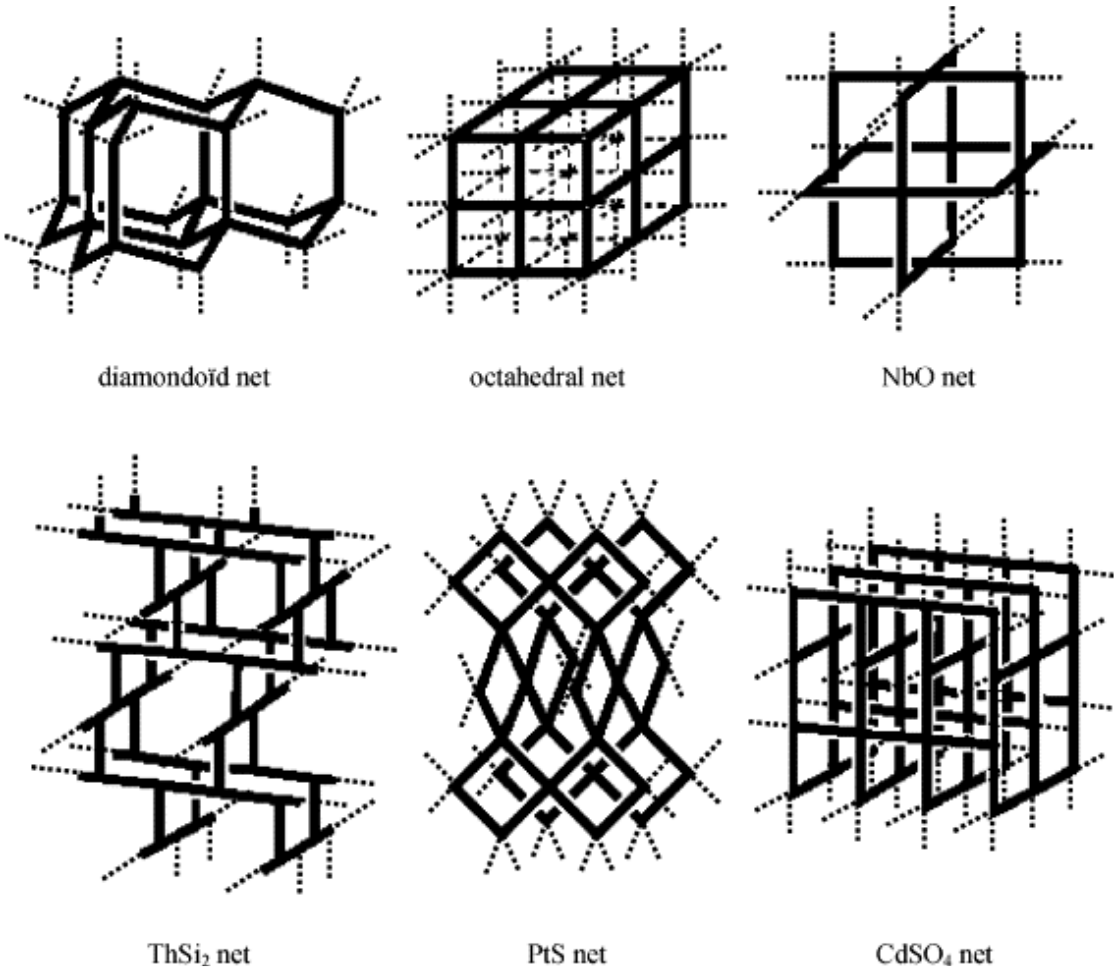

Figure 1.11. Structural patterns of 3D- coordination polymers. [30]

Diamondoid net

The diamondoid network is a commonly found and widely recognized 3-D motif. The connectivity of each node is established using four bridging ligands arranged in a tetrahedral manner, resulting in the formation of a three-dimensional diamondoid network. This pattern is observed in the structure formed by using Cd (II) ions as metal nodes of connection and the dicarboxylate 3,3-azodibenzoate (3,3-azdb) as linkers.[39] The cadmium ions have a coordination number of eight, yet they function as four-connecting nodes due to the bidentate nature of the carboxylate groups. **Figure 1.12a** illustrates that this configuration results in the formation of large voids, mostly due to the dimensions of the ligand. Specifically, the average separation between the cadmium atoms within the cavity is 15 Å. The significantly large voids in the structure allows other independent networks to interpenetrate with the existing network. **Figure 1.12b** depicts the co-existence of six independent and interwoven diamondoid networks in this structure.

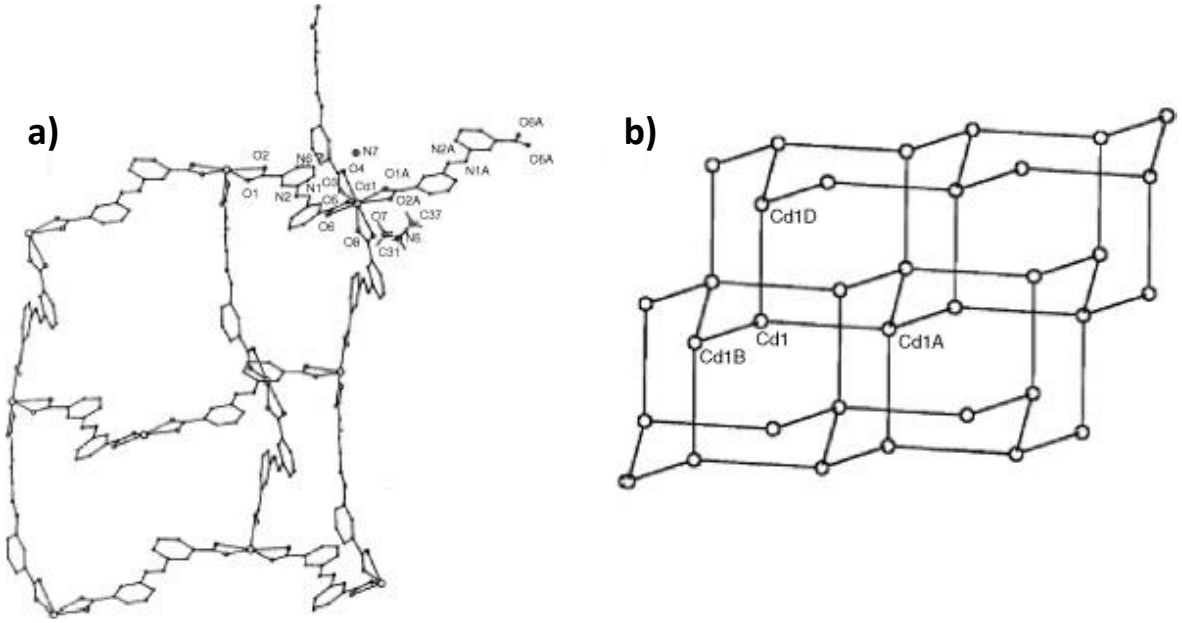

Figure 1.12. (a) Coordination arrangement in {[Cd(3,3-azdb)$_2$](H$_2$NMe$_2$)(NH$_4$)}n depicting large cavities and (b) schematic illustration of the diamondoid network in {[Cd(3,3- azdb)$_2$](H$_2$NMe$_2$)(NH$_4$)}$_n$.[39]

Octahedral net

Octahedral motifs are formed by extending the framework in three directions from the octahedral nodes. Coordinating six ligand molecules around a metal center is quite challenging due to steric hindrance. Typically, the apical positions of octahedral metal ions are coordinated by water molecules, solvent molecules, or counter anions. As a result, the resulting network has low dimensionality and apical positions are infrequently coordinated bond sites, often exhibiting Jahn-Teller distortion.[31] An effective approach involves employing two distinct molecules to construct the edge of the cubic unit. For instance, The SiF_6^{2-} anions have a greater affinity for linking metal atoms compared to water molecules. These anions serve as connectors between square grid layers composed of metal ions and four ligand molecules in the equatorial positions. Furthermore, the resulting three-dimensional framework is more robust due to the absence of any uncoordinated counter ion in the structure. This arrangement can be observed in{[Cu(SiF$_6$)(4,4′-bpy)$_2$]·8H$_2$O}$_n$ **(Figure 1.13)**.[40]

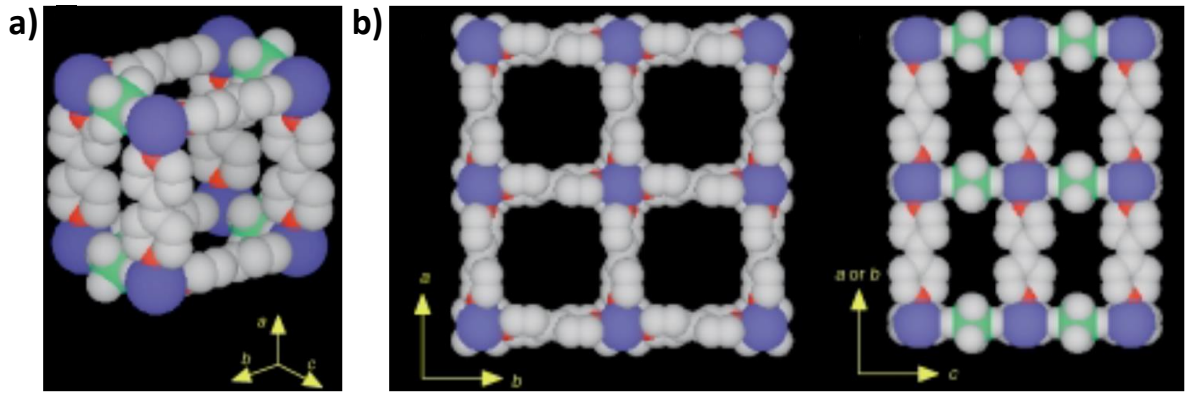

Figure 1.13. Representation of (a) cubical unit in {[Cu(SiF_6)(4,4-bpy)$_2$]·8H_2O}n and (b) cavities in {[Cu(SiF_6)(4,4-bpy)$_2$]·8H_2O}n (water molecules omitted for clarity) (Cu ions in blue, Si atom in green and nitrogen atoms in red). [40]

Octahedral motifs can also be constructed by using binuclear subunits as nodes. This is illustrated in the compound{[Co(terephthalate)(4,4-bpy)]}n,[41] where a layer is created with the help of terephthalate dianions capping the cobalt binuclear unit. This is clearly depicted in **Figure 1.14a and b** where the carboxylate groups are coordinated to the cobalt ions in the equatorial positions. Further, to extend the structure in the third dimension, the bipyridine molecules are connected to the cobalt anions through the apical positions acting as pillars in the framework **(Figure 1.14c)**. This system exhibits a 2-fold interpenetration.

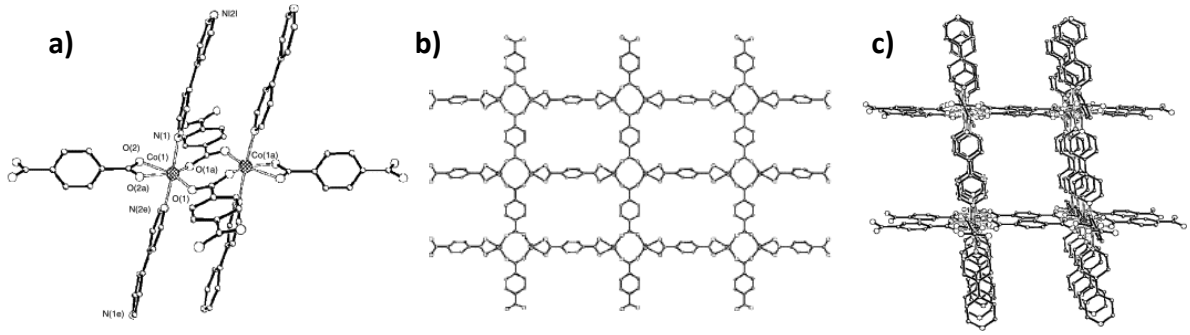

Figure 1.14. (a) Coordination arrangement of the cobalt binuclear unit in {[Co(terephthalate)(4,4-bpy)]}$_n$ (b) View of Co(terephthalate) sheet and (c) three-dimensional structural view. [41]

Subsequently, the utilization of secondary building units (SBUs) has become a prevalent approach for generating 3D-MOFs. Here, the metal clusters are introduced as connecting nodes and further aggregation of metal ions into secondary building units (SBUs) results into M-O-C clusters. [42] After establishing the synthesis of the SBU, it can be used to direct the

construction of structured frameworks using either rigid or flexible organic linkers.[43] The easy tunability of MOFs helps in designing porous frameworks by systematically varying their pore size and functionality while maintaining their basic structure. A large series of iso-reticular MOFs (IRMOFs) can be designed and synthesized by systematically changing the size and functionality of the linker. An IRMOF series based on MOF-5 were designed to produce stable and rigid porous frameworks with cubic topology where octahedral Zn-O-C clusters are connected by benzene dicarboxylic acid linkers to reticulate porous frameworks with cubic topology.[14] MOF-5 IRMOF series were synthesized by maintaining the same framework topology but systematically functionalizing the BDC units with the organic groups such as Br, NH_2, OC_3H_7, OC_5H_{11}, C_2H_4 and C_4H_4. The pore size was also increased by using longer linkers such as biphenyl, tetrahydropyrene, pyrene, and terphenyl. The IRMOF series obtained by the above-mentioned conditions are excellent porous materials for gas storage **(Figure 1.15)**.[44]

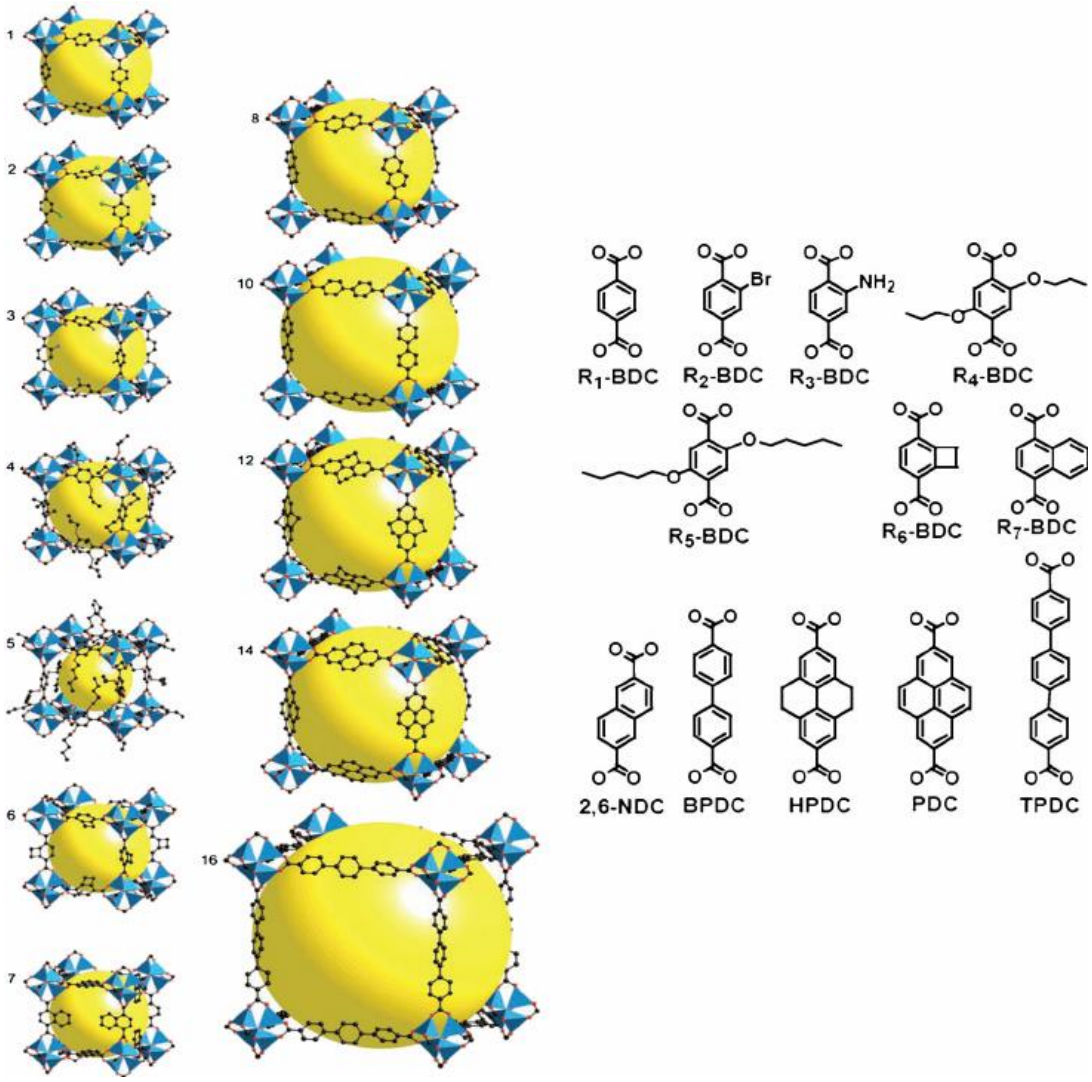

Figure 1.15. MOF-5 based Iso-reticular MOFs (left) and functionalization of BDC struts (right).[44]

1.4. Classification of porous coordination polymers

Porous coordination compounds are categorized into three generations based on the framework stability upon the removal of guest molecules. The compounds of the 1st generation possess microporous frameworks that are dependent solely on guest molecules for stability. Thus, removal of the guest molecules from these compounds results into irreversible collapse of the framework. The compounds of the 2nd generation exhibit stable and robust porous structures, demonstrating permanent porosity even in the absence of guest molecules within the pores.[45-49] The 2nd generation compounds encompass a variety of inorganic porous materials that are built through covalent bonds. The compounds of the 3rd generation possess flexible and dynamic structures. They can reversibly modify their channels or pores in response to the external stimuli such as guest molecules, light and electric field. However, porous coordination polymers have the potential to exhibit the characteristics of both robust 2nd generation compounds and flexible and dynamic 3rd generation compounds **(Figure 1.16)**.[28,50]

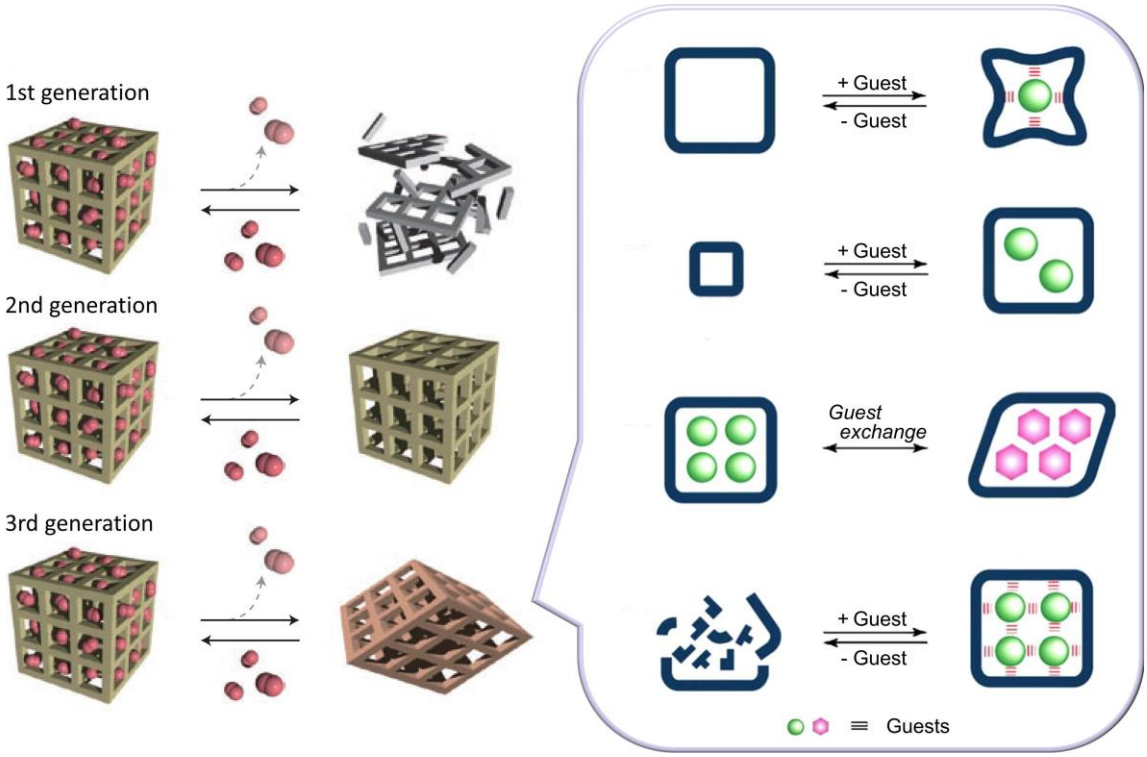

Figure 1.16. Categorization of porous compounds into three generations: 1st, 2nd, and 3rd.[28]

The 3rd generation PCPs can be classified into three distinct types. Type I frameworks experience a collapse of their network structure, resulting in the loss of crystallinity upon the removal of guest molecules. However, they can be regenerated to their original state under the

initial conditions. Type II frameworks experience structural changes in their networks as a result of the simultaneous exchange of guest molecules. Type III frameworks experience structural alterations in its networks when the guest molecules are eliminated, but the modified structure returns to its original state under initial conditions. In contrast to Type I porous coordination compounds, Type II and III frameworks maintain their crystal singularity during structural transformations.

1.5. Synthesis of MOFs

In general, the synthesis of MOFs is carried out by gentle blending of metal ions with organic linkers, resulting in the formation of porous and well-ordered crystalline structures. Several external factors such as choice of metal salts, organic ligands, molar ratios, solvents, temperature and pH of the reaction media plays an important role in the synthesis of MOFs.[51] The choice of metal salts, organic linkers and solvent system is crucial in both the synthesis of MOFs and in deciding the morphology of the framework. Solvents can either coordinate with metal ions or function as space-filling molecules and as structural directing agents. The solvents utilized in MOF synthesis should be polar and have a high boiling point. The selection of a solvent system is based on the solubility of the reactants, and in some cases, a combination of solvents is used. The synthesis process of MOF is also influenced by the reaction medium due to the polarity of the solvent utilized, as well as the solubility properties of the organic linker. Furthermore, it has been reported that employing various solvent systems under identical reaction conditions yields metal-organic frameworks (MOFs) with distinct morphologies.[52] This phenomenon may occur due to variations in the extent of deprotonation of the organic linker in different solvents. It is noted that the dimensionality of the MOF system is also determined based on the coordination ability of the solvent with the metal.

The synthesis of MOFs is significantly influenced by the temperature and pH of the reaction media. Linkers can adopt several coordination modes depending on the pH range. Moreover, as the pH value is increased, the extent of deprotonation of the linker increases. Similarly, the temperature of the reaction is a crucial variable that influences the characteristics of the synthesized MOFs. High temperatures also promote more crystallization as a result of the enhanced solubility of the reactants, resulting into large and high-quality crystals. Thus, the morphology, rate of nucleation and crystal growth is greatly dependent on the temperature of the reaction medium.[53]

Over the past few decades, various preparation methodologies have emerged and been employed for the synthesis of MOFs. The categorization of these approaches includes traditional solvothermal methods, unconventional, and alternative methods.

1.5.1. Solvothermal methods

The solvothermal technique has been extensively employed in the synthesis of metal-organic frameworks (MOFs). This approach is utilized based on its attributes of simplicity, ease of use, crystalline nature, and high productivity. In this methodology, metal salts and organic ligands are subjected to agitation in protic or aprotic organic solvents depending on the solubility of the reactants.[54] Aprotic solvents commonly employed in various chemical processes encompass DEF, DMF, NMP, DMSO, DMA, acetonitrile, and toluene. Protic solvents commonly used in many applications include methanol, ethanol, and mixed solvents. In order to mitigate the challenges arising from the disparate solubility of the constituent elements, it is possible to employ solvent combinations. When water is employed as the solvent in the synthesis of MOFs, this particular approach is commonly known as the hydrothermal technique.[55] The aforementioned mixture is introduced into the sealed container under conditions of increased pressure and temperature, and left to react for a duration of several hours or possibly up to one day. Glass vials are employed for low-temperature applications, where teflon-lined stainless steel autoclave is utilized for reactions conducted at high temperatures exceeding 400 K **(Figure 1.17)**. Subsequently, the enclosed container is subjected to elevated temperatures surpassing the boiling point of the aprotic or protic solvent, resulting in increased pressure.[54] The primary variable in this reaction mixture is the temperature. There are two distinct temperature ranges involved: the solvothermal reaction, which occurs in a sealed container above the boiling point of the solvent with autogenous pressure, and the non-solvothermal reaction, which occurs at or below the boiling point of the solvent under ambient pressure.[56] As a result of the elevated pressure, the solvent undergoes heating beyond its boiling point, leading to the dissolution of the salt and facilitating the progression of the reaction. Furthermore, the attainment of a substantial crystal possessing a considerable interior surface area necessitates the implementation of a gradual crystallization process originating from a solvent solution.

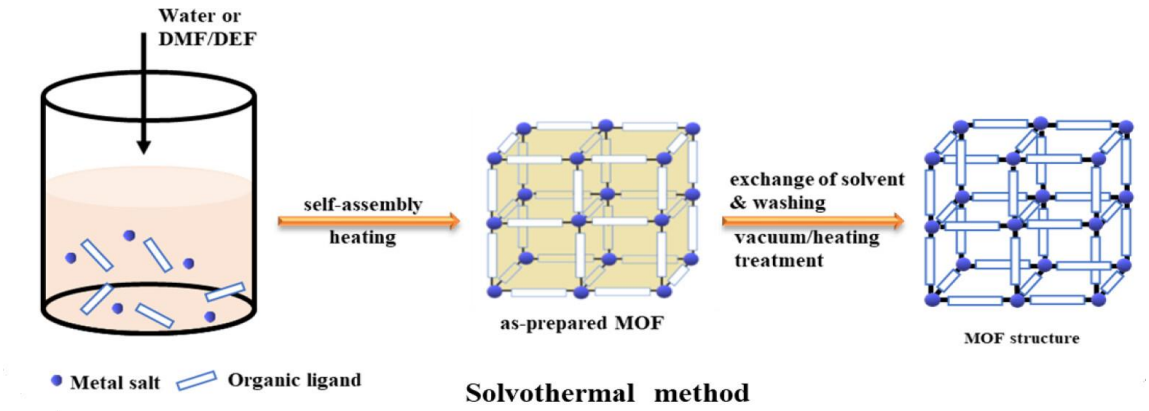

Figure 1.17. Schematic representation of solvothermal synthesis methods of MOFs.[57]

15.2. Alternative methods

In addition to these methods, alternative routes have been explored. These alternative routes can result in variations in crystallization rate, particle size, size distribution, adsorption characteristics, and morphologies. These variations can significantly impact the properties of the material.

Slow diffusion method

The diffusion technique facilitates the interaction between several species through a sequential process. The initial approach employed is known as solvent liquid diffusion. This process involves the formation of two layers with distinct densities. One layer consists of the precipitant solvent, while the other layer contains the product dissolved in a solvent. Crystallization occurs at the interface by two distinct mechanisms: (i) the gradual diffusion of the precipitant solvent into the next layer, and (ii) the sequential diffusion of reactants, overcoming physical barriers in the process. One significant advantage of employing this technique is the ease with which single crystals appropriate for X-ray diffraction (XRD) investigation can be obtained. The primary drawback of this strategy, in comparison to other prominent strategies, lies in its inherent time-consuming nature.[58]

1.5.3. Electrochemical method

The present methodology involves the liberation of metal ions through anodic dissolution within a reaction system consisting of organic linkers and electrolytes **(Figure 1.18)**.[57] The electrochemical technique is utilized for the large-scale production of MOF powders. Several advantages of this methodology include the ability

to avoid the presence of anions such as nitrates originating from metal salts, the utilization of low reaction temperatures, and the achievement of significantly faster synthesis rates as compared to solvothermal synthesis methods. The presence of conflicting thermal growth constants between the support structure and the MOF leads to this rupture. In relation to this matter, MOFs have a negative coefficient of thermal expansion. In comparison to the solvothermal method, electrochemical techniques offer a greater range of variables that can be finely adjusted through basic voltage modifications.[59]

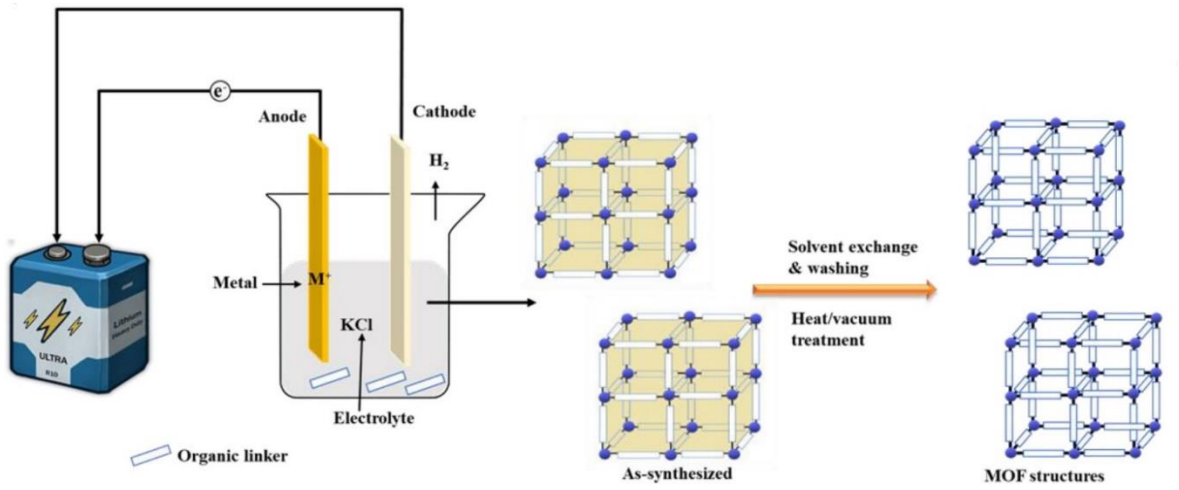

Figure 1.18. Schematic representation of electrochemical synthesis methods.[57]

1.5.4. Microwave-assisted method

The utilization of microwave irradiation in the synthesis process is an expeditious method for the production of MOFs. Upon subjecting the reaction mixture to microwave irradiation for a duration of one hour or longer, the formation of nanosized crystals occurs **(Figure 1.19)**.[57] The utilization of microwave-assisted techniques is an essential approach for achieving accelerated synthesis. This approach offers several advantages, such as high efficacy, rapid reaction kinetics, phase selectivity, consistent particle morphology, and particle size reduction, among others.[60] Nevertheless, this particular approach often fails to produce crystals of sufficient size for individual X-ray examination.[61]

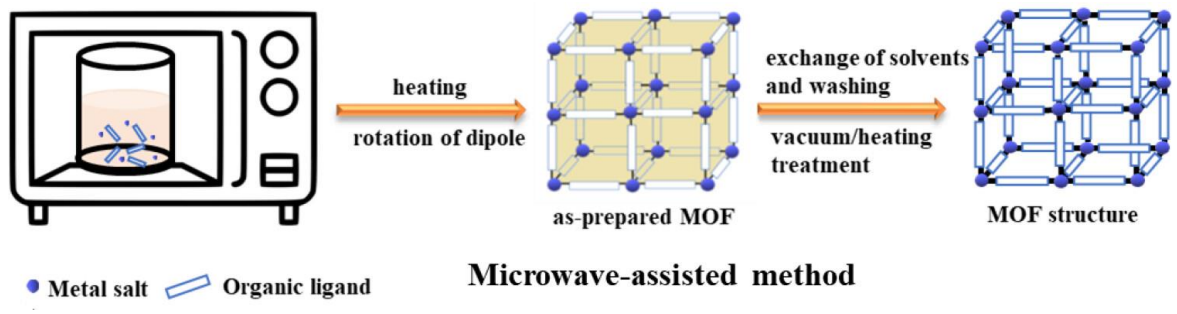

Figure 1.19. Schematic representation of the synthetic procedure using microwave-assisted method.[57]

1.5.5. Sonochemical method

Sonochemical synthesis involves subjecting the reaction mixture to ultrasound waves within the frequency range of 20 kHz to 10 MHz, resulting in chemical transformations of the molecules **(Figure 1.20)**.[57] This process leads to the formation of MOFs with unique morphologies, crystal sizes, and specific characteristics.[62] Ultrasonic radiation has the capability to induce elevated temperatures and pressures within the reaction media. The primary benefits of this technology include its economic viability, typically rapid execution, reproducibility, and environment friendly characteristics.[63] By employing rapid nucleation, this approach can effectively decrease the time required for crystallization and produce smaller particle size crystals compared to those obtained through solvothermal synthesis. Similar to the microwave process, this particular approach often fails to provide crystals of sufficient size for individual X-ray investigation.

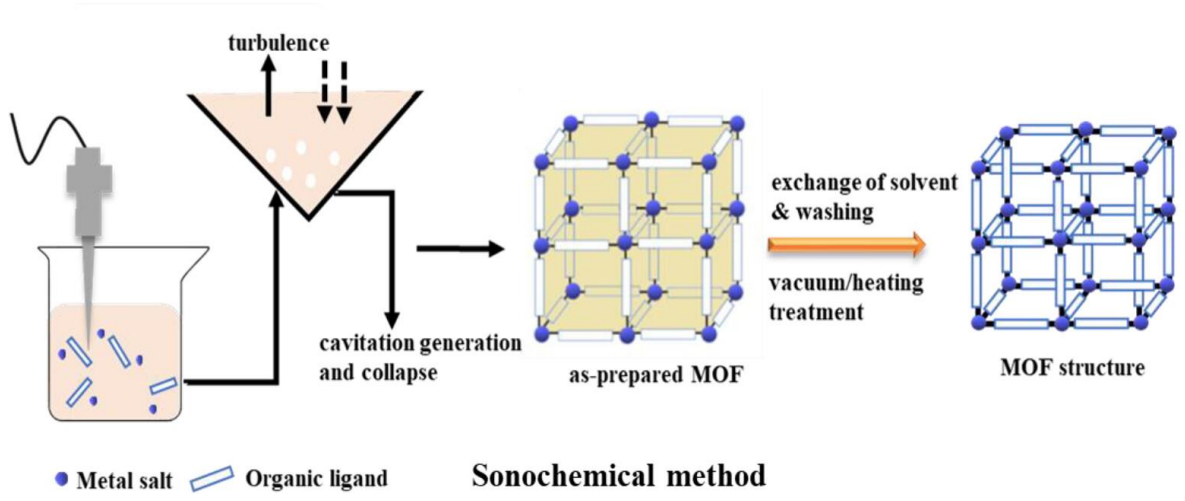

Figure 1.20. Schematic representation of the synthetic procedure using sonochemical method.[57]

1.5.6. Mechanochemical method

The metal salt and organic linker are mechanically ground together in a mortar pestle or ball mill, without the use of a solvent or very minimal amount of solvent. After grinding, the mixture is gently heated to remove water or other volatile byproducts that are generated during the reaction. The mechanochemical method entails the utilization of mechanical energy to facilitate chemical reactions **(Figure 1.21)**.[57] This approach involves the mechanical disruption of intramolecular bonds, which is subsequently followed by chemical synthesis. One notable benefit of employing this particular technique is that the chemical reaction takes place at room temperature without the need for potentially hazardous organic solvents. Another noteworthy characteristic of this approach involves the utilization of metal salts in lieu of metal oxides. Nevertheless, this approach is accompanied by the drawback of undesired product amorphization resulting from the process of meticulous milling.[64]

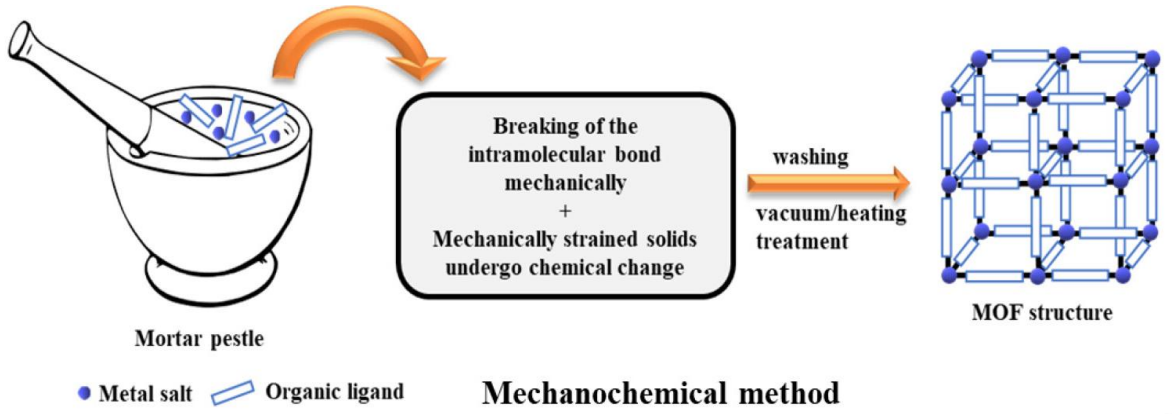

Figure 1.21. Schematic representation of the synthetic procedure using mechanochemical method.[57]

1.6. Application of MOFs

The unique properties of MOFs have garnered the interest of chemists, physicists, and material scientists for various applications, including gas storage, separation, heterogeneous catalysis, drug delivery, photocatalysis, carbon capture, and biomedical applications, etc.[65-80] Furthermore, the utilization of MOF materials for sensing applications has emerged as another promising area of research. The permanent porosity in MOFs coupled with their ease of structure tunability makes them a viable choice for designing materials for sensing applications and further develop fluorescence, electrochemical, capacitance and chemiresistive sensors. The various factors that encourage the use of MOFs for sensing applications have been listed below.

(1) The inherent porosity of MOFs offers significant surface areas and abundant active sites to enhance host-guest interactions. The confined pores also facilitate the accumulation of target gases and VOCs potentially amplifying the sensing sensitivity.
(2) The remarkable reversibility of MOFs in capturing and releasing guest molecules makes them highly capable of being restored and reused. This also ensures that the entire process is less energy intensive.
(3) The tunable properties, pore volumes, pore sizes, and surface environments of MOFs have the potential to enhance their ability to selectively and accurately detect guest molecules. Additionally, the incorporation of functional groups (such as Lewis acid or base sites) into the framework can also modify the chemical selectivity and sensitivity.
(4) The highly crystalline nature of MOFs allows for accurate structure determination, providing detailed insights into the interactions between the host and guest molecules at the atomic level.
(5) Numerous applications generally demand high temperature and/or moisture stability. MOFs possessing high thermal and water stability can meet these demands with ease.[81-83]

Keeping the scope of thesis in mind, only the sensing related applications of MOFs have been discussed in the following sections.

1.6.1. Chemiresistive sensing

Chemiresistive sensors operate based on the fundamental premise that the electrical characteristics such as current, capacitance or resistance of the sensing material undergo a considerable change upon adsorption and interaction with the target guest molecules. MOFs possess significantly greater surface areas compared to other porous materials, enabling enhanced interaction with guest molecules. Nevertheless, the intrinsic lack of electrical conductivity in the majority of MOFs has significantly restricted their usage in electrical sensing applications. Over the last decade, advancements in 2D electrically conductive MOFs and MOF-based electronic devices have positioned them as excellent candidates for a wide range of electrochemical applications, including supercapacitors, electrocatalysis, proton conduction, and field-effect transistors. In addition, the simultaneous presence of a high surface area, adjustable pore size, and conductivity in 2D electrically conductive MOFs establishes a novel foundation for advancements in chemiresistive sensors of the future generation.[84-88]

The primary mechanism of chemiresistive MOF-based sensors is the absorption of guest molecules by the functional material, which induces electron and hole transfer. The resistance, current or capacitance changes of the sensing materials can also be due to the interaction of the guest molecules on the surface of the functional material. MOFs can be potent materials as chemiresistive sensors due to their structural uniqueness. The alterations in the electrical resistance of the sensor can be attributed to the interactions of the guest molecules with the framework. These interactions could be occurring between the guest molecules and active functional organic groups or active metal sites in MOFs resulting in conductivity of MOFs. Furthermore, the conductivity of MOFs can be subjected to the structural modifications induced by the adsorption of guest molecules. Due to its cost-effective manufacturing and ease of miniaturization, chemiresistive sensors have been extensively used. However, selectivity and sensitivity are still the major challenges that chemiresistive sensors face.

Zhang et. al.[89] conducted the initial investigation on a MOF-based chemiresistive sensor where the researchers developed a sensor using highly porous Co-based ZIF-67, that exhibited a remarkable ability to detect formaldehyde at concentrations as low as 5 ppm **(Figure 1.22)**. Nevertheless, the ZIF-67 had a significant limitation in terms of its room temperature conductivity, as evidenced by its operating temperature reaching as high as 150 °C. The inadequate electrical conductivity of the majority of MOFs has significantly restricted their usage in electrical sensing applications.

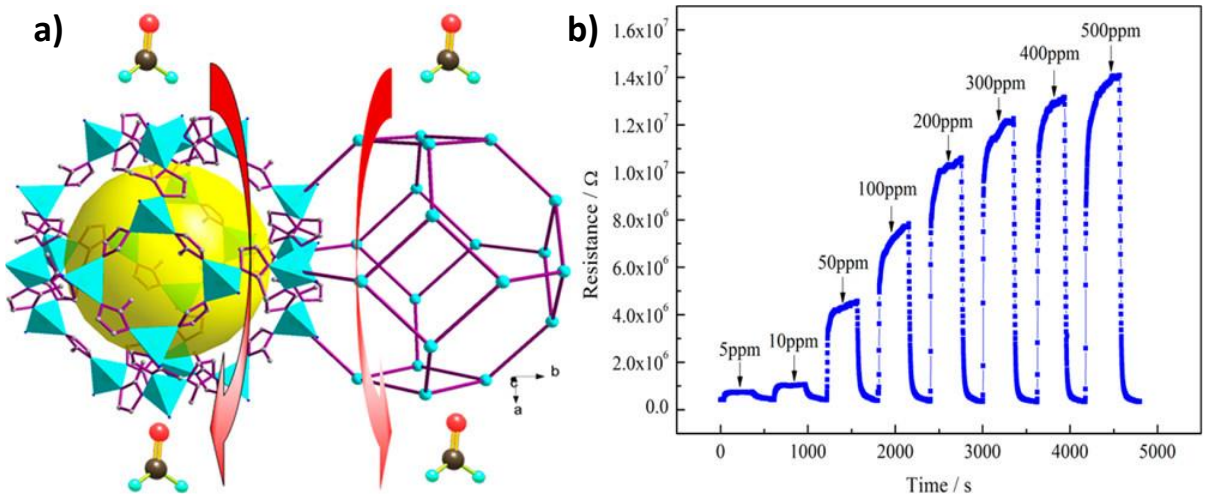

Figure 1.22. (a) ZIF-67 MOF structure and (b) response-recovery curve of the ZIF-67 sensor towards formaldehyde.[89]

Significant advancements have been made in the utilization of 2D electrically conductive MOFs, MOFs with electrically conductive guest, and MOF membranes as chemiresistive sensors. Xu, Marti-Gastaldo, and Dinca groups have conducted several investigations on 2D electrically conductive MOFs. 2D- electrically conductive MOFs, which possess superior electrical conductivity, are considered promising candidates for chemiresistive sensors. Furthermore, the use of MOF membranes or MOF coatings onto sensing devices is a viable approach to address the intrinsic poor selectivity and sensitivity limitations of chemiresistive sensors. Xu et al.[90] reported a 2D electrically conductive MOF $Cu_3(HHTP)_2$ for sensing ammonia. The thin film of $Cu_3(HHTP)_2$ exhibits high selectivity towards NH_3 in the presence of several interfering gases, a low limit of detection (LOD), rapid response time, and exceptional stability and reproducibility **(Figure 1.23)**. Thus, MOFs can be considered as suitable materials for chemiresistive sensors and there is ample scope for further advancement in the MOF-based electrical sensor related research.

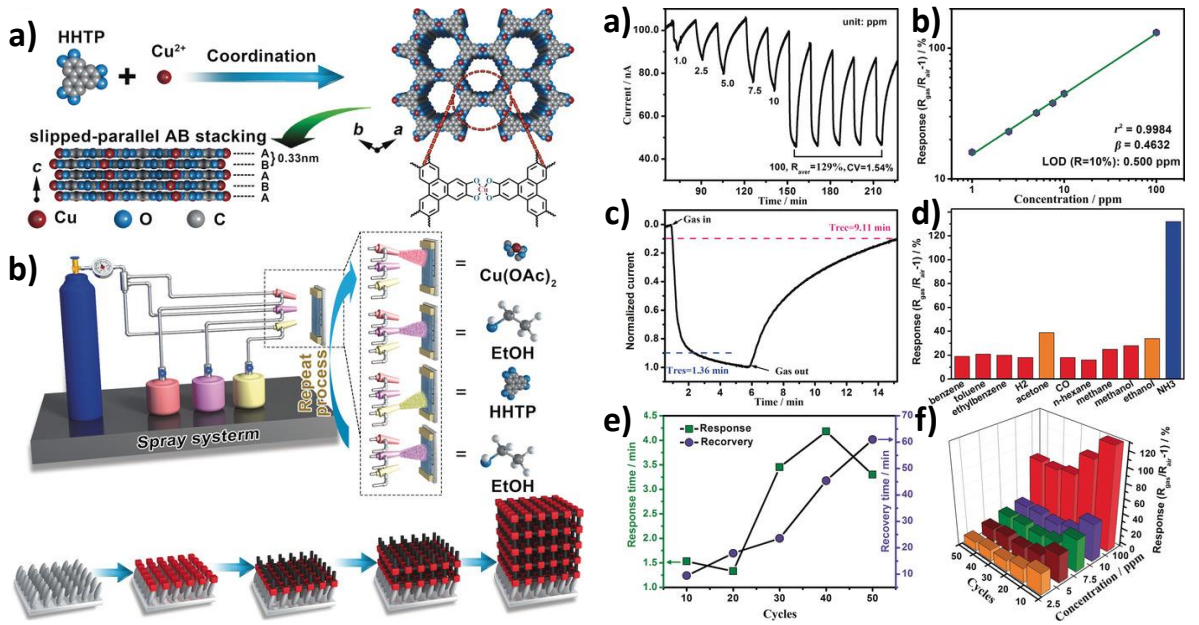

Figure 1.23. Schematic illustration of (a) the crystal structure of $Cu_3(HHTP)_2$ and b) the preparation of $Cu_3(HHTP)_2$ thin-film gas sensors (left). (Right) the gas-sensing performances of $Cu_3(HHTP)_2$-xC: a) the response and recovery curves for different concentrations of NH_3, b) the response-concentration relationship on a log-log scale, c) the response and recovery time curves for 100 ppm NH_3, d) bar graph representation of responses of $Cu_3(HHTP)_2$-10C to various reducing gases, e) Comparison of response-recovery time to 100 ppm NH_3 and f) Comparison of responses to NH_3 with varying concentrations.[90]

1.6.2. Capacitive sensing

Capacitive sensors work by recording the changes in the dielectric permittivity of the sensing material upon adsorption and interaction of analyte molecules. With features like downsizing, simplicity of structure, high sensitivity and ease of signal treatment, capacitive type sensors act as low-cost, rapid, portable and highly efficient sensors. Capacitive sensors offer advantage over other sensors by selectively detecting the analytes with distinct dielectric constants. When making capacitive sensors, two primary geometries are often used: parallel plates (PP) and interdigitated electrodes (IDE). In the case of parallel-plate capacitors, the sensing layer is sandwiched between two metal layers- one serving as the down electrode and the porous layer of metal as the up electrode.[91] The sensing layer is sandwiched between the two electrodes in a parallel plate configuration, and the top electrode must be deposited onto it using complex patterning in order for the analyte to penetrate. Thus, increasing the potential for an electrical short circuit or contact between the two electrodes. Whereas, interdigitated electrodes are created by deposition of single layer of metal onto a substrate in the shape of two interdigitated combs with the sensing material deposited onto the electrodes. IDE capacitive sensors are more favorable than parallel plate sensors in a number of ways, including their simple fabrication process, minimal amount of the sensing material and the fact that the sensing layer is deposited last on top of the IDE structure, allowing it to have maximum exposure to the analyte molecules.[92,93] The sensing material layers are fabricated using certain common methods, including directed self-assembly, layer-by-layer deposition, and drop casting.

The intrinsic insulating characteristics of most MOFs, caused by low mobility and limited concentration of charge carriers, severely restricts their use in chemiresistive sensing. However, the insulating nature of MOFs can be effectively utilized as dielectric layer of capacitors. Local polarity changes are induced upon exposure of MOF sensing layer to different analytes with varied concentrations. As a result of changes in local polarity, the permittivity or dielectric constant of the MOF layer changes. Thus, a correlation between the capacitance changes and the measured analyte concentration can be established.[94,95] A. H. Assen, Eddaoudi, et al,[96] reported the fabrication of a MOF-based capacitive sensor for the detection of hydrogen sulfide (H_2S) at ambient temperature by employing thin films of rare-earth metal (RE)-based MOF with underlying fcu topology. The MOF thin films were directly grown on a capacitive interdigitated electrode. The sensor demonstrated high sensitivity with the detection

limit as low as 5 ppb and high selectivity towards H_2S over other analytes such as CH_4, NO_2, H_2, and C_7H_8 **(Figure 1.24a)**.

Yuan, Zhao et. al.[97] demonstrated a highly CO_2 selective capacitive sensor by integrating thin films of Mg-MOF-74 via in-situ approach on to the surface of IDE. Benzene vapors and carbon dioxide can be detected selectively at room temperature by the sensors that were produced. Modifying Mg-MOF-74 films post-synthetically with ethylenediamine improves CO_2 selectivity while decreasing the sensitivity to benzene. Amine coordination reduces porosity and blocks open metal sites of the framework, which leads to a decline in benzene sensing efficacy of about 60 %. However, the sensor showed increased sensitivity to CO_2 by about 25 % due to strong amine-CO_2 interactions **(Figure 1.24b, c)**. Similarly, Chernikova, K. N. Salama, et al,[98] developed a capacitive sensor for the detection of sulfur dioxide (SO_2) at ambient temperature. The functionalized capacitive interdigitated electrodes are solvothermally coated with a sensing layer based on an indium metal-organic framework (MOF), namely MFM-300. With an exceptional low detection limit of about 5 ppb, the fabricated sensor also demonstrates good stability, reproducibility and high SO_2 selectivity relative to CH_4, CO_2, NO_2, and H_2 **(Figure 1.24d-f)**.

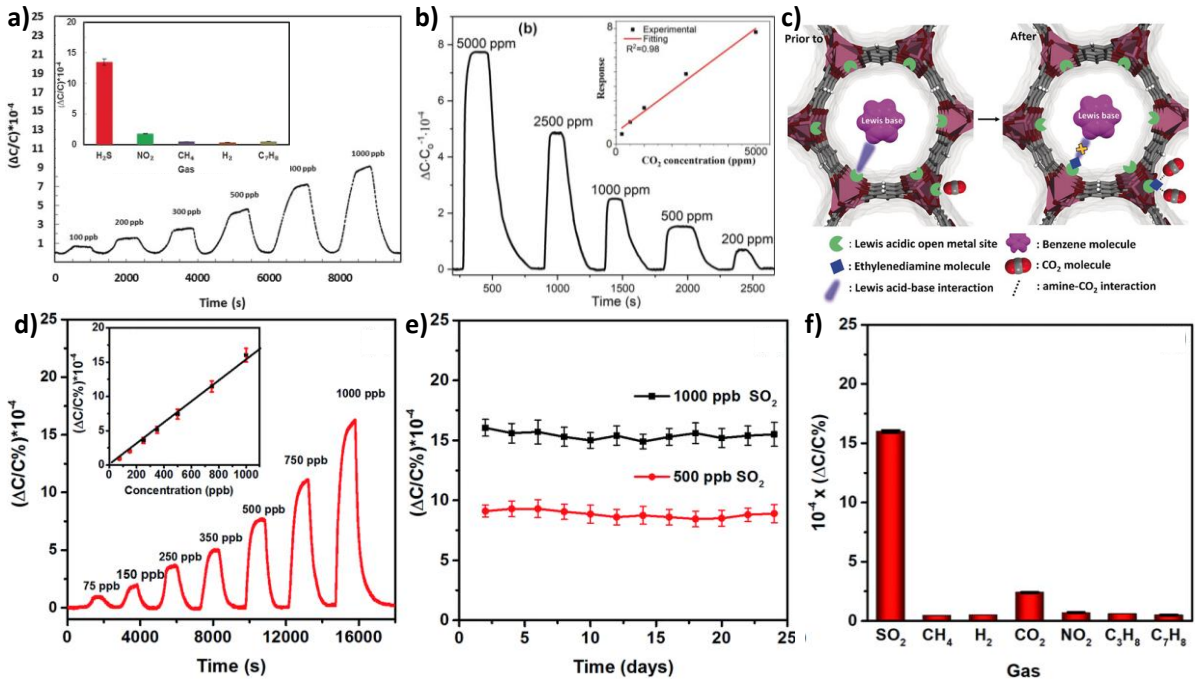

Figure 1.24. Sensing experiments of the MOF sensor towards different concentrations of H_2S (a) 100-1000 ppb with insets depicting the linear response for the corresponding range with inset depicting selectivity studies of the MOF sensor towards H_2S. (b) Capacitive responses of Mg-MOF-74-based capacitive gas sensor upon exposure to

different concentrations of CO_2. (c) Illustration of the interactions between MOF and analyte before and after ethylenediamine functionalization. (d) Capacitive sensing experiments of MFM-300 MOF sensor towards the detection of SO_2 in the concentration range of 75 to 1000 ppb with inset depicting linear response for the corresponding range, (e) stability studies of the sensor SO_2 over a period of 24 days (f) selectivity of the MFM-300 MOF sensor towards SO_2 vs other gases at 1000 ppb.[96-98]

1.6.3. Electrochemical sensing

An electrochemical sensor operates by utilizing the redox reactions of the analytes within an electrochemical system. An electrochemical measurement is typically conducted using a three-electrode setup comprising a working electrode, a counter electrode, and a reference electrode. The concentration of the analytes participating in the reaction can be ascertained by quantifying the current, electric potential, or other electrical signals.[99,100] Electrochemical sensors provide the advantage over other type of sensors due to their high sensitivity towards analytes at very low detection limits, have wide linear response ranges, and have great repeatability. Additionally, the electrochemical sensing capabilities of the electrodes can be adjusted by modifying the surface chemistry.

Due to the swift advancement of synthesis techniques, researchers have been able to successfully design and synthesize stable MOFs with exceptional electrical conductivity.[101-103] Owing to the porosity, high surface area and high catalytic activity, MOFs are promising materials for electrochemical sensing applications.[104,105] However, the majority of MOFs exhibit inadequate electrical conductivity and comparatively limited stability in aqueous solution, mostly due to the reversible characteristics of the coordination bonds. Furthermore, MOFs typically possess a micron-scale dimension, leading to a restricted ability to adhere to the electrode surface. The drawbacks of MOFs impose restrictions on their utilization in electrochemical sensors. To achieve efficient electrochemical signals, it is crucial to design MOFs with high redox active ligands and unsaturated metal centers while still maintaining their unique pore structure. The selectivity of MOFs towards certain analytes is enhanced by size exclusion effects, which are influenced by the actual shape and size of the accessible channels and unoccupied sites of the MOF. Inspired by these intriguing characteristics, a variety of pristine MOFs possessing outstanding electrocatalytic capabilities have been employed as electrocatalysts for the detection of desired analytes. Another

effective approach to address these issues is to integrate MOFs with other functional materials possessing significant electrical conductivity to obtain composite materials.[106,107] Carbon-based composites of MOFs are favored due to their superior conductivity, improved stability, affordability, and the chemical inertness of carbon components.[108-110]

Recent advancements have demonstrated the development and application of numerous electrochemical sensors for the detection of harmful substances, including heavy metal ions, organic pollutants, biomolecules, and toxic compounds, etc. Guo et. al.[111] developed a MOF-based electrochemical sensor for the detection of Pb^{2+}. Monitoring the presence of Pb^{2+}, particularly in trace quantities, in the aquatic environment is crucial for public health. NH_2-MIL-53(Cr) MOF with flake-like structure, was synthesized by a reflux technique and subsequently coated onto a glassy carbon electrode (GCE) to prepare an electrochemical sensor. This sensor exhibited exceptional electrical reactions for Pb^{2+} ions. The oxidation current of Pb^{2+} exhibited a linear increase with increasing concentration within the range of 0.4-80 µM under ideal conditions. The limit of detection (LOD) was determined to be 30.5 nM **(Figure 1.25a)**. The electrode treated with NH_2-MIL-53(Cr) demonstrated exceptional selectivity and stability in detecting Pb^{2+}.

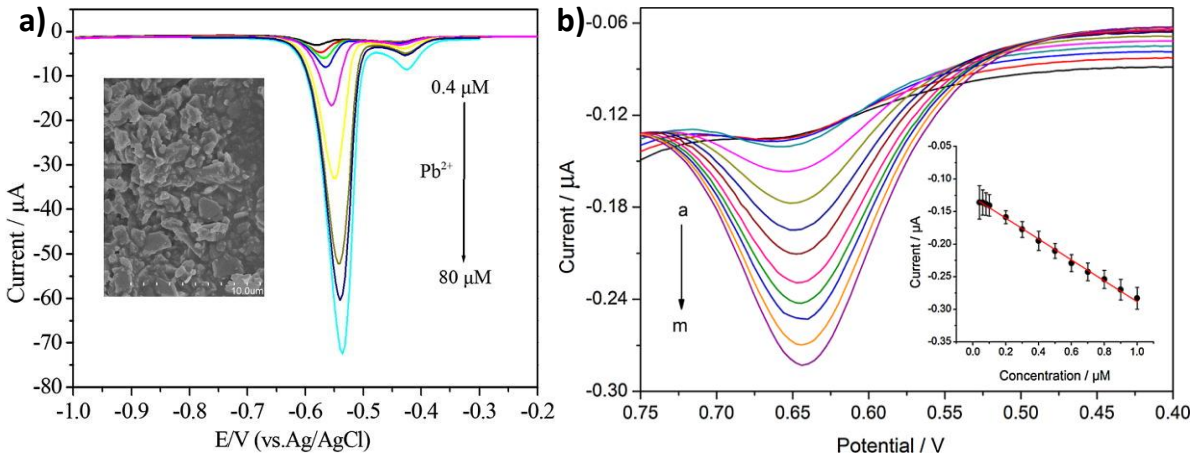

Figure 1.25. (a) Electrochemical response of the NH_2-MIL-53(Cr) modified glassy carbon electrode (GCE) investigated at different concentrations of Pb^{2+}, SEM images of NH_2-MIL-53(Cr) MOF (inset), (b) DPV curves recorded for different concentrations of 2,4-DCP ranging from 0.04 to 1.0 µM in a 0.1 M PBS solution (pH 7.0), linear calibration curve of peak current and concentration of 2,4-DCP (inset).[111,112]

Dong et. al.[112] developed an electrochemical sensor using 1,3,5-benzenetricarboxylic acid copper ($Cu_3(BTC)_2$) as the sensing material to detect 2,4-DCP with high sensitivity. 2,4-dichlorophenol (2,4-DCP) is a type of chlorinated phenol that can be found in water and has the ability to build up in the human body through the food chain. Even at a minimal concentration, it poses a threat to human health. The fabricated MOF sensors demonstrated exceptional selectivity towards 2,4-DCP in comparison to other interfering substances. Additionally, they displayed a broad linear detection range spanning from 0.04 to 1.0 µM, with a limit of detection (LOD) of 9 nM **(Figure 1.25b)**. The utilization of $Cu_3(BTC)_2$ MOF offers numerous benefits, including a substantial specific surface area, a high adsorption capacity, and a commendable electron transfer efficiency. These advantages significantly boost the performance of the electrochemical sensor.

1.6.4. Fluorescence sensing

Luminescent metal organic frameworks (LMOFs) are a significant branch of MOFs that have numerous potential uses in lighting, optical communications, biomedical devices, and chemical sensing. So far, a significant number of LMOFs have been identified, and their luminescence can arise from diverse origins. (1) Organic ligands give rise to luminescence via fluorescence and phosphorescence. Molecular fluorescence refers to the spin-allowed transition from the first singlet state S_1 to the ground singlet state S_0. This type of fluorescence has a very brief excited state lifetime, typically ranging from 1 to 100 ns. Phosphorescence occurs when there is a transition from the triplet state T_1 to the ground state S_0. This transition is not allowed by the rules of spin and is characterized by excited state durations of 1 µs or longer. (2) Emission originating from metal atoms, specifically lanthanide metal ions, d^{10} transition metal ions, and silver clusters, has also been detected. Lanthanide ions exhibit distinct and narrow 4f-4f transitions, resulting in emission ranging from ultraviolet (UV) to near-infrared (NIR) wavelengths. (3) Charge transfer luminescence occurs when there is a transition from the charge transfer excited state to the ground state. This includes ligand-to-ligand charge transfer (LLCT) and metal-to-ligand charge transfer (MLCT). (4) Luminescence can also occur by guest emission from lanthanide ions and fluorescent dyes that are enclosed within the pores of MOFs. Another type of luminescence is guest-sensitization luminescence **(Figure 1.26)**.[81]

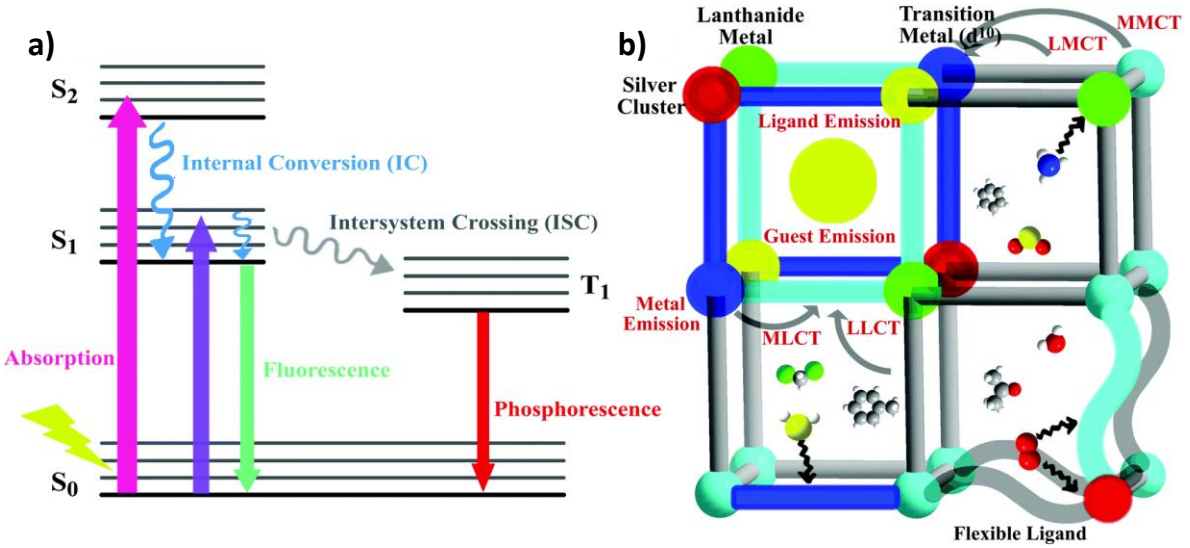

Figure 1.26. (a) Schematic representation of the various photophysical processes. (b) The illustration of the possible sensing mechanisms of luminescent MOF-based sensors.[81]

Furthermore, the diverse interactions between the guest and host framework have the potential to alter the luminous characteristics of MOFs. LMOFs have gained significant attention owing to their distinct properties. For instance, the inherent porosity of the material allows the adsorption of guest molecules into the framework. the guest molecules can interact with the MOF material through weak forces like van der Waals interactions, halogen bonding, hydrogen bonding, and π-π stacking interactions. Furthermore, the pore size of the MOF material can be tuned, which allows for precise control over the guest molecules that can be targeted and analyzed. The inherent crystallinity of MOFs has enabled the investigation of sensing mechanism by modelling the guest molecules inside the framework. This allows for the examination of the specific interactions between the analyte and the host framework.[81]

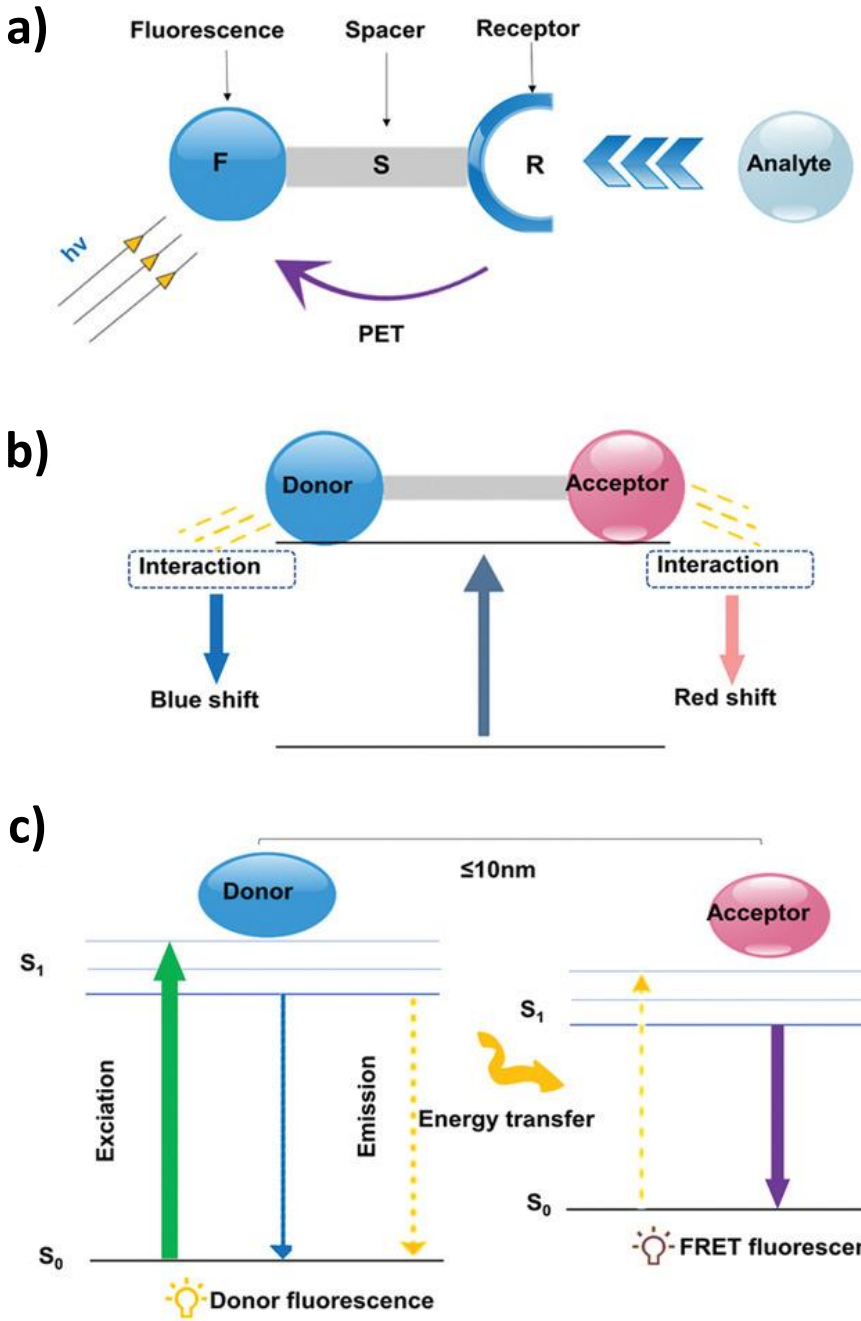

Figure 1.27. Schematic representation of a) PET, b) ICT, c) FRET mechanisms.[121-123]

The main sensing mechanisms observed in LMOFs include photoelectron transfer (PET), intermolecular charge transfer (ICT), Forster resonant energy transfer (FRET), and competitive adsorption, among others.[113-120] The detailed sensing mechanisms are illustrated as follows: i) Photoinduced electron transfer (PET) is a mechanism that involves the transfer of electrons. The receptor, which is linked to the fluorophore by the spacer, interacts with the analytes to accomplish luminous sensing **(Figure 1.27a)**.[121] ii) The interaction between the analytes and LMOFs that have electron-

withdrawing or electron-donating groups can result in intramolecular charge transfer (ICT). This leads to changes in luminescence, such as a blue shift or red shift **(Figure 1.27b)**.[122] iii) Förster energy transfer (FRET) can be demonstrated in the model containing two distinct energy fluorophores **(Figure 1.27c)**,[123] with further consideration of the following contributing factors: 1) the separation between the molecules that donate and accept; 2) the transfer of energy due to the alignment of their dipoles; 3) the extent to which the energy levels of the fluorescence and absorption spectra of the donor and receptor overlap, respectively.[124] PET and ICT mechanisms typically aid in the development of sensors based on LMOFs. Comparatively, the FRET process is inclined towards the creation of ratiometric luminescent sensors.

Several recent review articles have summarized LMOF-based sensors. However, with the rapid growth of the MOF field, new types of MOFs and new types of sensing mechanisms are emerging. Luminescence sensing is a fast and precise method that exhibits excellent sensitivity, selectivity, and reproducibility. This technique has been employed to detect several types of analytes, including inorganic pollutants such as heavy metal ions and radioactive ions, organic pollutants such as antibiotics, pesticides, nitro explosives, poisonous small molecules, and air pollutants such as hazardous gases and volatile organic compounds.[125-130] Wang group reported a fluorescent MOF sensor for the detection of radioactive ions. These hazardous and radioactive contaminants pose a significant risk to the well-being of humans and other organisms. A sensor based on Ln-MOF, specifically $[Eu_2(MTBC)(OH)_2(DMF)_3(H_2O)_4]$, was developed by wang et. al.[131] The sensor demonstrated a doubly interpenetrated structure, as shown in **Figure 1.28a**. The spectroscopic results showed that the Eu-MOF demonstrated highly selective sensing behavior via turn-off mechanism towards Cu^{2+} and UO_2^{2+} ions among other mono, di, tri and tetravalent cations. The detection limits for Cu^{2+} and UO_2^{2+}, were determined to be 17.2 μg L^{-1} and 309.2 μg L^{-1}, respectively, as shown in **Figure 1.28c, d** and c. Further, the quenching mechanism is supported by UV-vis absorption studies, luminescence experiments and lifespan studies. This MOF acts as an excellent luminescence probe for the detection of both radioactive and nonradioactive elements.

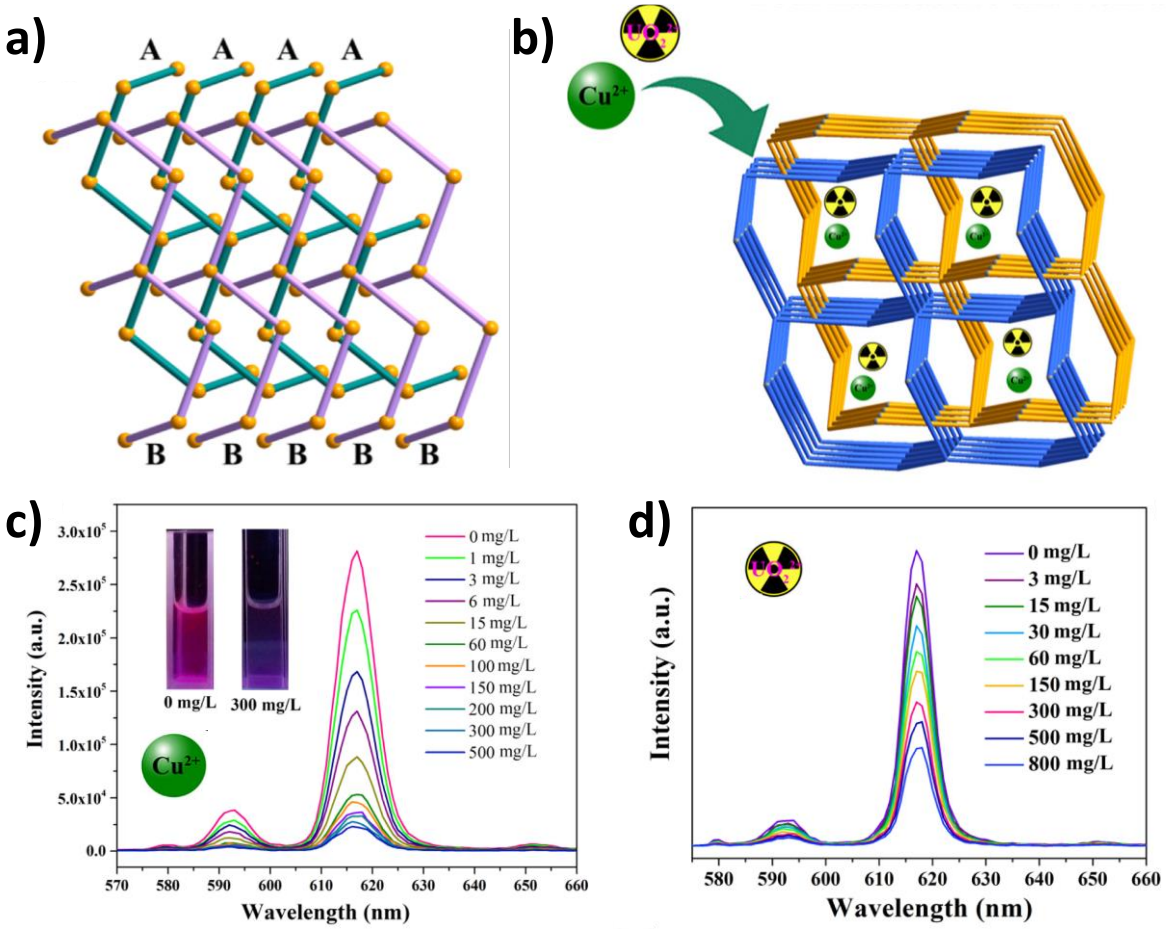

Figure 1.28. (a) The ABAB packing mode of the Eu-MOF, (b) schematic representation of the MOF sensing behavior towards Cu^{2+} and UO_2^{2+} metal ions. Luminescence spectra of the MOF towards increasing additions of (c) Cu^{2+} and (d) UO_2^{2+} metal ions.[131]

Zhou et. al.[132] prepared a three-dimensional porous metal-organic framework using a cyclotriphosphazene-derived hexadentate ligand, which exhibits spiral topologies and numerous connection modes. This MOF exhibits unique solvochromic sensing behavior towards small ketone molecules such as acetone, acetophenone, and 2,5-diketohexane due to the existence of multiple interaction sites decorating the helical channels of the framework. Upon exposure to ketone molecules, the MOF undergoes a color change that is easily noticeable by naked eye, as depicted in **Figure 1.29**. The potential sensing mechanism can be ascribed to the strong hydrogen bonding interactions between guest ketone molecules and μ_2-bridged oxygen of the framework. These experimental results also demonstrate the critical importance of selection of organic ligands with desired functional sites in constructing multifunctional luminescent MOFs.

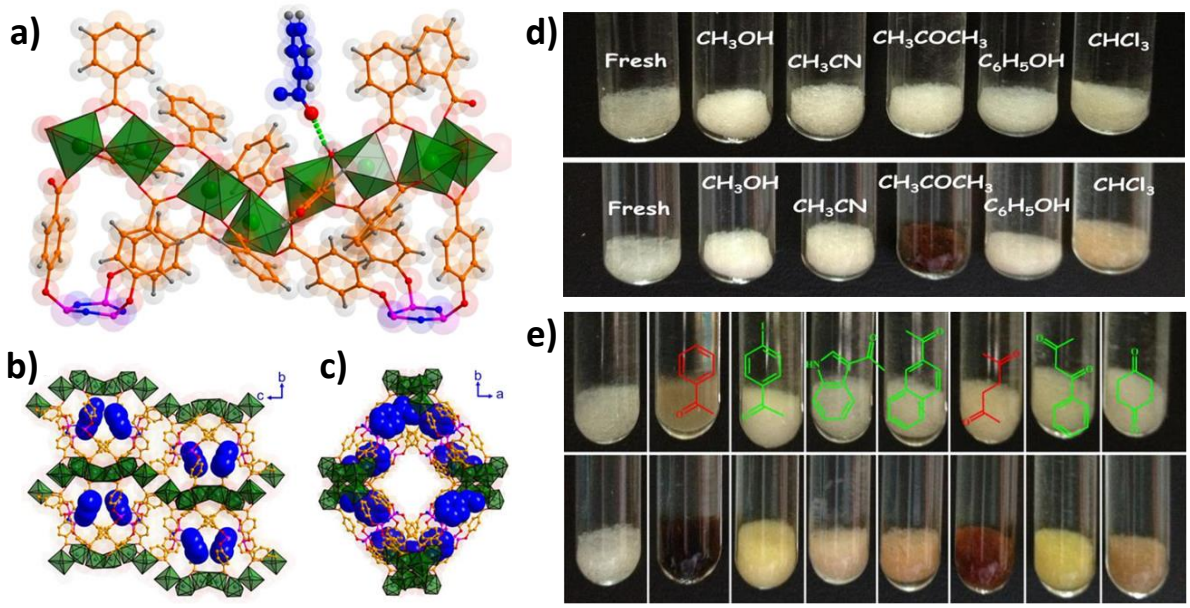

Figure 1.29. (a) Depiction of hydrogen-bonding interaction between the acetophenone molecule (shown in blue) and the host framework, (b, c) 3D representation of the framework after the introduction of acetophenone molecules along the a and c axial directions, (d) solvochromic behavior of the framework towards different solvents and solvochromic behavior of the MOF towards different ketones.[132]

1.7. Research gaps/ Thesis objectives

- The fabrication of materials into electronic devices is an important and extremely practical approach from the application point of view since it shows the prospects of using the material under real conditions. MOFs have not been much explored in this aspect.
- MOFs are renowned for their remarkable water adsorption capabilities. However, despite this fact, MOFs have not yet been investigated for real-time breath sensing applications in healthcare monitoring.
- The study of MOF materials for real-time humidity sensing in glove-box applications is indeed a promising but relatively unexplored area. Incorporating MOFs into sensor fabrication could offer unique advantages, such as high sensitivity and selectivity. Further research in this direction could yield innovative solutions for improved humidity monitoring in controlled environments like glove boxes.

- Developing highly sensitive MOF-based chemical sensors for the detection of harmful analytes such as amines and ammonia that are pervasive in nature and pose a significant threat to human safety is crucial.
- Designing multifunctional MOFs that can rapidly and effectively discriminate chemically similar substances such as aliphatic and aromatic amines is still challenging. Notably, reports on discriminative sensing of amines are very rare.
- Developing MOFs that are highly sensitive and efficient in sensing the analytes in both solution and vapor phases is crucial. This versatility allows for wider applicability, ranging from environmental monitoring to industrial processes, where analytes may exist in different states.
- MOFs, so far, have not been studied meticulously for the practical detection of food spoilage indicators, which could potentially address the challenges in the food sector.
- Developing electrochemical and fluorescent MOF-based sensors holds significance for the swift and sensitive detection of analytes. Additionally, the utilization of dual sensors can provide a more thorough understanding of the sensing phenomenon. Therefore, the development of MOF-based dual sensors is essential, and it's worth mentioning that there is limited literature on such sensors. Interestingly, there are no existing reports on MOF-based dual sensors specifically designed for detecting nicotine.

1.8. Thesis outline

The thesis is structured into eight chapters in accordance with the goals of the investigation.

Chapter 2 provides a thorough description of the techniques such as Single-crystal X-ray Diffraction (SC-XRD), Powder X-ray Diffraction (PXRD), Thermo Gravimetric Analysis (TGA), Brunauer-Emmett-Teller (BET), X-ray Photoelectron Spectroscopy (XPS), Field Emission Scanning Electron Microscopy (FE-SEM), etc. that were employed in studying the MOF systems reported in this dissertation.

Chapter 3 demonstrates the study of MOFs for breath sensing application. The chapter aims to develop a MOF-based breath sensor for studying different breath patterns and sleep apnea problems. To obtain more profound understanding of the sensor performance, a possible mechanism was investigated and discussed in detail. Additionally, a smartphone-based prototype was developed, wherein the breath sensor

was incorporated into a mask and the data was gathered using a smartphone, to demonstrate the real-time applicability of the fabricated breath sensor. Chapter 3 highlights the importance of developing sensors that are capable of monitoring the moisture content in breath especially for sleep apnea diagnosis.

Similarly, **chapter 4** focusses on the study of MOFs for monitoring trace moisture and further analyze their sensing behavior towards different solvents such as water, polar solvents and non-polar solvents. This chapter describes in detail the fabrication of a MOF-based capacitive sensor and its ability to act as a dual sensor that can detect ultralow humidity levels and also discriminate between polar and non-polar solvents. Additionally, the sensor was examined as a real-time humidity sensor for glove box related applications.

Chapter 5 emphasizes on synthesizing two novel Co-based MOFs-**BITSH-1** and **BITSH-2** (Birla Institute of Technology and Science, Hyderabad), and explored them for sensing harmful biogenic amines and food spoilage indicators such as putrescine and cadaverine. Detailed characterization of **BITSH-1** and **BITSH-2** were carried out for better understanding the properties of these frameworks. **BITSH-1** and **BITSH-2** were critically examined for sensing biogenic amines through fluorescence technique and both the frameworks exhibited exceptional fluorescence sensing behavior even at low concentrations of biogenic amines. The underlying sensing mechanism has also been discussed in detail. Additionally, MOF membranes were prepared and investigated for real-time sensing studies to detect food spoilage indicators such as putrescine and cadaverine in fish and cheese samples.

In **Chapter 6,** the work is further extended to check the potential of **BITSH-1** and **BITSH-2** towards the detection of ammonia and discriminative sensing of aliphatic and aromatic amines. Both the frameworks exhibited unique fluorescence behavior with aliphatic amines leading to fluorescence quenching and aromatic amines leading to fluorescence enhancement. The sensing results were further supported by density functional theory (DFT) studies. DFT studies revealed the presence of distinct host-guest interactions with aliphatic and aromatic amines. Further, vapochromic sensing behavior of **BITSH-1** and **BITSH-2** towards amine vapors was examined with the help of MOF pellets. Additionally, the on-site detection of ammonia from a lab-scale chemical reaction was investigated with the help of mixed-matrix MOF membranes.

Chapter 7 focuses on developing multifunctional chemical sensors for the detection of harmful analytes. The multifunctional sensing ability of BITSH-1 in sensing amines and

biogenic amines encouraged us to further check the sensing capability of BITSH-1 towards nicotine. Nicotine sensing studies were carried out systematically using both fluorescence and electrochemical techniques. BITSH-1 displayed high sensitivity and selectivity in detecting nicotine and thus acting as an efficient dual sensor. Real-time sensing studies were carried out to detect the nicotine content in cigarette and urine samples. Additionally, the sensing mechanism was proposed with the help of HOMO-LUMO studies and XPS studies were carried out to show the presence of nicotine in the framework after sensing experiments.

Chapter 8, the final chapter of the thesis, assesses the extent to which the outlined objectives of the study have been accomplished. Comprehensive conclusions drawn from each study (chapters 3-7) are detailed. Additionally, the future scope of work is thoroughly discussed.

CHAPTER 2

Characterization Techniques

The research detailed in this thesis necessitated the utilization of diverse instrumental techniques and methodologies. This chapter provides comprehensive descriptions of characterization techniques, and further details on instrumental and synthetic procedures used can be found in the respective chapters.

2.1. Single crystal X-ray diffraction (SC-XRD)

SC-XRD studies were carried out to determine the MOF structure and the coordination environment in the framework. Structural analysis is important to topology, composition and interactions at the molecular level in the MOF structure. The possible interactions with the targeted analytes can also be visualized using this study. The SCXRD measurements were performed on the Rigaku XtaLAB P200 diffractometer using graphite monochromate Cu-Kα radiation (λ = 1.54184 Å). The data was collected and reduced using CrysAlisPro (Rigaku Oxford Diffraction) software. The data collection was carried out at 100 K in most cases and the structures were solved using Olex2 software with the ShelXT structure solution program and refined with the ShelXL refinement package using Least Squares minimization.

2.2. Powder X-ray Diffraction (PXRD)

The crystallinity and phase purity of the as-synthesized crystals were determined from the powder X-ray diffraction (PXRD) pattern. The PXRD patterns were recorded using a Rigaku Ultima-IV diffractometer supplied with Cu K-α radiation (40 kV, 40 mA) as the source in the 2θ range of 5°- 40° with a step size of 0.1 °/min. The patterns were plotted using origin software. The phase purity of the experimental PXRD pattern was confirmed by comparing it with the simulated PXRD pattern generated from the single crystal structure. The framework stability after a particular experiment can also be examined with the help of PXRD patterns.

2.3. Thermo Gravimetric Analysis (TGA)

The thermal stability of the as-synthesized samples was analyzed by TGA by studying the weight loss of the material as a function of temperature. The TGA curves are recorded under a N_2 atmosphere using a Shimadzu DTG-60 instrument in the temperature range of 30 ℃ to 800

°C. The heating rate was maintained at 10 °C min^{-1}. The thermograms were plotted using origin software.

2.4. Brunauer-Emmett-Teller (BET) Analysis

Microtrac Bel- BELSORP mini II model surface area analyser was used to collect nitrogen adsorption isotherms. Before recording the nitrogen adsorption isotherms, the as-synthesized crystals were desolvated by heating under a dynamic vacuum. The BET surface area, pore size, and pore volume of the samples were determined from the N_2 adsorption isotherms. Vapour dsorption studies were carried out using Autosorb (automated gas sorption analyzer) iQ, Quantachrome instrument. The framework porosity and the uptake capacity of the material towards each solvent can be determined with the help of this study.

2.5. X-ray Photoelectron Spectroscopy (XPS)

X-ray photoelectron spectroscopy (XPS) experiments were performed to identify the elemental composition and the oxidation state of the elements present in the MOF sample. XPS analysis was performed using a Thermo Scientific K-α instrument with multi-element, high-transmission spectrometer input lens and 128-channel detector for high quality spectra operating with Kinetic energy: 5-1500 eV. The source used for the XPS analysis is Al K-α source [X-ray source 1486.8 eV].

2.6. Field Emission Scanning Electron Microscopy (FE-SEM)

The as-synthesized MOF crystals were washed with DMF thoroughly and dried before the analysis. The morphology and surface analysis of the as-synthesized crystals was studies using FE-SEM analysis. SEM images were obtained using an FEI Apreo LoVac instrument. The elemental information can be obtained at magnifications of 10x to 300,000x, with a high resolution of 1.5 to 2 nm. Energy-dispersive X-ray analysis (EDX) and elemental mapping is also carried out using Aztec Standard EDS system - resolution 127 eV to determine the elemental composition of the MOF material.

CHAPTER 3

MOF-based Flexible, Low-cost Chemiresistive Device as a Respiration Sensor for Sleep Apnea Diagnosis

Breath sensors that are fast, robust, convenient to use, and can function under real time conditions can be useful in monitoring various respiratory disorders. This can be achieved by detecting important compounds such as water, acetone, or ethanol from human breath. As water constitutes a major portion of our breath, the detection of water molecules is more convenient out of all other compounds. Conventional materials such as dichalcogenides and metal oxides have been mostly used to design breath sensors till date. However, MOFs have not been explored as breath sensors and have never been reported for breath sensing applications, despite their good water retention properties and high porosity. In the present chapter, HKUST-1 MOF with excellent water stability and water adsorption properties was chosen for breath sensing studies. Further, MOF-based electronic sensor was fabricated with the help of conducting MoS_2 material for sleep apnea problems by monitoring different breath patterns. Extensive breath sensing experiments have been performed with the sensor and interestingly the fabricated sensor shows high sensitivity in detecting various kinds of breaths such as slow, fast, deep, and hydrated breath. The MOF-based breath sensor shows a very fast response time and displays excellent atmospheric stability with no decline in its performance even after a month. A plausible mechanism has also been proposed to support the sensing studies. A smartphone-based prototype has been further designed to demonstrate the real time application of the MOF-based hybrid device. This work demonstrates great potential for the application of MOFs in healthcare with a special focus on breath sensing and sleep apnea diagnosis.

3.1. Introduction

Metal-organic frameworks (MOFs), hybrid materials consisting of organic–inorganic building units, have emerged as a popular class of porous materials which have shown widespread applications in the areas of gas storage, separation, drug delivery, catalysis, etc.[1-5] Owing to their high porosity, stability and ease of fine tuning, MOFs are a desirable choice for chemists for designing materials for challenging applications.[6,7] The easy tunability and uniform pore size of MOFs provide an edge over their counterparts such as zeolites and silica. Besides gas sorption and storage, MOFs have also been used for various types of sensing applications, such as sensing of gases, volatile-organic compounds (VOCs), biomolecules, amines and

explosives.[8-13] In most of the cases, sensing is demonstrated with the help of well-known techniques such as UV-Vis spectroscopy, fluorescence and IR spectroscopy.[14,15] These methods do provide important information on the sensing behavior of an MOF material towards different analytes. However, attempts to fabricate MOF materials into fully electronic devices for real time applications have rarely been made.[16,17] The fabrication of the materials into electronic devices is an important and extremely practical approach from an application point of view since it shows the prospects of using the materials under real time conditions. The role of MOFs in water capture and storage has lately gained a lot of attention.[18] In 2014, Yaghi and co-workers showed how MOFs could be a potential candidate for capturing water from air in the desert areas that suffer from high water scarcity.[19,20] Since then there have been various reports on using MOFs for water capture, dehumidification and humidity sensing.[21,22] Recently, the Eddaoudi group reported Cr-soc-MOFs for indoor humidity control with exceptional water uptake capacity.[23] Due to their excellent water capturing capabilities, it could be interesting to employ MOFs for studying human breath patterns which has not been done to date. The amount of water present in different types of breaths such as slow, fast, hydrated, and dehydrated breath is different and such changes could be monitored using an electronic device that can function at different humidity levels.

A recent surge in healthcare demands makes it imperative to design better materials for detection and cure of numerous common health related problems.[24] MOFs, so far, have not been studied meticulously for the fabrication of sensing devices that may offer solutions to challenges pertaining to the healthcare sector. One of the common health problems that needs to be taken care of is Obstructive Sleep Apnea (OSA) which is severe sleep disorder with issues such as excessive day time sleeping, fatigue and cardiovascular diseases associated with it.[25,26] OSA is caused by air blockage during sleep which reduces the blood flow to the brain. Approximately 2 % of women and 4 % of men are affected by OSA but more than 90 % of the cases go undiagnosed.[27] This is due to the lack of handy techniques for diagnosis of OSA. Polysomnography is a common technique which needs bulky instruments and is also invasive and disturbs sleep, which results in inaccurate readings.[28] Lately, there have been research on breath and flow sensors for diagnosis of OSA.[29] However, most of the devices are contact based sensors which have strict positional requirements and hence do not serve the purpose of patient comfort. There are recent reports on non-contact breath sensors for various applications,[30-32] but the signal to noise ratio of such sensors is low, which leads to inaccurate results. To achieve a high signal to noise ratio, the materials utilized for sensing should be highly sensitive to breath and should be able to provide a large signal output even for smaller

quantities of input. For this, it is important to explore materials that have excellent water adsorption properties. MOFs are well known for their water adsorption capacities,[33] and it will be fascinating to study them for real time breath sensing applications for healthcare monitoring. However, a big challenge in the case of employing MOFs for the fabrication of electronic devices is their inherently poor conductivity.[34] MOFs are generally not good conductors and therefore it becomes necessary to have an underlying conducting support that offers a viable route for electron transport for smooth functioning of the devices. In search of a conducting support, transition metal dichalcogenides (TMDs), which are a class of 2-dimensional materials that are atomically thin, have gained significant attention due to their intriguing electronic, chemical and mechanical properties.[35,36] MOFs are well known for their adsorption properties that assist in capturing a greater amount of water molecules exhaled from breath and MoS_2 acts as an active site for electron exchange and transport due to its excellent electron mobility.[37-39] In the present work, a MOF-MoS_2 based sensor has been designed to utilize the individual properties of both materials for enhanced sensing behavior towards breath sensing for obstructive sleep apnea applications.

3.2. Experimental Section

3.2.1. Materials

Cupric Nitrate Trihydrate [$Cu(NO_3)_2 \cdot 3H_2O$] extrapure, N,N′- dimethyl formamide (DMF), methanol were purchased from SRL, 1,3,5- benzene tricarboxylic acid (BTC) was purchased from TCI chemicals. All the reagents and solvents were used as such without additional purification.

3.2.2. Synthesis procedure of HKUST-1

$Cu_3(BTC)_2$, (HKUST-1)] was synthesized according to the reported procedure[40] with slight modifications. $Cu(NO_3)_2 \cdot 3H_2O$ (1.4 mmol) and 1,3,5-benzene tricarboxylic acid (0.8 mmol) were dissolved in 10 ml of water, ethanol and DMF mixture in the ratio 2:1:1. The solution was sonicated for about 10 min until the reagents were dissolved completely. The vial was then placed in the oven at 373 K. The vial was removed from the oven after 12 h and cooled to room temperature. The blue crystals thus obtained were washed thoroughly with DMF and ethanol. The resulting product was then dried at 343 K for further characterization.

3.2.3. MOF-MoS_2 device preparation

MoS_2 is directly grown by a hydrothermal process. For drop casting MOF on MoS_2, 1 wt % of MOF solution was dispersed uniformly in ethanol and 100 ml of this solution was then drop cast on to the MoS_2 coated flexible support.

3.2.4. Details of the Android Application

This app aims to showcase a practical functionality of the fabricated device. It can be seen from the attached graphs that there is a marked drop in the resistance as the device is exposed to moisture. This property of the material is exploited in building this app. An Arduino based setup is used to make this work. Using a potential divider circuit, the resistance of the device is measured. The average of the first five readings is taken as a reference. Once the device is in use, the very first reading (R_0) will be compared against this reference value (R_f). The percentage change between two readings is measured as the 'change' integer. $change = \frac{R_{i-1} - R_i}{R_{i-1}} \times 100$

If this change is greater than 30%, there has been a drop in the resistance, i.e., the user has taken a breath, which exposed the device to moisture. When this change is noticed, the Arduino transmits a **'NORMAL'** message via Bluetooth, which can be received on a mobile phone app. We also have an integer variable 'alert', which will be set to zero every time breath is taken. If change is lesser than 30%, there has not been a change in resistance for a certain period of time. This means there was no breath taken, and **'ABNORMAL'** message is transmitted by Arduino via Bluetooth. Also, after this event, integer variable 'alert' is incremented. When 'alert' is greater than or equal to three, it means that there has been no breath taken by the user for three consecutive readings (three consecutive ABNORMAL signals)- this prompts Arduino to transmit an **'ALERT'** message via Bluetooth. This will trigger the app to send an SMS to the user's family, notifying them that there has been no breath taken for a while.

The flowchart of the algorithm for this function is as below:

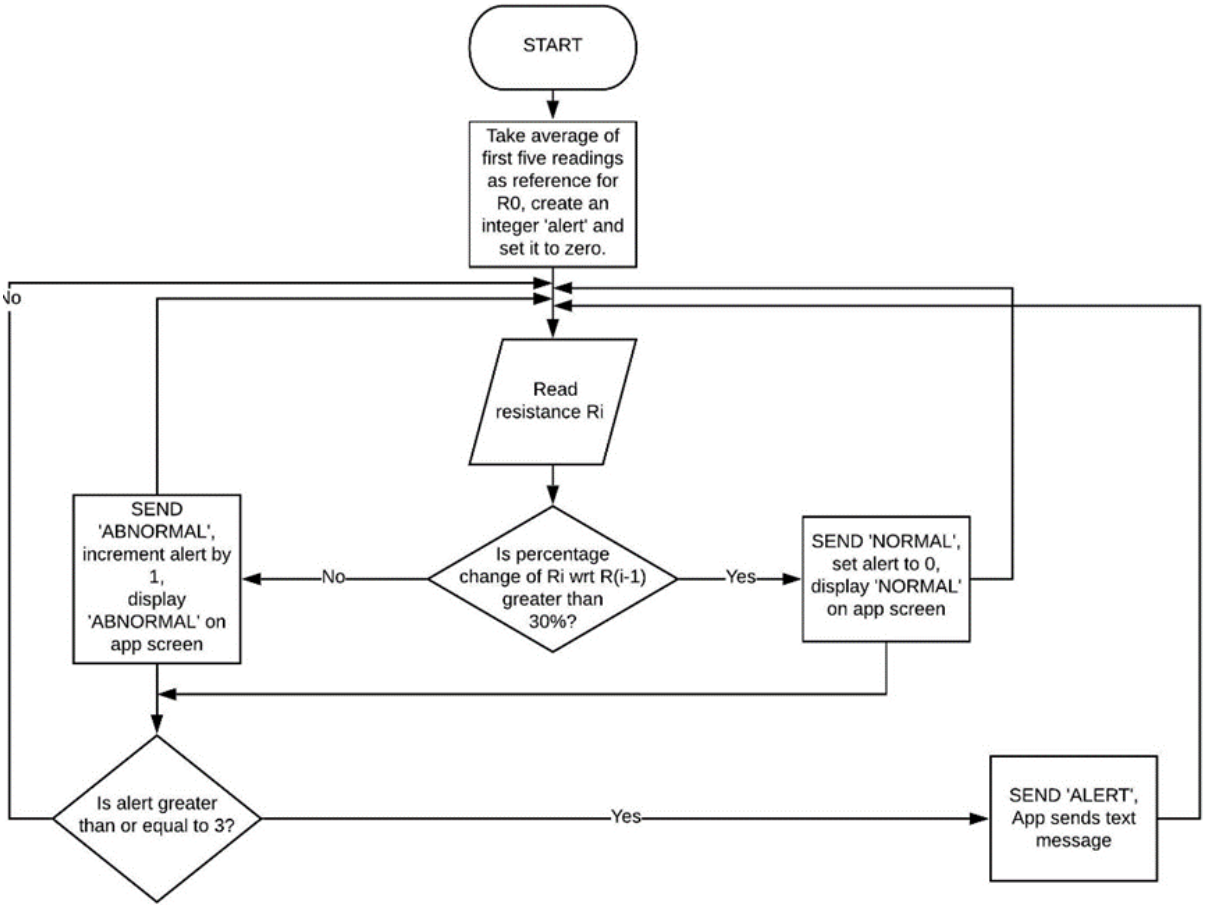

3.3. Results and Discussion

The current chapter discusses the design and fabrication of HKUST-1 MOF/MoS_2 based hybrid flexible respiration sensor for sleep apnea diagnosis. HKUST-1 was synthesized by a solvothermal approach using a reported procedure **(Figure 3.1)**.[40] The secondary building unit (SBU) of the HKUST-1 structure consists of a Cu paddlewheel where the Cu-Cu dimers are coordinated to benzene tricarboxlyate linkers (BTC). The tricarboxylate linker acts as a 3-c node, whereas the SBU, $Cu_2(-CO_2)_4$, acts as a 4-c node. The underlying net is bi-nodal with a (3,4)- coordinated *tbo* topology. The metal clusters also contain coordinated water molecules that can render active metal sites upon complete activation **(Figure 3.1)**.

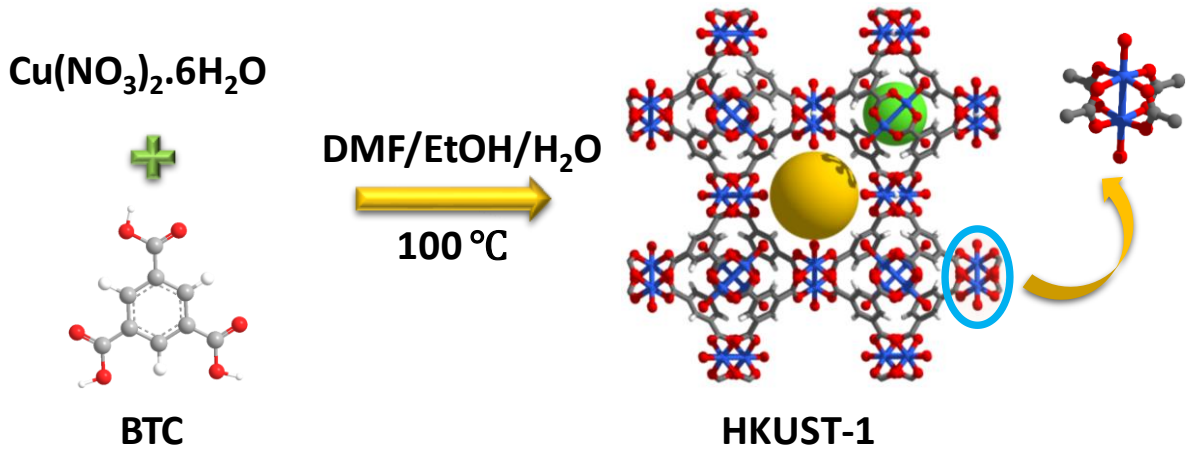

Figure 3.1. Schematic illustration of HKUST-1 synthesis and its crystal structure.

The phase purity of the as-synthesized material was confirmed by comparing the powder X-ray diffraction (PXRD) patterns of the as-synthesized material with those of the reported structure **(Figure 3.2a)**. HKUST-1 has a pore diameter of about 9 Å with a pore window size around 6 Å.[41] Thermogravimetric analysis shows solvent loss till 150 ℃ and decomposition beyond 300 ℃ **(Figure 3.2b)**. The sample showed good thermal stability up to 300 ℃. The BET surface area for the pristine and the ground samples was determined using nitrogen gas at 77 K and both the samples displayed similar N_2 uptake **(Figure 3.2c, d)**. Prior to the adsorption experiment, the crystals were activated at 125 ℃ under dynamic vacuum. The framework showed a BET surface area of 1498 $m^2\ g^{-1}$ with 0.665 $cm^3\ g^{-1}$ pore volume **(Figure 3.2e)**. The experimental pore diameter is around 8 Å which is very close to the literature value.[41] The water stability of the MOF sample was established before carrying out humidity experiments, by immersing the crystals in water for 24 h and the PXRD patterns were recorded before and after exposure to water. The MOF sample showed no deterioration in crystallinity and the PXRD patterns matched closely with those of the as-synthesized sample **(Figure 3.2a)**.

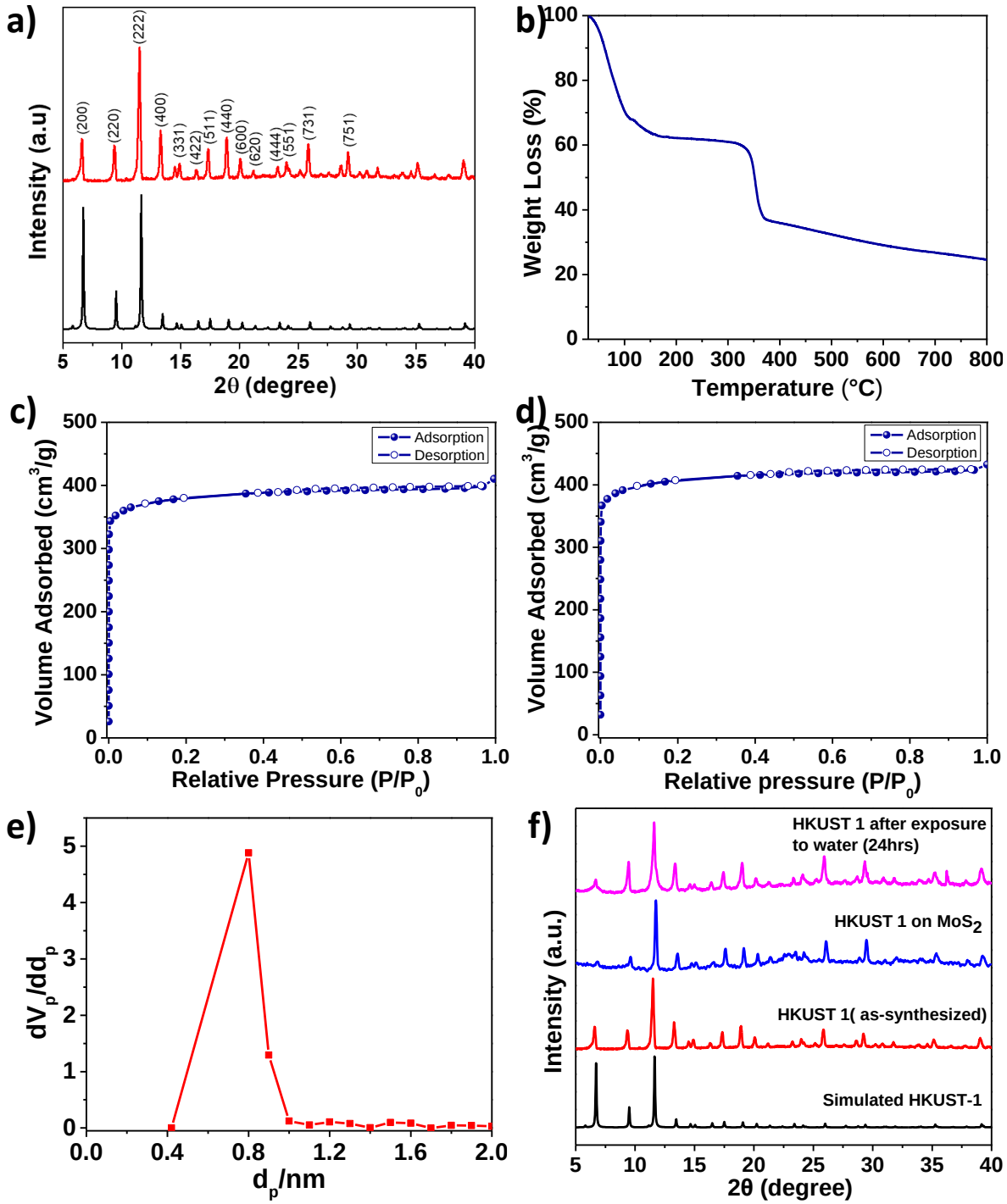

Figure 3.2. (a) Comparison of the experimental and simulated XRPD patterns of HKUST-1, (b) TGA profile of as-synthesized HKUST-1 crystals, N_2 sorption isotherm for the (c) pristine and (d) grinded HKUST-1 samples. N_2 adsorption isotherm of HKUST-1, (e) Pore size distribution of activated Cu-BTC MOF, and (f) the comparison of XRPD pattern of as-synthesized HKUST-1 crystals, HKUST-1 sample drop casted on MoS_2, and HKUST-1 sample after exposure to water for 24 h.

MoS_2 was grown directly on a cellulose paper substrate using a solution processed hydrothermal method as shown in **Figure 3.3**. The direct growth of MoS_2 on paper involves two steps: a seeding process followed by hydrothermal growth. Seed solution was prepared by properly mixing $Na_2MoO_42H_2O$ (10 mM) and CH_4N_2S (20 mM) in deionized (DI) water (10 ml). A paper substrate of dimension 3 cm × 3 cm was immersed in the seed solution for 40 min followed by drying at 70 °C for 15 min. Nutrient solution was prepared by mixing Na_2MoO_4 $2H_2O$ (50 mM) and CH_4N_2S (100 mM) in 30 ml of DI water.

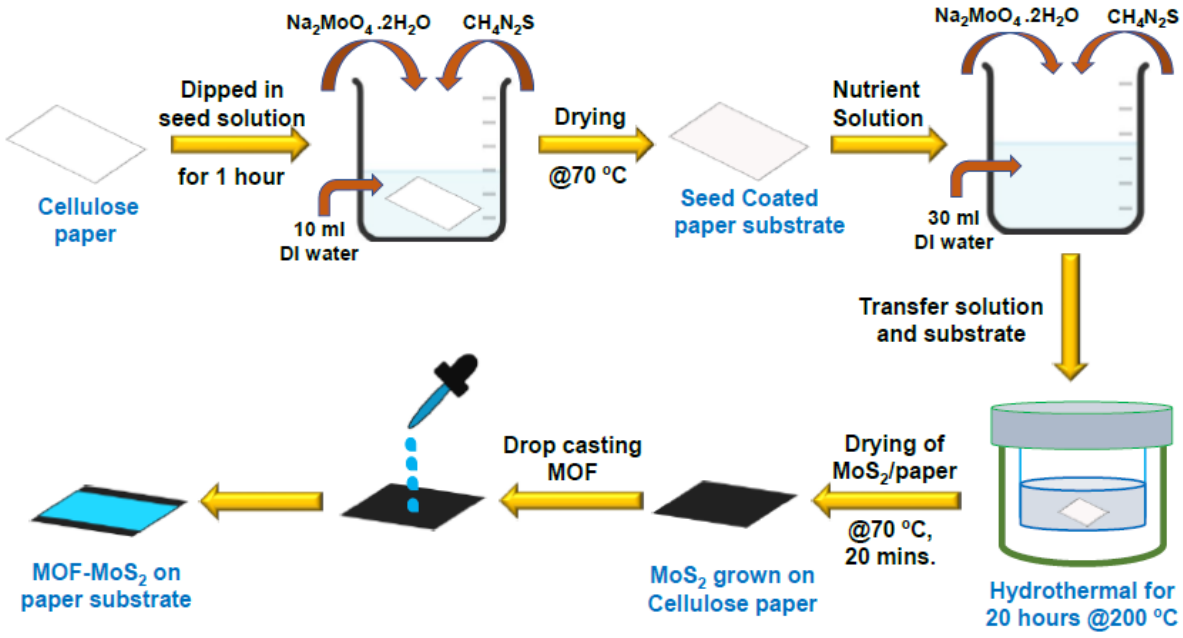

Figure 3.3. Schematic illustration of growing MoS_2 on a cellulose paper substrate and drop casting of MOF powder on MoS_2 support for device fabrication.

The seed coated cellulose paper and the well dispersed nutrient solution were transferred to a Teflon lined stainless steel autoclave and kept in a hot air oven for 20 h at 200 °C. After that, the autoclave was allowed to cool down and the resultant MoS_2 coated cellulose paper was annealed at 70 °C for 20 min. In order to have uniform coating, the MOF crystals were first gently ground with a mortar and pestle in the presence of ethanol and then the ground sample was dropcasted on the MoS_2/cellulose paper **(Figure 3.3)**. The PXRD patterns of the dropcasted HKUST-1 sample on MoS_2 and the as-synthesized crystals were compared to confirm the integrity of the MOF sample after coating on the MoS_2 support **(Figure 3.2f)**. To study the morphology, FESEM analysis was carried out on the as-synthesized single crystals, ground sample, MoS_2 on cellulose paper and ground MOF sample coated on MoS_2 **(Figure 3.4a-c)**. The size of the as-synthesized single crystals ranges from 10 to 30 μm **(Figure 3.4a)**.

The uniform coating of the MOF material on the support can be observed in **Figure 3.4c**. **Figure 3.4d** shows the XPS survey spectra of the MOF coated on the MoS_2/paper, wherein the binding energy peaks confirm the presence of Cu, Mo, S, C and O elements.

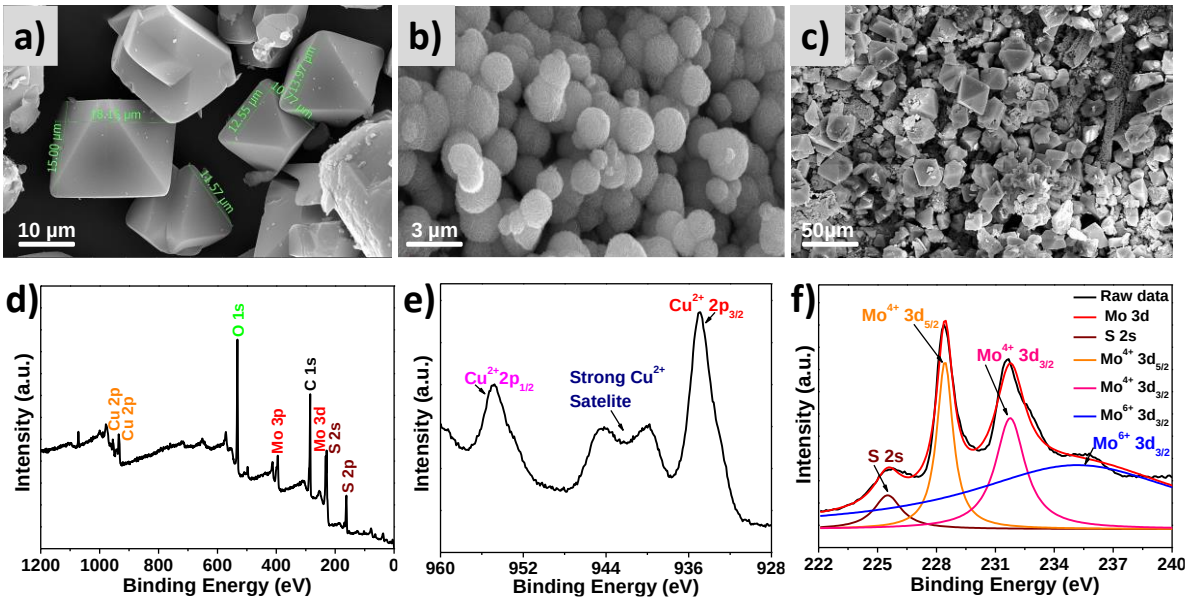

Figure 3.4. SEM images of (a) HKUST-1 single crystals, (b) MoS_2, (c) HKUST-1 grinded sample drop casted on MoS_2 support and XPS data of HKUST-1-MoS_2 sample (d) full XPS spectrum, (e) Cu 2p XPS spectrum and (f) Mo 3d S 2s XPS spectrum.

Figure 3.4e shows a high resolution XPS spectrum of Cu 2p, wherein two characteristic peaks corresponding to Cu $2p_{3/2}$ and Cu $2p_{1/2}$ were observed at 934.8 eV and 954.8 eV, respectively, suggesting that Cu exists as the Cu^{2+} oxidation state.[42,43] A deconvoluted Mo 3d high resolution spectrum is shown in **Figure 3.4f**; it contains two doublet peaks at 228.4 eV and 231.7 eV, which signifies the presence of Mo^{4+} $3d_{5/2}$ and Mo^{4+} $3d_{3/2}$, respectively. Two more peaks were observed at 225.5 eV and 235.7 eV corresponding to S 2s and Mo^{6+} 3d, respectively, and the presence of the Mo^{6+} oxidation state can be attributed to the existence of a small amount of unreacted MoO_4^{2-} during the synthesis of MoS_2.[44] The high resolution spectrum of S 2p, wherein two spin orbit coupling peaks of S $2p_{3/2}$ and S $2p_{1/2}$ are observed at 161.4 eV and 162.5 eV respectively, suggests the S^{2-} state of S as shown in **Figure 3.5**.[45] Similarly, the binding energies for O 1s and C 1s have also been shown **(Figure 3.5**, bottom**)**. EDX analyses were also carried out to ascertain the elemental composition of the HKUST-1 samples **(Figure 3.5**, top**)**.

a)

Element	Weight%	Atomic%
C	44.07	61.01
O	31.33	32.56
Cu	24.60	6.44
Totals	100.00	

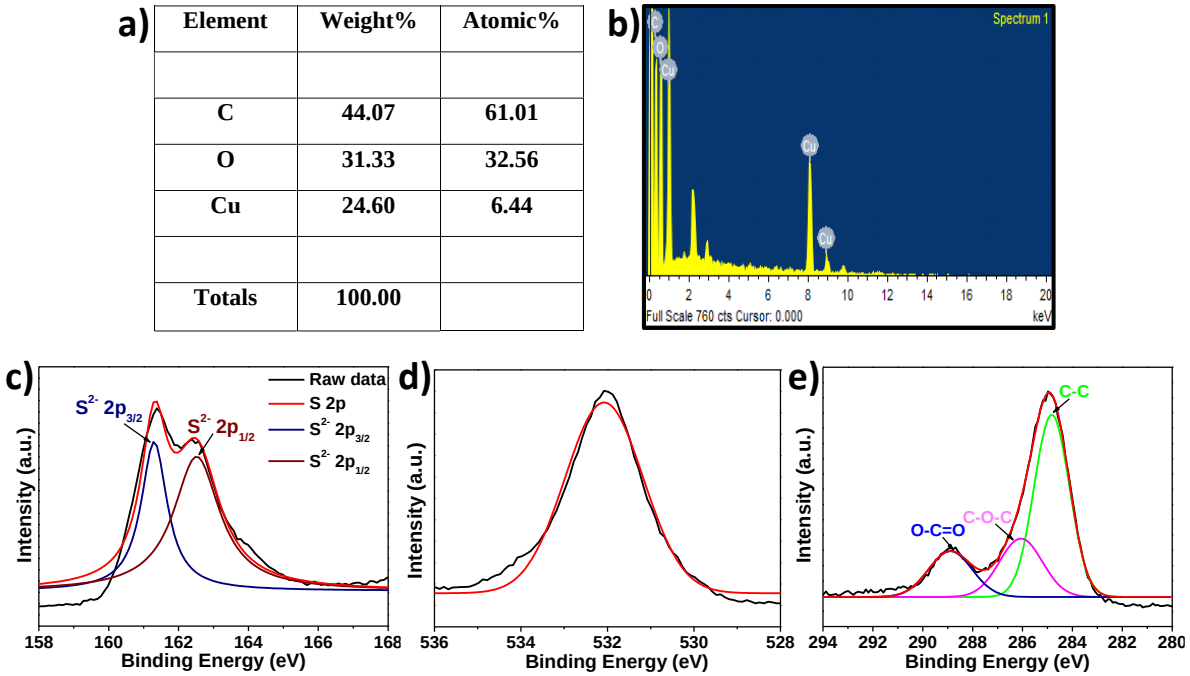

Figure 3.5. (a) Elemental data of Cu-BTC MOF, (b) EDX spectrum (top), XPS spectrum of HKUST-1 MOF on MoS_2 showing binding energies for (c) S 2p, (d) O 1s and (e) C 1s (bottom).

Breath sensing experiments were conducted in a sequential manner, whereby the response of the MOF coated device was tested by keeping the device 4 cm away from the nose of an individual. **Figure 3.6** shows the temporal response of the fabricated device under normal breath (12 breaths per min) where a few seconds delay was given in between consecutive breaths under ambient conditions. Interestingly, during exhalation, an increase in the device current was observed and during inhalation the current decreased, which clearly shows that the fabricated device can be useful for detecting variations in breath. It should be noted that the current does not return to its initial value, which can be attributed to the slow rate of desorption/removal of water molecules. HKUST-1 is known to retain water even at 0 % relative humidity under nitrogen stream and complete desorption takes place only after reactivation of the material.[46] Also, achieving a stable baseline is not important in breath sensing, as the application demands counting of the number of breaths which corresponds to the number of current peaks. To further analyse the capability of the device, it is tested for breath patterns such as slow (6 breaths per min) and fast breath (17 breaths per min), wherein the frequency of the breath pattern is the key observation.

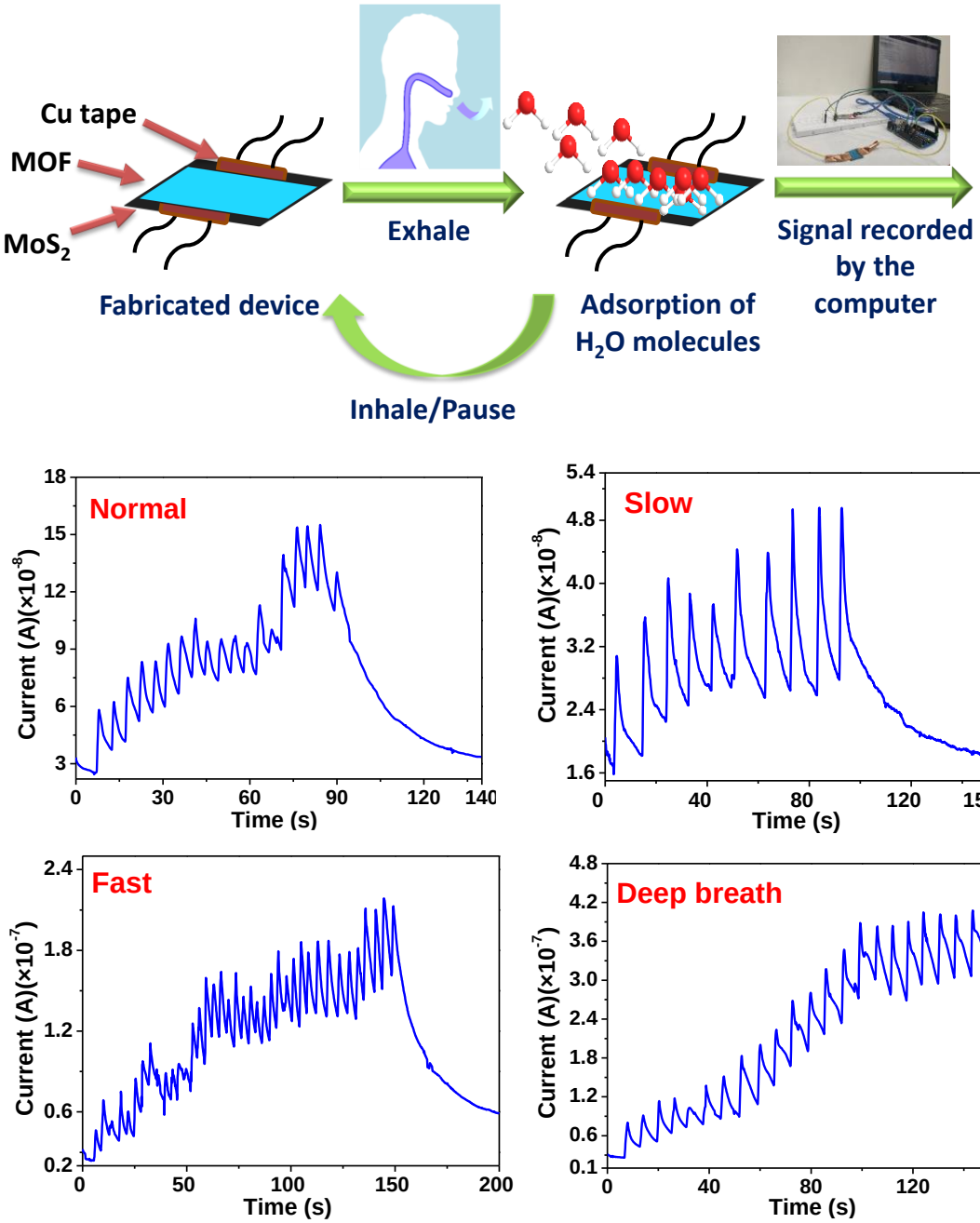

Figure 3.6. HKUST-1-MoS_2 fabricated sensor for breath sensing (top), and breath sensing experiments showing variation in current in response to different types of breaths; normal breath, slow breath, fast breath and deep breath (bottom).

Figure 3.6 shows the temporal response of the fabricated sensor under a slow and fast breath pattern, respectively. Compared to a normal breath pattern, in a fast breath pattern, the frequency of the peaks increased by ~ 42 %. Similarly, in the case of a slower breath pattern, the frequency decreased by ~ 50 %. The temporal response of the fabricated device under a deep breath pattern (8 breaths per min) is also shown in **Figure 3.6**, and an 8-14 % increment in the peak value of the sensor current was observed.

To check the repeatability of the experiments, the fabricated device was tested for iterative breath patterns, wherein the individual was asked to take 3 consecutive exhalations. The same experiment was repeated for 5 cycles with a suitable time gap in between each cycle for the sensor current to regain its initial value **(Figure 3.7a)**. Further, the same experiment with three iterative breathing patterns was performed for ~ 1000 s **(Figure 3.7b)** and a negligible change in the device performance was observed, which demonstrates the robustness and reliability of the fabricated sensor. This clearly shows that if the delay time between the two consecutive cycles is more than the desorption time, then the sensor current regains its initial current value. In addition, the fabricated device was tested at different hydration levels **(Figure 3.7c)**. When the hydration levels of the breath are high, a higher amplitude of the device current upon breath exhalation was observed. Similarly, an inverse experiment was also performed, wherein the individual was not allowed to drink water for 6 hours and then breath exhalation experiments were performed, and as observed, the amplitude of the device current was low when compared to the normal breath **(Figure 3.7d)**. The variation in the amplitude of the device current suggests that it could be potentially applied as a diagnostic tool for hydration monitoring.

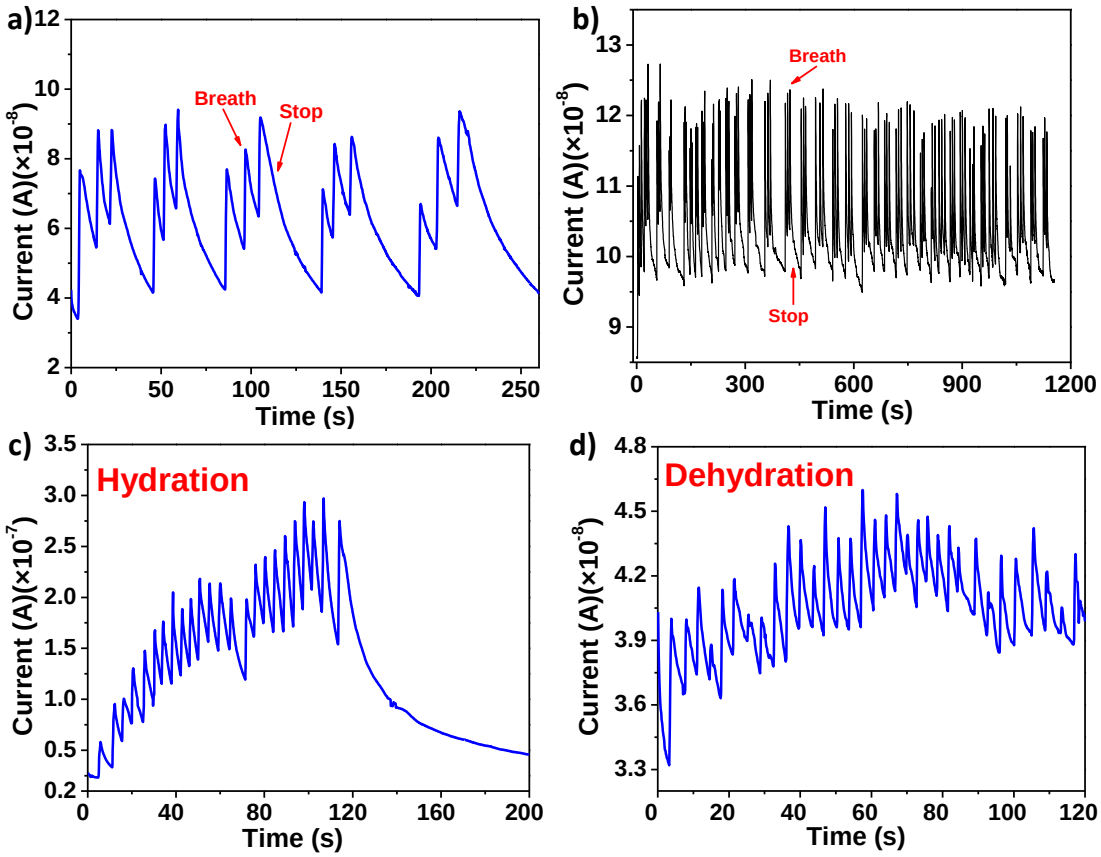

Figure 3.7. (a) Breath cycles showing five breath cycles of three breaths each, (b) three breath iterative breathing pattern for around 1000 sec, breath sensing experiments for (c) hydrated, and (d) dehydrated breaths.

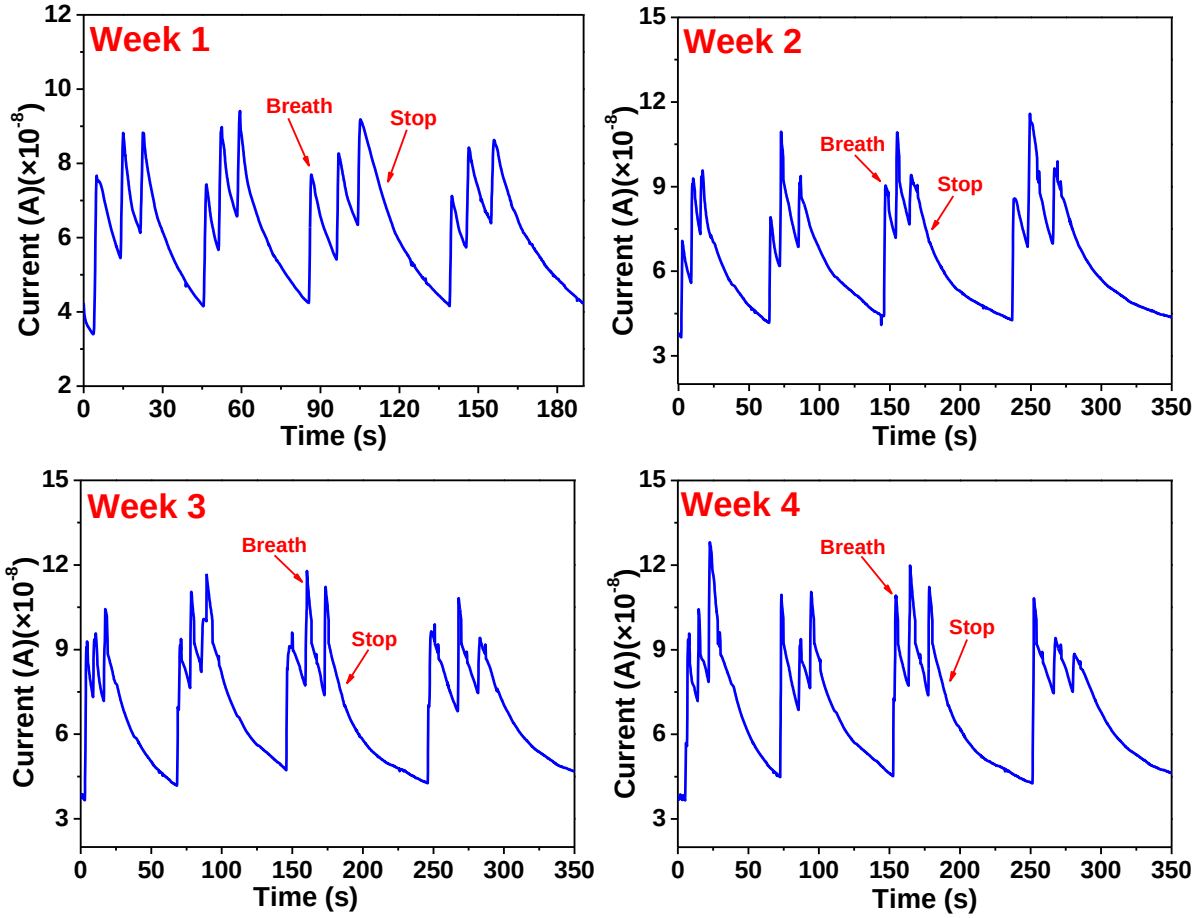

Figure 3.8. Breath sensing experiments showing stability of HKUST-1-MoS_2 sensor over a period of 4 weeks.

Further to verify the long-term durability, the fabricated device was tested over a period of 4 weeks under ambient conditions, wherein readings were taken once in a week **(Figure 3.8)**. It is noteworthy that the HKUST-1-MoS_2 hybrid device showed excellent stability with no decline in its performance even after a month. Similar breath pattern experiments were performed for pristine MoS_2, and temporal response graphs were recorded, **(Figure 3.9a)**. It was observed that the performance of the HKUST-1-MoS_2 hybrid device is superior to that of the pristine MoS_2 due to better water adsorbing properties of the MOF material. Besides testing the long-term stability of the device, we also calculated its response time. The response time is an important parameter that defines the efficiency of the device in terms of the time that it takes to reach the maximum value (current in this case) upon expiration. Interestingly, the response time for the HKUST-1-MoS_2 device is only ~ 0.38 s, which shows that it is feasible for this device to work in sleep apnea diagnosis **(Figure 3.9b)**.

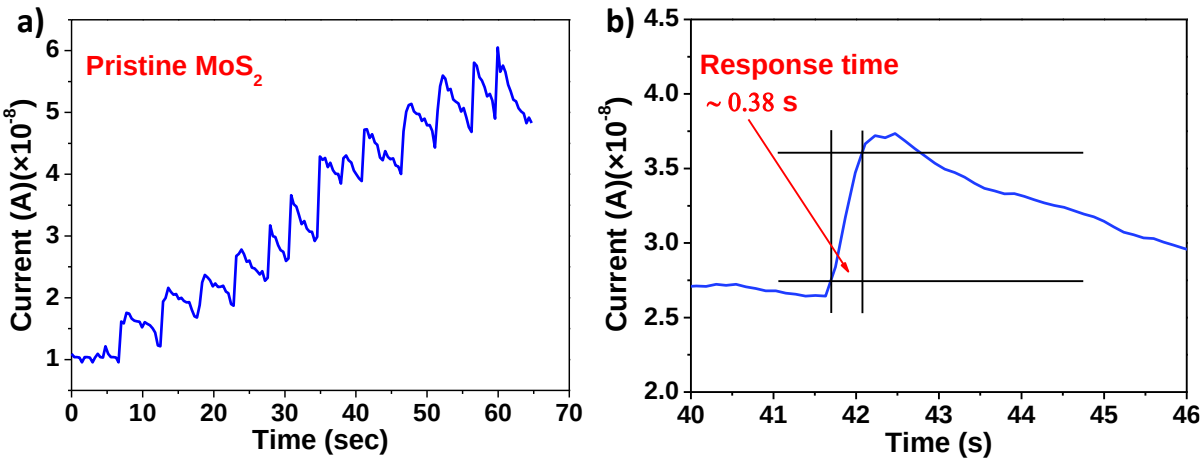

Figure 3.9. (a) Breath sensing experiments for pristine MoS_2, and (b) Response time of HKUST-1-MoS_2 breath sensor.

The response time of the HKUST-1-MoS_2 hybrid device has been compared with those of various benchmark materials reported in the literature that include metal oxides, polymers, zeolites, graphene oxides, etc. **(Table 3.1)**. To the best of our knowledge, there are no reports available on MOF based breath sensors and the current work is the first study in this direction that realizes the potential of MOF materials for real time healthcare-based applications. Moreover, the response time of our device is better than those of many other materials that have been reported for breath sensing. Additionally, the use of a cellulose paper based flexible support in the present case provides a much more economical alternative when compared to other support materials such as ceramics or silicon.

Table 3.1. A comparison of the response time and support used for various breath sensor materials reported in the literature with the MOF sensor in the present study.

Sensor	Support	Material Type	Flexible	Response time (s)	Smartphone Integration	Ref.
Al_2O_3	SiO_2	Metal Oxide	No	0.3	No	**[47]**
Carbon nanocoil	Liquid crystal polymer	CNC	Yes	1.6	No	**[48]**
Polyimide	Silicon	Polymer	No	1	No	**[49]**

Polyelectrolyte (PMDS)	Ceramic plate	Polymer	No	0.29	No	**[50]**
Polyester tape	Paper	Polyester	Yes	49	No	**[51]**
PEDOT:PSS Nanowires	PET	Nanowires	Yes	0.63	Yes	**[52]**
Zeolite Clinoptilolite	---	Zeolite	No	---	No	**[53]**
WS_2 film	PDMS	2D Semiconductor	Yes	5	No	**[54]**
MoS_2/Ag films	SiO_2/Si	MoS_2 Composite	No	1.5	No	**[55]**
HKUST-1/MoS_2	**Cellulose Paper**	**MOF**	**Yes**	**0.38**	**Yes**	**This work**

In order to gain deeper insights into the humidity sensing performance of the HKUST-1-MoS_2 hybrid device, we looked into the possible mechanism of water and charge transport through the MOF and MoS_2 layers. Due to its large pore diameter, pore volume and open metal sites, HKUST-1 adsorbs a large amount of water molecules in a short span of time. As per the literature reports, the water loading can go up to 32 mmol g^{-1} for HKUST-1.[56] On the other hand, MoS_2 is an excellent charge carrier which can enable rapid electron transport, thus ensuring a smooth response in current change with a change in humidity. The physical sensing mechanism can be attributed to the resistance modulation of MoS_2 due to the adsorption of water molecules exhaled from breath. Hence, when the MOF/MoS_2 device is exposed to breath, the relative humidity increases in the vicinity of the device and the excellent water adsorbing capability of HKUST-1 leads to maximum amount of water molecules being captured and transported to MoS_2. Moreover, the metal clusters in HKUST-1 have coordinated water molecules that are known to have sufficient acidic character, and therefore these water molecules lose protons much faster as compared to the uncoordinated water molecules.[57] These acidic water molecules contribute protons to the water and ethanol molecules present in the pores which leads to an enhancement of conductivity **(Figure 3.10)**. Also, water molecules are electron donating species, and they donate electrons to n-type MoS_2 which increases the

majority of carrier concentration of MoS_2, thereby increasing the current value. Further, as the water molecule gets adsorbed on MoS_2, the energy band bends downwards which creates an easy path for the electrons to flow towards the metal.

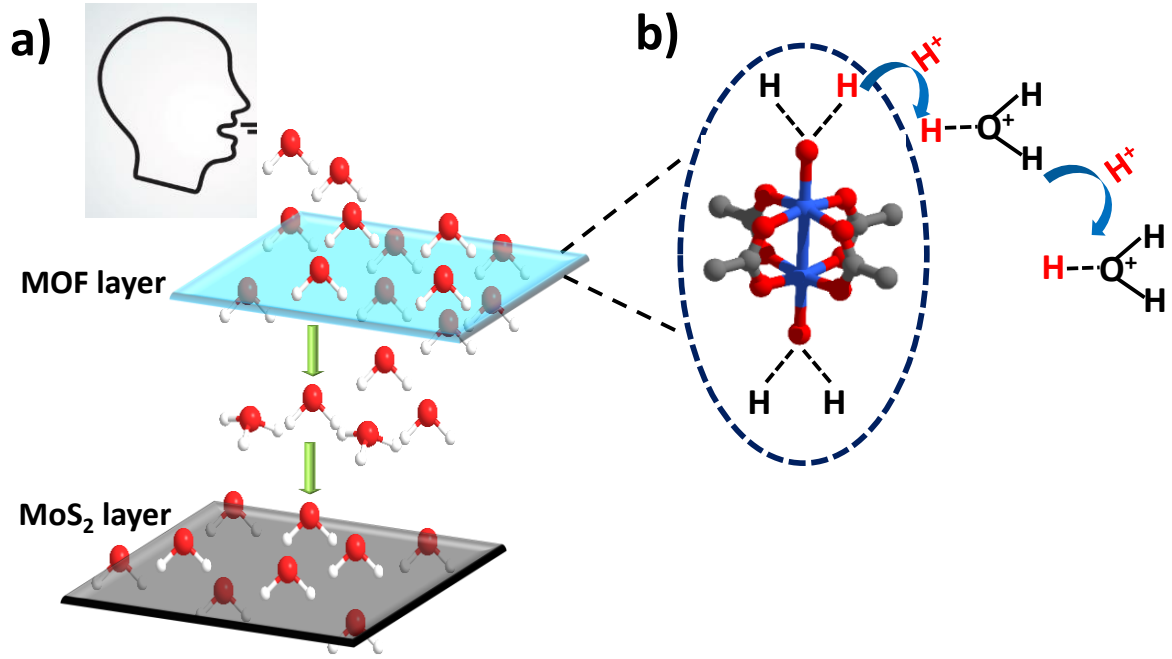

Figure 3.10. Breath sensing mechanism in HKUST-1-MoS_2 integrated device. (a) adsorption and transfer of water molecules from MOF to MoS_2 layer and (b) mechanism of proton conduction in the MOF layer involving proton transfer from acidic water molecules coordinated to the metal cluster to the solvent molecules present in the channels. Only one cluster has been shown for clarity.

Upon inhalation, a reverse process occurs. As soon as the inhalation process starts, the water molecules that were adsorbed on the surface of MoS_2 now start to remove/desorb from the surface which creates an upward band bending, thereby allowing the fabricated device to start coming to its initial resistance. However, since HKUST-1 has a slow desorption rate, the device does not get enough time to reach its baseline (i.e. when all the water molecules are desorbed/ removed) resistance/current value and the current value once again increases with the next breath. Hence, the combination of HKUST-1 and MoS_2 provides a remarkable system that works in tandem for the smooth functioning of the device. Furthermore, to demonstrate the real time application of the fabricated respiration sensor, a proof-of-concept prototype was developed, wherein the sensor was integrated onto a mask and the data were collected via a smartphone **(Figure 3.11)**. For doing so, the fabricated device was integrated into an Arduino microcontroller which measures the data and then transfers it to the smartphone using

Bluetooth wireless communication. The data received by the smartphone were analyzed for the risk of a patient towards sleep apnea through a dedicated user-friendly Android application. The analysis was performed by observing the breath pattern and also by counting the number of breaths. Importantly, the device triggers an alarm whenever there is a risk of patient breath slowing down. **Figure 3.11** shows the real time fabricated device and its integration on the mask which is connected to Arduino and the smartphone. For sleep apnea diagnosis, it is important to continuously monitor the breath and not the amplitude of the breath. With variation in the distance, the amplitude of the signal may vary which does not affect the intended application.

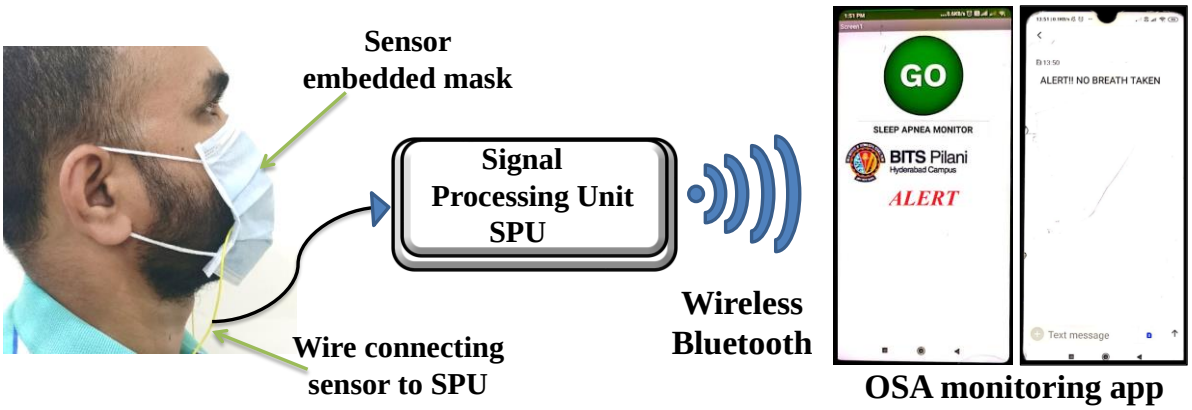

Figure 3.11. Schematic illustration of the face mask with the embedded HKUST-1-MoS_2 device showing real time operation using a smartphone device.

A prototype face mask is prepared as shown in **Figure 3.11** to ascertain the appropriate working of the device under real time conditions. A simple resistive circuit was employed to measure the resistance of the sensor. For the transfer of sensor data, the Bluetooth Module (HC-05) was employed which utilized the serial port communication. To verify the reliability of the fabricated sensor and the effective communication between the controller and the smartphone, three different instances were tested: (1) normal breathing (no alert), (2) breathing stopped but again continued (abnormal- no alert), and (3) breathing stopped (abnormal- alert) **(Figure 3.11** and **Figure 3.12)**. **Figure 3.11** shows the snapshots of the Android applications for the transmission of the alert message to the doctor/ nurse/ guardian when the patient missed a breath. The typical breath rate of a healthy adult is in the range of 10 - 20 times per minute. If the breath pattern is not in this specified range, it is considered as an abnormal breathing pattern.[58,59] If the patient does not breathe for 20 seconds, then the alarm for breathing stopped would be triggered. This would alert the doctor about the abnormal respiratory condition of the patient and thus help the doctor in saving the patient's life.

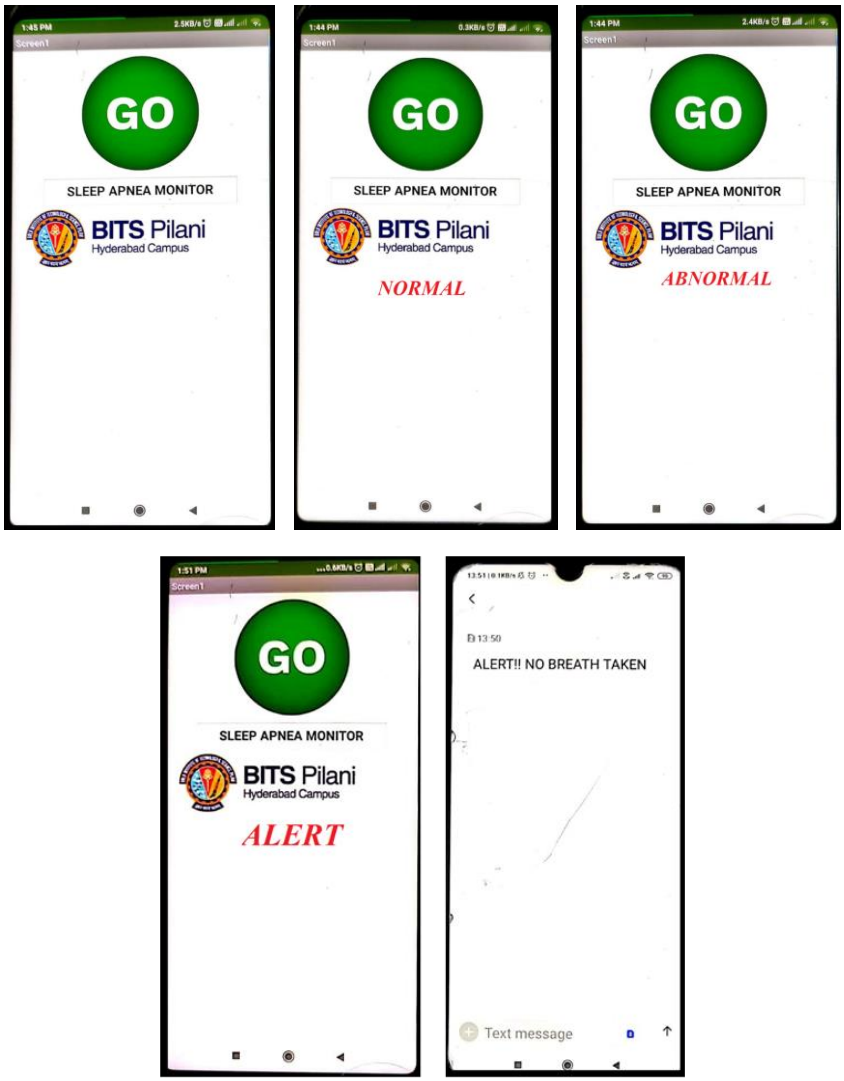

Figure 3.12. Different types of signals shown by the android app; normal and abnormal (top) and alert (bottom).

3.4. Conclusions

The work here shows an important application of MOF materials in the healthcare sector. MOFs have not been studied previously for breath sensing and sleep apnea related health problems and we believe more attention is warranted in this direction. A HKUST1-MoS_2 hybrid sensor has been prepared on a flexible and economical support that makes it a sustainable and user-friendly breath sensor which is stable and responsive to various breath types. The current work will open up a new area for MOF applications and more MOF materials on various flexible supports will be studied in future to design and test breath sensors under different humidity conditions.

CHAPTER 4

A Low-cost, Swift Response, Highly Sensitive MOF-based Dual Sensing Device Enables Detection of Ultralow Humidity Levels and Solvent Polarity Changes

In the previous chapter, the potential of MOFs in detecting the moisture content in the breath was studied with the help of a MOF-based breath sensor under ambient humidity levels. In the current chapter, a MOF-based sensing device has been designed for monitoring trace moisture levels. Developing a highly sensitive and rapid ultra-low humidity sensor is challenging due to the low water adsorption capacity, lack of hydrophilic interaction sites, and limited stabilities of most materials. Metal-Organic Frameworks (MOFs), a burgeoning class of porous materials, known for their high porosity and stability, could be potential candidates for designing humidity sensing devices. In the present chapter, fabrication of a MOF-based capacitive dual sensor that can detect ultralow humidity levels and distinguish between polar and non-polar solvents has been detailed. The solvent vapor adsorption experiments have been carried out to correlate the adsorption trends with the sensor's capability to detect different solvents such as water, methanol, ethanol, acetone, hexane, etc. [Eu(BTC)]-MOF exhibits higher water adsorption capacity over other polar and non-polar solvents. The detection limit of the sensor is as low as 0.84 ppm and it displays a very low hysteresis of ~ 0.03 % [$\Delta C/C_0$ (%)]. The device also shows an exceptional atmospheric stability over a period of one month with no decline in its performance. Additionally, the [Eu(BTC)] MOF-based device has been investigated as a real-time humidity sensor for glove box related applications and a suitable mechanism has been proposed for the exceptional sensing behavior of the MOF device.

4.1. Introduction

Humidity monitoring is critical for maintaining desirable atmospheric conditions for the physiological survival and daily life activities. Notably, the real-time monitoring of humidity changes is of utmost importance in the fields of agriculture (grain storage), medical, biotechnology, meteorology, and the manufacture of electrical goods.[1-3] There has been a growing need for ultralow humidity sensors for maintaining highly inert conditions with no or exceptionally low moisture content for some prime applications like glove boxes in the range of 0 - 10 ppm. Similarly, for circuit fabrication and the functioning of transformer oil and

plutonium trays, the moisture content should be in the range of 10 - 30 ppm.[4-8] Nevertheless, it is highly challenging to design humidity sensors operating at such low concentrations due to their poor sensitivity, high noise, and challenging signal digitization. Limited hydrophilicity of the material is another important reason which restricts their operation at low humidity conditions. It is thus important to design low cost, stable, selective, and reliable humidity sensors that can rapidly and precisely detect small humidity changes in the ppm or even ppb ranges.

The fabrication of ultralow humidity sensors necessitates careful selection of the sensing material that demonstrates excellent water stability and can adsorb a good amount of water molecules at low relative humidity levels (RH < 10 %). This can be achieved by synthesizing materials that possess open metal sites or hydrophilic functional groups like OH and NH_2, etc. Due to their unique structural characteristics and highly porous nature, metal-organic frameworks (MOFs), a unique class of hybrid porous materials, have piqued the interest of numerous researchers in various sectors such as catalysis, sensing, gas storage and separation.[9-13] MOFs are frequently used in the field of humidity sensing because of their good water adsorption properties, uniform pore size, high stability, and versatile design possibilities compared to conventional amorphous materials, metal oxides, and polymers.[14-18] MOFs such as HKUST-1, NH_2-MIL-125(Ti), and MIL-96(Al) have been previously explored for humidity sensing due to their good water ad-sorption capacity and hydrophilicity.[19-22] However, there are handful of reports on MOF-based capacitive-type humidity sensors that can operate under ultra-low relative humidity ranges of below 10 %.[23,24]

Despite their excellent water adsorption capacities, MOF materials have been seldom used for fabrication of real-time humidity sensing devices. This is owing to their inherent low electrical conductivity. The electrical humidity sensors work on the principle of detecting changes in electrical signals produced by the transduction mechanism. The change in the output electrical signal brought by the adsorption of water molecules by the humidity sensitive material of sensors can be expressed in numerous ways based on the choice of sensor type. Depending on different sensing platforms, humidity sensors can be capacitive, resistive, impedance, optical, electrical conductivity, and thermal-based.[25]

Out of these, capacitance-based sensors are more attractive than the other listed sensors because they are highly sensitive, operate at low cost, have fast response time, consume less power, and can be operated at room temperature.[26-28] Moisture-induced changes in the dielectric properties of humidity-adsorbing materials are the basis for the operation of capacitive humidity sensors. The fabrication process of capacitance-based sensors is simple and can be

well integrated with the sensing material even by simple drop-casting methods. In the present work, we have developed a lanthanide-based MOF sensor, an [Eu(BTC)]-MOF coated-IDE sensor to detect ultra-low humidity levels using a capacitive sensing technique.

Additionally, the behavior of the [Eu(BTC)]-MOF sensor has been investigated as a polarity sensor for detecting different solvent polarities. Solvent polarity and the local environment significantly impact the rates, kinetics, and product outcomes during chemical reactions. Solvent polarity also has profound effects on the spectral properties, such as absorbance, fluorescence, and optical properties of a molecule. Therefore, determining the polarity of a solvent is crucial.[29] Generally, solvatochromic dyes such as pyridinium N-phenolate betaine dyes are used to determine the solvent polarity.[30] However, the synthesis of these dyes is laborious, time-consuming, and costly. Thus, there is a need to design materials with facile synthesis conditions and analyze their behavior with respect to the changes in the polarity of the solvent using a simple and rapid technique. The present chapter examines the vapor sorption properties of [Eu(BTC)]-MOF towards water and different categories of solvents. The study focuses on the design and fabrication of MOF-coated IDE device, and explores the device capability to detect trace moisture levels and solvent polarity changes.

4.2. Experimental Section

4.2.1. Materials

Europium (III) nitrate pentahydrate [$Eu(NO_3)_3 \cdot 5H_2O$] was purchased from Chem Scene chemicals, and 1,3,5-benzene tricarboxylic acid was purchased from TCI chemicals. All the solvents were purchased from SRL chemicals and used as such without further purification.

4.2.2. Synthesis of [Eu(BTC)]-MOF

[Eu(BTC)]-MOF was synthesized by reacting [$Eu(NO_3)_3 \cdot 5H_2O$] metal salt (32 mg, 0.074 mmol) with 1,3,5-benzene tricarboxylic acid linker (15.6 mg, 0.074 mmol) in a scintillation vial containing the solvent mixture of DMF (3 ml), ethanol (3 ml) and water (2 ml). The vial was tightly sealed and placed in the oven at 80 ℃ after dissolving the contents completely. The vial was removed after 24 h and colorless crystals were obtained. The crystals were thoroughly washed with DMF and ethanol before proceeding to characterizations.

4.2.3. Designing Inter-digitated electrodes (IDE)

AutoCAD® was used to design the IDEs, which were then milled on a copper clad FR4 sheet using a MITS PCB milling machine. Various finger dimensions and widths were tried with

different milling settings, with the optimized dimensions being as follows: finger width = 0.4 mm, spacing between fingers = 0.5 mm, and number of IDE fingers = 12.

4.2.4. Fabrication of MOF-coated IDE device

The fabricated IDEs were cleaned with isopropyl alcohol (IPA). Further to prepare a MOF-coated IDE sensor, MOF crystals were gently powdered using a mortar and pestle. MOF suspensions were prepared in methanol and drop casted onto the IDE. MOF-coated IDE was dried in the oven before proceeding to the characterization and sensing measurements.

4.2.5. Details of the custom-built volatile organic compound (VOC) sensing setup

The setup consists of two mass flow controllers (MFCs), one with a maximum flow rate of 500 sccm (standard cubic centimeters per minute) and the other with a maximum flow rate of 20 sccm connected with the carrier gas which is synthetic air in this case. The carrier gas passes through the solvent bubbler, generates vapors, and carries the vapors to the sample chamber. The electrodes of a thermostat were dipped in the solvent bubbler to record the temperature of the liquid bubbled into the sensing chamber. The humidity sensing measurements were carried out at 23 ℃. The sensor in the chamber was connected to the LCR meter for recording capacitive measurements. The sensor's baseline capacitance value was recorded after dehumidifying the chamber by purging carrier gas. Different concentrations of solvent vapors were sent to the sample chamber by altering the flow rates in both the MFCs and the capacitance change was recorded with the help of an LCR meter. The carrier gas was purged through the chamber after each experiment to return the capacitance value to its baseline. In this way, the capacitance values were recorded for different ppm concentrations of each solvent and were represented as $\Delta C/C_0$ (%) where ΔC is the change in the capacitance of the sensor at the desired concentration (C_v) with respect to the baseline capacitance (C_0).

4.3. Results and Discussions

4.3.1. Structural details and characterization of the MOF

[Eu(BTC)]-MOF was prepared according to the reported procedure.[31] Briefly, the metal salt [$Eu(NO_3)_3 \cdot 5H_2O$] and the acid linker [1,3,5-benzene tricarboxylic acid] were taken in a 1:1 ratio and dissolved in a solvent mixture containing DMF:EtOH:H_2O (in 1:1:1 ratio) and heated in the hot air oven at 80 ℃ for 24 h. The crystals thus obtained were washed with DMF and used for further analysis. Structural details and the coordination environment of the as-synthesized MOF were analyzed using the structure file from the literature.[31] [Eu(BTC)]-

MOF thus obtained crystallizes in the tetragonal *P4(3)22* space group. Each Eu metal atom is coordinated to one water molecule and six carboxylate groups of BTC linker. The removal of these coordinated water molecules can render open metal sites in the framework. **Figure 4.1a** shows the coordination environment of the MOF, with each BTC linker coordinating to six Eu metal clusters. The MOF structure displays tetragonal packing with square channels measuring 6.6×6.6 Å along the c axis **(Figure 4.1b)**. **Figure 4.1c, d** depicts the packing diagrams of the framework along b and a axis, respectively.

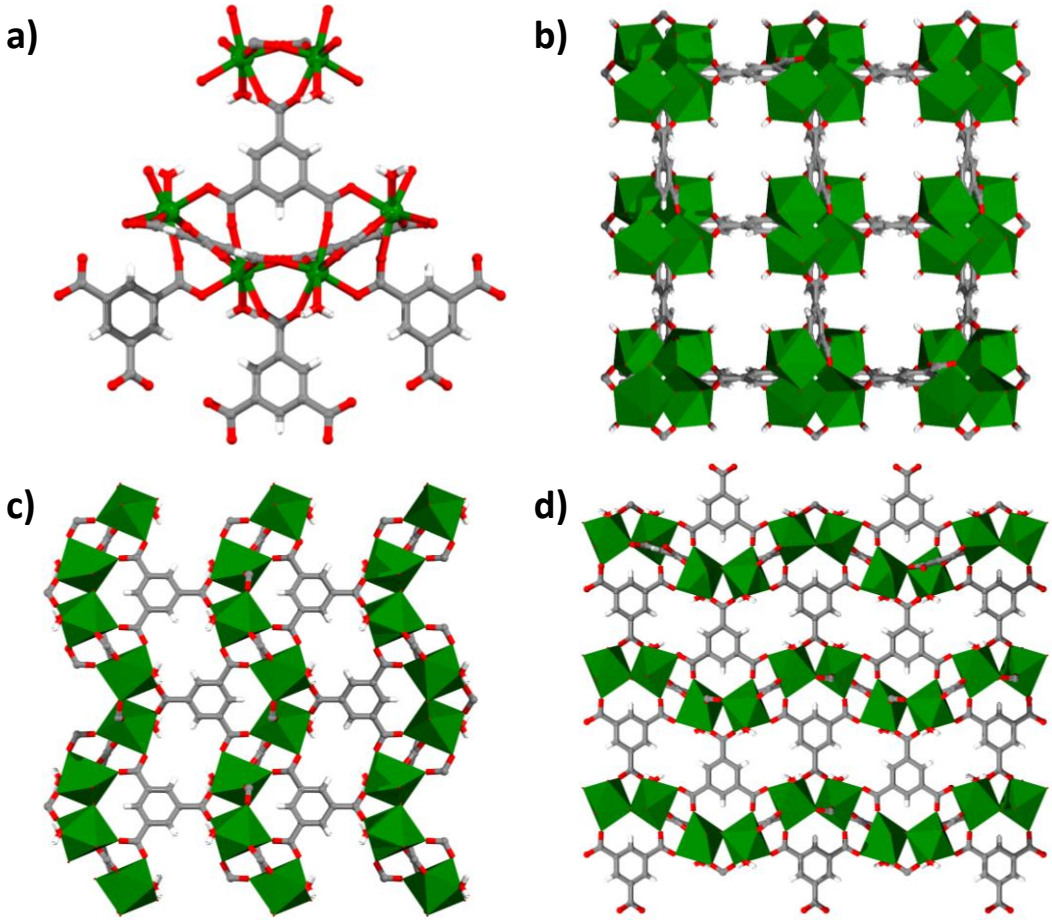

Figure 4.1. (a) Coordination environment of [Eu(BTC)]-MOF. Packing diagrams of [Eu(BTC)]-MOF (b) along the c axis, (c) along the b axis and (d) along a axis. C, H, O, and Eu atoms have been shown in gray, white, red, and green, respectively.

The as-synthesized MOF crystals were washed with DMF and ethanol. PXRD patterns of as-synthesized MOF crystals were recorded and compared with the simulated PXRD pattern collected from single crystal data. The as-synthesized PXRD patterns were in good agreement with the simulated PXRD patterns confirming the bulk purity of the MOF sample **(Figure 4.2a)**. The surface morphology and elemental composition of the MOF were studied using FE-SEM analysis. SEM images showed rod-shaped crystals of [Eu(BTC)]-MOF ranging from 20-

40 µm **(Figure 4.2b)**. The as-synthesized MOF crystals were washed with DMF and ethanol. The MOF crystals were solvent exchanged with ethanol and activated at 200 °C for 5 h under a dynamic vacuum before collecting the N_2 adsorption isotherm at 77 K. The framework exhibited high porosity with a BET surface area of 397 m^2/g, and an average pore volume of 0.164 cm^3/g **(Figure 4.2c).** The thermal stability of MOF crystals was studied with the help of thermogravimetric analysis (TGA) that showed weight loss of water molecules till 200 °C, followed by framework decomposition beyond 400 °C **(Figure 4.2d).**

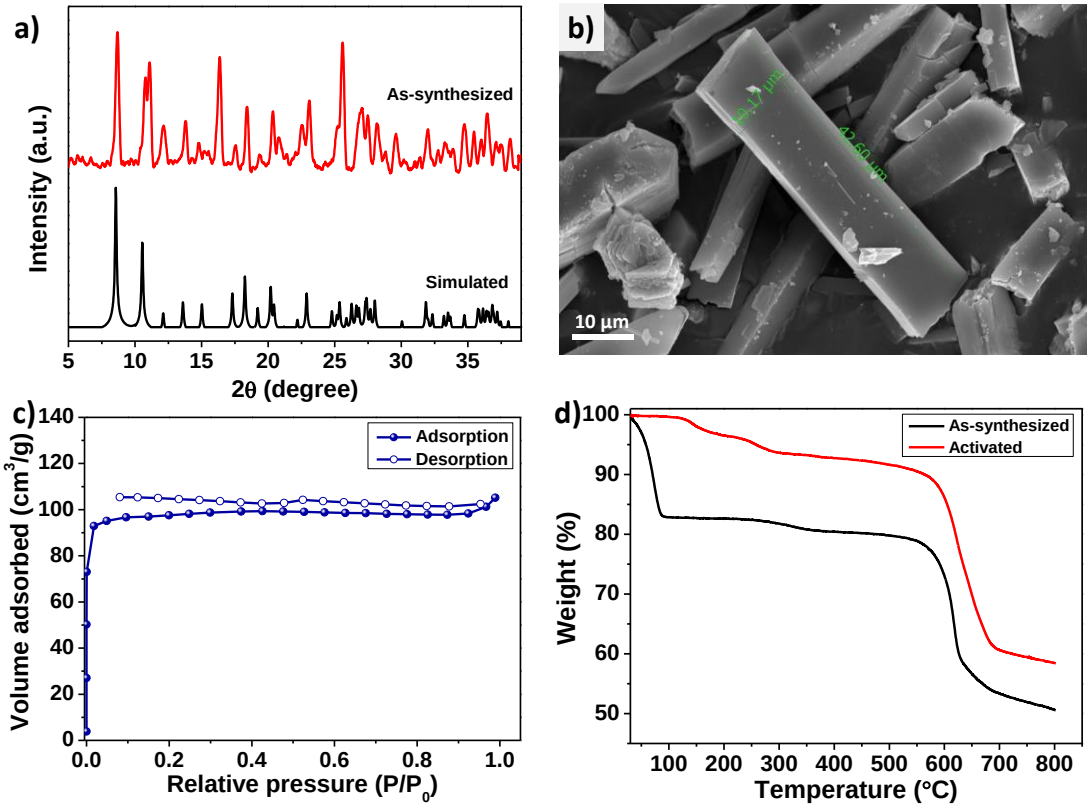

Figure 4.2. (a) Comparison of simulated and as-synthesized PXRD patterns of [Eu(BTC)]-MOF to confirm the bulk phase purity, (b) SEM images of [Eu(BTC)]-MOF. (c) N_2 adsorption isotherm of the MOF at 77 K, and (d) thermogravimetric analysis (TGA) of as-synthesized and activated crystals of [Eu(BTC)]-MOF.

Energy dispersive X-ray spectroscopy (EDS) and elemental mapping confirm the presence of Eu, C, and O elements in the framework **(Figure 4.3)**. **Figure 4.4a** shows the X-ray photoelectron spectroscopy (XPS) survey spectra of [Eu(BTC)]-MOF with corresponding binding energies of Eu, C, and O elements. The high resolution XPS binding energy peaks at 1136 eV correspond to Eu^{3+} $3d_{5/2}$ and at 1166 eV correspond to Eu^{3+} $3d_{3/2}$, thus confirming the existence of Eu in the +3 oxidation state **(Figure 4.4b)**. **Figure 4.4c, d** depicts the binding energies of C 1s and O 1s elements.

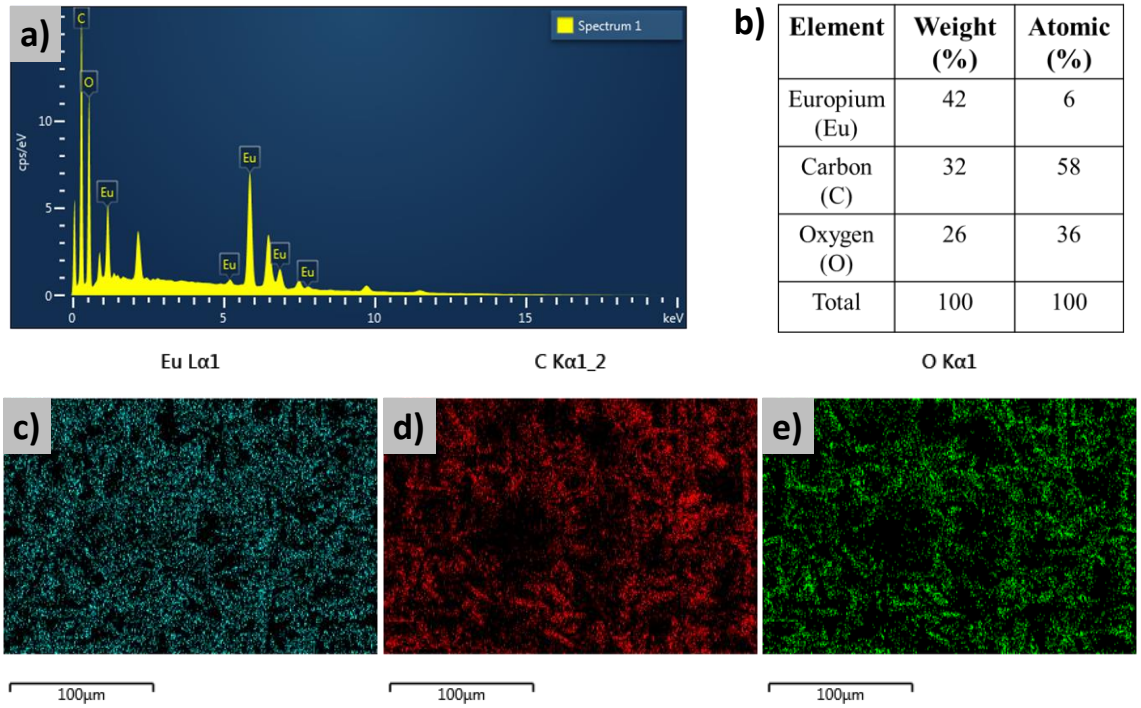

Figure 4.3. (a) Energy-dispersive X-ray spectroscopy (EDS) spectrum of the MOF, (b) EDS analysis of [Eu(BTC)]-MOF showing the atomic and weight % of the elements present in the MOF system, and (c) Elemental mapping of [Eu(BTC)]-MOF depicting the presence of (a) Eu, (b) C, and (c) O elements.

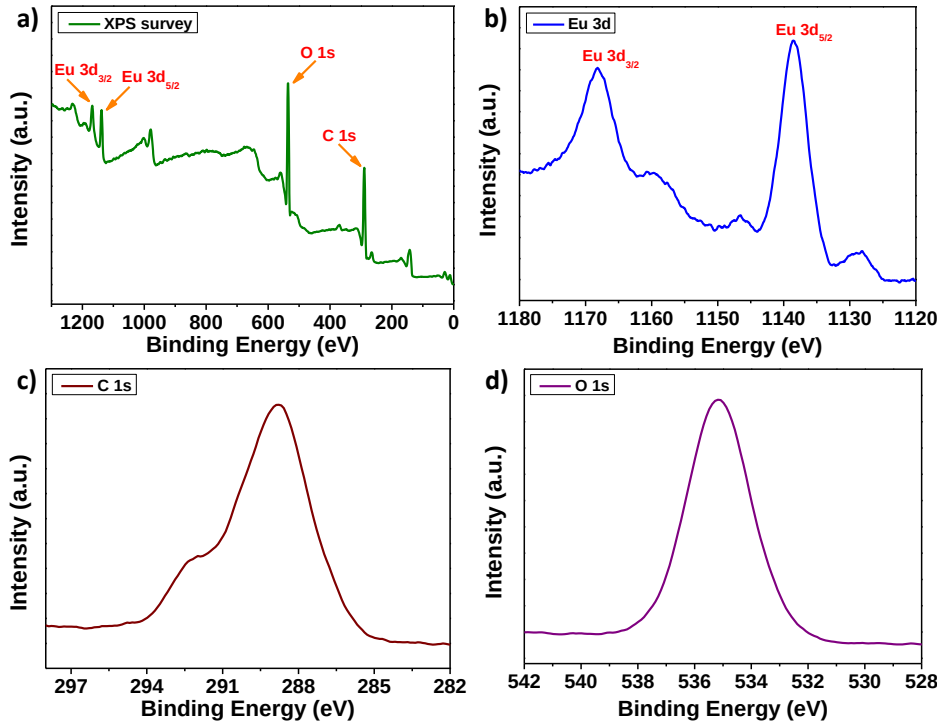

Figure 4.4. X-ray photoelectron spectroscopy (XPS) analysis of [Eu(BTC)]- MOF depicting (a) XPS survey spectra, (b) Eu 3d spectrum, (c) C 1s spectrum, and (d) O 1s spectrum.

4.3.2. Water adsorption properties

The [Eu(BTC)]-MOF contains coordinated water molecules that can render open metal sites upon their removal from the cluster sites. These open metal sites can serve as potent adsorption sites in humidity sensing or for capturing water molecules. The MOF crystals were thus activated at 200 ℃ for 5 h under a dynamic vacuum to ensure all the water molecules are removed from the framework. The structural integrity of the activated framework was examined with the help of PXRD patterns **(Figure 4.5a)**. Before proceeding further to explore the water adsorption characteristics of the MOF, the framework was checked for its water stability. PXRD patterns of the MOF sample were recorded after immersing the MOF crystals in water for 24 h. **Figure 4.5a** shows that the structural integrity and the crystallinity of the framework remain unaltered, suggesting strong water stability. The water sorption isotherm of [Eu(BTC)]-MOF was recorded at 25 ℃ to check the water adsorption capacity of the framework. The framework displayed steep water uptake in the low P/P_0 pressure ranges of 0 to 0.1, corresponding to low humidity ranges of 0 to 10 %, indicating high water affinity of the MOF. [Eu(BTC)] MOF exhibited an uptake of 130 cc/g at $P/P_0 = 0.1$ (10 % RH), which reached a maximum of 220 cc/g till $P/P_0 = 0.9$ **(Figure 4.5b)**. Interestingly, the framework displayed more than half of its total water uptake at very low pressure $P/P_0 = 0.1$. These results suggest that [Eu(BTC)]-MOF could be a potent material for humidity sensing, particularly at ultra-low humidity levels. Inspired by the high water affinity of the framework at very low humidity levels, we studied [Eu(BTC)]-MOF as an ultra-low humidity sensor using a capacitive transducer.

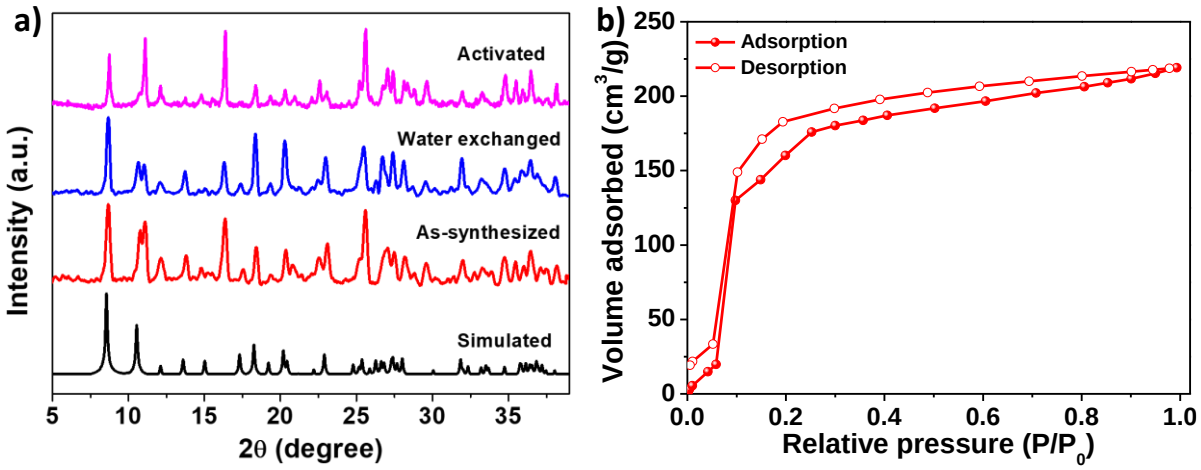

Figure 4.5. (a) PXRD analysis of as-synthesized with simulated patterns, water exchanged and activated crystals of [Eu(BTC)]-MOF. (b) Water sorption isotherm of [Eu(BTC)]-MOF.

4.3.3. Ultra-low humidity sensing studies

Figure 4.6a illustrates the schematic representation of the detailed fabrication process of preparing the MOF-coated IDE device. The structural integrity and crystallinity of the MOF on IDE was assessed through PXRD before advancing to the sensing experiments. The recorded PXRD patterns were in good agreement with the as-synthesized and simulated patterns of the MOF affirming the structural integrity. Following the successful deposition of MOF onto the IDE and verification of the framework's structural integrity, sensing experiments were conducted using a custom-built setup, as depicted in **Figure 4.6b.**

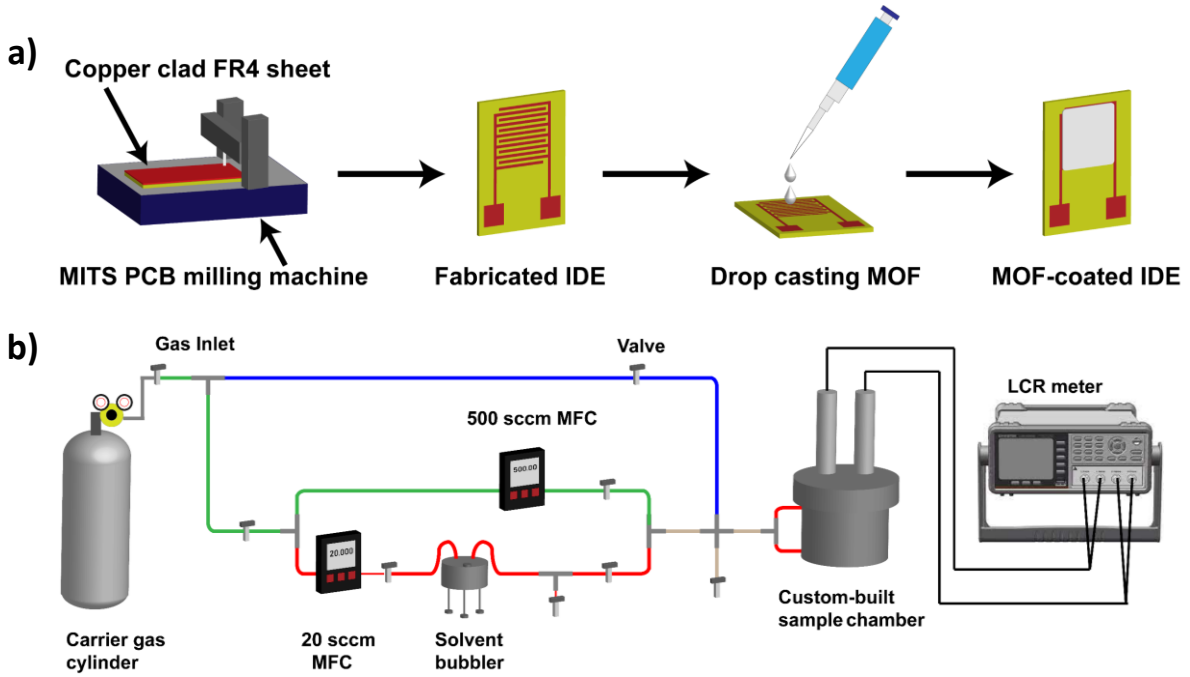

Figure 4.6. (a) Schematic illustration of device fabrication. (b) Custom-built setup for VOC sensing with LCR meter.

The MOF-coated IDE's sensing capabilities towards water were examined in different concentration ranges of 0 to 2000 ppm. **Figure 4.7a** shows the uncoated IDE and MOF-coated IDE sensor responses towards water in the low concentration ranges of 10 - 100 ppm. The sensor showed an exceptionally good capacitive response of 0.3 % even at a 10 ppm concentration of water and a capacitive response of 0.4 % at 20 ppm (0.1 % RH), corresponding to an increase in capacitance of 0.1 % for a 10 ppm increase in concentration. A similar almost linear increase trend was seen in the whole concentration range of 10 - 100 ppm with an increase in capacitive response from 0.3 % to 0.6 % **(Figure 4.7c)**. The sensor had a sensitivity of 0.0027 $\Delta C/C_0$ (%)/ppm and a LOD of 0.84 ppm. This clearly signifies the high sensitivity of the MOF sensor at extremely low humidity levels. The sensing behavior of the MOF towards

high concentration ranges of water was further studied. **Figure 4.7b** shows the increase in capacitance response of the sensor for the water content in the range of 100 - 2000 ppm (relative humidity levels of 0.4 % to 7.2 % RH). The sensor also exhibited a linear trend for high concentration ranges of 100 - 400 ppm with a sensitivity of 0.000947 $\Delta C/C_0$ (%)/ppm **(Figure 4.7d).**

Figure 4.7e depicts the capacitance response curves of the sensor towards increasing relative humidity levels. On raising the humidity levels from 0.4 % to 7.2 % RH, the sensor exhibits a change in capacitance of nearly two times larger in magnitude from 0.56 % to 1.1 %. Response and recovery time play an important role in assessing the efficiency of the sensor. The time required to reach 90 % of the total capacitive response is considered as response time. The sensor, on exposure to the water vapours, showed a good response time of ~ 270 s. The device could be revived back to its initial state by purging with air for 100 s **(Figure 4.7f)**. It is noteworthy that the sensor can display better response and recovery time but is limited by the flow rate (100 cm^3/min) used for purging in the study. Thus, humidification and dehumidification of the sample chamber of 1.5 L capacity requires a longer time.

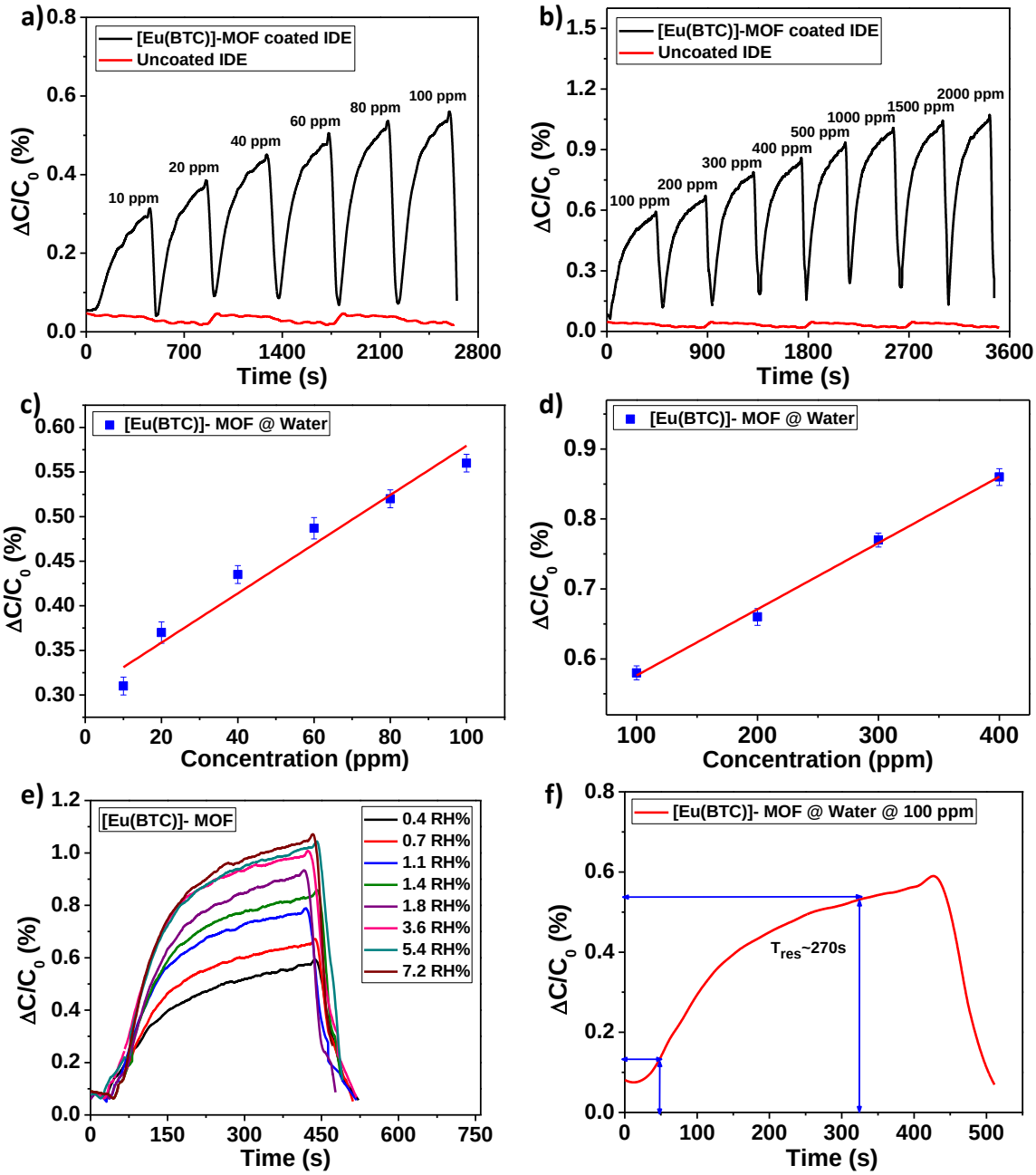

Figure 4.7. (a) MOF-coated IDE sensor response (a) towards ultra-low concentrations of water vapor at 23 ℃, (b) towards increased concentrations of water vapor measured at 23 ℃, (c) Linear response of the sensor towards the water in the concentration range of 10 - 100 ppm, (d) Linear response of the sensor towards the water in the concentration range of 100 - 400 ppm, (e) Response curves of the sensor towards increasing relative humidity levels (% RH) and (f) response time of the sensor towards water.

4.3.4. Sensing mechanism

The aforementioned findings show that the MOF system has a significant affinity for water even at such extremely low humidity conditions. This can be attributed to the highly porous

nature of the MOF system with large pore size and pore volume. Also, the water sorption profile of the framework displayed a steep water uptake at a very low pressure of P/P_0 = 0.1 (10 % RH), exhibiting a high water affinity of the system. The presence of open metal sites is another significant factor contributing to this high water affinity. These open metal sites function as sites for host-guest interaction which aids in capturing water molecules effectively, leading to good hydrophilic interactions with water even at ultra-low humidity levels. Moreover, the framework with a pore size of 8 Å can readily accommodate water molecules that have a kinetic diameter of 2.6 Å, exhibiting excellent water uptake. Therefore, there is a significant change in the capacitance of the MOF-coated IDE sensor even when exposed to low humidity levels. This shows that the MOF is water sensitive and the interactions of water molecules with the MOF system is predominant. On exposing the MOF-based sensor to increasing humidity levels, the water molecules are adsorbed onto the available active sites in the MOF system. The adsorbed water molecules get ionized and pro-duce a large number of hydronium ions (H_3O^+) as charge carriers due to the application of an external electric field.[32] As a result, the ionic conductivity increases and this charge transport mechanism can be explained by a Grotthuss chain reaction ($H_2O + H_3O^+ \rightarrow H_3O^+ + H_2O$) conductivity.[33] As the humidity levels increase, multilayer adsorption of water molecules occurs, leading to more proton transfer. This enhances the ionic conductivity and, as a result, capacitance value increases as the dielectric constants of the material gets significantly altered.

The majority of the sensors reported in the literature display slow response times **(Table 4.2)**. It is noteworthy that our sensor provides high sensitivity to ultra-low humidity conditions with quick response and recovery time and thus offering competitive edge over other sensors reported.

4.3.5. Reliability and stability studies of MOF-coated IDE sensor

Stability and reliability are two important parameters that an effective sensor should possess for the application of the sensor under real conditions. It is to be noted that designing MOF-based humidity sensors with these features is challenging because most MOFs exhibit poor water stability which results in framework disintegration. However, the MOF system employed for this study showed good water stability and water adsorption properties. Further, the stability of the sensor was examined for a period of 4 h (short-term stability) and for a period of 1 month (long-term stability). Further, to evaluate the short-term stability of the sensor, the first cycle was recorded by exposing the sensor to a relative humidity of 5.4 % RH (1500 ppm concentration of water) for 6 min, and the sensor exhibited a capacitive response of 0.95 %.

The sensor exhibited nearly the same capacitive response of 0.95 % for 40 cycles (or for a period of 4 h) with no deterioration in its response, as shown in **Figure 4.8a**.

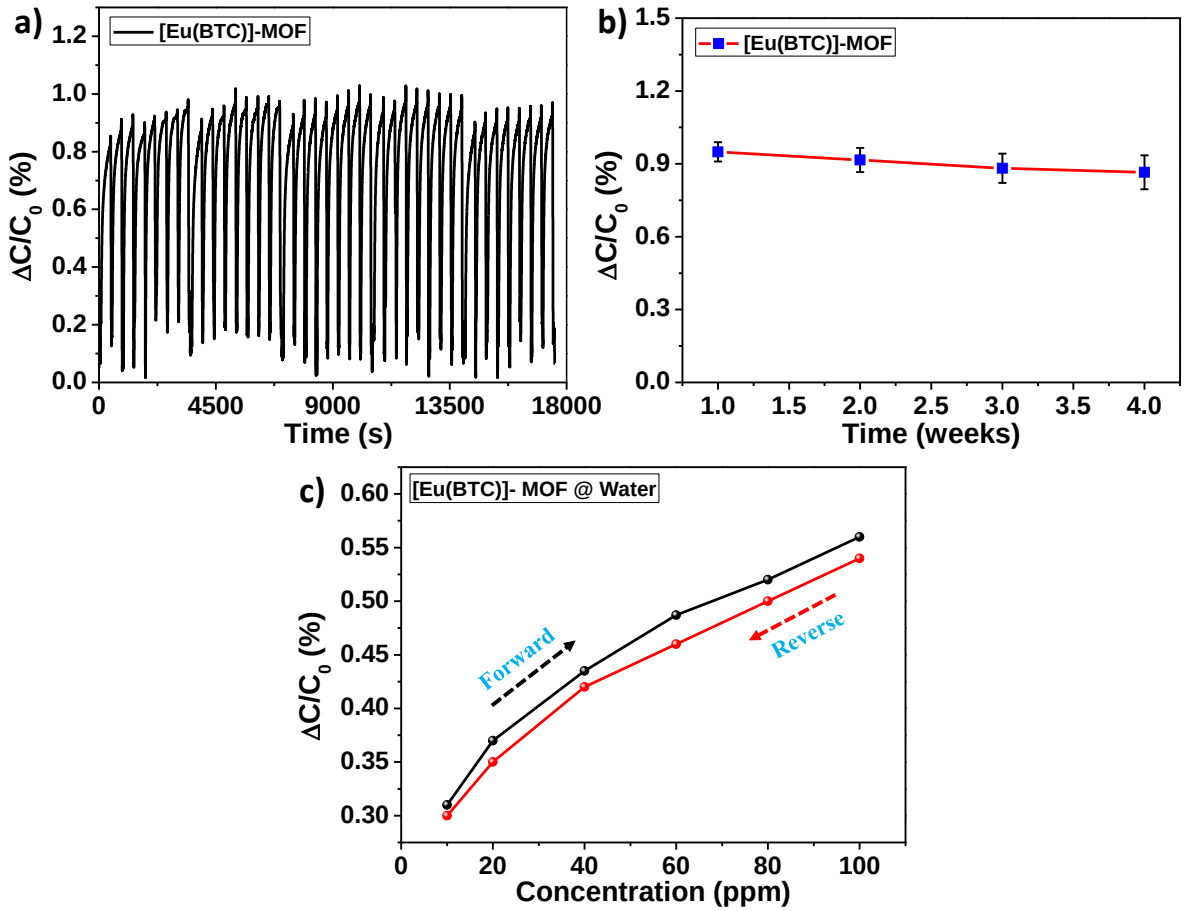

Figure 4.8. (a) Capacitive response of the sensor showing recyclability towards 1500 ppm concentration of water (b) Stability cycles of the sensor towards water over a period of 4 weeks (c) Humidity hysteresis curve of the sensor.

The aforementioned findings show that the sensor performs with exceptional sensitivity and accuracy. Long-term stability studies of the sensor were carried out for a period of 1 month. The capacitive response of the sensor on exposure to 1500 ppm concentration of water was checked once every week. The sensor showed excellent stability and displayed good performance over a period of 4 weeks with a very slight decline of capacitive response of ≤ 0.1 % **(Figure 4.8b)**. This clearly demonstrates the sensor's long-term capability in detecting and operating in ultra-low humidity conditions.

The hysteresis curve, which is defined by the highest difference during the sensor's adsorption and desorption cycle, is an important measure for evaluating the performance of humidity sensors. The hysteresis curve is examined by recording the adsorption and desorption cycle of the MOF-based sensor to ultra-low humidity levels. The adsorption cycle (forward scan) was

recorded by exposing the sensor to increasing concentrations of water (10 to 100 ppm), and the desorption cycle (reverse scan) was recorded by decreasing the concentration from 100 to 10 ppm. On comparing the adsorption and desorption cycles, the sensor showed very low hysteresis with a small capacitance shift of ~ 0.03 % **(Figure 4.8c)**, ascertaining a good reliability of the sensor.

4.3.6. [Eu(BTC)]- MOF as a polarity sensor

The MOF's remarkable water adsorption capacity inspired us to investigate its adsorption properties towards other solvents. We chose three categories of solvents to study the behavior of the MOF with respect to the polarity changes of the solvent. The first category consists of polar protic solvents such as ethanol and methanol. The second category consists of polar aprotic solvents such as acetonitrile and acetone. The third category consists of non-polar solvents such as toluene and hexane. **Table 4.1** shows the relative solvent polarity index of the three categories of solvents, along with their kinetic diameters.

Table 4.1. Relative solvent polarity index of the solvents analyzed for the study.

Solvent	Relative solvent index
Water	1
Methanol	0.76
Ethanol	0.65
Acetonitrile	0.46
Acetone	0.35
Toluene	0.099
Hexane	0.009

The sorption isotherms of the MOF towards different categories of solvents were collected **(Figure 4.9)**. The MOF system exhibited high uptake of 220 cc/g with water, which is highly polar, followed by methanol and ethanol, with uptake capacities of 85 and 80 cc/g, respectively. Acetonitrile and hexane were chosen for the sorption studies from the polar aprotic and non-polar categories. Acetonitrile displayed a moderate affinity with uptake capacities less than polar protic solvents. With poor adsorption capacity, hexane showed the least affinity towards the MOF system. It is interesting to note that the MOF uptake capacity of ethanol was more compared to hexane despite having a similar kinetic diameter of ~ 4.5 Å. This can be attributed

to the difference in their solvent polarities, with ethanol being polar and exhibiting a strong affinity towards the MOF system, whereas hexane is non-polar and has a low affinity.

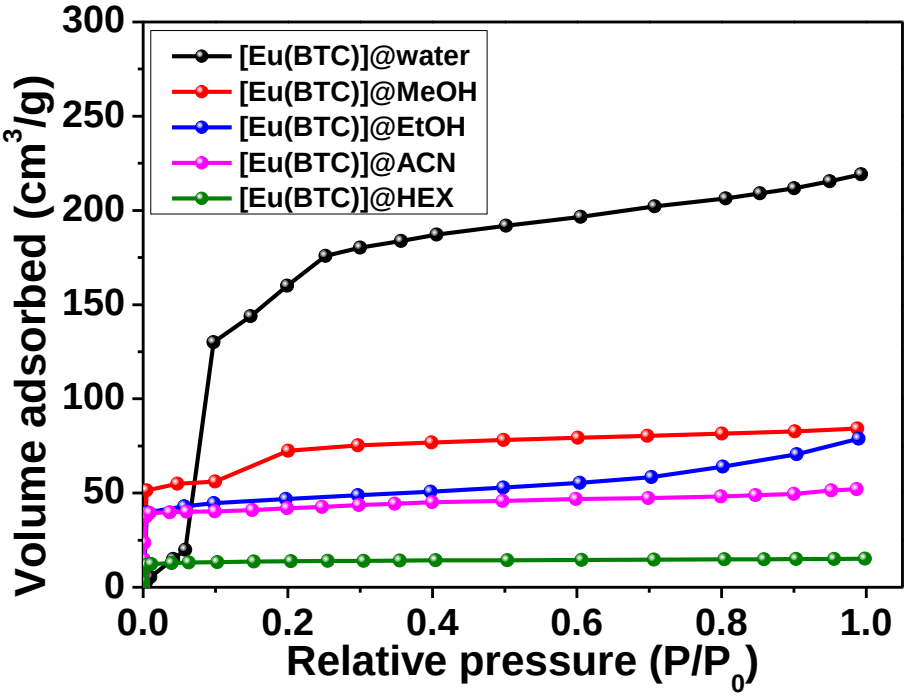

Figure 4.9. Vapor adsorption isotherm of [Eu(BTC)]-MOF towards solvents.

Inspired by the above observations, we went ahead to further investigate the sensing behavior of the MOF system towards the solvents with different polarities. The capacitive responses of the MOF system towards polar protic solvents (ethanol, methanol), polar aprotic solvents (acetonitrile, acetone), and non-polar solvents (toluene, hexane) in the concentration range of 100 to 2000 ppm were recorded and analyzed. The MOF-coated IDE, after each solvent run, was heated in the oven at 200 ℃ for 1 h to desorb the solvent adsorbed in the MOF system. The analysis showed that the capacitive response of the sensor increases linearly with an increase in solvent polarities. **Figure 4.10a** depicts that the sensor shows the best capacitive response towards water compared to other solvents due to the high polarity of water and high affinity towards water due to its good hydrophilic interactions with the framework. **Figure 4.10b** shows that the sensor shows an almost linear response between the concentration of the solvents and their relative polarity values. Thus, the current MOF-based sensor acts as a simple, quick, handy, and efficient polarity sensor with high sensitivity for a known concentration. **Table 4.2** presents a comprehensive analysis of MOF-based sensors in terms of their capabilities for detecting humidity and polarity. It is noteworthy to mention that our sensor functions as a dual sensor, exhibiting the capability to detect moisture while simultaneously serving as a solvent polarity sensor.

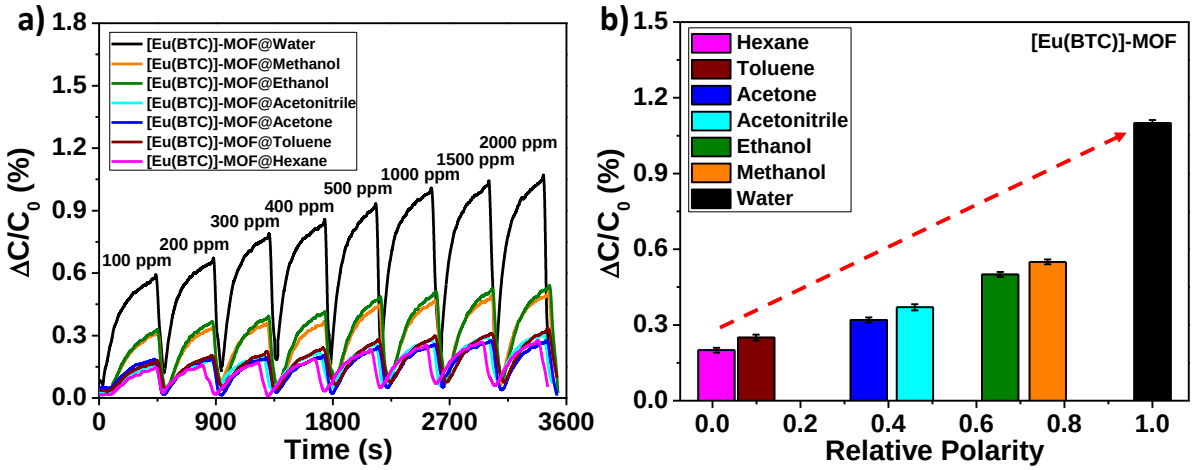

Figure 4.10. (a) Capacitance response of the sensor towards water and other solvents (Ethanol, methanol, acetonitrile, acetone, toluene, and hexane) and (b) Illustration of an increasing trend of the capacitive response of the sensor in agreement with the polarities of the solvents.

Table 4.2. A comparative analysis of MOF-based sensors for the detection of humidity and polarity.

MOF material	**Sensing technique**	**Range**	**Response time**	**Features**	**Humidity & Polarity Dual sensor**	**Ref.**
MIL-96 (Al)	Capacitance	3.7-90% RH	~20 min	Textile sensor with LB film	NO	**[19]**
MIL-96 (Al)	Capacitance	0-5000 ppm	10-15 min	Si IDE, also selective to MeOH	NO	**[20]**
Cu-BTC	Capacitance	20-100 ppm	~10 min	Parallel plate capacitor, electrochemical coating of MOF	NO	**[21]**
Cu-BDC	Capacitance	10-90% RH	Not evaluated	SAM modified, Si IDE	NO	**[34]**
[Eu(BTC)]-MOF	**Capacitance**	**10-2000 ppm**	**~ 270 s**	**MOF coated IDE sensor**	**YES**	**This work**

4.3.7. MOF-coated IDE as a real-time humidity device

The high sensitivity of the sensor towards ultra-low humidity levels and exceptionally low ppm levels of water encouraged us to develop a real-time humidity sensor to detect the moisture content in the glove boxes. The need to maintain inert conditions in the glove boxes demands for an efficient sensor to monitor and detect water content below 10 ppm. Further, an electronic prototype has been designed to demonstrate the working of a real-time humidity sensor. The electronic prototype consists of MOF-coated IDE device placed in a transparent box connected to a custom-built solvent jar filled with water. A TI FDC 1004 breakout board along with Arduino UNO microcontroller was further connected to the MOF-coated IDE device. Additionally, to visualize the sensor changes on exposure to humidity, a light-emitting diode (LED) was directly connected to the microcontroller as an output.

The electronic prototype functions by exposing the water vapors created by the solvent bubbler to the MOF-coated IDE device and the resulted capacitance changes was measured with the help of FDC. The role of FDC here is to supply and receive AC signals as capacitance measurement is not possible through the direct interfacing of the IDE with the Arduino UNO, as the microcontroller uses the direct current. Thus, FDC in connection with the IDE and the Arduino UNO functions as a sensor which triggers a red LED on reaching a set threshold capacitance. This threshold capacitance can be written as a code into the Arduino microcontroller, which further prints the capacitance values (in pF) on the serial monitor. **Figure 4.11** shows the schematic representation of the real-time humidity sensor layout and the sensor response to humidity. The performance of the sensor was initially checked with extremely low humidity levels of ($\leq$ 0.1 % RH, 10 - 20 ppm), we found that there was too much inherent variability in capacitance readings, and this couldn't be reduced due to the limitations of the real-time setup. The sensor was further checked on exposure to higher humidity levels of 7 % RH and the sensor displayed good capacitance changes in response to the humidity. The capacitance response thus recorded was above the set threshold capacitance written as code and consequently, the alarm is triggered in the form of LED ON as depicted in **Figure 4.11b**. **Figure 4.11a** depicts the sensor does not trigger an alarm when the set threshold capacitance is not reached and thus, LED is OFF. This work exemplifies the potential of a MOF material as a real-time ultralow humidity device.

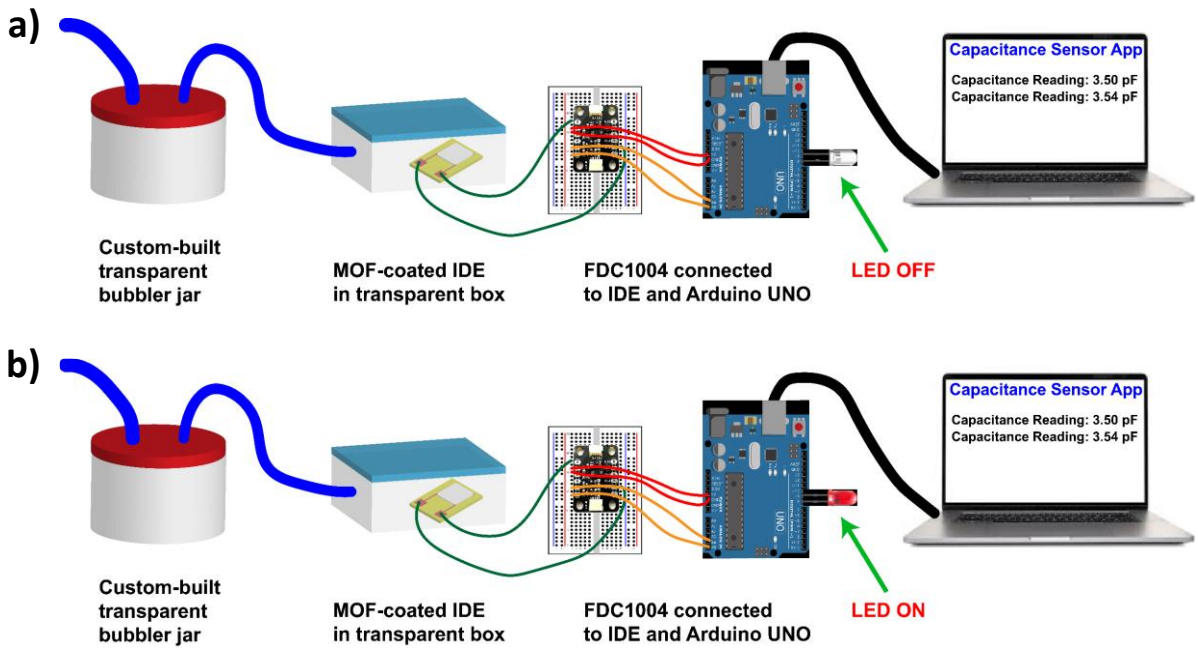

Figure 4.11. Illustration of operation of real-time humidity sensor in response to humidity depicted with (a) LED OFF (in the presence of negligible humidity levels) and (b) LED ON (in the presence of humidity).

4.4. Conclusions

In summary, we have developed a lanthanide MOF-based capacitive sensor and demonstrated it as an efficient and highly sensitive sensor for monitoring ultra-low humidity levels at ambient temperature. The sensor exhibits a very quick response time of ~270 s and can detect low humidity levels as low as 0.1 %. The sensor exhibits excellent atmospheric stability for a period of 1 month with no deterioration in its performance. The capacitive response of the sensor was also studied upon exposing it to solvents of different polarities. Interestingly, the sensor demonstrates the capability to distinguish between polar and non-polar solvents, effectively functioning as a polar sensor. We further developed a real-time humidity sensor for monitoring ultra-low humidity levels, that can offer practical utility in environments such as glove boxes. Ultra-low humidity sensing devices with long term stability are highly warranted for sustainable and green future. The current work successfully demonstrates the dual sensing potential of MOF-based sensors for monitoring ultra-low humidity levels with good precision and distinguish polar and non-polar solvents. We believe this work will encourage more reports on the usage of MOFs as electronic sensors. Such studies may also pave the way for the commercialization of MOF-based humidity sensors and polarity sensors in the near future.

CHAPTER 5

MOF Sensors for Food Safety: Ultralow Detection of Putrescine and Cadaverine in Protein-rich Foods

The humidity sensing abilities of the MOFs along with the device fabrication were critically studied in the previous chapters which resulted in MOF-based breath sensor, polarity sensor and ultra-low humidity sensor. In the current chapter, we have explored MOFs for the real-time detection of food spoilage indicators such as putrescine and cadaverine in protein rich foods such as fish and cheese. Biogenic amines (BAs) such as putrescine and cadaverine present in protein rich foods like cheese and fish are an important class of amine compounds required in small amounts for the normal functioning of cells. However, a large amount of these substances in foods lead to food spoilage and consumption of such foods can lead to cytotoxicity and other severe complications in the human body. It is highly desirable to design suitable materials that can detect such food spoilage indicators at low concentrations. Metal-organic frameworks (MOFs) due to their porous nature and well-defined 3D structures can serve as potential candidates for the sensing of biogenic amines. Herein, two new Co-based MOFs have been reported for the detection of putrescine and cadaverine in protein rich foods using the fluorescence technique. In addition to putrescine and cadaverine, various other biogenic amines such as spermine, spermidine, tyramine, and tryptamine have also been studied to check the wide sensing ability of these new materials. Both the MOFs show unprecedented ‘‘turn-off’’ fluorescence behavior with more than 90 % quenching efficiency in the presence of very low concentrations of putrescine and cadaverine. The phenomenon can be observed in both solution and solid states. Real-time sensing experiments with fish and cheese samples have been performed, which demonstrate the potential of these MOF materials in sensing biogenic amines. A plausible mechanism has also been proposed for the underlying detection mechanism.

5.1. Introduction

Biogenic amines (BAs) are naturally occurring amine compounds that are important for the normal cell growth and differentiation. The presence of BAs in low concentrations in tissues is essential for their physiological function but a high concentration of certain BAs in the human body can lead to cytotoxicity.[1] Putrescine (PUT) and cadaverine (CAD) are two such BAs, which, if present in high concentrations, can have serious toxicological effects in humans. PUT

and CAD are mainly obtained from protein rich foods such as fish, shrimps, meat and cheese.[2] Small amounts of these BAs are used by the body for normal cell functioning and the excess is excreted. It has been observed that excess amounts of PUT and CAD are often produced when processed meats and seafood get spoiled by the microorganisms that break amino acids into BAs with the help of decarboxylase enzyme.[3] PUT also acts as a precursor for the synthesis of other biogenic amines such as spermine and spermidine which means that an increase in the amount of putrescine release can also trigger the accumulation of other BAs in foods.[4,5] Putrescine and cadaverine are the main indicators for detecting food spoilage caused by microorganisms. In fact, the biogenic amine index (BAI) used for establishing the taste and freshness of meat products is calculated from the amounts of putrescine, cadaverine, spermine, spermidine and histamine present in foods. More importantly, putrescine can also react with nitrates to form nitrosamines which are known to be carcinogenic.[2] Consumption of such spoiled food stuffs can compromise the immunity of a healthy person and can lead to severe health complications which in turn paves the way for deadly diseases. Ensuring the safety of foods is a big challenge and it needs urgent attention. A big difficulty in the case of processed foods is that the contamination of such foods often goes unnoticed since foods once packed are rarely checked for the release of BA during prolonged storage and transportation. Additionally, the lack of suitable materials or techniques for the detection of BAs makes this task more difficult. Therefore, sensitive and selective detection of BA is vital for maintaining the food safety. Although various analytical techniques such as electrophoresis, colorimetric sensing, gas chromatography, high-performance liquid chromatography, etc., have been developed to date, these are time-consuming and require handling of sophisticated instruments.[6-9] Fluorescence based optical sensors still hold a lot of importance due to their cost effectiveness and high sensitivity. Therefore, a fluorescent sensor that can rapidly detect biogenic amines such as putrescine and cadaverine at low concentrations from food products is a viable choice. It is noteworthy that only a handful of fluorescent sensors have been reported to date for the sensing of biogenic amines.[10-17] Most of these sensors comprise purely organic materials.[10-14] Porous materials such as metal organic frameworks (MOFs) possessing a high surface area, permanent porosity, and good thermal and chemical stability with tunable properties are known for various applications.[18-22] Due to their unique properties and advantage of pre-selecting suitable building blocks, MOFs have been used for designing fluorescent sensors for detection of nitro explosives, volatile organic compounds, heavy metal ions, amines, drugs, etc.[23-27] Recently, our group also reported the first MOF based sensor for breath sensing and sleep apnea diagnosis.[28] In the present work, we designed two new Co-based MOFs, **BITSH-1** and

BITSH-2 (Birla Institute of Technology and Science, Hyderabad), for the sensing of putrescine and cadaverine, besides other biogenic amines like spermine, spermidine, tyramine, and tryptamine **(Figure 5.1)**. These mixed-linker MOFs have been prepared solvothermally by reacting cobalt nitrate and biphenyl dicarboxylic acid (BPDC) with 4,4 -bipyridine (BPY) and 1,2-bis(4-pyridyl)ethane (BPE), respectively.

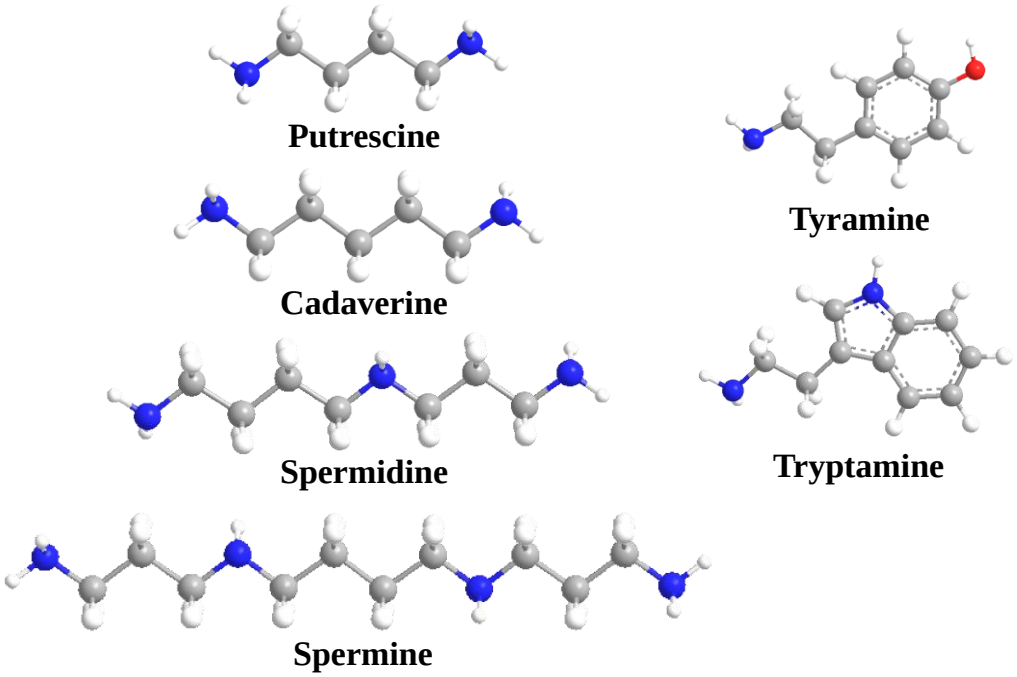

Figure 5.1. Chemical structures of the biogenic amines used in the present study.

5.2. Experimental Section

5.2.1. Materials

Cobalt nitrate hexahydrate [$Co(NO_3)_2 \cdot 6H_2O$], N,N′- dimethyl formamide were purchased from SRL, biphenyl-4,4'-dicarboxylic acid (bpdc), 1,2-bis(4-pyridyl)ethane (bpe) and 4,4'-bipyridine (bpy) were purchased from TCI chemicals. All the reagents, solvents and analytes putrescine (PUT), cadaverine (CAD), spermine (SPM), spermidine (SPD), tyramine (TYRM), tryptamine (TRYP) were obtained from commercial sources and used as such without additional purification.

5.2.2. Synthesis of BITSH-1 and BITSH-2

BITSH-1 MOF was synthesized by reacting $Co(NO_3)_2 \cdot 6H_2O$ (29.1 mg, 0.1 mmol), biphenyl-4,4'-dicarboxylic acid (bpdc) (24.2 mg, 0.1 mmol) and 4,4'-bipyridine (bpy) (7.8 mg, 0.05 mmol) in 10 ml of DMF and heating the reaction mixture at 130 ℃ for 24 h. The purple crystals thus obtained were washed thoroughly with DMF and ethanol before further study. **BITSH-2**

was synthesized in a similar manner by reacting $Co(NO_3)_2 \cdot 6H_2O$ (29.1 mg, 0.1 mmol), biphenyl-4,4'-dicarboxylic acid (bpdc) (24.2 mg, 0.1 mmol) and 1,2-bis(4- pyridyl)ethane (bpe) (9.2 mg, 0.05 mmol) in 10 ml of DMF and heating the reaction mixture at 130 ℃ for 24 h. The pink crystals thus obtained were washed thoroughly with DMF and ethanol before further study.

5.2.3. MOF + PVDF membrane strip synthesis

Polyvinylidene fluoride (PVDF) polymer (0.15 g) was dissolved in DMF (1 ml) and stirred for 15 min. Then 60 wt % of MOF samples, i.e. **BITSH-1** and **BITSH-2**, were separately added to the PVDF solution and stirred for 15 min to obtain uniform suspensions. The suspension was slowly drop-casted onto a glass substrate which was pre-heated at 120 ℃ for 20 min and left in the oven at 120 ℃ for 20 min. Flexible MOF + PVDF membrane strips for both **BITSH-1** and **BITSH-2** were obtained separately and used for the real-time sensing experiments.

5.2.4. Photoluminescence (PL) Measurements

MOF crystals were thoroughly washed with DMF and ethanol. The crystals were vacuum dried and were gently grinded with a mortar pestle. 1 mg of the grinded sample was well dispersed in 2 ml of ethanol via sonication for the measurements. The UV-vis absorbance and PL measurements were carried out for **BITSH-1** and **BITSH-2**. PL studies were carried out with 1 mM concentration of biogenic amines in ethanol medium for both the MOF systems.

5.2.5. Electrochemical measurements

Electrochemical nature of **BITSH-1** and **BITSH-2** were studied using cyclic voltammetry with three electrode cell setup. The reduction and oxidation potentials were obtained at room temperature using Fluorine-doped Tin Oxide (FTO) as the working electrode, platinum mesh as counter electrode and Ag/AgCl as reference electrode. The measurements were carried out using 0.1 M tetrabutylammonium perchlorate in acetonitrile as electrolyte solution. The HOMO and LUMO energy levels were calculated considering the onset oxidation potential and reduction potential values obtained from the Cyclic Voltammogram (CV) and using the following equation. E_{HOMO} = -e [$E_{ox\ onset}$ + 4.741] eV and E_{LUMO} = -e [$E_{red\ onset}$ + 4.741] eV.[29] The band gap of BITSH-1 and BITSH-2 was calculated using E_g = LUMO - HOMO.[29]

5.3. Results and Discussion

5.3.1. Structural details and characterization of the MOF

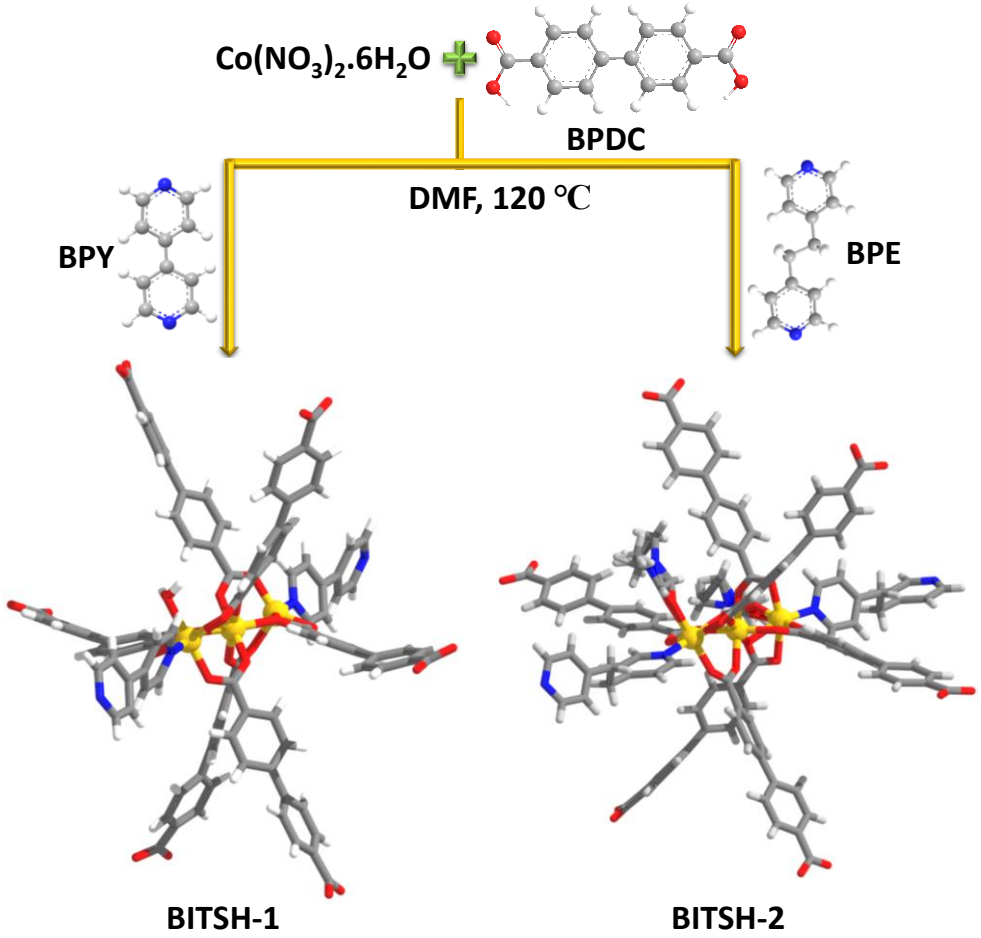

Figure 5.2. Synthesis procedure for **BITSH-1** and **BITSH-2** MOFs.

BITSH-1 and **BITSH-2** have been successfully synthesized using mixed-linker approach and **Figure 5.2** shows the schematic representation of the synthesis procedure. The as-synthesized frameworks are completely characterized for further experiments. The suitable crystals of BITSH-1 and BITSH-2 for single crystal X-ray diffraction (SCXRD) analysis were selected. The single crystal data was collected and reduced using CrysAlisPro (Rigaku Oxford Diffraction) software. The data collection was carried out at 100 K and the structures were solved using Olex2 with the ShelXT structure solution program and refined with the ShelXL refinement package using Least Squares minimization. The details of the crystal data for both compounds are given in **Table 5.1**. The solvent molecules in BITSH-1 could not be modelled with certainty and the structure was squeezed using Olex2 mask function. The structure of BITSH-1 was collected several times and the best possible data set was used for structure elucidation. BITSH-1 contains one molecules of water coordinated to the Co cluster whereas BITSH-2 contains DMF molecules coordinated to the cluster. No disorder was observed for the linker units.

Table 5.1. Crystallographic data for BITSH-1 and BITSH-2.

Identification code	**BITSH-1**	**BITSH-2**
Empirical formula	$C_{64}H_{62}Co_3N_6O_{17}$	$C_{60}H_{50}Co_3N_4O_{14}$
Formula weight	1363.99	1227.884
Temperature/K	100.0	100
Crystal system	monoclinic	orthorhombic
Space group	$P2_1/n$	*Pbcn*
a/Å	13.8779(3)	13.6216(3)
b/Å	18.0470(4)	26.3669(7)
c/Å	25.8568(5)	20.1175(4)
α/°	90	90
β/°	91.577(2)	90
γ/°	90	90
Volume/Å^3	6473.5(2)	7225.4(3)
Z	4	4
ρ_{calc}g/cm^3	1.400	1.129
μ/mm^{-1}	6.563	5.790
F(000)	2802.9	2505.8
Crystal size/mm^3	0.25 × 0.2 × 0.1	0.1 × 0.05 × 0.02
Radiation	Cu Kα (λ = 1.54184)	Cu Kα (λ = 1.54184)
2θ range for data collection/°	6.84 to 159.64	8.02 to 160.1
Index ranges	-17 ≤ h ≤ 8, -22 ≤ k ≤ 11, -32 ≤ l ≤ 31	-8 ≤ h ≤ 16, -32 ≤ k ≤ 33, -25 ≤ l ≤ 19
Reflections collected	39926	27877
Independent reflections	13648 [R_{int} = 0.0429, R_{sigma} = 0.0388]	7701 [R_{int} = 0.0507, R_{sigma} = 0.0494]
Data/restraints/parameters	13648/0/815	7701/8/397
Goodness-of-fit on F^2	1.042	1.001
Final R indexes [I>=2σ (I)]	R_1 = 0.0938, wR_2 = 0.2843	R_1 = 0.0617, wR_2 = 0.1756
Final R indexes [all data]	R_1 = 0.1023, wR_2 = 0.2916	R_1 = 0.0749, wR_2 = 0.1867

CCDC	2121260	2121259

The bulk phase purity of MOF crystals was confirmed by comparing their as-synthesized and simulated PXRD patterns. Thermogravimetric analysis (TGA) of **BITSH-1** and **BITSH-2** was carried out under a N_2 atmosphere. Both the frameworks show gradual loss of solvent molecules up to 150 ℃, followed by decomposition beyond 350 ℃ **(Figure 5.3)**. The N_2 adsorption experiments were performed at 77 K, and the as-synthesized crystals were activated at 90 ℃ under a dynamic vacuum before the adsorption experiments. N_2 adsorption measurements revealed BET surface areas of 330 m^2 g^{-1} and 734 m^2 g^{-1} for **BITSH-1** and **BITSH-2** with pore volumes of 0.13 cm^3 g^{-1} and 0.32 cm^3 g^{-1}, respectively. The pore diameters were approximately the same for both materials, around 8 Å **(Figure 5.4a-d)**. The FESEM technique was used to study the morphology and size of the as-synthesized crystals. Both the crystals are block-shaped with sizes ranging from 40 to 220 µm **(Figure 5.4e-h)**.

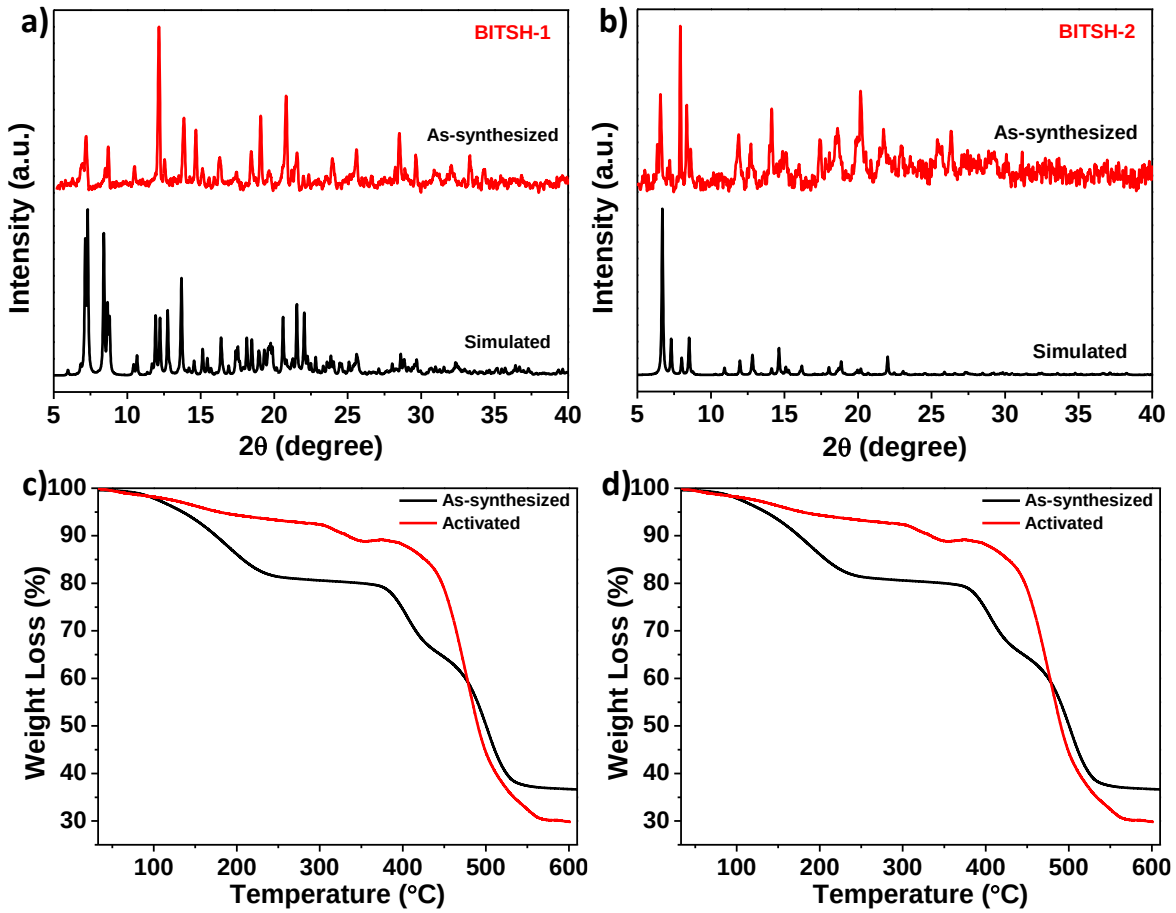

Figure 5.3. Comparison of the experimental and simulated PXRD patterns of (a) **BITSH-1** and (b) **BITSH-2**. TGA profile of as-synthesized and activated (c) **BITSH-1** and (d) **BITSH-2** crystals.

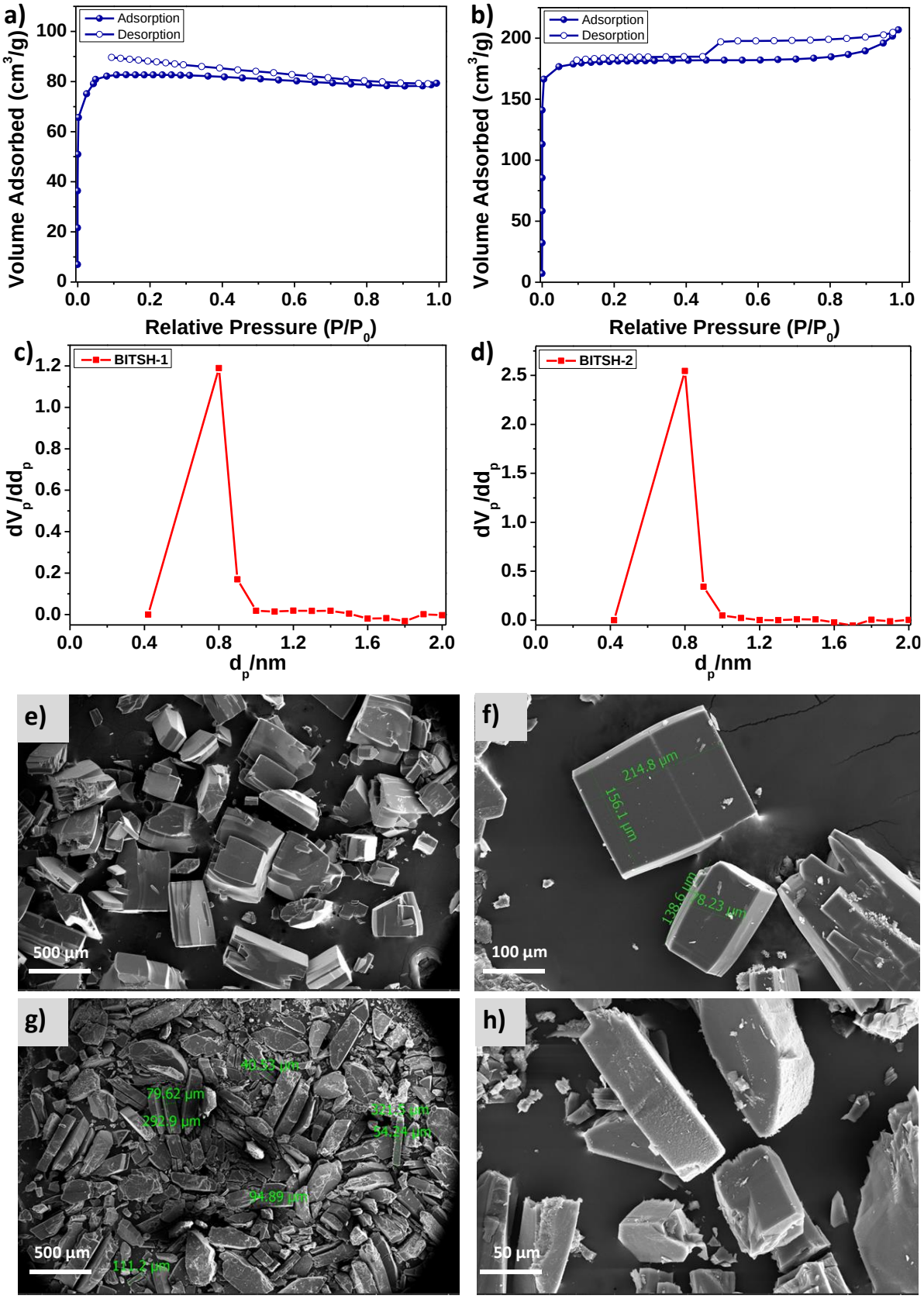

Figure 5.4. N_2 adsorption isotherm of a) **BITSH-1** and b) **BITSH-2** and pore diameter of c) **BITSH-1** and d) **BITSH-2** samples. SEM images of (e, f) **BITSH-1** and (g, h) **BITSH-2** crystals.

BITSH-1 crystallizes in the monoclinic *P21/n* space group, whereas **BITSH-2** crystallizes in the orthorhombic *Pbcn* space group **(Table 5.1)**. The asymmetric unit of **BITSH-1** contains three Co^{2+} ions, three BPDC linkers, one BPY linker and one water molecule coordinated to the metal cluster. The solvent molecules (DMF) present in the channels could not be located due to the diffused electron densities. In the case of **BITSH-2**, the asymmetric unit comprises two Co^{2+} ions, 1.5 BPDC ligands, one half of the BPE ligand, and one DMF molecule coordinated to the Co cluster. The coordinated DMF molecule is disordered over two positions with equal occupancies. Both the structures are very similar in the manner where the acid linkers form hexagonal layers **(Figure 5.4a, c)** and the pyridyl linkers act as pillars **(Figure 5.4b, d)**. Both the structures are 2-fold interpenetrated. The packing diagrams of **BITSH-1** and **BITSH-2** reveal the presence of 1D channels along the a, b and c axes **(Figure 5.5)**.

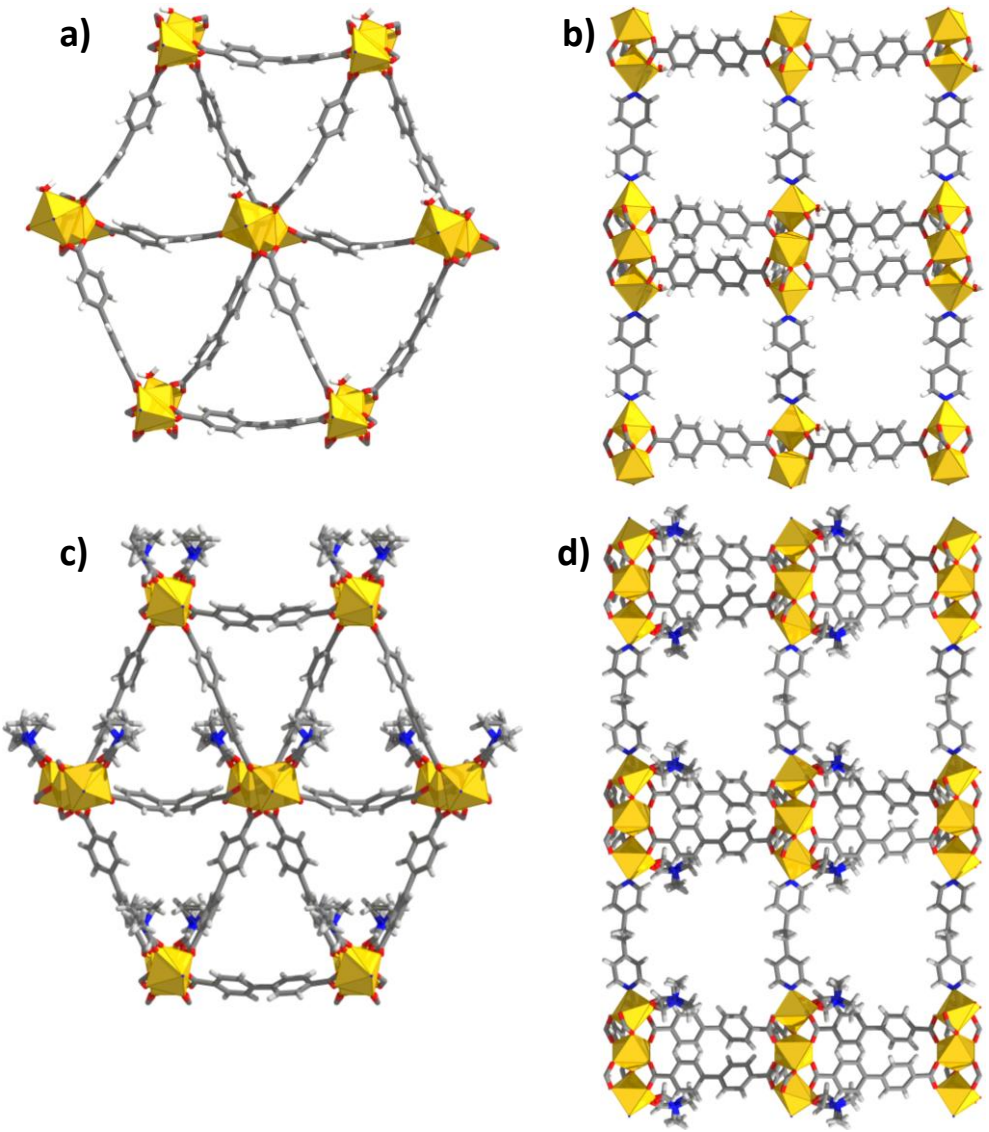

Figure 5.5. Packing diagrams of **BITSH-1** along the b and a *axis* (a and b) and **BITSH-2** along the c and a *axis* (c and d), respectively.

5.3.2. Turn-off fluorescence sensing of biogenic amines by BITSH-1 and BITSH-2

The porous nature of **BITSH-1** and **BITSH-2** frameworks encouraged us to study these materials for the sensing of harmful biogenic amines and food chemicals such as putrescine (PUT) and cadaverine (CAD). The UV absorption spectra of both the MOFs were first recorded in ethanol and it was observed that **BITSH-1** and **BITSH-2** displayed strong absorption bands at 278 nm and 280 nm, respectively. Upon excitation at these particular wavelengths, **BITSH-1** and **BITSH-2** displayed strong emission bands with λ_{max} at 332 nm and 333 nm, respectively, which can be ascribed to π-π* transitions **(Figure 5.6a)**. The fluorescence sensing experiments were carried out systematically where incremental additions of 20 µL of 1 mM putrescine (PUT) and cadaverine (CAD) solutions were made to a well dispersed MOF solution in ethanol, and a total of 200 µL of the biogenic amine was added in each case. Interestingly, the fluorescence intensity of both the MOFs was strongly quenched upon the addition of small amounts of PUT and CAD as shown in **Figure 5.6b-e** and **Figures 5.8-5.10**. These results further encouraged us to check other biogenic amines such as spermidine (SPD), spermine (SPM), tyramine (TYRM) and tryptamine (TRYP) which also showed a significant decrease in the fluorescence intensities of the MOFs **(Figures 5.11-5.13)**. The quenching efficiencies were calculated to corroborate these results, and it was observed that the MOF fluorescence intensities were quenched by almost 90 % for most of the biogenic amines **(Figure 5.6f)**. The values were even more impressive for **BITSH-1**, which showed an unprecedented 40 % quenching efficiency for PUT and CAD even at a low concentration of ca. 10 µM **(Figure 5.7a, b)**. The stability of both the MOFs towards biogenic amines was confirmed by the PXRD patterns collected after fluorescence experiments, followed by heating at 100 °C **(Figure 5.7c, d)**.

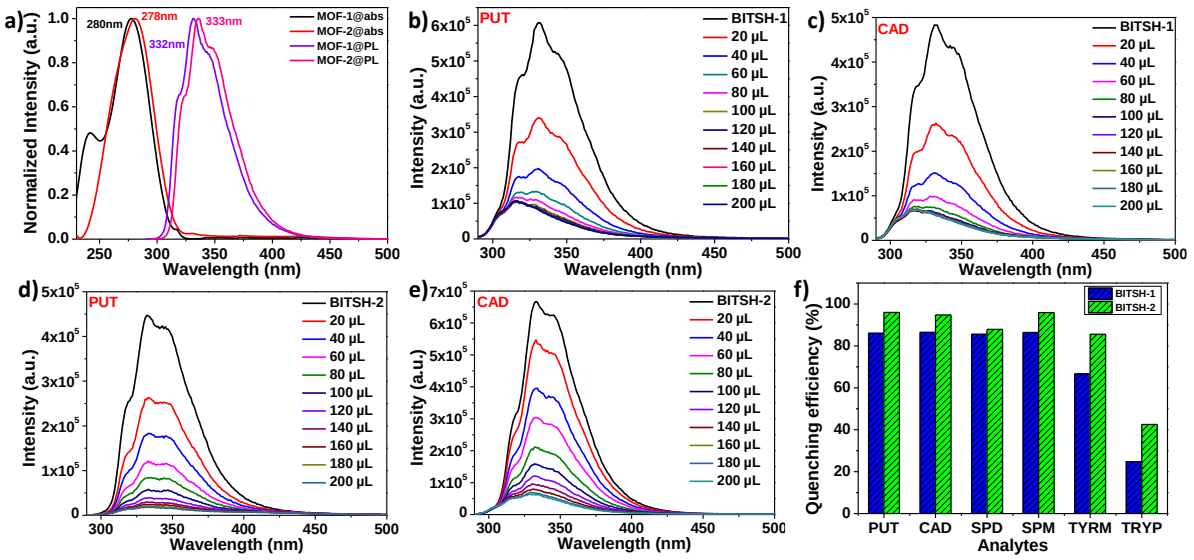

Figure 5.6. (a) UV absorption spectra and PL emission spectra of **BITSH-1** and **BITSH-2** systems. Decrease in the PL emission intensity of **BITSH-1** (excitation at 278 nm) and **BITSH-2** (excitation at 280 nm) upon incremental additions of putrescine (b and d) and cadaverine (c and e), respectively. (f) Quenching efficiency of biogenic amines on addition to **BITSH-1** and **BITSH-2** systems (incremental addition of 200 µL of each analyte in ethanol medium).

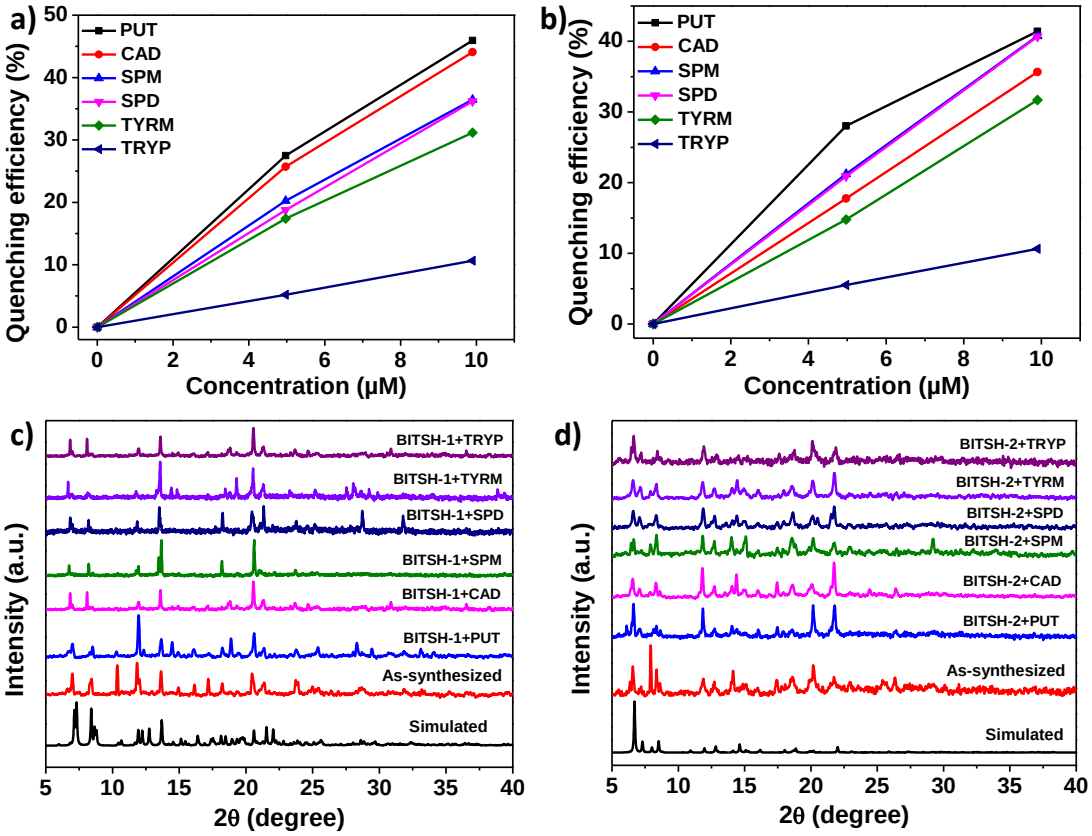

Figure 5.7. Quenching efficiencies of analytes in the concentration range of 0 - 10 µM on addition to (a) **BITSH-1** and (b) **BITSH-2**. Comparison of the PXRD patterns of as-synthesized (c) **BITSH-1** and (d) **BITSH-2** in the presence of biogenic amines (BA) obtained by collecting the sample through centrifugation after fluorescence experiments and collected samples were dried at 100 ℃.

5.3.3. Quenching mechanism for the sensing of biogenic amines

To analyze the underlying quenching mechanism, a detailed analysis of the results of photoluminescence emission studies was done. Stern-Volmer constants were obtained from the linear fitting of the Stern-Volmer plot, i.e. $(I_0/I)-1 = K_{SV}[Q]$,[30] where I_0 is the initial fluorescence intensity of the MOF before the addition of the analyte, I is the fluorescence intensity on addition of the analyte with the respective molar concentration [Q] of analytes and

K_{SV} stands for the Stern-Volmer constant **(Figures 5.8-5.13)**. Considering the linear fitting of the SV plot, the K_{SV} obtained is in the region of 10^4 M^{-1}, stating the dynamic quenching process as $K_q \leq 10^{10}$.[31]

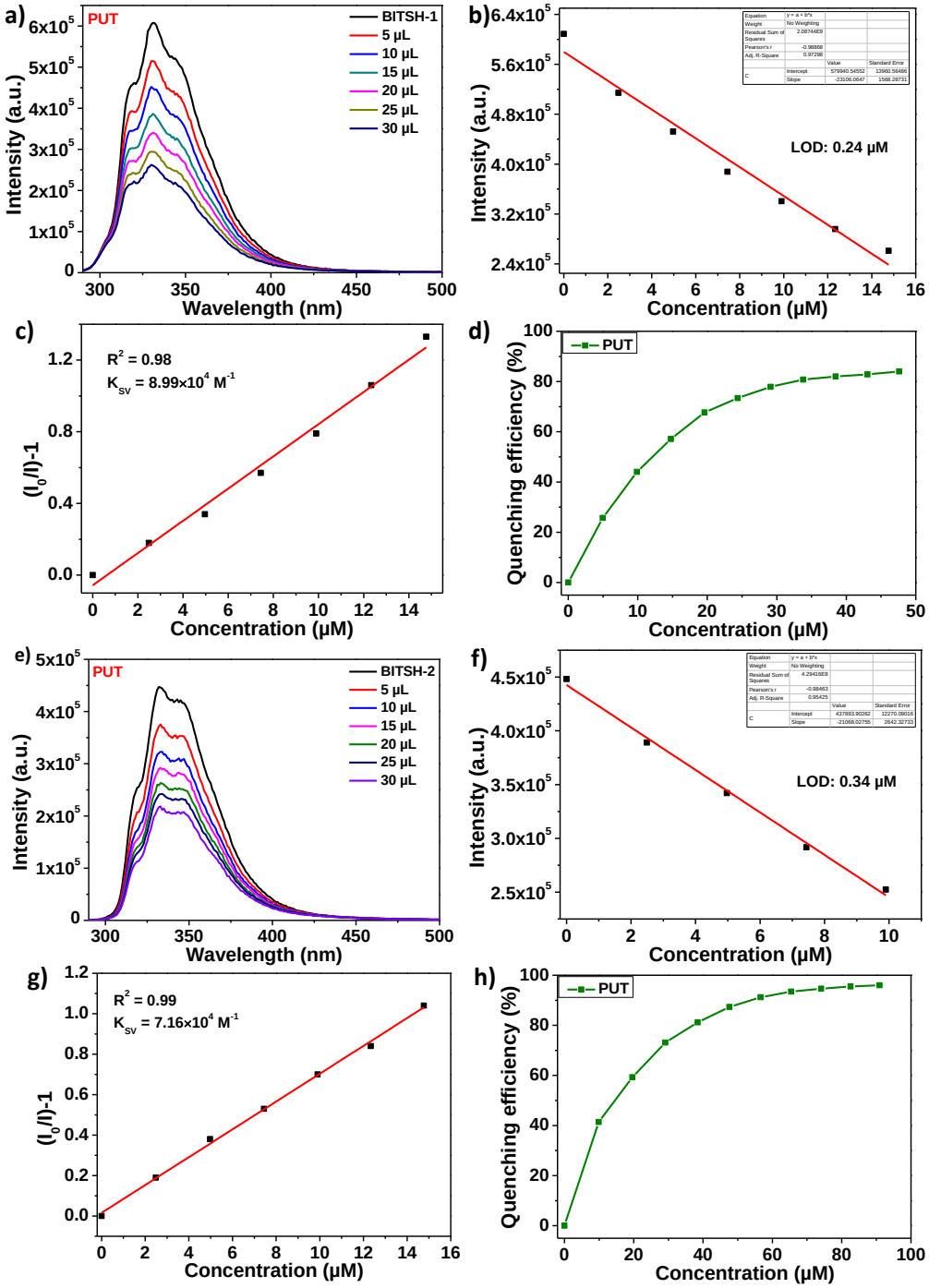

Figure 5.8. PL emission spectra of (a) **BITSH-1** and (e) **BITSH-2** against the incremental additions of 1 mM of putrescine (PUT) in ethanol, (λ_{ex} = 278 nm). Detection limit (LOD) of PUT with respect to (b) **BITSH-1** and (f) **BITSH-2**. Linear fit of Stern-Volmer plot of (c) **BITSH-1** and (g) **BITSH-2** in response to PUT. Quenching efficiency of PUT with respect to (d) BITSH-1 and (h) **BITSH-2**.

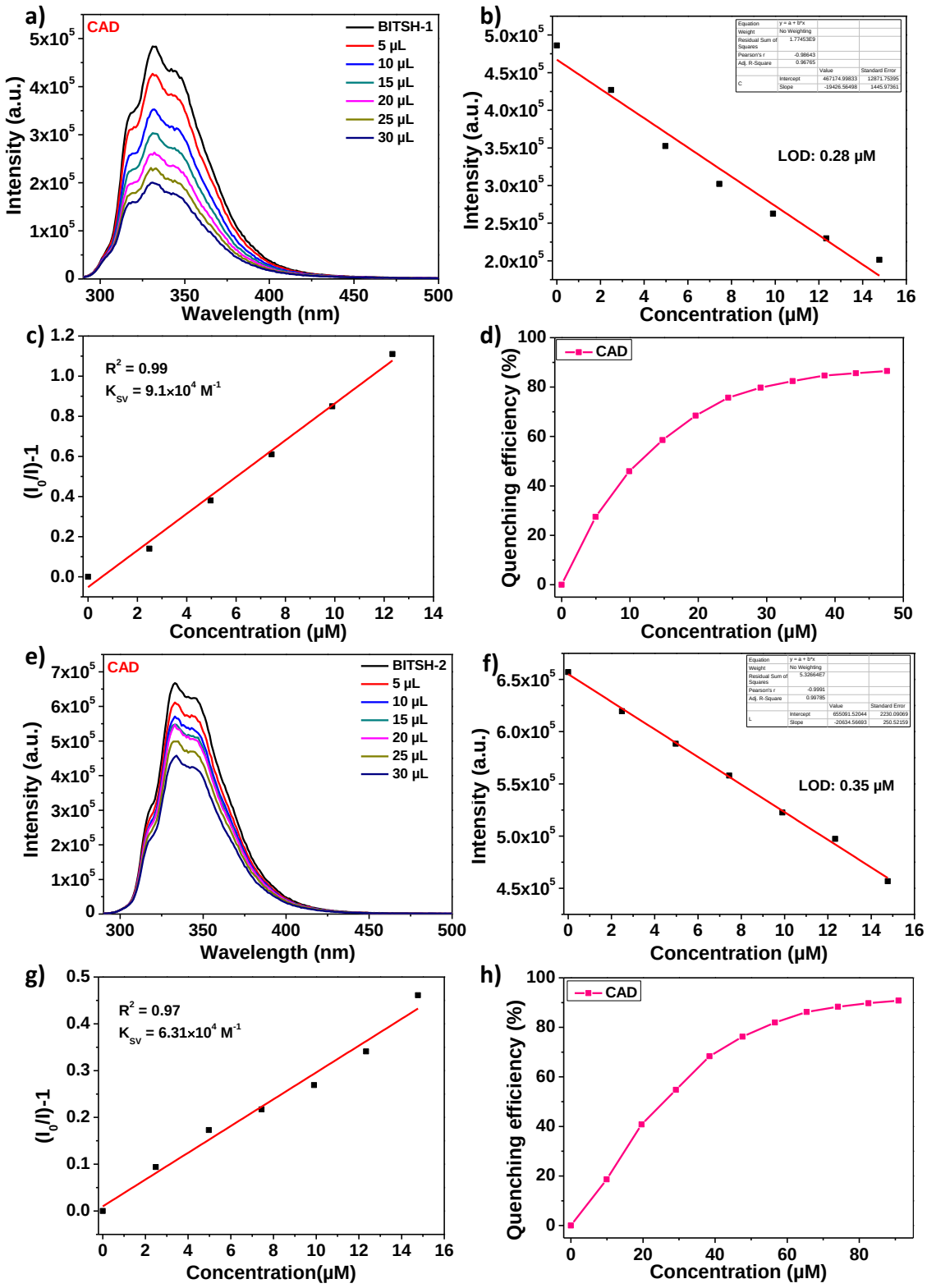

Figure 5.9. PL emission spectra of (a) **BITSH-1** and (e) **BITSH-2** against the incremental additions of 1 mM of cadaverine (CAD) in ethanol, (λ_{ex} = 278 nm). Detection limit (LOD) of CAD with respect to (b) **BITSH-1** and (f) **BITSH-2**. Linear fit of Stern-Volmer plot of (c) **BITSH-1** and (g) **BITSH-2** in response to CAD. Quenching efficiency of CAD with respect to (d) **BITSH-1** and (h) **BITSH-2**.

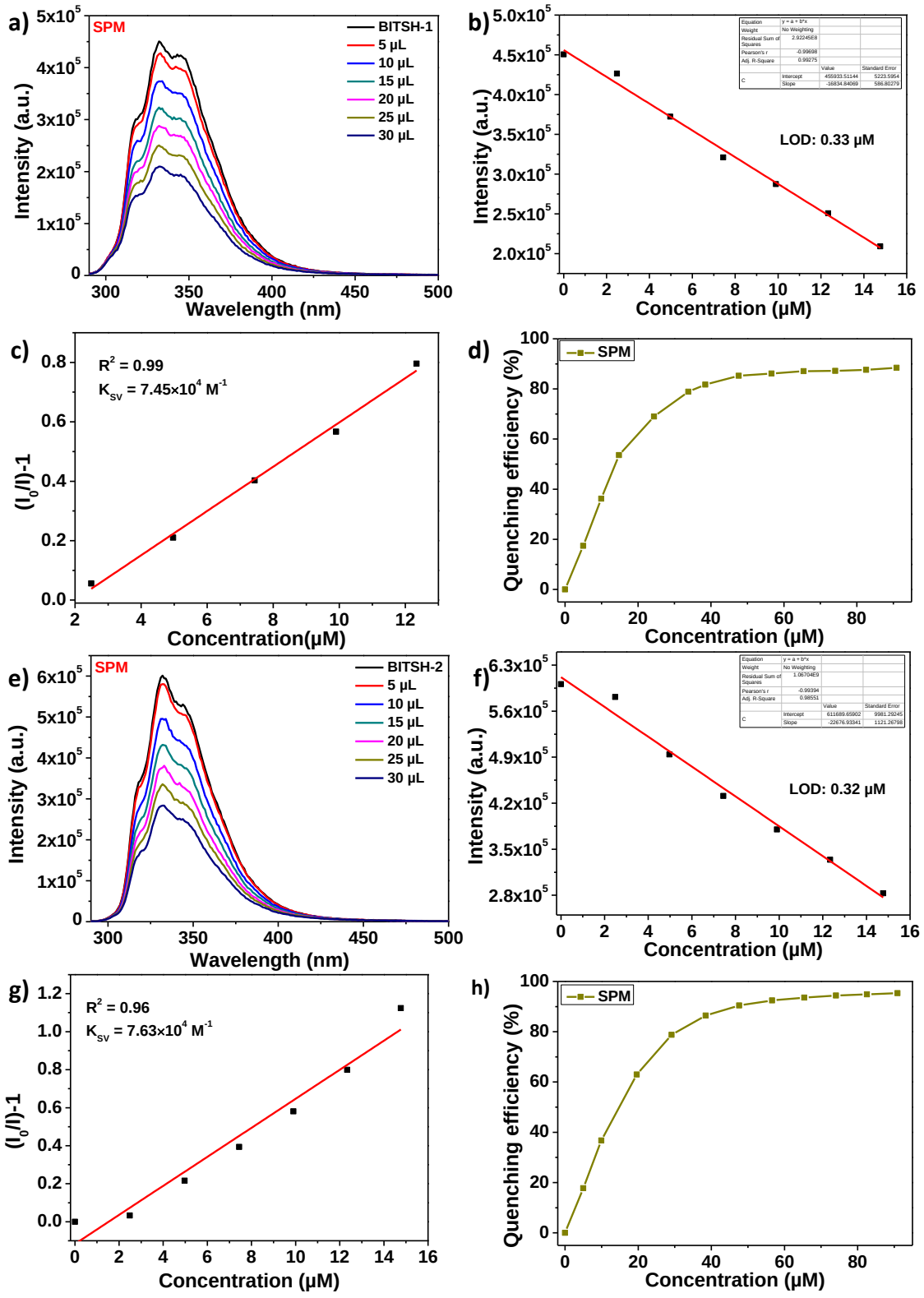

Figure 5.10. PL emission spectra of (a) **BITSH-1** and (e) **BITSH-2** against the incremental additions of 1 mM of spermine (SPM) in ethanol, (λ_{ex} = 278 nm). Detection limit (LOD) of SPM with respect to (b) **BITSH-1** and (f) **BITSH-2**. Linear fit of Stern-Volmer plot of (c) **BITSH-1** and (g) **BITSH-2** in response to SPM. Quenching efficiency of SPM with respect to (d) **BITSH-1** and (h) **BITSH-2**.

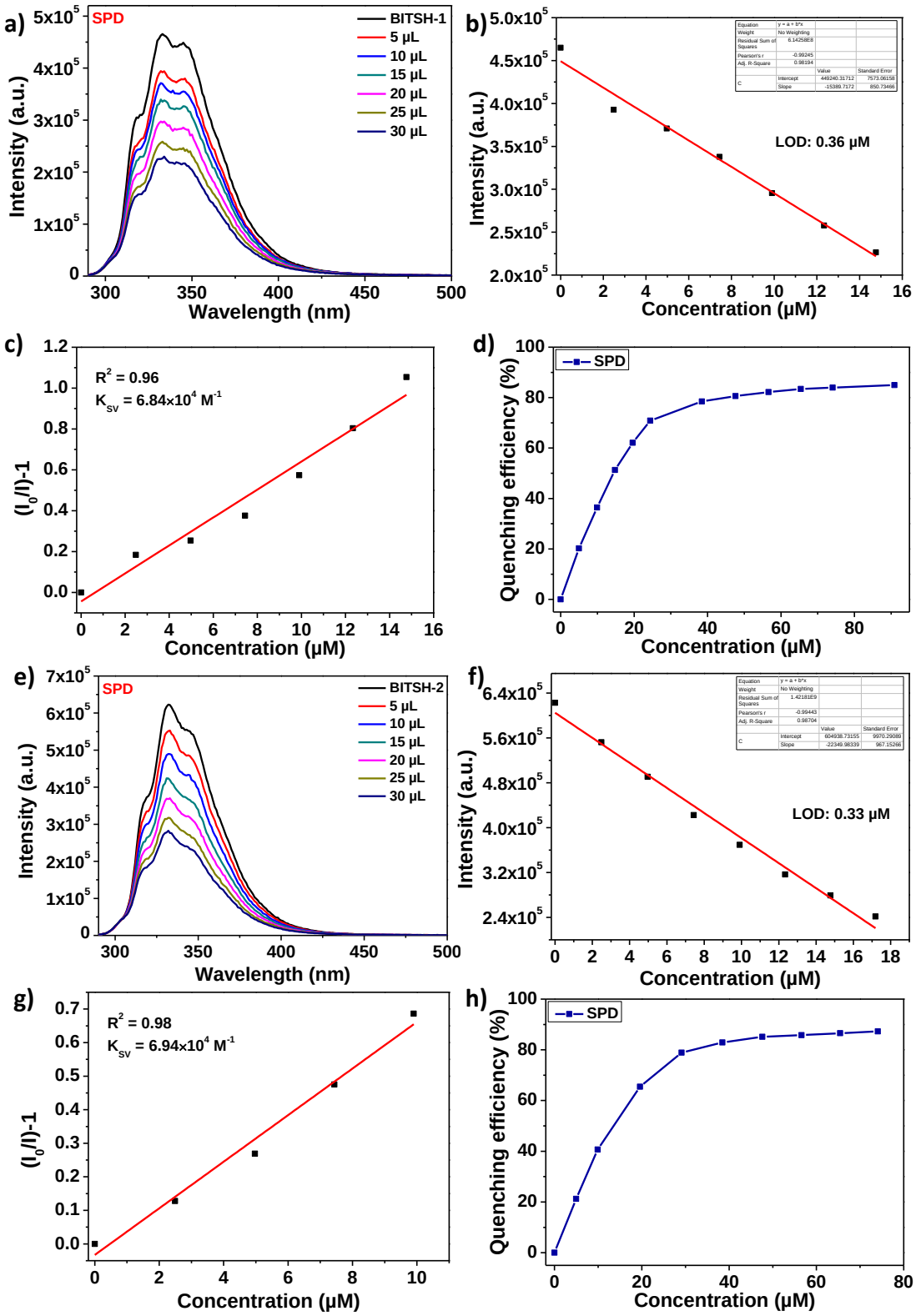

Figure 5.11. PL emission spectra of (a) **BITSH-1** and (e) **BITSH-2** against the incremental additions of 1 mM of spermidine (SPD) in ethanol, (λ_{ex} = 278 nm). Detection limit (LOD) of SPD with respect to (b) **BITSH-1** and (f) **BITSH-2**. Linear fit of Stern-Volmer plot of (c) **BITSH-1** and (g) **BITSH-2** in response to SPD. Quenching efficiency of SPD with respect to (d) **BITSH-1** and (h) **BITSH-2**.

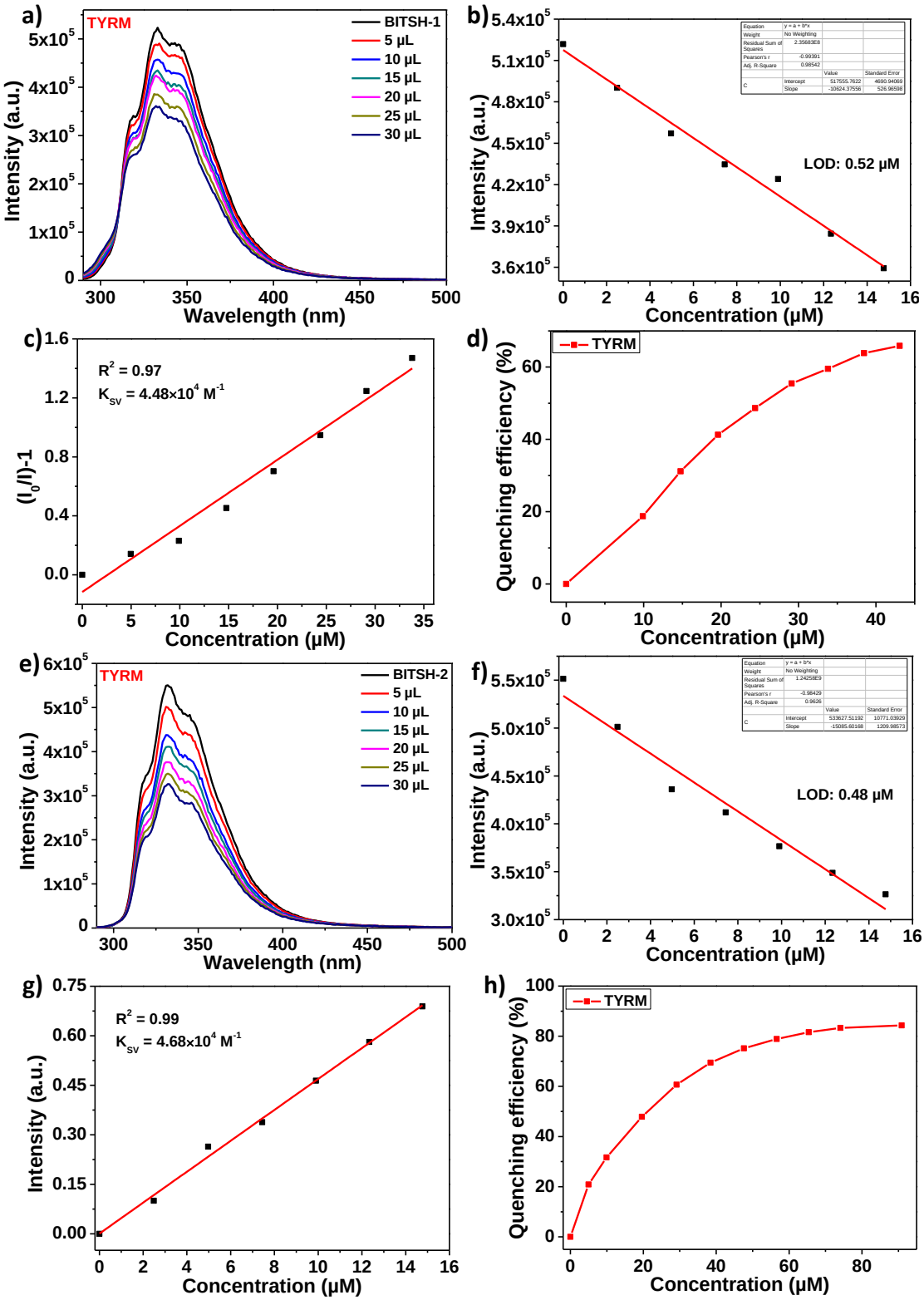

Figure 5.12. PL emission spectra of (a) **BITSH-1** and (e) **BITSH-2** against the incremental additions of 1 mM of tyramine (TYRM) in ethanol, (λ_{ex} = 278 nm). Detection limit (LOD) of TYRM with respect to (b) **BITSH-1** and (f) **BITSH-2**. Linear fit of Stern-Volmer plot of (c) **BITSH-1** and (g) **BITSH-2** in response to TYRM. Quenching efficiency of TYRM with respect to (d) **BITSH-1** and (h) **BITSH-2**.

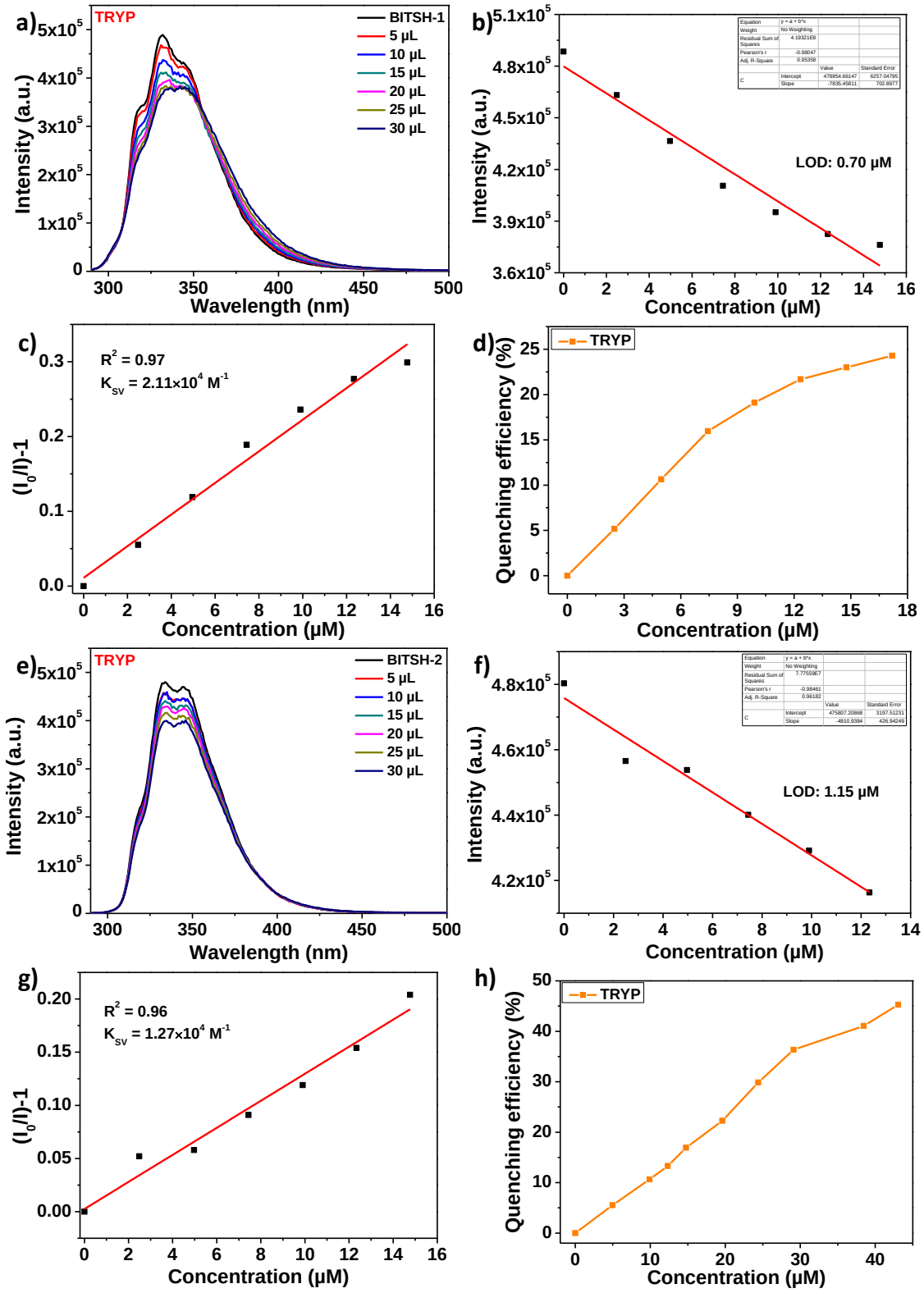

Figure 5.13. PL emission spectra of (a) **BITSH-1** and (e) **BITSH-2** against the incremental additions of 1 mM of tryptamine (TRYP) in ethanol, (λ_{ex} = 278 nm). Detection limit (LOD) of TRYP with respect to (b) **BITSH-1** and (f) **BITSH-2**. Linear fit of Stern-Volmer plot of (c) **BITSH-1** and (g) **BITSH-2** in response to TRYP. Quenching efficiency of TRYP with respect to (d) **BITSH-1** and (h) **BITSH-2**.

5.3.4. Studies to support dynamic quenching mechanism

To further explain the underlying dynamic quenching mechanism, fluorescence experiments were performed at different temperatures of 288 K, 293 K, and 298 K. It was observed that, with an increase in temperature, there is an increase in the K_D value (D stands for the dynamic constant) which confirms the operation of the dynamic quenching mechanism[31] in this case **(Figures 5.14-5.15** and **Table 5.2)**. Time-resolved lifetime studies could not be carried out due to the non-availability of the suitable wavelength LED excitation source. However, to rule out the static quenching possibility, the absorption spectra of the MOFs on the addition of analytes was recorded. It was observed that there was neither a bathochromic nor a hypsochromic shift in the absorption spectra and no new peak was observed on the addition of the analytes **(Figures 5.16-5.17)**. This rules out the static quenching process due to the absence of ground-state complex formation. The quenching process can be attributed to the electron transfer process, which can be either photoinduced electron transfer (PET) or resonance induced electron transfer (RET). The spectral overlap between the emission spectrum of the MOF and the absorption spectra of the analytes was checked, which showed a minimal spectral overlap, thus ruling out the possibility of RET in the present case **(Figure 5.18)**. Thus, it can be concluded that the PET process is responsible for this sensing property in both the frameworks. The favourable host-guest interactions between the biogenic amines and the MOFs could result from the donor-acceptor electron transfer process.

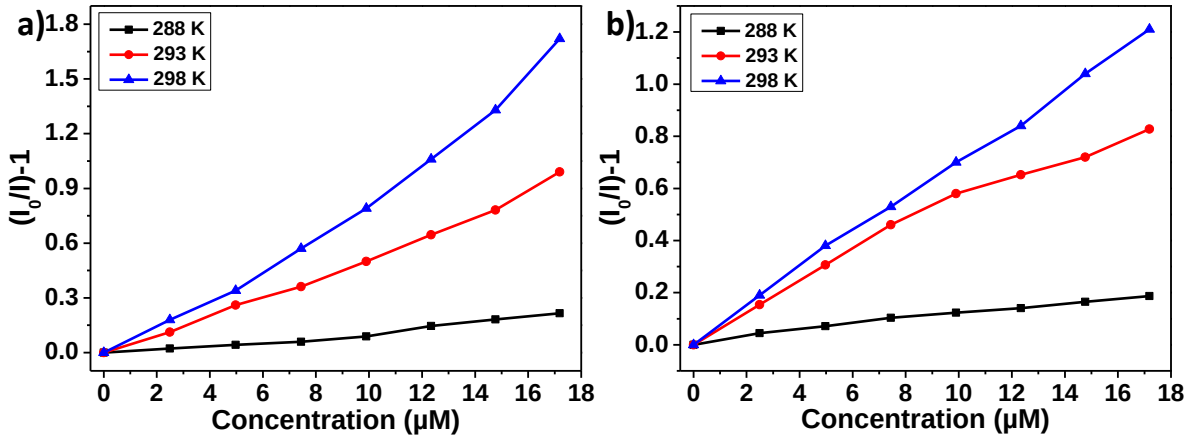

Figure 5.14. Stern Volmer plot of a) **BITSH-1** and b) **BITSH-2** on incremental additions of PUT (1 mM) recorded at different temperatures.

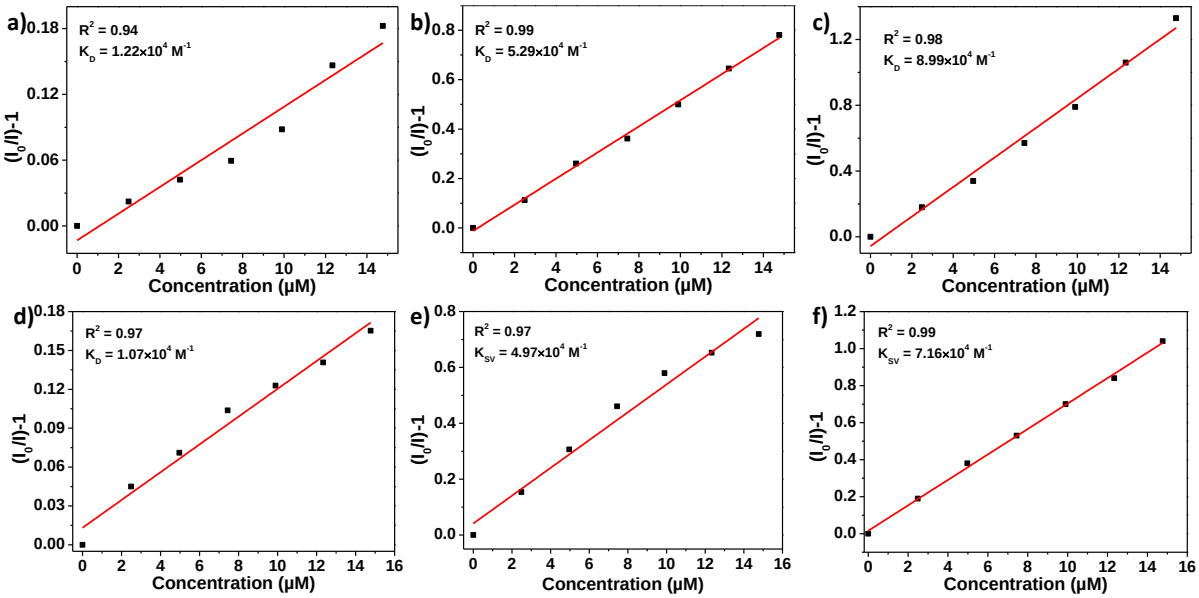

Figure 5.15. Linear fit of Stern-Volmer plot of **BITSH-1** and **BITSH-2** in response to PUT at different temperatures (a, d) 288 K (b, e) 293 K and (c, f) 298 K respectively.

Table 5.2. K_D values of **BITSH-1** and **BITSH-2** obtained on incremental additions of PUT (1 mM) at different temperatures.

Temperature (K)	**BITSH-1 K_D (M^{-1})**	**BITSH-2 K_D (M^{-1})**
288 K	1.22×10^4	1.07×10^4
293 K	5.29×10^4	4.97×10^4
298 K	8.99×10^4	7.16×10^4

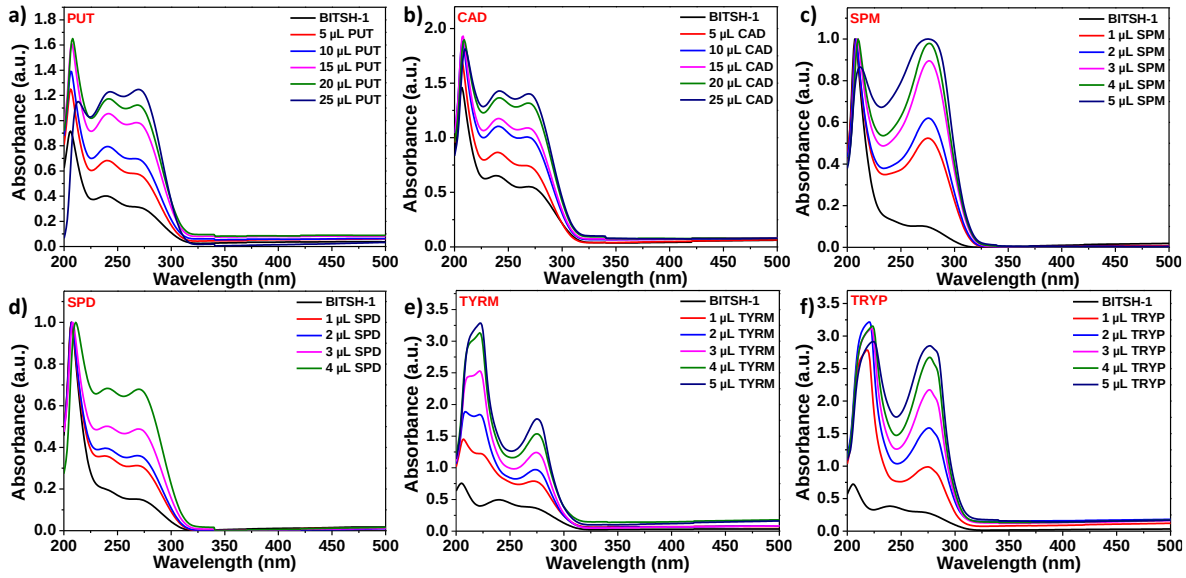

Figure 5.16. UV-vis spectra of **BITSH-1** on addition of (a) PUT (b) CAD (c) SPM (d) SPD (e) TYRM (f) TRYP in ethanol medium.

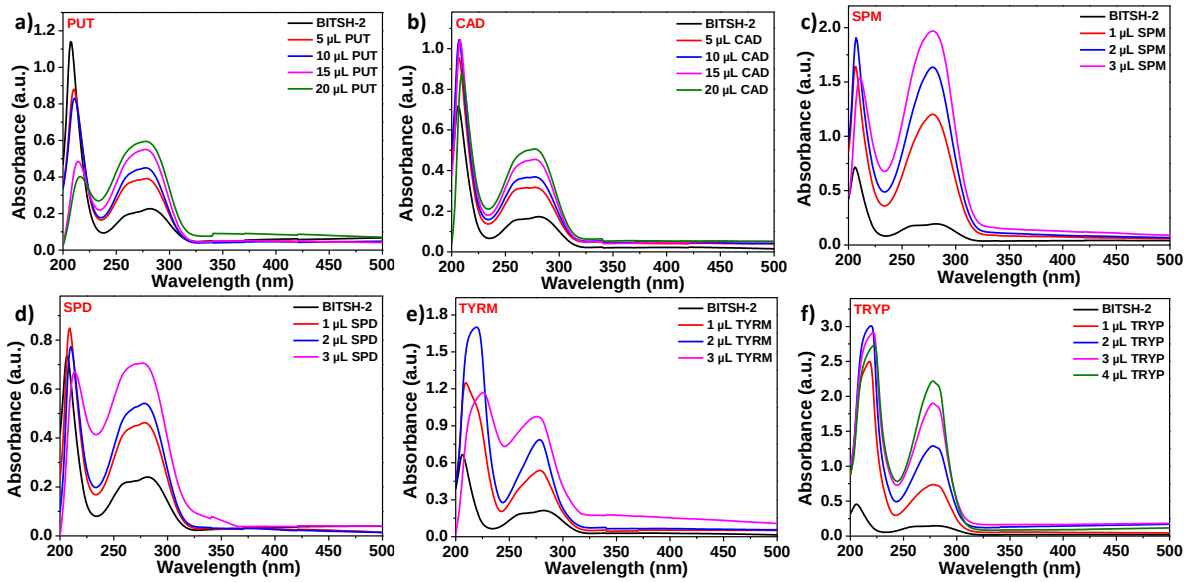

Figure 5.17. UV-vis spectra of **BITSH-1** on addition of (a) PUT (b) CAD (c) SPM (d) SPD (e) TYRM (f) TRYP in ethanol medium.

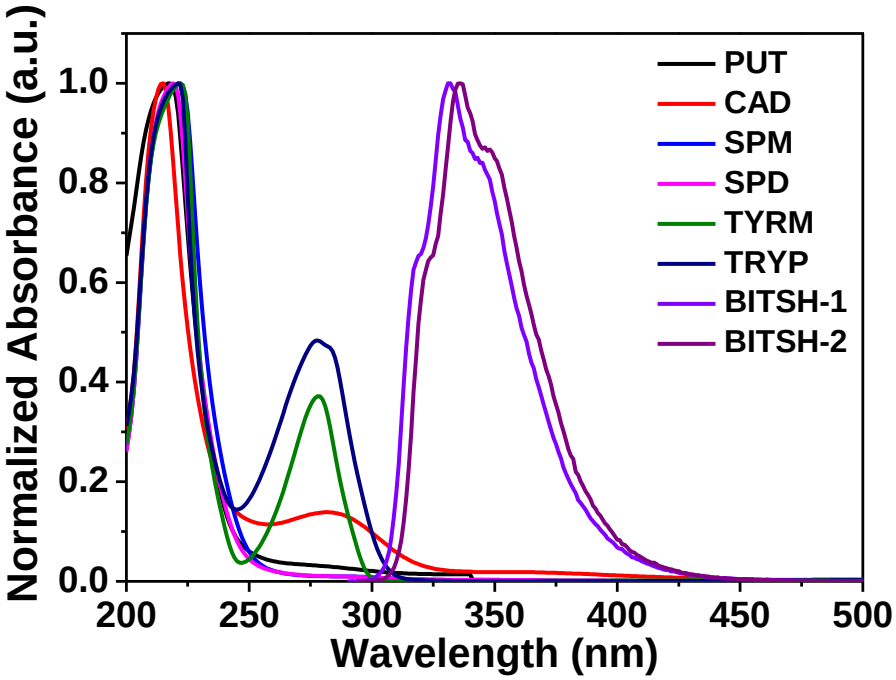

Figure 5.18. Spectral overlap between absorption spectra of analytes and emission spectra of both the MOF systems.

5.3.5. HOMO-LUMO studies

To verify this, the HOMO-LUMO energy values of the MOFs and the BAs were compared with the help of the cyclic voltammetry technique **(Figure 5.19)**. The HOMO energy levels of both the MOFs were found to be nearly same ~ -6.24 eV **(Figure 5.20)** and are lower than the HOMO energy levels of the BAs. It is noteworthy that the HOMO energy levels of BAs are higher than those of the MOF systems. This facilitates facile electron transfer from the HOMO of BA to the HOMO of the MOFs leading to efficient fluorescence quenching. Further, the higher the energy difference between the HOMO energy levels of MOFs and BAs, the more effective the overall quenching process and the better the limit of detection (LOD) values. The LOD values were calculated according to the formula 3s/k,[32] where s is the standard deviation obtained from five blank readings of the MOF and k represents the slope obtained from the linear fitting of the intensity vs. concentration of analyte [Q] plot. The LOD values for **BITSH-1** follow the order: PUT > CAD > SPM > SPD > TYRM > TRYP with PUT and CAD displaying LOD values as low as 0.24 mM (21.15 ppb) and 0.28 mM (29.97 ppb), respectively. It can be ascertained that both the MOFs can detect a variety of biogenic amines via turn-off behavior rapidly and drastically and the LOD values are better than many reported materials **(Table 5.3)**. Attempts were also made to collect the single crystal structures of PUT and CAD

loaded MOF crystals, but due to the poor diffraction of the crystals suitable datasets could not be obtained.

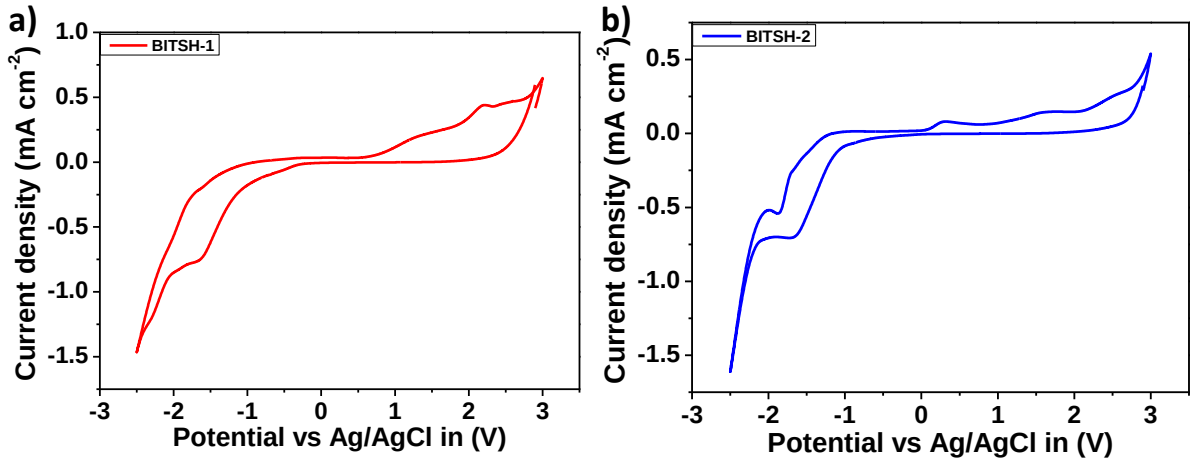

Figure 5.19. Cyclic Voltammogram (CV) of (a) **BITSH-1** and (b) **BITSH-2** recorded in acetonitrile medium.

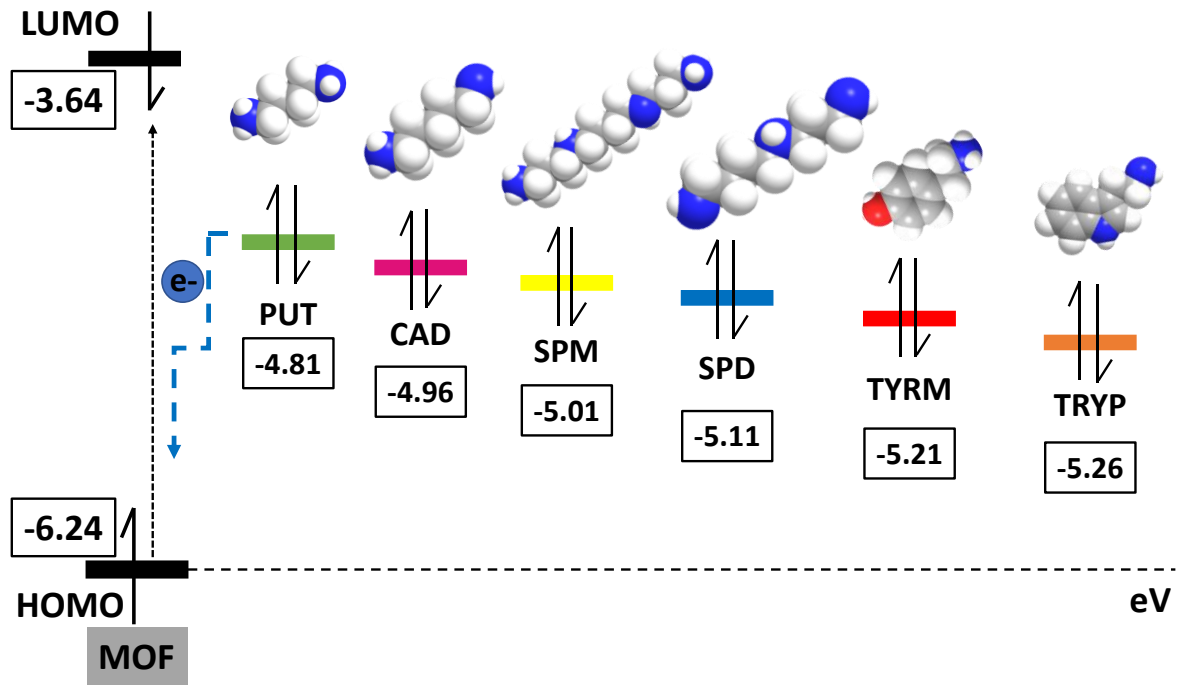

Figure 5.20. Schematic representation of the HOMO (π) and LUMO (π^*) energy levels of **BITSH-1** and the HOMO energy levels of the biogenic amines analyzed.

Table 5.3. Comparison of different probes, techniques and detection limits for sensing biogenic amines.

Biogenic amines	**Sensor**	**Detection technique**	**Limit of Detection**	**Linear range**	**Ref.**
SPM, SPD	Anionic organic dye-zincon	Colorimetric method	25.1 and 30.7 nM	0-5 µM	**[33]**
PUT-CAD-SPM-SPD-HIS	Zn(II) schiff-base complex	Colorimetric method	2.2 to 1.02 µM	0-18 µM	**[34]**
PUT-CAD-TYR-HIS	Amino-reactive chameleonstain Py-1	Capillary electrophoresis	0.2 to 0.9 µM	1-100 µM	**[35]**
SPM, SPD	Complexes of Pb(II), Cd(II), and Zn(II)	Fluorescence turn-on	25 µM	25-250 µM	**[36]**
PUT-CAD-SPM-SPD-TYR-HIS	Dansyl chloride derivatization	HPLC	0.09 to 0.3 mg L^{-1}	NA	**[37]**
PUT, CAD	Trifluoroacetylacetone (TFAA)/on-fibre derivatization	GC-MS	0.5-0.6 µg cm^{-3}	0-100 µg cm^{-3}	**[38]**
PUT, CAD	PSAO@Nafion-MnO_2 in the SPCE	Electrochemical method	0.3 µM	1-50 µM	**[39]**
PUT, CAD	4-MBA-functionalized Au@ZIF-8SERS paper	Surface-enhanced Raman scattering (SERS) technique	76.99 and 115.88 ppb	0-10^{-4} (v/v)	**[40]**
SPM	Zwitterionic Cd-MOF	Fluorescence quenching	0.3 µM	NA	**[41]**
SPM	Pyrene derivative and squarine containing self-assembled system	Fluorescence quenching	4.73 µM	1-10 µM	**[42]**
PUT, CAD	**Co-MOF**	**Fluorescence quenching**	**0.24 µM, 0.28 µM**	**0-16 µM**	**This work**

5.3.6. X-Ray photoelectron spectroscopy (XPS) analysis for biogenic amines detection

Direct evidence for the detection of biogenic amines by **BITSH-1** and **BITSH-2** MOF systems was provided by XPS studies. The XPS analysis was performed on MOF crystals before and after the sensing experiments **(Figure 5.21)**. The MOF crystals were collected by filtration after the fluorescence experiment and dried at 100 °C in an oven to ensure the complete removal of solvent molecules and biogenic amines that may be present on the crystal surface. Later these crystals were analysed for XPS studies and their spectra were compared with the XPS spectra of the pristine MOFs. Interestingly, upon comparing the N 1s spectra, we could observe a shift in the binding energy values of MOFs on addition of biogenic amines **(Figure 5.22a and c)**. The N 1s deconvoluted spectra of the MOF system on addition of PUT and CAD are shown in **Figure 5.22b and d**, respectively. The predominant peak observed at a binding energy of 399.5 eV can be attributed to the nitrogen atoms in C-N-C groups[43] present in the MOF system. The additional peak at 400.4 eV is attributed to the N-H (-NHx) amine groups of biogenic amines.[43] Similar observations were made for the characteristic N-H binding energy peak on adding other biogenic amines such as SPM, SPD, TYRM and TRYP to the MOF crystals **(Figures 5.23-5.24)**. This provides clear evidence for the highly selective nature of **BITSH-1** and **BITSH-2** towards detection of biogenic amines.

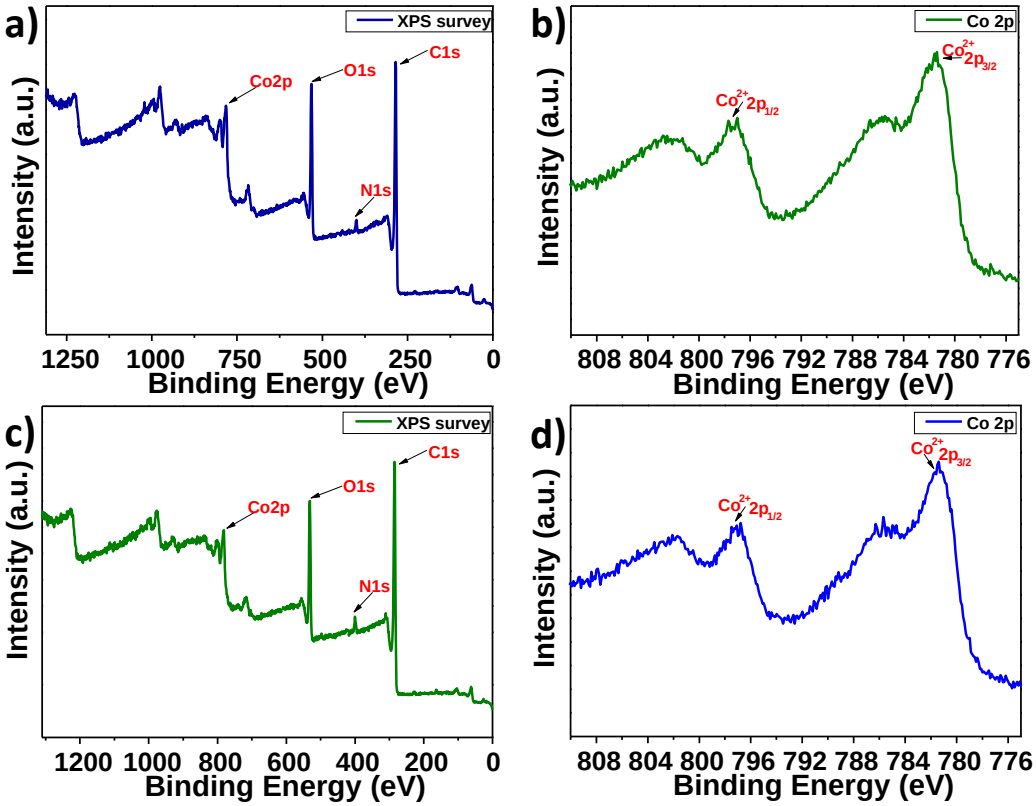

Figure 5.21. XPS survey spectrum (a) and Co 2p XPS spectrum (b) of **BITSH-1** sample, XPS survey spectrum (c) and Co 2p XPS spectrum (d) of **BITSH-2** sample.

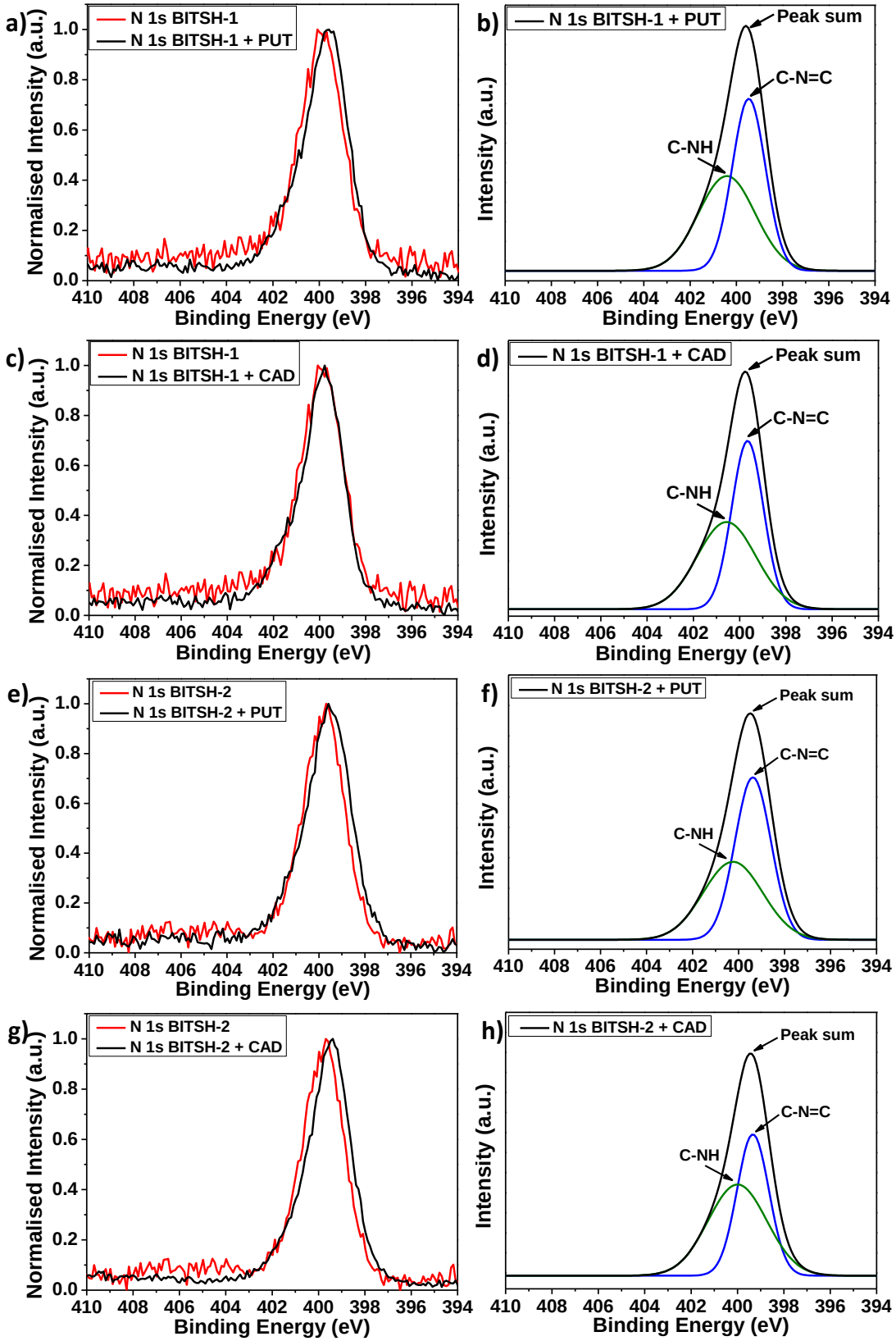

Figure 5.22. (a, e) N 1s XPS spectrum of **BITSH-1** and **BITSH-2** on addition of PUT and (b, f) deconvoluted spectrum of **BITSH-1 + PUT** and **BITSH-1 + PUT**. (c, g) N 1s XPS spectrum of **BITSH-1** and **BITSH-2** on addition of CAD and (d, h) deconvoluted spectrum of **BITSH-1 + CAD** and **BITSH-2 + CAD**.

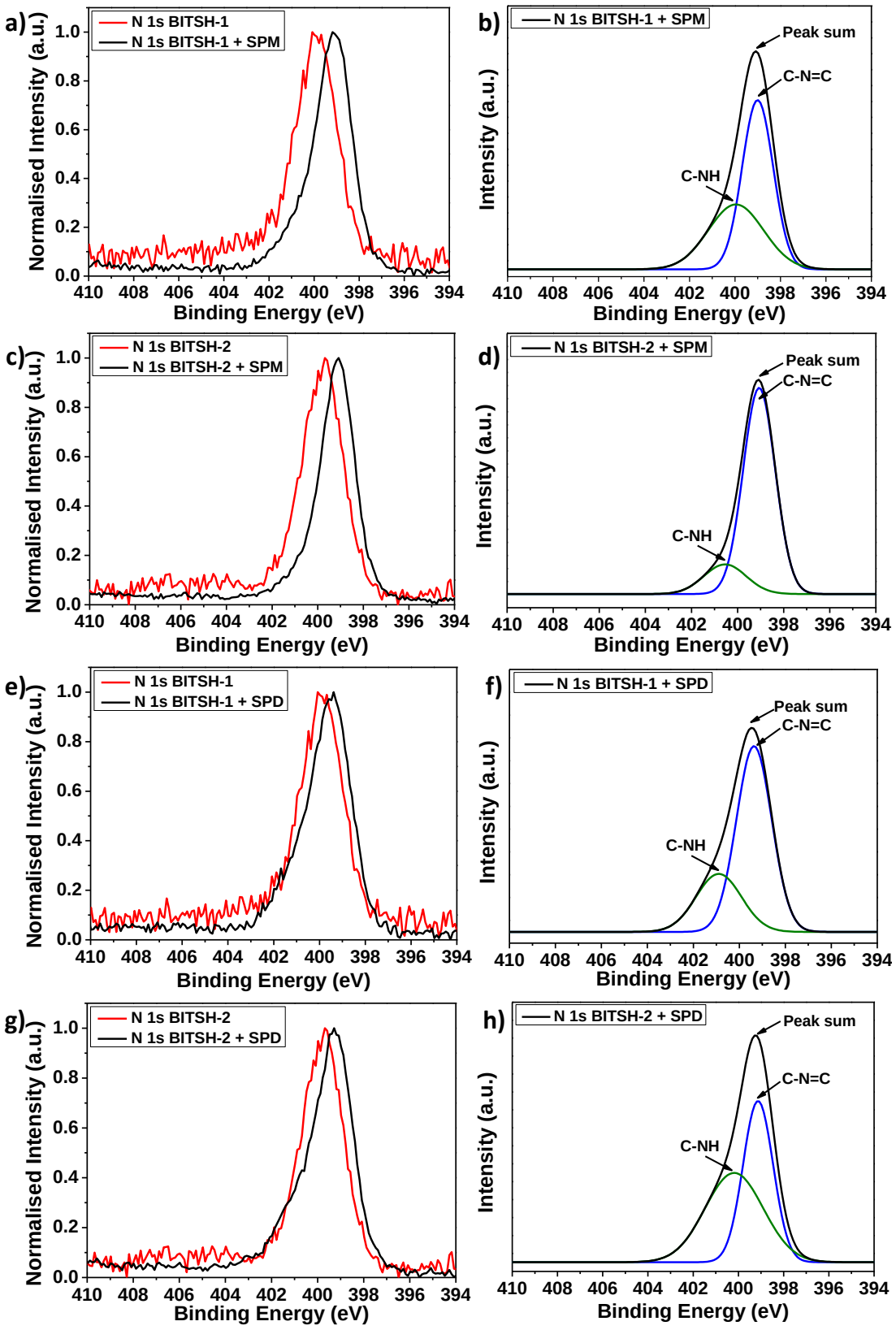

Figure 5.23. N 1s XPS spectrum of **BITSH-1** and on addition of (a) SPM and (e) SPD. Deconvoluted spectrum of (b) **BITSH-1 + SPM** and (f) **BITSH-1 + SPD**. N 1s XPS spectrum of **BITSH-2** on addition of (c) SPM and (g) SPD. Deconvoluted spectrum of (d) **BITSH-2 + SPM** and (h) **BITSH-2 + SPD**.

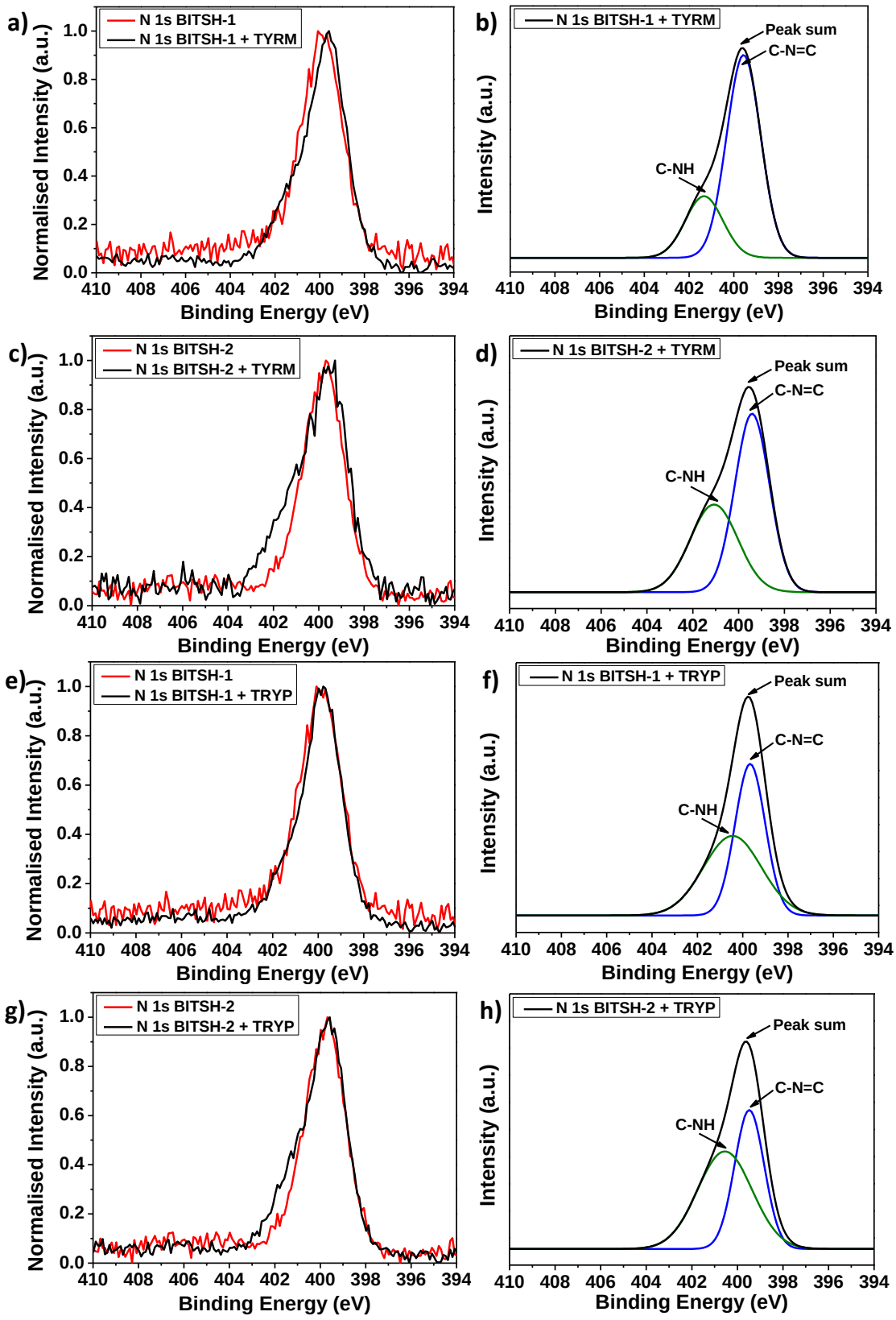

Figure 5.24. N 1s XPS spectrum of **BITSH-1** and on addition of (a) TYRM and (e) TRYP. Deconvoluted spectrum of (b) **BITSH-1 + TYRM** and (f) **BITSH-1 + TRYP**. N 1s XPS spectrum of **BITSH-2** on addition of (c) TYRM and (g) TRYP. Deconvoluted spectrum of (d) **BITSH-2 + TYRM** and (h) **BITSH-2 + TRYP**.

5.3.7. Visual evidence for the detection of biogenic amines

Based on the observations made from the fluorescence studies of both MOFs, we tried to examine these MOFs for visual detection of BAs. MOF-polymer composite membranes were prepared by mixing the MOF samples with a suitable polymer solution. The membranes were then cut into strips of proper shape and size as visual sensors and placed inside air tight zip covers containing fish and cheese samples **(Figure 5.25)**. The real-time experiments were performed at room temperature. The strips were placed at a distance from the food samples so as to ensure that there is no direct contact between the membrane strips and the food samples. In less than 2 h, the colours of the MOF strips changed dramatically, whereas the PVDF strip did not show any colour change. This clearly demonstrates that both the MOFs are excellent materials for the real-time detection of biogenic amines present in protein-rich food stuffs.

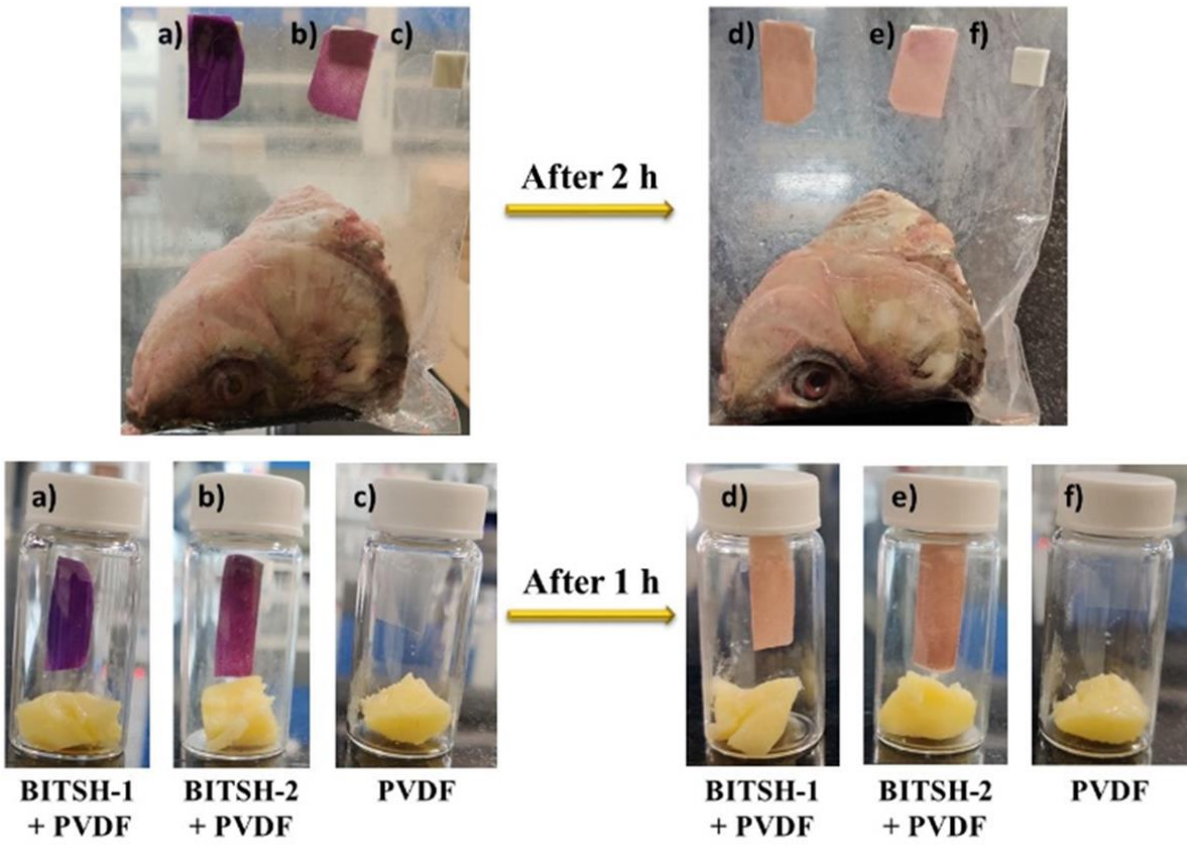

Figure 5.25. Visual detection of biogenic amines from the fish (top) and cheese (bottom) samples using MOF + polymer membrane strips as real-time sensors: (a) the **BITSH-1 + PVDF** strip, (b) the **BITSH-2 + PVDF** strip, and (c) only the PVDF strip before exposure and (d, e, and f) show the corresponding sensor strips after exposure to the food samples.

5.4. Conclusions

Two novel cobalt-based MOFs, **BITSH-1** and **BITSH-2**, were synthesized and studied for detection of harmful biogenic amines. The frameworks display excellent sensing properties in both solution and solid states. The quenching efficiencies and LODs are the best for any MOF studied for biogenic amines to date. Remarkably, both materials showed excellent potential for the real-time detection of biogenic amines in protein rich foods. The current work highlights the capability of MOF materials to sense harmful biogenic amines and stresses the need to design new materials for the sensing of various other dangerous chemicals present in food items.

CHAPTER 6

Cobalt Metal-Organic Frameworks and its Mixed-Matrix Membranes for Discriminative Sensing of Amines and On-site Detection of Ammonia

Developing suitable materials that can differentiate between chemically similar substances such as aliphatic and aromatic amines is challenging. Aliphatic and aromatic amines the same functional group which leads to them having very similar electronic and chemical properties. This makes the entire separation process more tedious. Metal-organic frameworks known for their inherent permanent porosity can be designed using appropriate building blocks that can lead to multifunctional materials. The potential investigation of MOFs for the real-time detection of food spoilage markers such as putrescine and cadaverine (categorized as biogenic amines) in protein-rich food products like fish and cheese and developing a MOF-based food sensor was achieved in the previous chapter. In this chapter, **BITSH-1** and **BITSH-2** MOFs are examined for discriminative sensing of amines and on-site detection of ammonia. Both the MOF materials display unique fluorescence behavior where aliphatic amines lead to "turn-off", and aromatic amines show "turn-on" fluorescence intensities of the two MOFs. Real-time sensing experiments with MOF-based mixed matrix membranes show an instant color change when ammonia is liberated from a chemical reaction. Density functional theory calculations unravel that the aliphatic and aromatic amines interact with the MOF structures in different ways that lead to "turn-off" and "turn-on" fluorescence behavior, respectively.

6.1. Introduction

Amines, an important class of organic compounds are derived from ammonia. Amines are categorized as primary (RNH_2), secondary (R_2NH) and tertiary (R_3N) depending on the replacement of hydrogen atoms by alkyl or aryl groups in ammonia. These are further classified as aliphatic amines if it contains only alkyl groups and aromatic amines if aryl groups are attached. Amines are pervasive chemicals that are present in household cleaning products, refrigerant gas, pesticides, plastics, dyes, and other chemicals. The corrosive nature of amines poses a serious and persistent threat to the environment.[1-4] Exposure to amines, both aliphatic and aromatic, can lead to various health complications, including skin irritation, respiratory disorders, and lung damage.[5-8] It has been observed that the most common pathway of

exposure to amines is through inhalation of ammonia which is a key starting material. This can also occur due to accidental leakage of ammonia from an industrial plant. Therefore, detection of amines at low concentrations is highly desired. Although there are segregated reports on the detection of amines, the reports on discriminative sensing of amines are quite rare.[9,10] The probable reason behind this is the difference in the size, structure, and electronic properties of a wide range of amines, making it quite challenging to design a material that can display excellent discriminative molecular recognition of aliphatic and aromatic amines.[11-13] Besides this, most of the materials for amine sensing have been studied in either solution or solid-state which limits the universality of the sensor.[9,14] Thus, there is a need to develop multifunctional sensors that can rapidly and discriminately detect different types of amines in both solution and vapor phases.

Metal-organic frameworks (MOFs), a class of porous hybrid materials have shown great potential for sensing applications due to their fast and robust sensing features.[15-18] The reticular design of MOF structures using desired linkers as struts offers plenty of possibilities for fine-tuning their molecular level interactions with the probe analytes. This has helped researchers use MOFs to detect various analytes, including amines.[19,20] However, most of these reports are based on "turn-off" fluorescence intensities, and very few are based on "turn-on" fluorescence behavior.[21,22] Also, not much emphasis has been given to processing the MOF crystals to a usable form that can be tested under actual conditions. It is increasingly desired to produce materials that can display "turn-off" and "turn-on" fluorescence properties separately for analytes that contain the same functional groups but differ slightly in their chemical properties. Additionally, designing visual and efficient sensors for multiphase sensing is significant in enhancing the practicability for real-time-based applications. There are various techniques for sensing, but researchers have widely used fluorescence-based sensing methods due to their sensitivity and fast response time.[23-25] In the current chapter, we explore two Co-based MOFs, **BITSH-1** and **BITSH-2**, for the visual detection of ammonia and discriminative sensing of aliphatic and aromatic amines. Interestingly, the fluorescence intensity of both frameworks gets quenched via "turn-off" fluorescence with the addition of aliphatic amines. In contrast, the addition of aromatic amines leads to an increase in fluorescence intensity. Impressively, both the frameworks are efficient in sensing amines in both solution and vapor states, thus paving the way to utilize these MOF materials as suitable devices for the real-time detection of amines.

6.2. Experimental Section

6.2.1. Materials

All the reagents, solvents and analytes (Ammonia (NH_3), Methylamine (MA), Triethylamine (TEA), Aniline (AN), N-Methylaniline (N-MA), were purchased from commercial sources and used as such without further purification. Cobalt Nitrate hexahydrate [$Co(NO_3)_2 \cdot 6H_2O$], N,N′- dimethyl formamide were procured from SRL, biphenyl-4,4'-dicarboxylic acid (bpdc), 1,2-bis(4-pyridyl)ethane (bpe) and 4,4'-bipyridine (bpy) were purchased from TCI chemicals.

6.2.2. Synthesis of BITSH-1 and BITSH-2

Synthesis of **BITSH-1**: **BITSH-1** [Co(bpdc)(bpy)] was synthesized by reacting $Co(NO_3)_2 \cdot 6H_2O$ (29.1 mg, 0.1mmol), biphenyl-4,4'-dicarboxylic acid (bpdc) (24.2 mg, 0.1 mmol) and 4,4'-bipyridine (bpy) (7.8 mg, 0.05 mmol) was dissolved in 10 ml of DMF and placed in the oven at 130 ℃. Purple crystals were obtained after 24 h. The crystals were washed using DMF and exchanged with ethanol for further study.

Synthesis of **BITSH-2**: **BITSH-2** [Co(bpdc)(bpe)] was synthesized by reacting $Co(NO_3)_2 \cdot 6H_2O$ (29.1 mg, 0.1mmol), biphenyl-4,4'-dicarboxylic acid (bpdc) (24.2 mg, 0.1 mmol) and 1,2-bis(4-pyridyl)ethane (bpe) (9.2 mg, 0.05 mmol) was dissolved in 10 ml of DMF and placed in the oven at 130 ℃. Pink crystals were obtained after 24 h. The crystals were washed using DMF and exchanged with ethanol for further study.

6.2.3. Photoluminescence (PL) Measurements

The as-synthesized MOF crystals were exchanged with ethanol after washing thoroughly with DMF. The as-synthesized crystals were activated in the vacuum oven to remove the solvent molecules from the MOF system. The activated crystals were further used for preparing MOF suspensions. Well-dispersed MOF suspensions were prepared by adding 1 mg of the ground MOF sample to 2 ml of ethanol. Thus, prepared MOF suspensions were used for the absorbance and fluorescence sensing studies. The fluorescence behavior of both the MOF systems were examined on incremental additions of 0.1 M amines.

6.2.4. Preparation of MOF-based mixed matrix membranes

MOF-based mixed matrix membranes were prepared using MOF crystals and PVDF polymer solution (polyvinylidene fluoride). The polymer solution was prepared by dissolving 0.15 g of PVDF in 1 ml of DMF with the help of stirring. After the complete dissolution of PVDF in DMF, a slightly ground MOF sample was added to the mixture in different weight percentages

and stirred for 30 min to get a uniform suspension. We prepared three different weight percentages: 30, 60 and 90 wt %, and we found 60 wt % of MOF-PVDF mixture was more suitable for the study. We prepared flexible MOF-PVDF membranes that were obtained separately using **BITSH-1** and **BITSH-2**, were separately added to the PVDF solution and stirred for 15 min to obtain uniform suspensions. The uniform suspension was slowly drop-cast onto a glass substrate which was pre-heated in the oven at 120 ℃ for 20 min. The drop-cast mixture was left in the oven for 20 min. We obtained MOF + PVDF membranes which were able to fold in entirely half and refold back showing the flexible nature of the MOF membranes. These membranes were further used for sensing amines.

6.2.5. Electrochemical measurements

In order to obtain HOMO and LUMO values for the MOF system, cyclic voltammetry plots were collected for **BITSH-1** and **BITSH-2**. CV for both the MOF samples were recorded with the help of three electrode cell setup using Fluorine-doped Tin Oxide (FTO) as the working electrode, platinum mesh as counter electrode and Ag/AgCl as reference electrode. 0.1 M tetrabutylammonium perchlorate in acetonitrile was used as an electrolyte with a scan rate of 100 mV/s.

6.2.6. Computational Methods

All the density functional theory (DFT) calculations were carried out with REV-PBE[26] exchange-correlation functional using the CP2K package.[27] Grimme's D3 method[28] was used to account for dispersion forces. We used the DZVP basis with Goedecker, Teter, and Hutter (GTH) pseudopotentials with a kinetic energy cutoff of 500 Ry for DFT calculations.

6.3. Results and Discussion

6.3.1. Structural details and characterization of the MOF

BITSH-1 and **BITSH-2** were prepared as per our previously reported procedure using solvothermal approach by mixing $Co(NO_3)_2 \cdot 6H_2O$ and biphenyl-4,4'-dicarboxylic acid (BPDC) with 4,4'-bipyridine (BPY) and 1,2-bis(4-pyridyl)ethane (BPE) in DMF, respectively.[19] The coordination environment and overall packing in both the frameworks is very similar where BPDC linkers form 2D layers with trinuclear Co clusters and the pyridyl linkers act as pillars **(Figure 6.1a, b)**. **BITSH-1** structure also contains a coordinated water molecule whereas two DMF molecules are coordinated to the Co cluster in the case of **BITSH-2**. This results in an unsaturated metal site in the case of **BITSH-1**. **Figure 6.1a, b** shows the

presence of well-defined channels along the *c* axes that are responsible for the adsorption of guest analyte molecules.

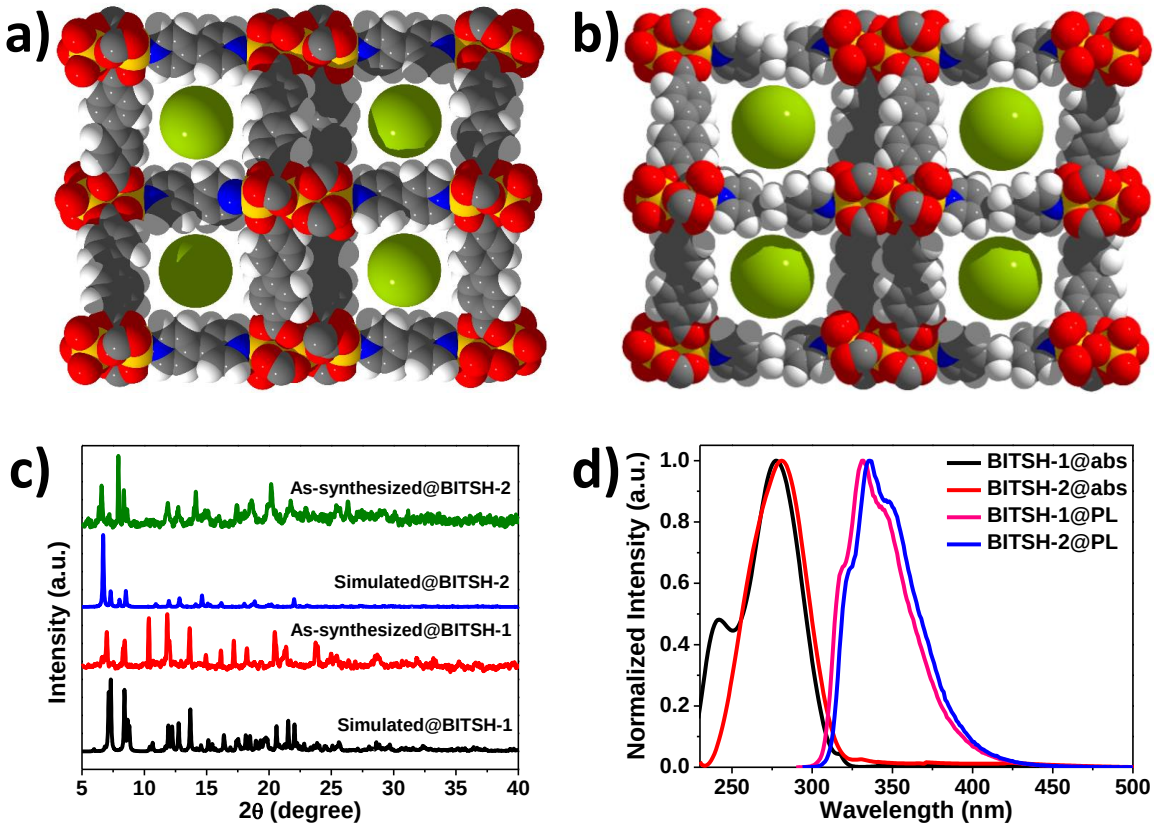

Figure 6.1. Packing diagrams of (a) **BITSH-1** and (b) **BITSH-2** shown along the *c* axes, where cobalt, carbon, oxygen, nitrogen and hydrogen atoms are shown in yellow, dark grey, red, blue, and white colors, respectively. All the solvent molecules have been omitted for clarity. Green spheres represent the guest-accessible void space in both the MOFs. (c) comparison of simulated and experimental PXRD patterns of **BITSH-1** and **BITSH-2**, and (d) UV-vis absorption and emission spectra for **BITSH-1** and **BITSH-2** MOF crystals in ethanol.

Powder X-ray diffraction (PXRD) patterns were collected for the as-synthesized frameworks and matched well with the simulated patterns, indicating the bulk phase purity of the material **(Figure 6.1c)**. Both these mixed-linker MOFs produced excellent block-shaped crystals with sizes ranging from 40 µm to 220 µm **(Figure 6.2a, b)**. The thermal stability of **BITSH-1** and **BITSH-2** frameworks were analyzed using TGA from 30 °C to 800 °C under a N_2 atmosphere. The MOFs are thermally stable up to 350 °C **(Figure 6.2c, d)**.

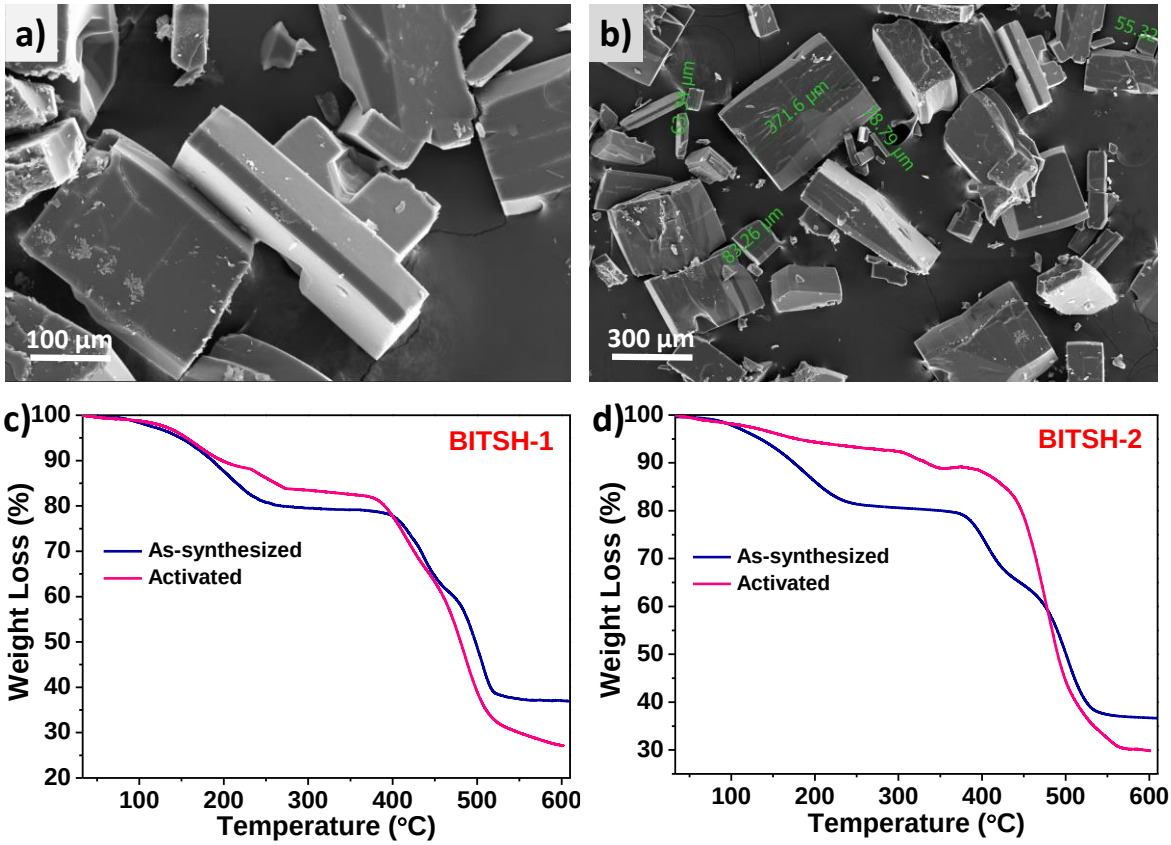

Figure 6.2. SEM images of as-synthesized (a) **BITSH-1** crystals and (b) **BITSH-2** crystals. TGA analysis of as-synthesized (blue) and activated (pink) (c) **BITSH-1** crystals, (d) **BITSH-2** crystals.

Before the N_2 measurements, the crystals were desolvated by activating at 90 °C in the vacuum oven for 24 h. The BET surface area values are nearly 330 $m^2 g^{-1}$ and 734 $m^2 g^{-1}$ for **BITSH-1** and **BITSH-2**, respectively **(Figure 6.3a, b)** with both the frameworks exhibiting pore diameters of approximately 8 Å **(Figure 6.3c, d)**. X-ray Photoelectron Spectroscopy (XPS) analysis was carried out for both **BITSH-1** and **BITSH-2**, and the XPS survey confirms the presence of Co, C, N, and O elements in both the frameworks. Co 2p XPS spectrum of both the frameworks show that Co is present as Co^{2+} with characteristic Co $2p_{1/2}$ and Co $2p_{3/2}$ binding energy peaks at 781.5 eV peak at 797 eV **(Figure 6.3e-h)**.

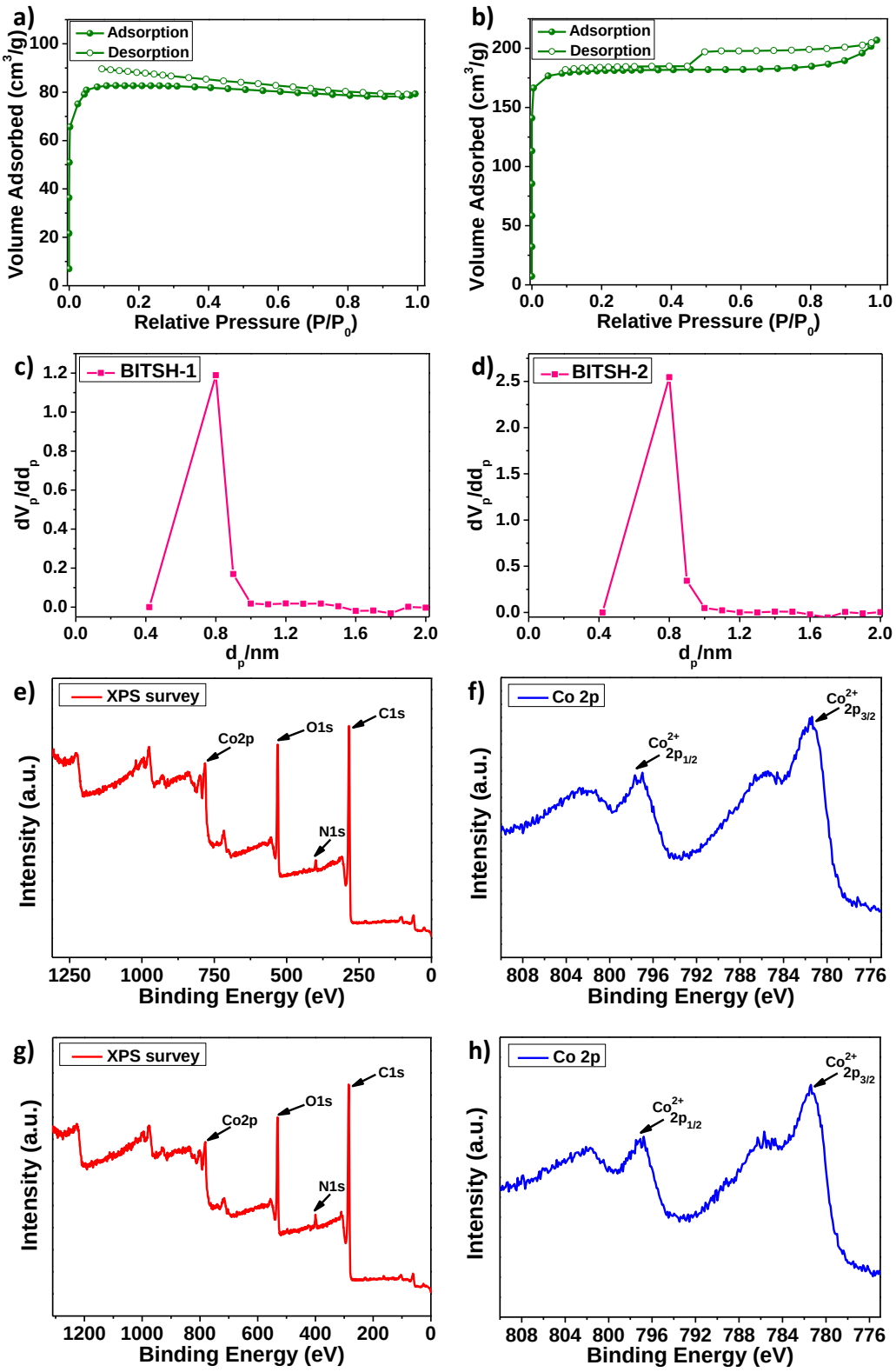

Figure 6.3. N_2 adsorption isotherm of activated crystals of (a) **BITSH-1** and (b) **BITSH-2** and corresponding pore diameter of (c) **BITSH-1** and (d) **BITSH-2** crystals collected at 77 K, (e) XPS survey spectrum of **BITSH-1** crystals and its corresponding (f) Co 2p XPS spectrum exhibiting the presence of Co^{2+} (g) XPS survey spectrum of **BITSH-2** crystals and its corresponding (h) Co 2p XPS spectrum exhibiting the presence of Co^{2+}.

6.3.2. Photoluminescence Studies

BITSH-1 shows a strong UV absorption band at 278 nm with an emission around 331 nm, and **BITSH-2** displays absorption around 280 nm with an emission around 336 nm **(Figure 6.1d)**. The sensing studies were carried out using both aliphatic and aromatic amines, namely, ammonia (NH_3), methylamine (MA), triethylamine (TEA), aniline (AN), and N-methylaniline (N-MA). The fluorescence sensing experiments were conducted in a systematic way where the emission spectra of the MOFs were first recorded in an ethanol medium, followed by the incremental addition of 0.1 M analyte solution in ethanol. Interestingly, the MOF materials' fluorescence intensity was quenched by more than 90 % upon adding only 5 mM of ammonia solution **(Figure 6.4b)**. The results were even more pronounced with a substituted amine such as methylamine that showed almost complete quenching with the addition of just 0.25 mM solution **(Figure 6.5f)**. The quenching efficiencies of the aliphatic amines are in the order TEA (95.45 %) > MA (94.4 %) > NH_3 (94.14 %) for **BITSH-1**, and MA (94.7 %) ≥ TEA (94.5 %) > NH_3 (80 %) for **BITSH-2 (Figure 6.13f, Figure 6.4-6.7** and **Table 6.1)**. This follows the trend of decreasing basicity of amines which indicates that amines with stronger electron-donating ability can quench the fluorescence intensity of the MOFs strongly.

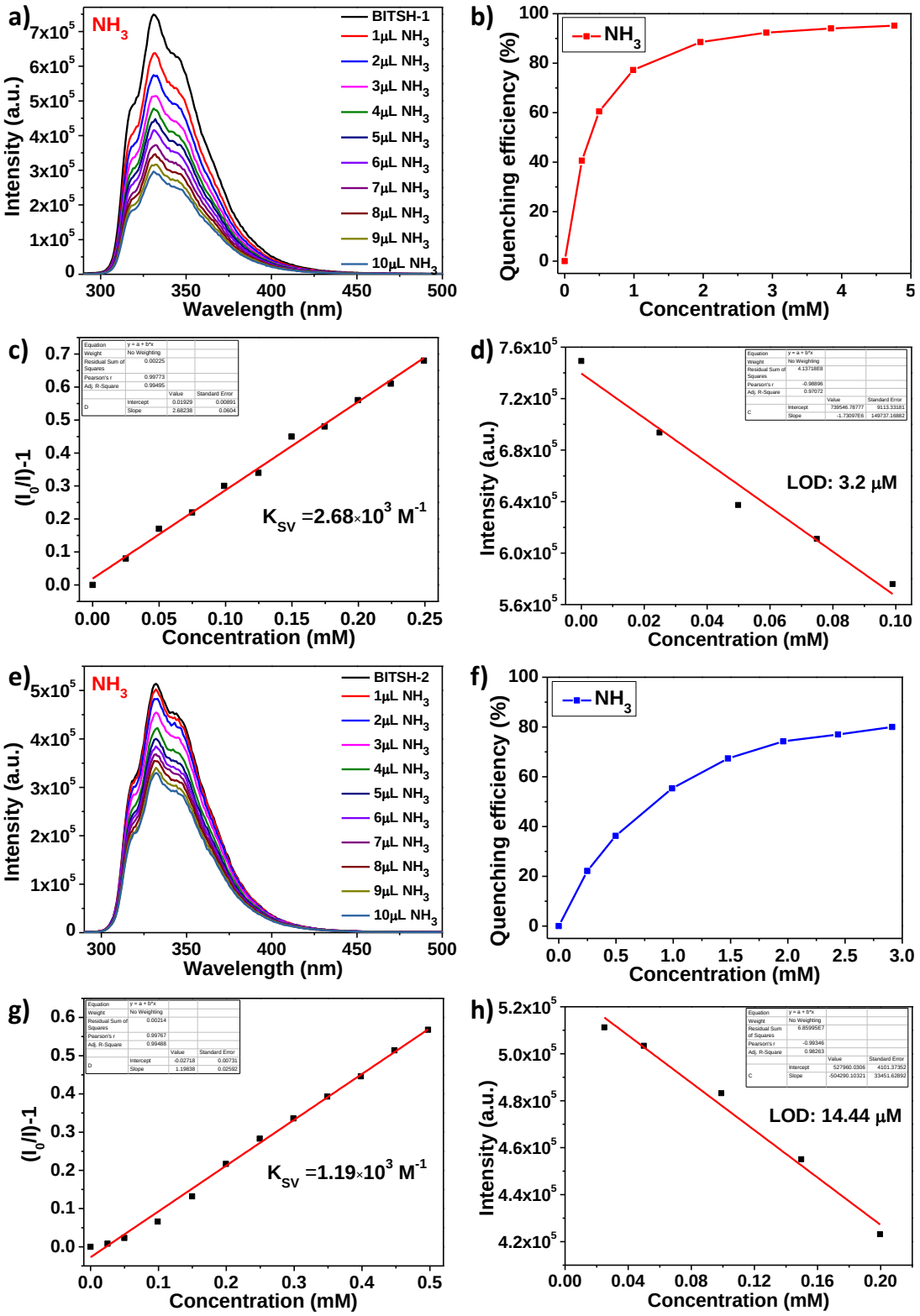

Figure 6.4. Emission spectra of (a) **BITSH-1** and (e) **BITSH-2** recorded upon the incremental additions of 10^{-1} M of Ammonia (NH_3) in ethanol medium. Quenching efficiency of (b) **BITSH-1** and (f) **BITSH-2** on addition of NH_3. Linear stern-Volmer plot of (c) **BITSH-1** and (g) **BITSH-2** fluorescence intensity against the addition of NH_3. Detection limit (LOD) obtained on addition of NH_3 to (d) **BITSH-1** and (h) **BITSH-2**.

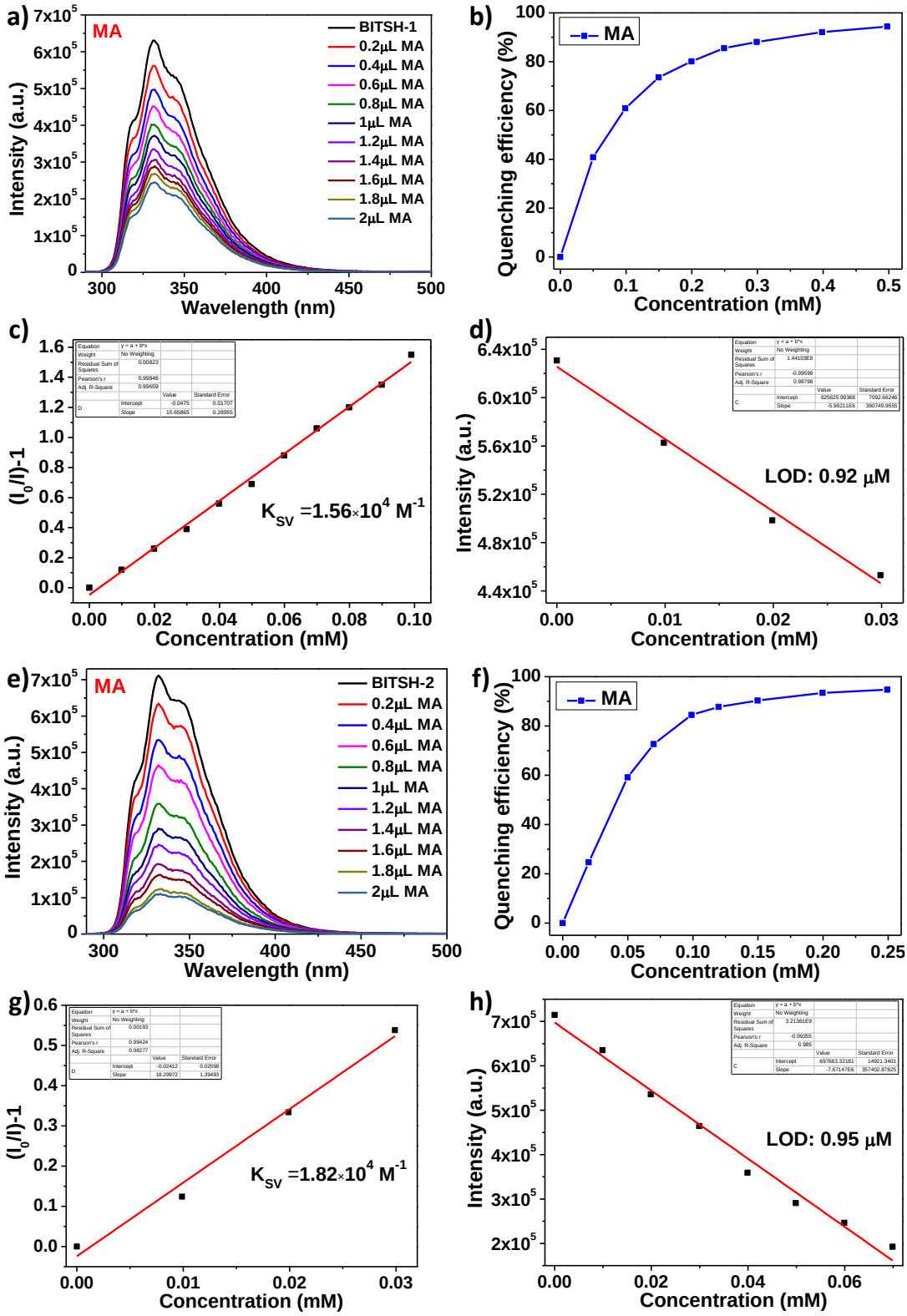

Figure 6.5. Emission spectra of (a) **BITSH-1** and (e) **BITSH-2** recorded upon the incremental additions of 10^{-1} M of Methylamine (MA) in ethanol medium. Quenching efficiency of (b) **BITSH-1** and (f) **BITSH-2** on addition of MA. Linear stern-Volmer plot of (c) **BITSH-1** and (g) **BITSH-2** fluorescence intensity against the addition of MA. Detection limit (LOD) obtained on addition of MA to (d) **BITSH-1** and (h) **BITSH-2**.

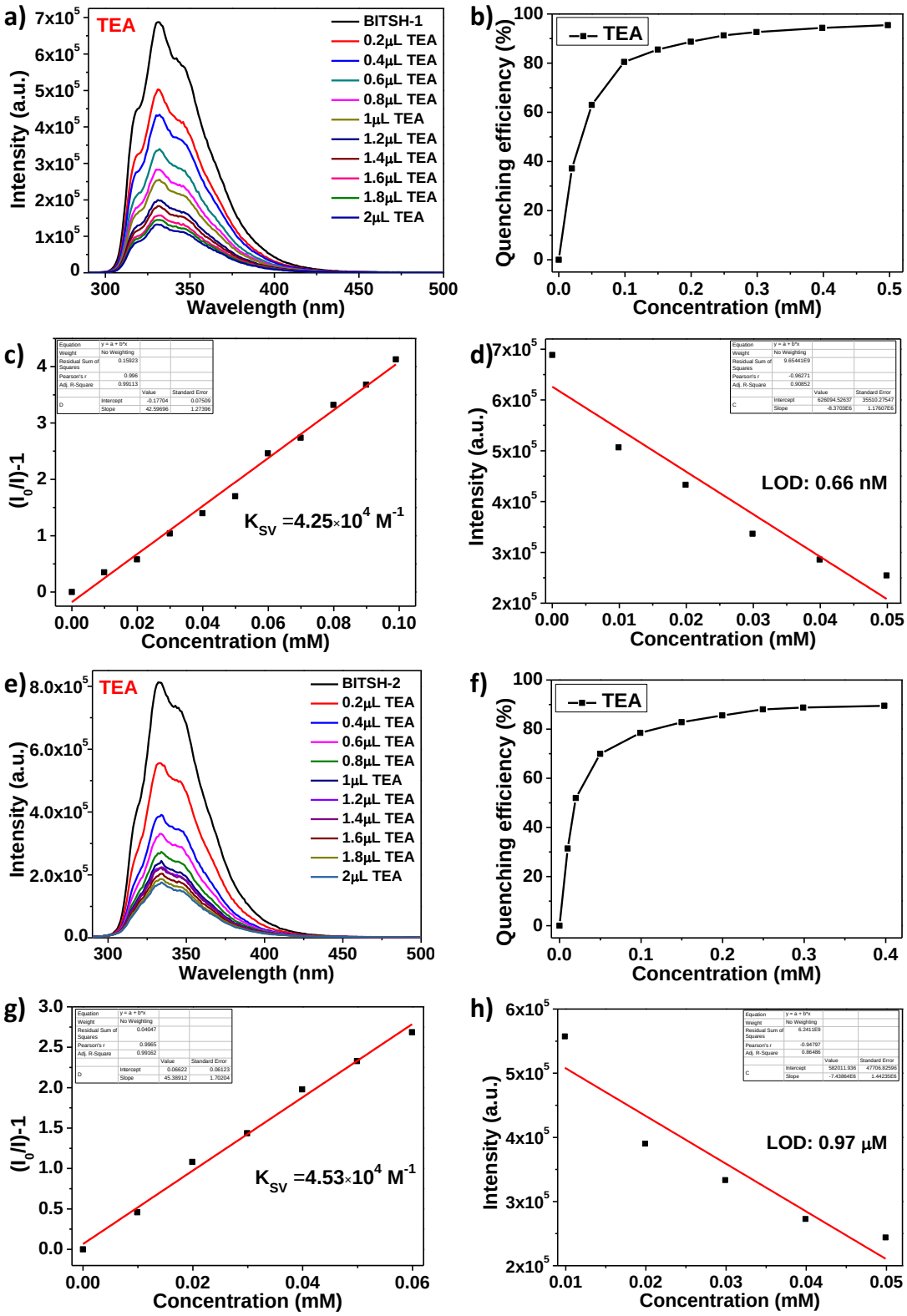

Figure 6.6. Emission spectra of (a) **BITSH-1** and (e) **BITSH-2** recorded upon the incremental additions of 10^{-1} M of Triethylamine (TEA) in ethanol medium. Quenching efficiency of (b) **BITSH-1** and (f) **BITSH-2** on addition of TEA. Linear stern-Volmer plot of (c) **BITSH-1** and (g) **BITSH-2** fluorescence intensity against the addition of TEA. Detection limit (LOD) obtained on addition of TEA to (d) **BITSH-1** and (h) **BITSH-2**.

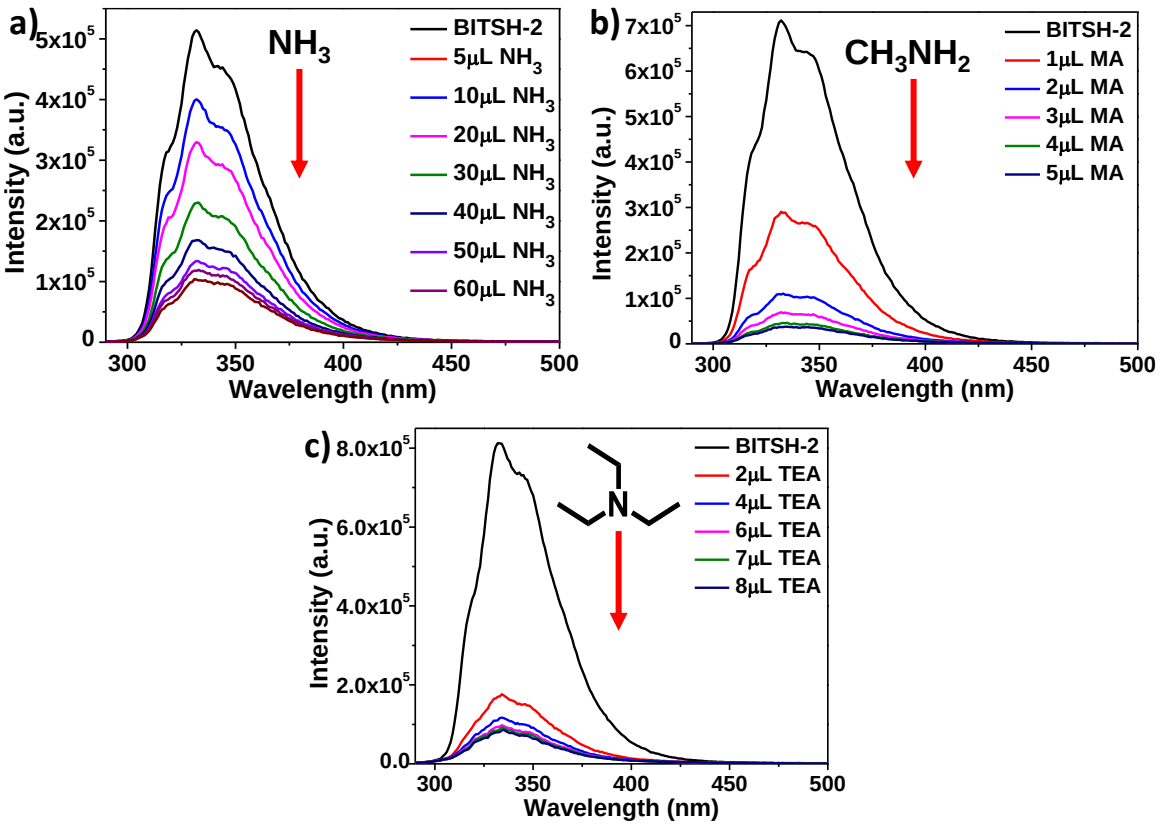

Figure 6.7. Photoluminescence emission spectra of **BITSH-2** showing quenching upon the incremental additions of 10^{-1}M of (a) Ammonia (NH_3) (b) Methylamine (MA) and (c) Triethylamine (TEA) in ethanol medium.

Table 6.1. Quenching efficiency (QE) of aliphatic amines analyzed for the study.

Amines	BITSH-1 (QE)	BITSH-2 (QE)
Triethylamine (TEA)	95.45 %	94.5 %
Methylamine (MA)	94.4 %	94.7 %
Ammonia (NH_3)	94.14 %	80 %

6.3.3. Studies to support dynamic quenching mechanism

To analyse the underlying quenching mechanism, a detailed analysis of the photoluminescence emission studies was carried out. K_{SV} values were obtained from the linear region of the Stern-Volmer plot i.e. $(I_0/I)-1 = K_{SV}[Q]$,[29] where I_0 and I are the initial and final fluorescence intensity of the MOF before and after the addition of the analyte with molar concentration respectively and K_{SV} stands for Stern-Volmer constant. The obtained K_{SV} value is in the range

of 10^3 M^{-1} to 10^4 M^{-1} which indicates the dynamic quenching process as $K_q \leq 10^{10}$.[30] Lifetime studies could not be carried out to support the dynamic process further as the suitable wavelength LED excitation source was unavailable. However, temperature-dependent studies were carried out which showed that on increasing the temperature from 288 K to 298 K and 308 K, there is an increase in the dynamic constant value (K_D), confirming the dynamic behavior[30] **(Figure 6.8-6.9** and **Table 6.2)**.

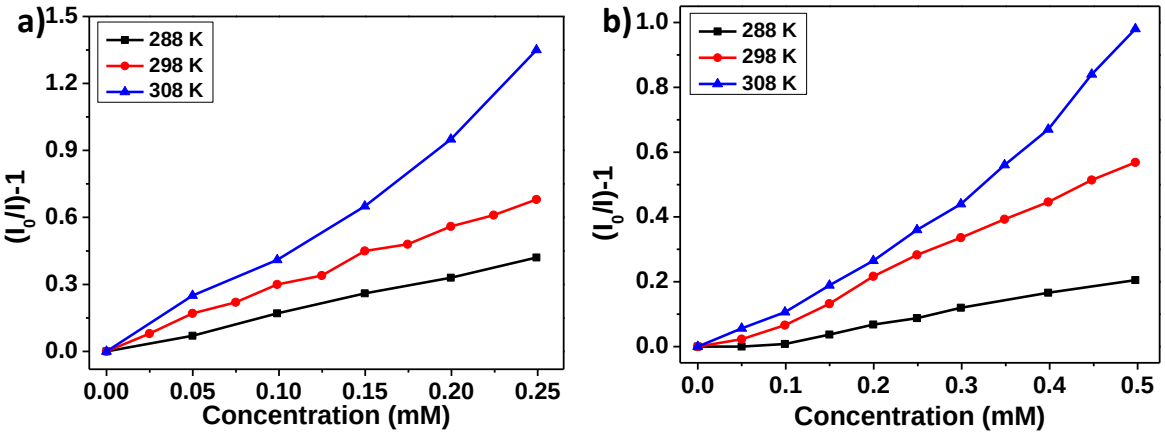

Figure 6.8. Stern-Volmer plots of **(a) BITSH-1** and **(b) BITSH-2** that were obtained upon the addition of NH_3 solution (10^{-1}M), recorded at 288 K, 298 K and 308 K temperatures.

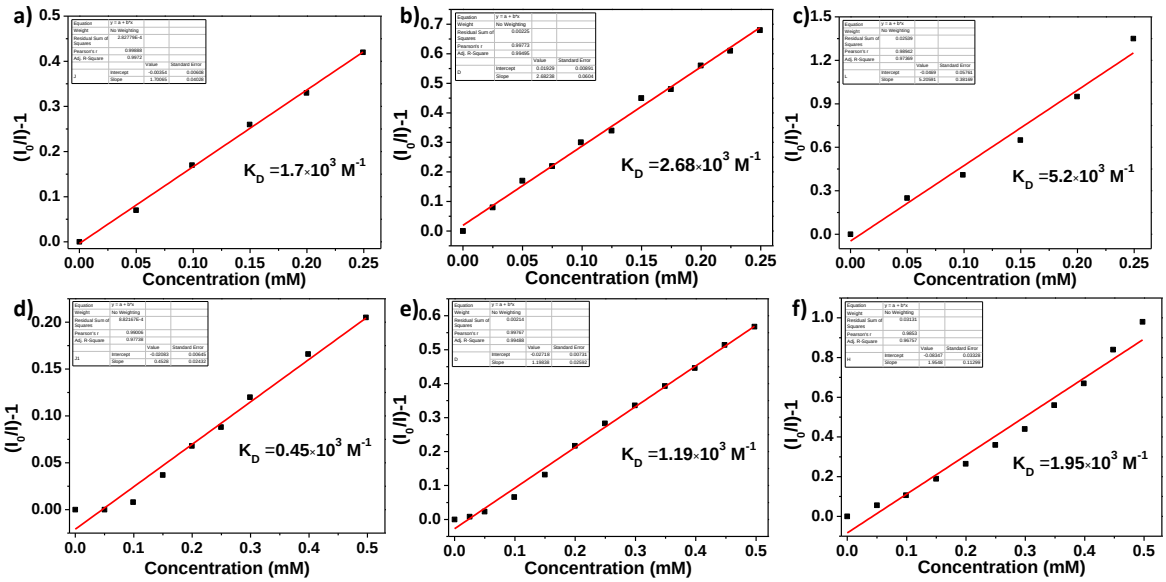

Figure 6.9. Linear fitting of Stern-Volmer plots in the concentration range of 0-0.25 mM upon addition of NH_3 solution (10^{-1}M) to **BITSH-1** and **BITSH-2** recorded at three different temperatures ranging from (a, d) 288 K, (b, e) 298 K and (c, f) 308 K respectively.

Table 6.2. Dynamic constant (K_D) values of **BITSH-1** and **BITSH-2** that were obtained upon the addition of NH_3 solution (10^{-1}M) at different temperatures ranging from 288 K to 308 K.

Temperature (K)	BITSH-1 K_D (M^{-1})	BITSH-2 K_D (M^{-1})
288 K	1.7×10^3	0.45×10^3
298 K	2.68×10^3	1.19×10^3
308 K	5.2×10^3	1.95×10^3

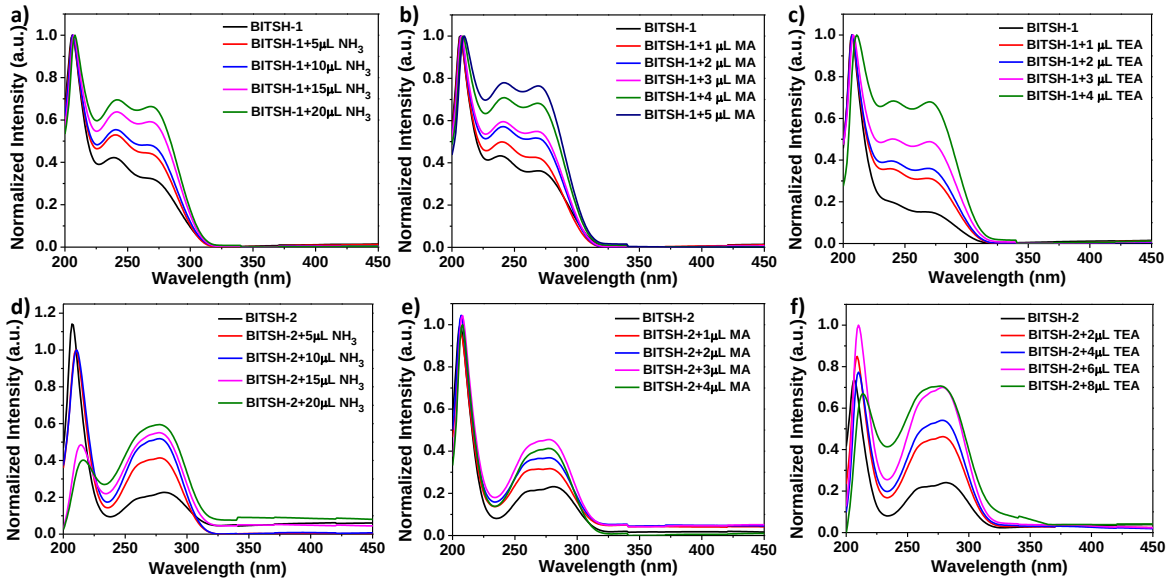

Figure 6.10. UV-vis absorption spectra of **BITSH-1** and **BITSH-2** upon incremental additions of (a, d) Ammonia (NH_3) solution, (b, e) Methylamine (MA) and (c, f) Triethylamine (TEA) in ethanol medium respectively.

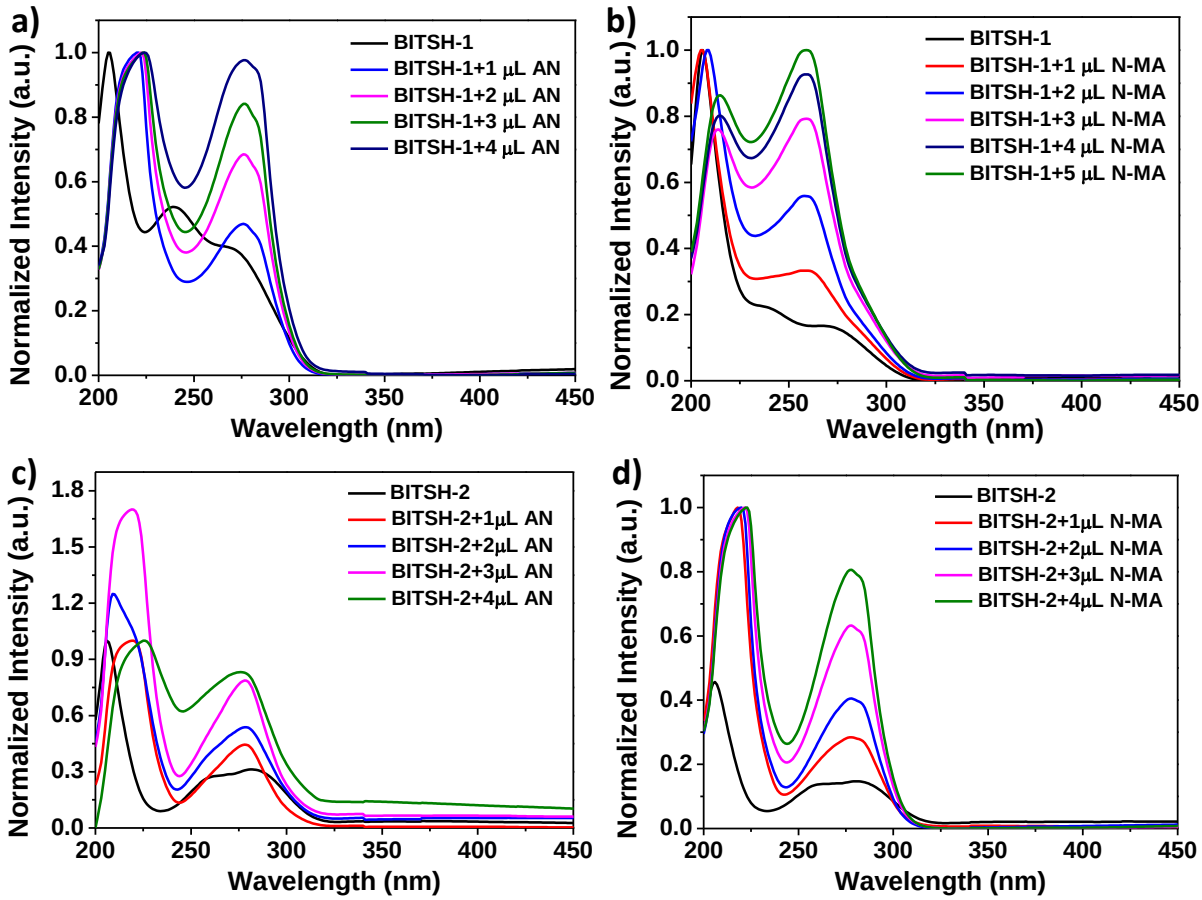

Figure 6.11. UV-vis absorption spectra of **BITSH-1** and **BITSH-2** upon incremental additions of (a, c) Aniline (AN) solution and (b, d) N-methylaniline **(N-MA)** solution in ethanol medium respectively.

Furthermore, absorption spectra of both the frameworks were recorded with the addition of the analytes, but no blue or red shift was observed in the spectra **(Figure 6.10-6.11)**. This ruled out the static quenching process due to the absence of ground-state complex formation. The quenching phenomenon can be ascribed to the electron transfer process, which can be either resonance-induced electron transfer (RET) or photoinduced electron transfer (PET) process. The emission spectrum of the MOF and absorption spectra of the analytes were checked for spectral overlap, but there is an absence of any spectral overlap **(Figure 6.12)**. This eliminated the possibility of RET operating in this case. The excellent sensing abilities of both the frameworks in sensing amines could be due to photoinduced electron transfer (PET) process and the host-guest interactions between aliphatic amines and the MOFs.

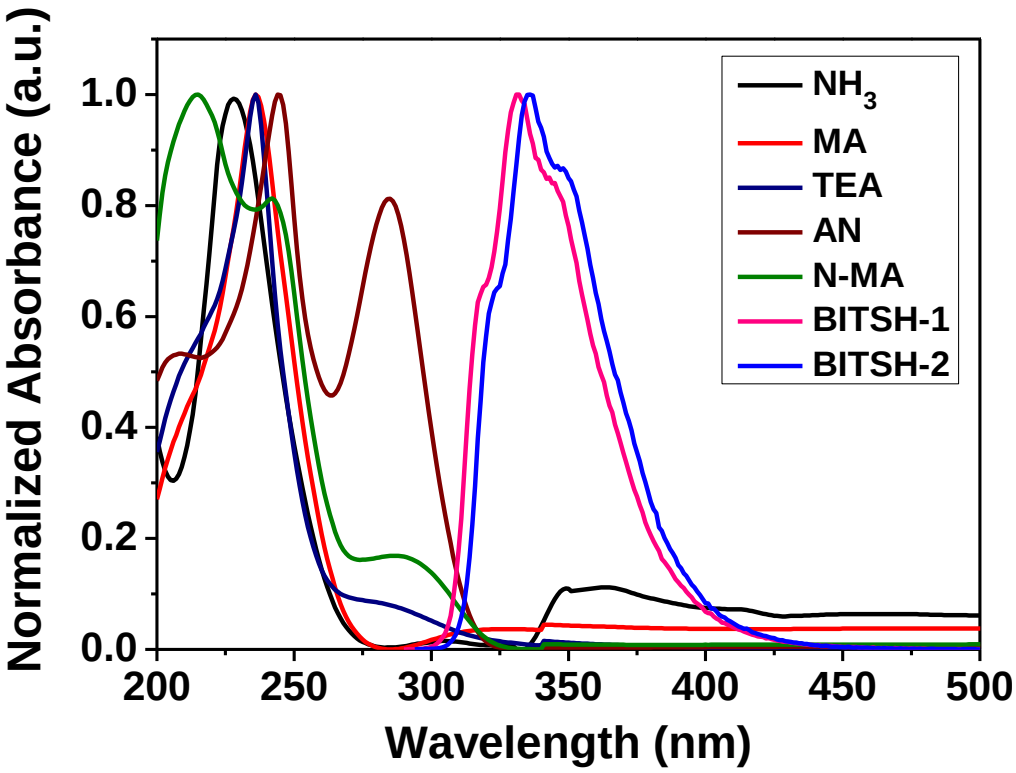

Figure 6.12. Spectral overlap between the absorption spectra of aliphatic and aromatic amines analyzed for the study and the emission spectra of **BITSH-1** and **BITSH-2.**

6.3.4. Turn-on fluorescence studies and Limits of Detection (LOD) calculations

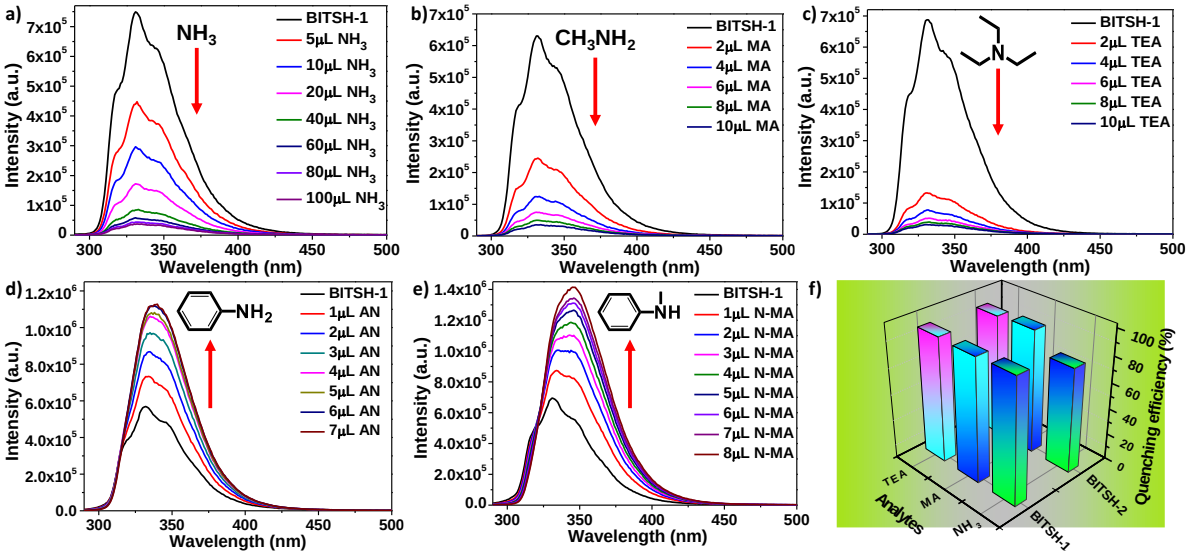

Figure 6.13. Fluorescence sensing experiments of **BITSH-1** MOF showing quenching of fluorescence intensity with aliphatic amines a) NH_3, b) methylamine, and c) triethylamine and enhancement of fluorescence intensity with aromatic amines, d) aniline, e) N-methylaniline, and f) bar graph showing quenching efficiencies of both the MOFs with aliphatic amines.

Remarkably, there was an increase in the fluorescence intensity on gradual additions of aromatic amines such as aniline, and N-methylaniline **(Figure 6.13).** The fluorescence enhancement was more in the case of N-methylaniline than aniline, probably due to higher electron transfer capability and strong interactions of N-methylaniline with the MOF frameworks. It is noteworthy that the example of same MOF showing both "turn-off" and "turn-on" discriminative sensing behavior is very rare **(Table 6.3)**.

Table 6.3. State of the art of discriminative sensing of amines.

Material	Selectivity	Detection limit	Ref.
Conjugated Porous polymers (CPPs) P1 and P2	Aliphatic amines (turn on) and aromatic amines (turn off)	Aniline (81 nM), MA (93 nM), TEA (43 nM)	**[31]**
Conjugated polymer	Aliphatic amines (turn on) and aromatic amines (turn off)	Aniline (0.64 mM)	**[32]**
Zr(IV) based MOF	Aliphatic amines (turn on) and aromatic amines (turn off)	Aniline (160 nM), MA (66.2 nM) TEA (259 nM)	**[10]**

The limits of detection (LODs) were calculated using the formula $3\sigma/k$,[33] where σ is the standard deviation calculated from five blank readings of the MOF and k represents the slope obtained from the plot of intensity vs. concentration of analyte [Q] plot. The LODs calculated for aromatic amines N-MA and AN are 2.29 µM and 2.28 µM for **BITSH-1** and 1.12 µM and 1.92 µM for **BITSH-2**, respectively **(Figure 6.14** and **Table 6.4)**. Similarly, the LODs obtained for TEA, MA, and NH_3 are 0.66 µM, 0.92 µM, and 3.2 µM for **BITSH-1** and 0.97 µM, 0.95 µM, and 14.4 µM for **BITSH-2**, respectively. The low LOD values prove that both MOFs can discriminately sense aliphatic and aromatic amines **(Table 6.5)**.

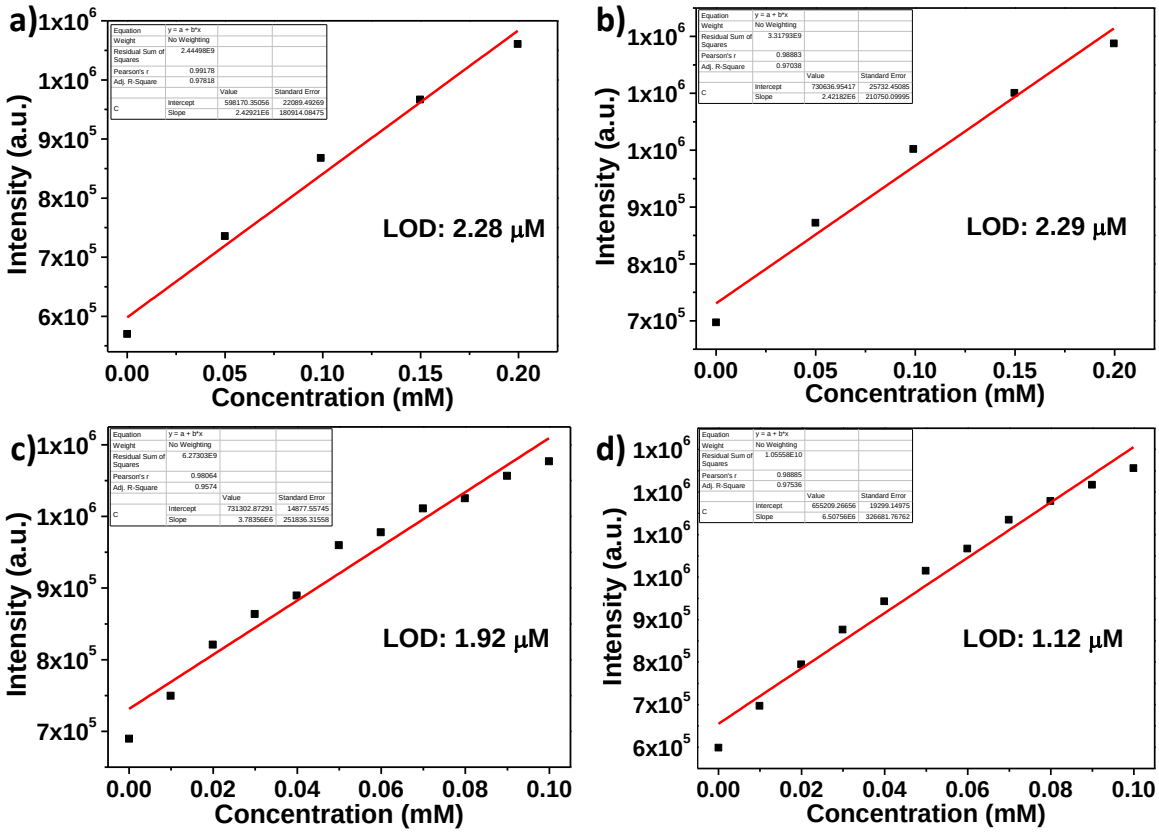

Figure 6.14. Detection limit (LOD) obtained from the linear fit of Intensity Vs [Q] plot of **BITSH-1** (top) upon additions of (a) Aniline (AN) and (b) N-methylaniline (N-MA) and **BITSH-2** (bottom) upon additions of (c) Aniline (AN) and (d) N-methylaniline (N-MA) solutions in ethanol medium.

Table 6.4. Detection limit (LOD) of aliphatic and aromatic amines analyzed.

Amines	BITSH-1	BITSH-2
Ammonia (NH_3)	3.2 µM, 54 ppb	14.4 µM, 245 ppb
Methylamine (MA)	0.92 µM, 28 ppb	0.95 µM, 29 ppb
Triethylamine (TEA)	0.66 µM, 66 ppb	0.97 µM, 98 ppb
Aniline (AN)	2.28 µM, 212 ppb	1.92 µM, 178 ppb
N-Methylaniline (N-MA)	2.29 µM, 245 ppb	1.12 µM, 120 ppb

Table 6.5. Comparison of fluorescence response and their detection limits of different MOFs used for sensing ammonia.

Material	Response type	Detection limit	Membrane/ Substrate	Ref.
MIL-124@Eu^{3+}	Solid-state Fluorescence Quenching	26.2 ppm	Al_2O_3 substrate	**[34]**
SNNU-88	Solution-state Fluorescence Quenching	1.5 ppm	Ag-Pd substrate	**[35]**
Ln(TTA/TAA)@UMOF	Solid-state Fluorescence Quenching	9 ppm	Linker-modified Al_2O_3 substrate	**[36]**
Zn_2(TCPE)	Turn-on fluorescence	-	-	**[37]**
ZnQ@Zn-BTC	Solid-state Fluorescence Quenching	1 ppb	Nano-discs	**[38]**
ZrUiO-68(bod)	Turn-on fluorescence	6.5 ppb	Paper strips	**[39]**
BITSH-1	**Solution-state Fluorescence Quenching**	**0.054 ppm**	**MOF membranes**	**This work**

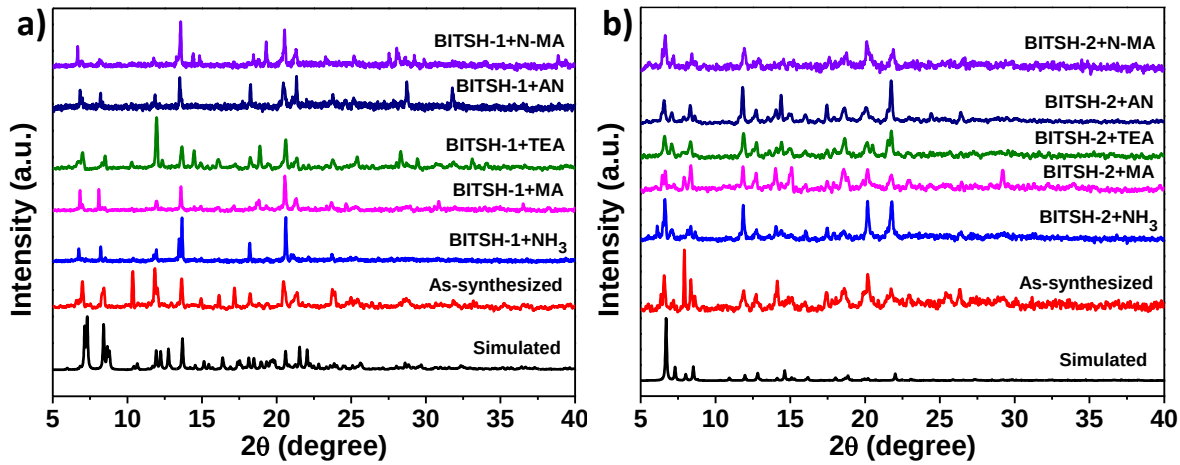

Figure 6.15. PXRD patterns of (a) **BITSH-1** and (b) **BITSH-2** in the presence of aliphatic amines and aromatic amines showing the structural integrity of the framework.

6.3.5. X-Ray photoelectron spectroscopy (XPS) studies for the detection of amines

Furthermore, the stability of the MOF samples upon exposure to amines was checked through PXRD. Both the frameworks retained the crystallinity and structural integrity on interaction with analytes. The MOF crystals retain their characteristic peaks after fluorescence experiments **(Figure 6.15)**. The MOF samples after the fluorescence experiments were also investigated for the presence of amines by XPS. N 1s spectral analysis reveals the presence of amines due to characteristic amine peak for the N-H group present in ammonia, primary, and secondary amines, and the C-N group present in tertiary amine around 400.2 eV and 400.8 eV, respectively along with the peak for C-N-C groups around 399.5 eV in the MOF system.[40,41] Whereas pristine frameworks don't show the presence of any characteristic amine peak **(Figure 6.16-6.20)**.

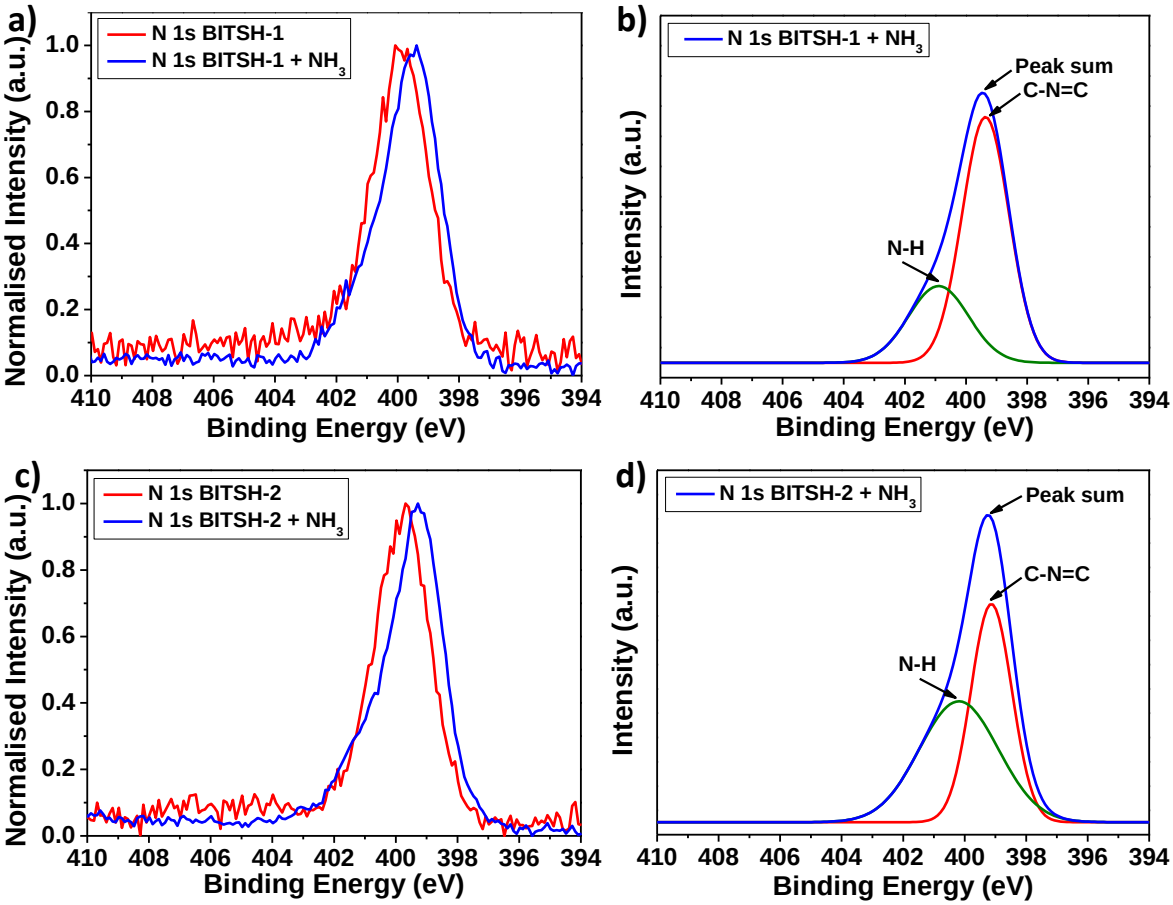

Figure 6.16. (a) N 1s XPS spectral analysis of pristine **BITSH-1** and in the presence of Ammonia (NH_3) (b) Deconvoluted N 1s spectrum of **BITSH-1 + NH_3**. (c) N 1s XPS spectral analysis of pristine **BITSH-2** and in the presence of Ammonia (NH_3) (d) Deconvoluted N 1s spectrum of **BITSH-2 + NH_3**.

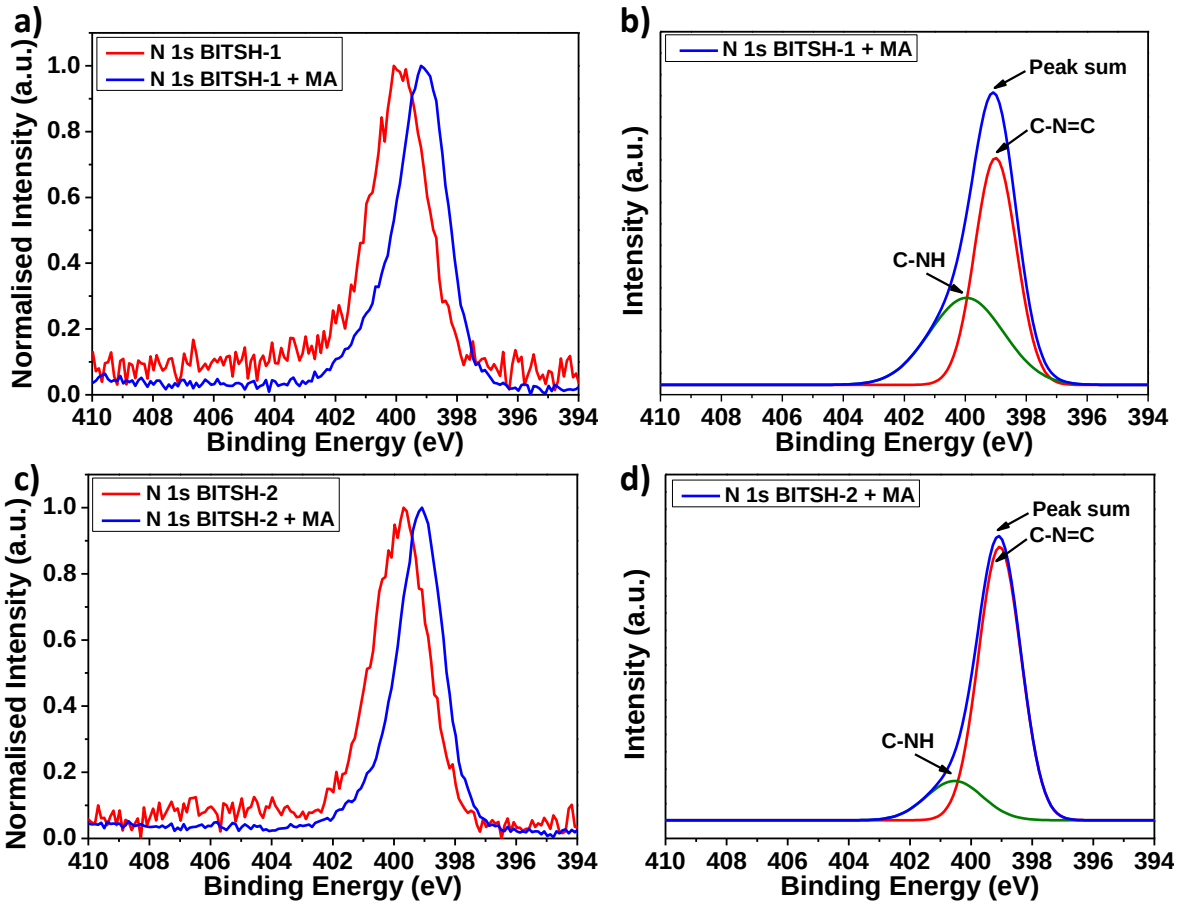

Figure 6.17. (a) N 1s XPS spectral analysis of pristine **BITSH-1** and in the presence of Methylamine (MA) (b) Deconvoluted N 1s spectrum of **BITSH-1 + MA**. (c) N 1s XPS spectral analysis of pristine **BITSH-2** and in the presence of Methylamine (MA) (d) Deconvoluted N 1s spectrum of **BITSH-2 + MA**.

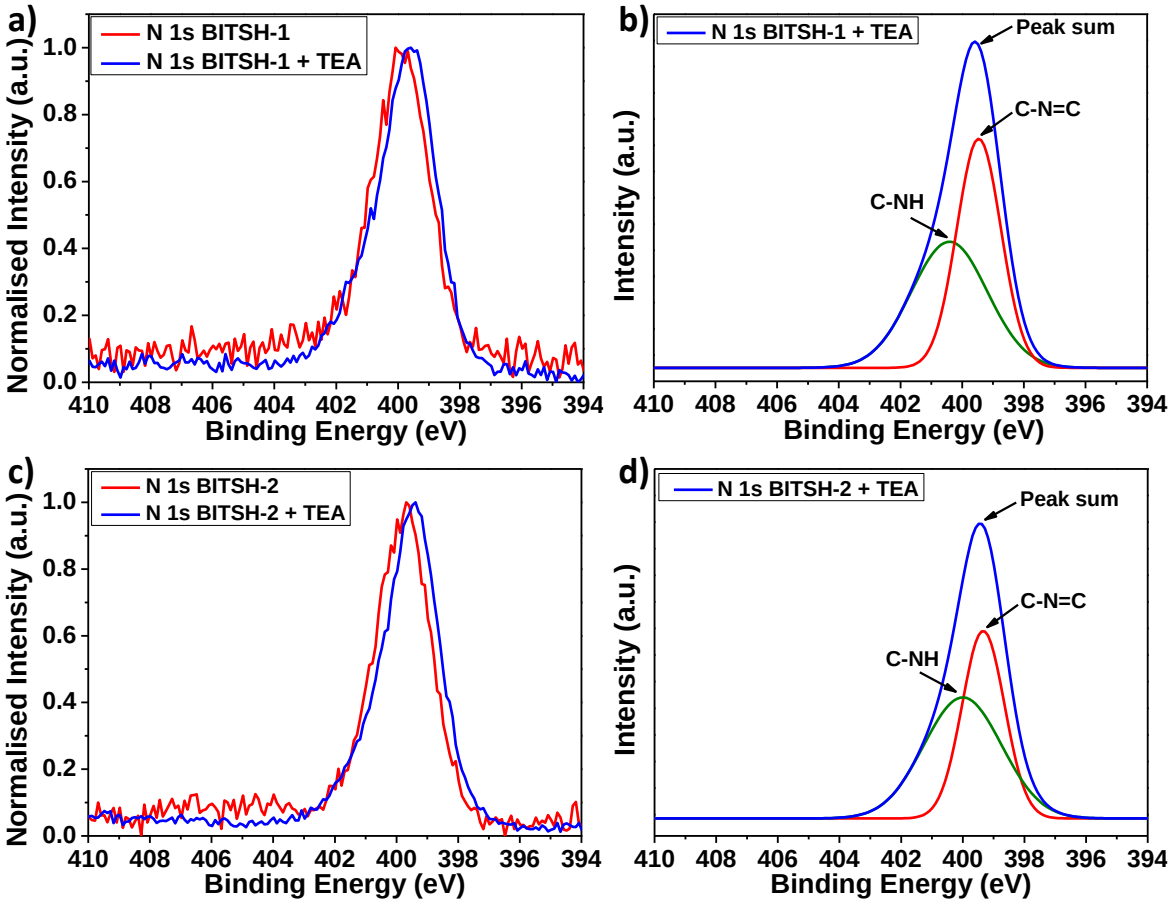

Figure 6.18. (a) N 1s XPS spectral analysis of pristine **BITSH-1** and in the presence of Triethylamine (TEA) (b) Deconvoluted N 1s spectrum of **BITSH-1 + TEA**. (c) N 1s XPS spectral analysis of pristine **BITSH-2** and in the presence of Triethylamine (TEA) (d) Deconvoluted N 1s spectrum of **BITSH-2 + TEA**.

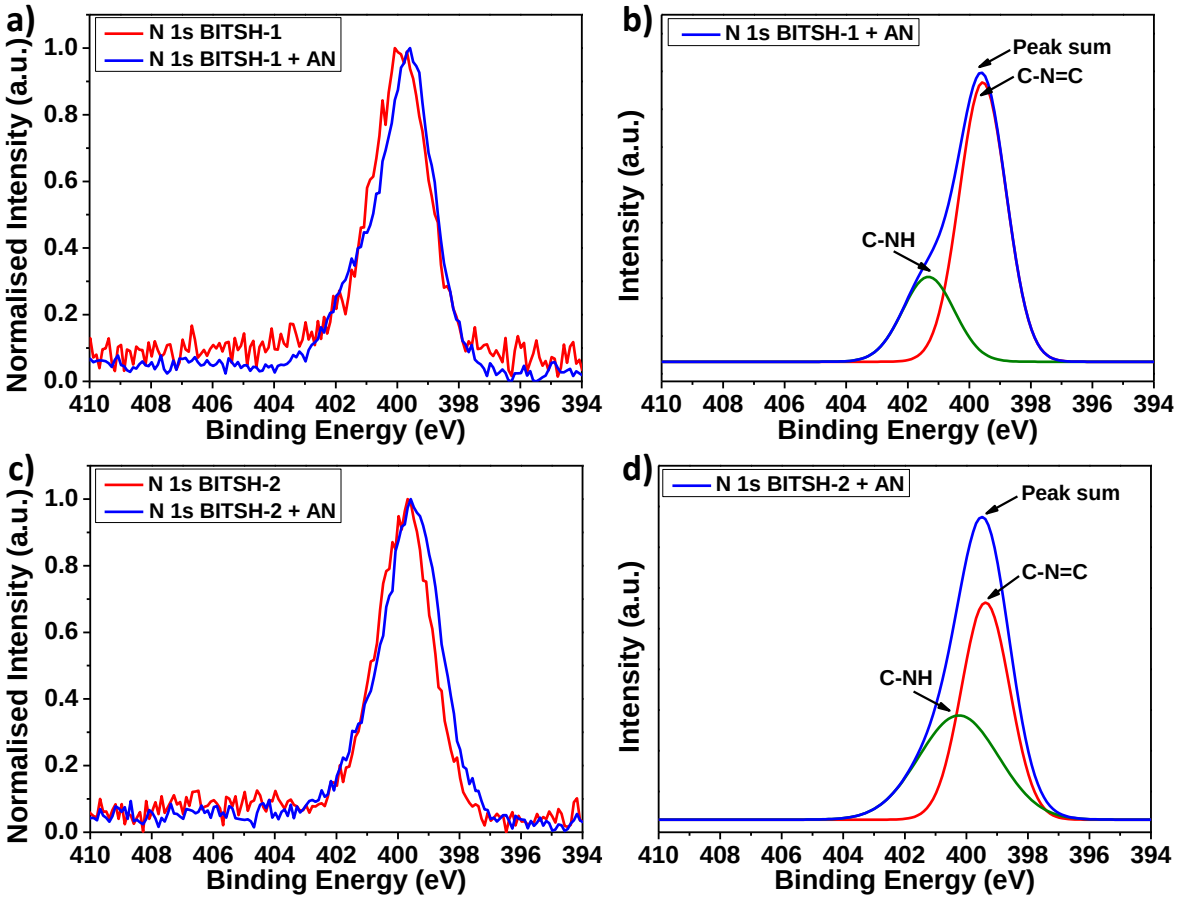

Figure 6.19. (a) N 1s XPS spectral analysis of pristine **BITSH-1** and in the presence of Aniline (AN) (b) Deconvoluted N 1s spectrum of **BITSH-1 + AN**. (c) N 1s XPS spectral analysis of pristine **BITSH-2** and in the presence of Aniline (AN) (d) Deconvoluted N 1s spectrum of **BITSH-2 + AN**.

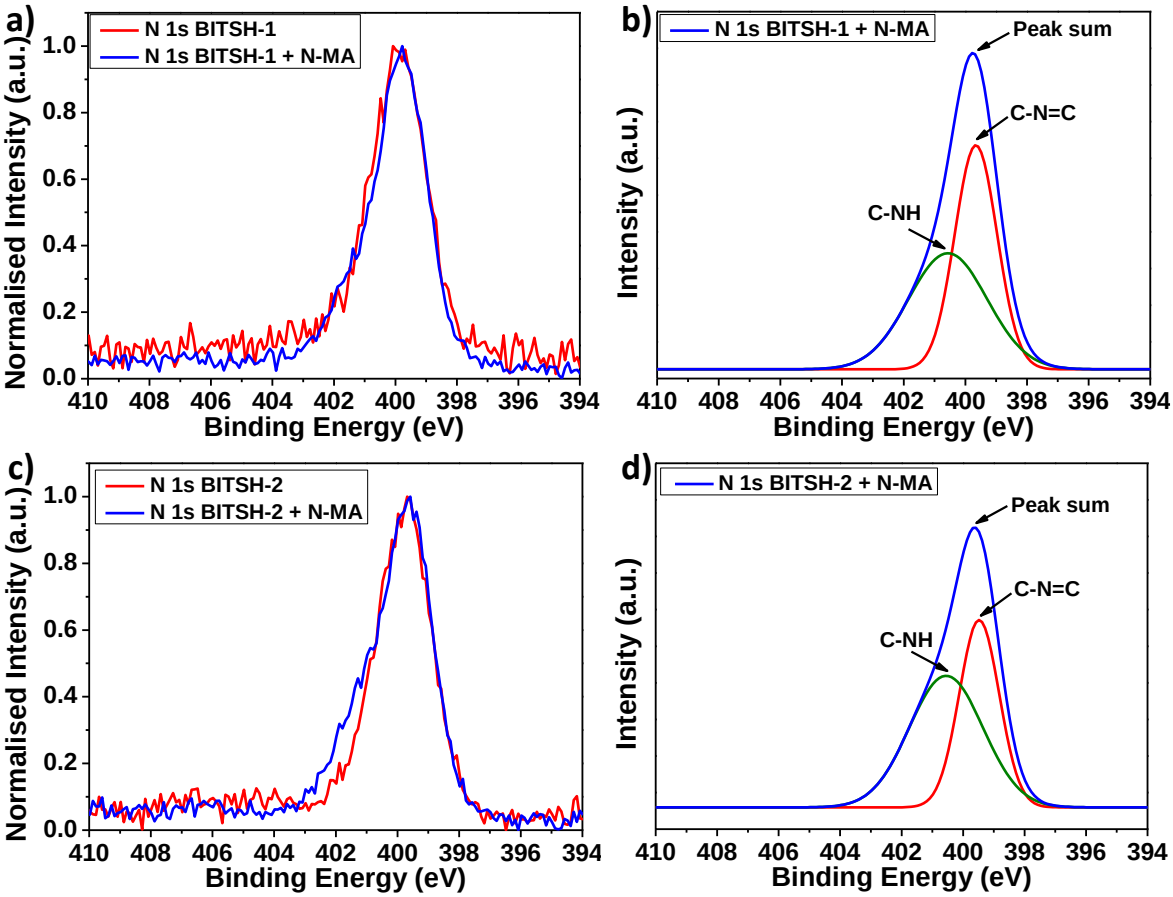

Figure 6.20. (a) N 1s XPS spectral analysis of pristine **BITSH-1** and in the presence of N-Methylaniline (N-MA) (b) Deconvoluted N 1s spectrum of **BITSH-1 + N-MA**. (c) N 1s XPS spectral analysis of pristine **BITSH-2** and in the presence of N-Methylaniline (N-MA) (d) Deconvoluted N 1s spectrum of **BITSH-2 + N-MA**.

6.3.6. Vapochromic sensing

It is desired of a chemical sensor to detect an analyte in its vapor phase since the analyte concentration in the vapor phase is less than its solution or solid-state. A rapid detection of a harmful volatile compound can be particularly useful in detecting a leak. Amines are known to be highly volatile and these are mostly released as gas or vapor. Thus, it becomes essential to design vapochromic probes that can rapidly detect volatile organic amines (VOAs) with a clear colour change of the sensor material.

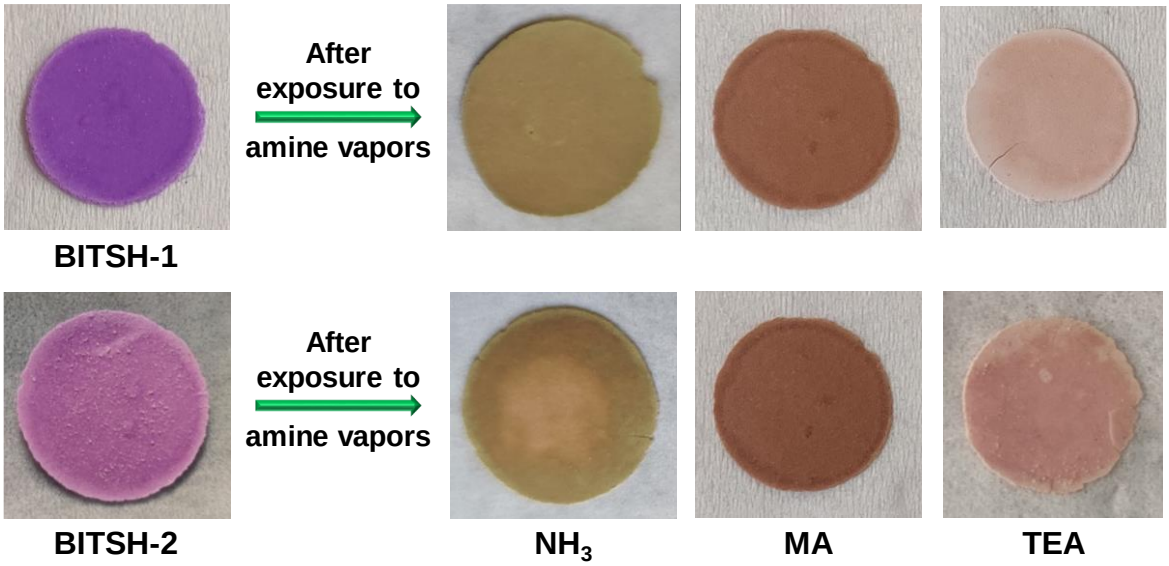

Figure 6.21. The visible change in the color of MOF pellets upon exposure to ammonia, methylamine (MA), and triethylamine (TEA).

Keeping this in mind, as-synthesized MOF crystals were used to prepare MOF pellets with a minimal quantity of KBr to stabilize the pellet. The MOF pellets were then placed inside a container and exposed to different amine vapours, namely ammonia, MA, and TEA. Interestingly, a rapid (≤ 1 min) and clear colour change in the MOF pellets was observed upon exposure to different amine vapours **(Figure 6.21)**. However, no colour change was observed in the case of aromatic amines such as aniline and n-methylaniline. This shows that both **BITSH-1** and **BITSH-2** have vapochromic properties.

6.3.7. Computational investigations and HOMO-LUMO studies

Density functional theory (DFT) calculations were carried out in conjunction with the experimental results to elucidate the underlying mechanism responsible for the identified discriminative sensing behavior of the frameworks with aliphatic and aromatic amines. The "turn-off" fluorescence in the case of aliphatic amines and "turn-on" fluorescence in the case of aromatic amines result from different electron transfer pathways operating in both cases. Both the frameworks' HOMO and LUMO energy levels were calculated using cyclic voltammetry **(Figure 6.22)**. The onset oxidation potential and reduction potential values obtained from CV measurements were used to calculate the HOMO and LUMO energy levels with the help of the following equation: E_{HOMO} = -e [$E_{ox\ onset}$ + 4.741] eV and E_{LUMO} = -e [$E_{red\ onset}$ + 4.741] eV.[42] Similarly, the band gap of **BITSH-1** and **BITSH-2** was calculated using the following formula: E_g = LUMO - HOMO and the band gap resulted as 2.6 eV for both the

frameworks. The HOMO and LUMO energy levels of both the frameworks were nearly the same, E_{HOMO} = -6.24 eV and E_{LUMO} = -3.64 eV, respectively.

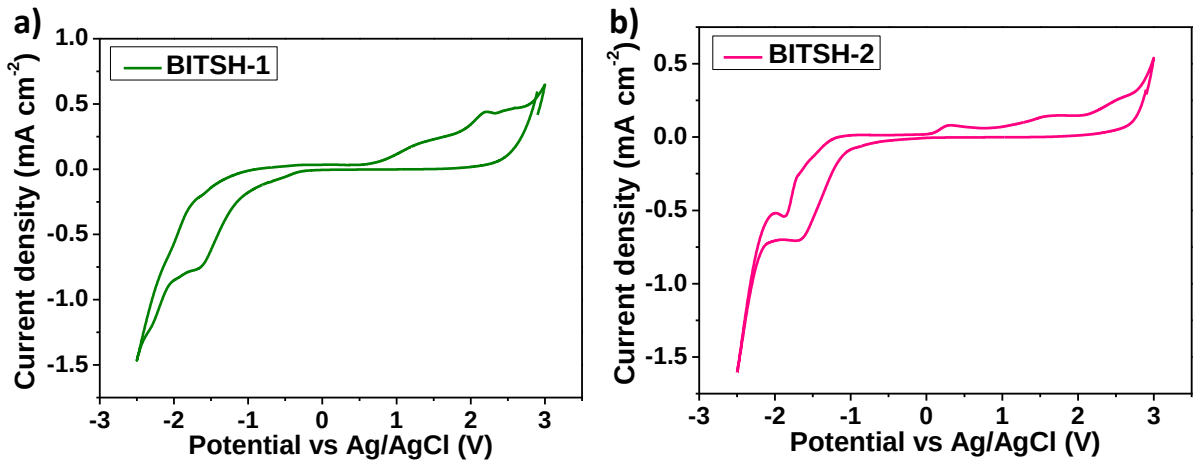

Figure 6.22. Cyclic Voltammetry plot of **(a) BITSH-1** and **(b) BITSH-2** obtained in acetonitrile medium with scan rate of 100 mV/s.

To understand the host-guest interactions between MOFs and analytes, we performed DFT calculations on the **BITSH-1**, analytes, and **BITSH-1** with analytes (NH_3 and aniline) as guest molecules. In all the calculations with **BITSH-1** metal-organic framework (MOF), the framework of MOF was fixed to an experimental structure. Multiple adsorption sites of ammonia and aniline were screened. It was noted that **BITSH-1** could favourably adsorb 8 molecules of ammonia and aniline with adsorption energies of -10.1 kcal/mol and -30.03 kcal/mol (per molecule), respectively. Notably, the adsorption energies of aniline are significantly more exothermic than ammonia even at the high loading of 8 molecules. Analogously, the adsorption energy (-12.46 kcal/mol, per molecule) for methyl amine at a loading of 8 molecules was found to be higher than ammonia but lower than aniline). We notice hydrogen bonding interaction with **BITSH-1** and aniline **(Figure 6.23a, b)** but ammonia interacts with MOF in a different manner **(Figure 6.23c)** where it is not found to be coordinating with any atom of **BITSH-1** within 3 Å. From computational studies, we identified the binding sites of the amine in **BITSH-1**. We note that the most preferred binding sites for ammonia and aniline are different due to differences in the nature of the interaction of aromatic and aliphatic amines with the MOF framework **(Figure 6.23)**.

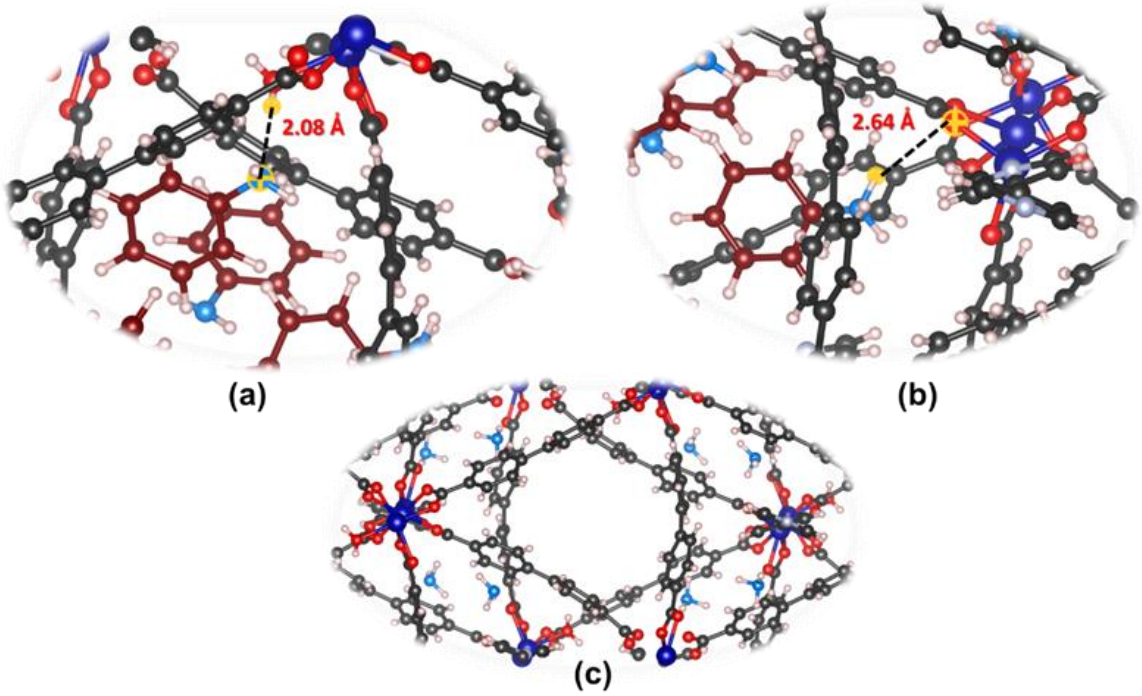

Figure 6.23. Zoom-in view optimized structure of AN@**BITSH-1** displaying the interaction of (a) a hydrogen bonding between the nitrogen of aniline and hydrogen of an H_2O molecule coordinated to a Co site of **BITSH-1** (b) a hydrogen bonding between the hydrogen of aniline and oxygen of COO- group coordinated to a Co site of **BITSH-1**. (c) Optimized structure of NH_3@**BITSH-1**, displaying no hydrogen binding (only weak dispersive interactions are expected). Colour codes C- Black, Co- blue, H- white, O- red, C of analytes- maroon and N of analytes- cyan.

Based on the alignment of frontier orbitals of analytes computed from DFT calculations and **BITSH-1**, it is expected that the interaction of the MOF with aliphatic amines involves electron transfer, primarily from the HOMO of analytes ($HOMO_{analyte}$) to the HOMO of the MOF ($HOMO_{MOF}$) due to the high energy HOMO of the analytes. The extent of electron transfer from $HOMO_{analyte}$ to $HOMO_{MOF}$ depends on the relative energy of $HOMO_{analyte}$ **(Figure 6.24)**, suggesting that the degree of electron transfer for aliphatic analytes follows the order TEA > MA > NH_3. Due to the increase in the electronic population of the $HOMO_{MOF}$ (as a result of electron transfer from analytes), quenching efficiencies of aliphatic amines are expected to follow an order TEA > MA > NH_3. Indeed, the electron transfer process is in good agreement with the experimental quenching efficiencies, which in turn follows the order of basicity of aliphatic amines i.e. TEA > MA > NH_3. Thus, TEA exhibits faster electron transfer than other analytes, such as MA and NH_3. Thus, the higher the HOMO energy level, the more facile is the

electron transfer.[9] This is attributed to the more significant energy difference between the HOMO levels of MOF and TEA compared to other analytes.

Table 6.6. HOMO and LUMO energy levels (in eV) of amines obtained from the computational studies.

Amines	E_{HOMO} (eV)	E_{LUMO} (eV)
Ammonia (NH_3)	-5.90	1.47
Methylamine (MA)	-5.2	1.56
Triethylamine (TEA)	-4.39	2.47
Aniline (AN)	-5.60	-0.88
N-Methylaniline (N-MA)	-4.41	-0.54

However, based on orbital alignment **(Figure 6.24)**, we noticed that in the case of aromatic amines, due to their relatively low-lying LUMOs, the electron transfer process occurs between the LUMO energy levels of the aromatic amines and LUMO energy levels of the MOF system **(Table 6.6)**. Specifically, it is expected that the interaction of MOFs with aromatic amines involves electron transfer primarily from the LUMO of the analytes ($LUMO_{analyte}$) to the LUMO of the MOF ($LUMO_{MOF}$). As the extent of electron transfer depends on the relative energy of the respective orbitals, the degree of electron transfer from $LUMO_{analyte}$ to $LUMO_{MOF}$ is expected to follow and order: N-MA > AN. In contrast to aliphatic analytes, the electron transfer from aromatic amines to MOF increases the population of the LUMO orbital of the MOF, which is expected to increase in fluorescence intensity. Interestingly, in line with computational results, the experimental increase in fluorescence intensity follows the same order (N-MA > AN).

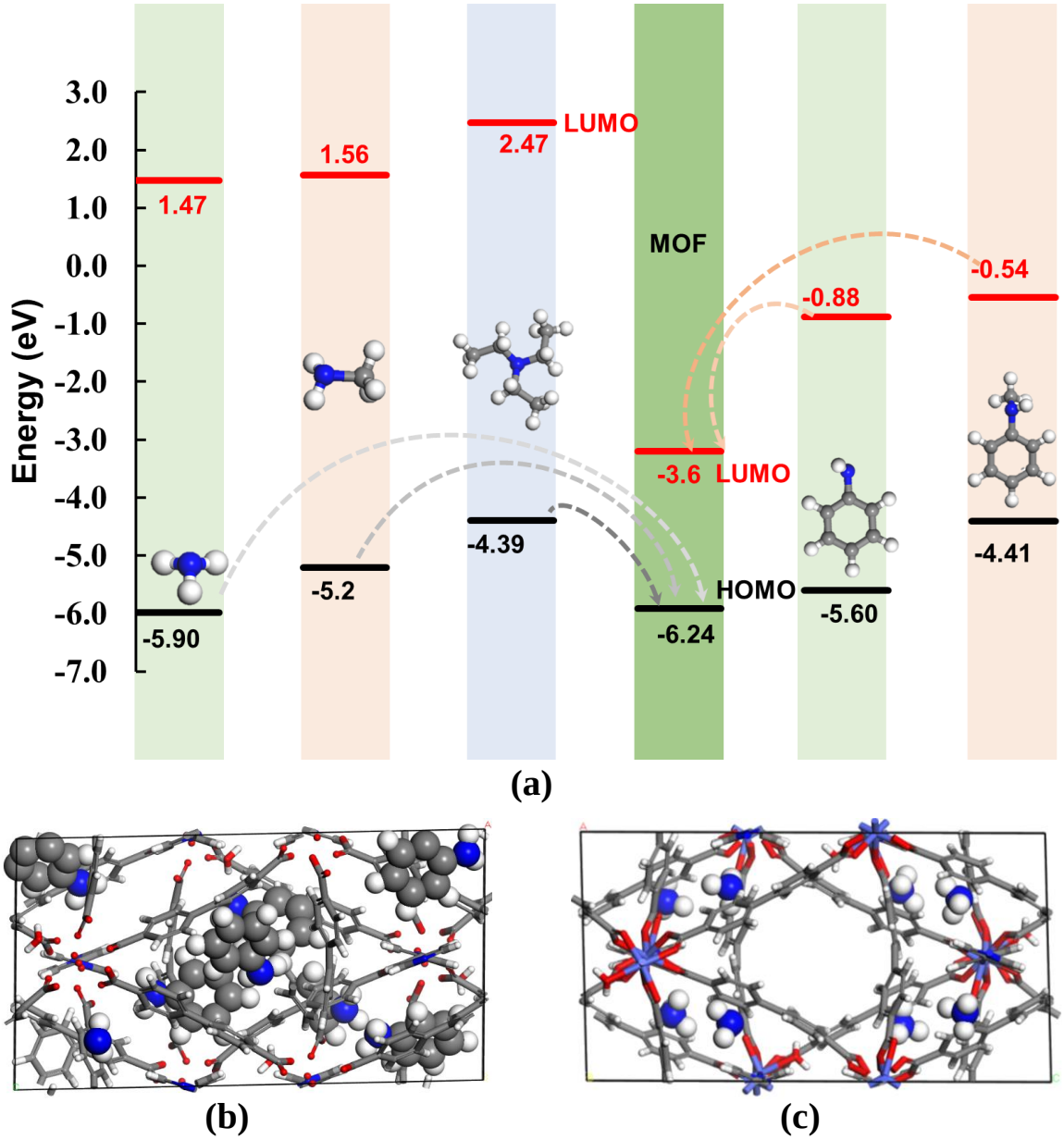

Figure 6.24. (a) The alignment of highest occupied molecular orbitals (HOMOs) and lowest unoccupied molecular orbitals (LUMOs) of adsorbates (Ammonia, methyl amine, triethylamine, aniline, and N-methyl aniline) computed at DZVP/PBE+D3 level of theory with experimentally obtained HOMO-LUMO of MOF. Optimized structures of (b) Aniline@**BITSH-1** and (c) NH_3@**BITSH-1**.

6.3.8. On-site detection of ammonia

The sensing experiments under actual conditions require sensing materials to be converted into a convenient and directly usable form. For this, we prepared MOF-based mixed matrix membranes and studied them for on-site ammonia detection **(Figure 6.25-6.26)**. The MOF membranes were prepared with different MOF weight percentages (30 %, 60 %, and 90 %) to

identify the best possible synthesis conditions that yielded membranes with maximum stability, fast response time, and visible colour change on exposure to amines. The best results were obtained using 60 wt % of the MOF sample. The prepared membranes were tested for their fragility and flexibility. Remarkably, these MOF membranes are flexible and can be folded entirely in half **(Figure 6.26)**.

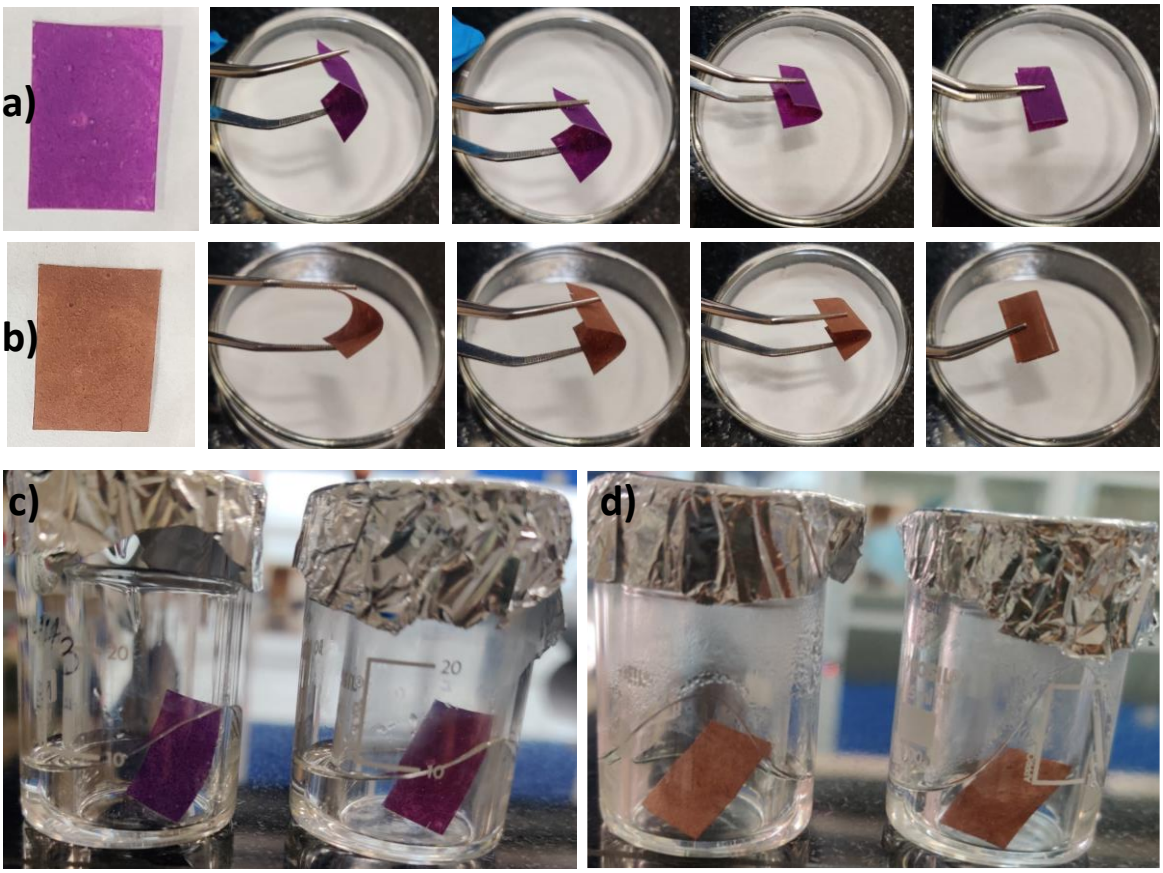

Figure 6.25. Flexible MOF membranes of **BITSH-2** (a) before and (b) after exposure to the vapors of ammonia. Illustration of experimental setup (c) before and (d) after the exposure of MOF membranes to ammonia vapors.

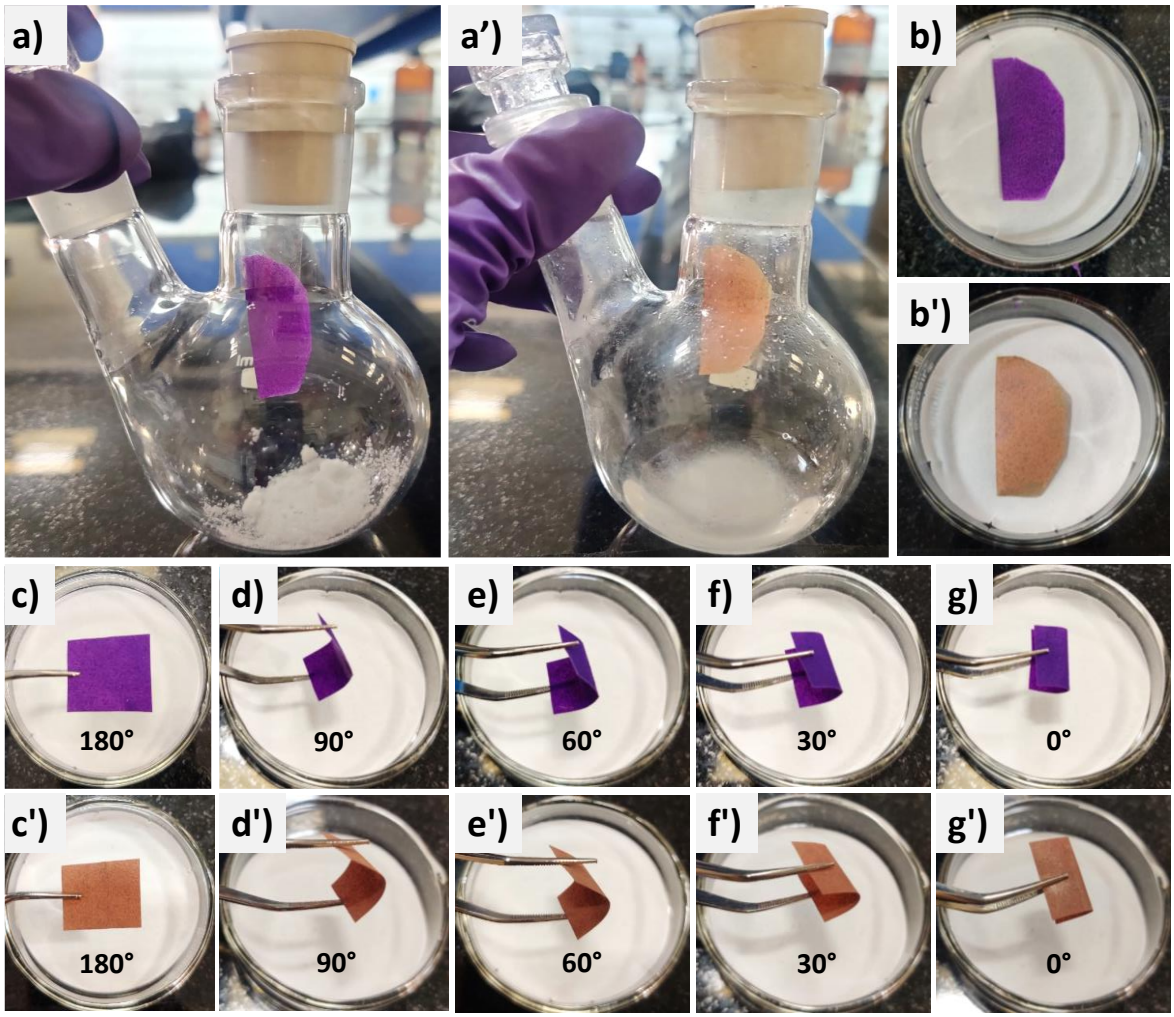

Figure 6.26. Experimental setup for ammonia sensing from a chemical reaction using MOF membranes a) before the experiment and a') after the experiment; MOF membrane color b) before and b') after exposure to the vapors of ammonia and c-g depicts the flexibility of the MOF membranes before ammonia exposure and c'-g' depicts the MOF membranes flexibility after ammonia exposure.

The ammonia sensing ability of the prepared MOF membranes was first investigated by exposing the MOF membranes to ammonia solution through vapor diffusion. A vial containing the membrane was kept inside a beaker containing ammonia solution, and the top of the beaker was sealed with aluminum foil. An apparent change in the color of the membrane was observed instantaneously from purple to light orange **(Figure 6.25)**. To rule out any possibility of color change due to water or moisture, the same membranes were also exposed to water, but no color change was observed in this case. This confirmed that an evident shift in color was only due to ammonia.

An evident color change upon exposure to ammonia vapors encouraged us to test the sensing ability of the membrane in a lab scale ammonia production reaction. It is well known that ammonium chloride and sodium hydroxide reaction liberates ammonia and water along with the formation of sodium chloride. Therefore, a small piece of the membrane was placed inside a stoppered round bottom flask containing the reaction mixture of ammonium chloride and sodium hydroxide. A distinct change in the color of the MOF membrane was observed within a few minutes of the addition of sodium hydroxide to ammonium chloride **(Figure 6.26)**, which confirms the ability of the MOF to detect ammonia under real conditions. Even more interestingly, the membrane showed no loss in its flexible behavior after the experiment as evident from images **(Figure 6.26c-g** and **Figure 6.26c'-g')**, taken before and after the experiment. This confirms that **BITSH-1** and **BITSH-2** are not only discriminative amine sensors but also potent ammonia sensing materials.

6.4. Conclusions

Two cobalt-based MOFs were synthesized and investigated in detail for discriminative sensing of amines. Both the frameworks are efficient luminescent probes for discriminative detection of aliphatic amines via "turn-off" fluorescence and aromatic amines via "turn-on" fluorescence behavior. Using DFT calculations we rationalized the difference in fluorescence behavior (quenching and enhancement) of these MOFs for aliphatic and aromatic amines. Both the MOFs were used to prepare MOF pellets and flexible MOF membranes that helped in the visual detection of ammonia. We believe that the present work will encourage the exploration of more MOF materials for discriminative sensing of various other harmful chemicals.

CHAPTER 7

MOF-based Dual Sensor for Electrochemical and Fluorescence Detection of Nicotine

Detection of nicotine is highly desired; therefore, there is an endless need to develop multifunctional sensors that can detect nicotine in more than one way. The ability of MOFs in sensing amines as studied in previous chapters piqued our interest in investigating the sensing capability of MOFs in detecting nicotine. In this chapter, we have developed a pure MOF-based dual sensor for highly selective detection of nicotine. Interestingly, the sensor can efficiently detect nicotine using fluorescence and electrochemical sensing techniques with a detection limit as low as 0.25 µM. Real cigarette and urine samples have been studied to evaluate the nicotine content in actual conditions where the sensor shows nearly 100 % nicotine recovery. Selectivity experiments demonstrated that the MOF sensor can efficiently detect nicotine in the presence of other interfering analytes such as glucose, dopamine, and various metal salts. A plausible mechanism has also been described for the MOFs' nicotine sensing ability. XPS analysis showed that nicotine is present in the MOF samples after the sensing experiment.

7.1. Introduction

Nicotine is one of the main components of cigarette smoke that has many adverse effects on human health, causing respiratory and cardiovascular disorders and various types of cancers, including lung, liver, kidney, breast, and neck cancer.[1,2] Nicotine can also severely affect the central nervous system causing mood swings and a sense of euphoria.[3] However, the most significant impact of nicotine is that it affects the health of active smokers and has an equally harmful effect on the health of passive smokers. According to the Centers for Disease Control and Prevention (CDC), nicotine has detrimental effects on non-smokers when exposed to second-hand smoke. Second-hand smoke causes severe respiratory infections, heart diseases, and lung infections, leading to many deaths among non-smoking adults and infants every year.[4,5] Electronic cigarettes (E-cigs) have become more prevalent in the last few years, and it has reduced the usage of cigarettes to some extent. Although E-cigs essentially mitigate the toxic effect of smoke inhalation, the adverse health effects of vaping are still a concern. E-cigs have increased the risk of exposure to teenagers and school kids. There is, hence, a solid need to design materials that can detect nicotine at sub-ppm levels. This will increase opportunities to develop new, more sensitive sensors for nicotine detection. The nicotine concentration in

tobacco products varies depending on the type and quality of the tobacco products, but the normal nicotine content present is around 1 to 3 %.[6] Thus, the nicotine level is a crucial factor in judging the quality of cigarette products, determination of nicotine amount is of significant importance for medicine, toxicology, and tobacco industry.

Various techniques have been used for the detection of nicotine such as high-performance liquid chromatography (HPLC), gas chromatography (GC), liquid chromatography-mass spectrometry (LC-MS), and spectrophotometry which requires sophisticated instrumentation, sample handling and purification complications that limits their usage.[7-9] On the other hand, highly sensitive and selective techniques such as fluorescence and electrochemical sensing are also widely used due to their ease of handling. They can achieve low detection limits with minimal sample preparation, less time, and low cost.[10,11] Thus, preparing fluorescence-based optical sensors and designing electrochemical sensors is of importance to achieve practical advantages such as real-time sensing, rapid analysis and sensitive detection. Notably, if a material can act as a dual sensor, it can provide even more comprehensive nicotine detection.

Recently, many researchers explored electrochemical sensing of nicotine using glassy carbon electrodes, carbon paste electrodes, and pencil graphite electrodes as unmodified electrodes.[12-14] Numerous composites have been prepared as electrochemical sensors using conducting materials such as graphene, multiwalled carbon nanotubes, metal oxides, nanoparticles, nanotubes, and polymers.[15-19] Such sensors, despite their better current sensitivities, involve tedious sample preparations. Metal-Organic Frameworks (MOFs), inorganic-organic hybrid porous materials with tunable properties, have been explored for various applications.[20,21] These can also be promising candidates as fluorescent and electrochemical sensors due to the feasibility of placing fluorescent linkers and metal/ligand redox centers inside the framework. MOFs have been explored for sensing of diverse analytes,[22-24] but there is only a handful of reports on nicotine detection using MOFs.[25-27] Recently, our group has also investigated MOFs for fluorescence and electrochemical sensing applications.[28-29] Encouraged by our recent findings, we have designed the first MOF-based dual sensor for nicotine detection. Such dual sensors can be highly useful in the preparation of nano composites for real-time sensing applications. It is noteworthy that preparing a dual sensor is challenging, and there are very few such sensors in the literature. Still, even these dual sensors have not been explored for sensing nicotine.[30-32]

7.2. Experimental Section

7.2.1. Materials

Cobalt Nitrate hexahydrate [$Co(NO_3)_2 \cdot 6H_2O$] was purchased from SRL, biphenyl-4,4'-dicarboxylic acid (bpdc), 1,2-bis(4-pyridyl)ethane (bpe) and 4,4'-bipyridine (bpy) were purchased from TCI chemicals. All the reagents, solvents and analytes nicotine (NIC) were obtained from commercial sources and used as such without further purification.

7.2.2. Synthesis of BITSH-1 and BITSH-2

BITSH-1 and **BITSH-2** MOFs were synthesized solvothermally by mixed ligand approach by reacting the metal salt $Co(NO_3)_2 \cdot 6H_2O$ (0.1mmol) and acid linker biphenyl-4,4'-dicarboxylic acid (bpdc) (0.1 mmol) in 1:1 ratio and 4,4'-bipyridine (bpy) (0.05 mmol) or 1,2-bis(4-pyridyl)ethane (bpe) (0.05 mmol) in 10 ml of DMF to obtain **BITSH-1** and **BITSH-2** respectively. The reaction mixture was heated at 130 ℃ for 24 h. The crystals thus obtained were washed thoroughly with DMF and ethanol before further study.

7.2.3. Photoluminescence (PL) Measurements

The MOF crystals were vacuum dried after washing with DMF and ethanol and the crystals were gently grinded with a mortar pestle. 2 mg of the grinded sample was well dispersed in 1 ml of ethanol via sonication for the measurements. The UV-vis absorbance and PL measurements were carried out for **BITSH-1** and **BITSH-2**. PL studies were carried out with 0.1 M concentration of nicotine in ethanol medium for both the MOF systems.

7.2.4. Electrochemical Measurements

Cyclic Voltammograms (CV) of **BITSH-1** and **BITSH-2** were obtained using cyclic voltammetry technique with three electrode cell setup. The working electrode used was Fluorine-doped Tin Oxide (FTO) with platinum mesh as counter electrode and silver (Ag/AgCl) reference electrode. The CV was collected using 0.1 M tetrabutylammonium perchlorate in acetonitrile medium at room temperature. The onset oxidation potential and reduction potential values obtained from the Cyclic Voltammogram (CV) and by using the following equation, the HOMO and LUMO energy levels were calculated.

E_{HOMO} = -e [$E_{ox\ onset}$ + 4.741] eV and E_{LUMO} = -e [$E_{red\ onset}$ + 4.741] eV.[33]

7.2.5. Preparation of cigarette and urine samples

Commercially available cigarettes were purchased and the tobacco leaves was collected from the cigarettes by removing the rolling paper of the cigarettes. The tobacco leaves were grinded and 500 mg of tobacco powder was weighed in a vial, 10 ml of water was added. The mixture was sonicated for 3 h. The as-prepared mixture was filtered and the clear filtrate was used for further study. Similarly, the urine sample was collected and it was diluted 100 times using water. The mixture was sonicated for 1 h and filtered for further analysis. The analysis was carried out with the real samples under the same conditions as used to obtain the calibration graph using square-wave voltammetry (SWV).

7.3. Results and Discussions

7.3.1. Structural details and characterization of the MOF

In the present chapter, two Co-based MOFs, **BITSH-1** and **BITSH-2** (Birla Institute of Technology and Science, Hyderabad) were examined for nicotine detection. Both the MOFs were synthesized solvothermally as per our recent report[29] **(Figure 7.1)**. **BITSH-1** and **BITSH-2** crystallizes in the monoclinic *P*21/*n* and orthorhombic *Pbcn* space groups, respectively. The presence of aliphatic amine functionality in nicotine and these two MOFs' ability to sense amines intrigued us to explore the potential of these frameworks in detecting nicotine **(Figure 7.1)**.

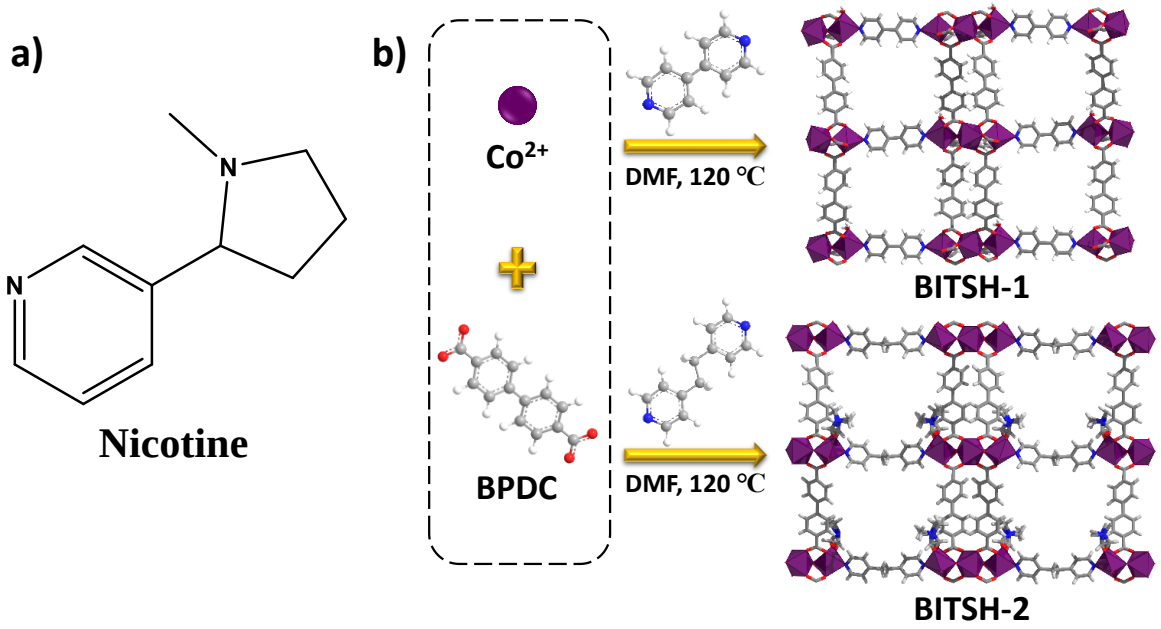

Figure 7.1. (a) Chemical structure of nicotine, (b) Synthesis and packing diagrams for **BITSH-1** and **BITSH-2**.

The phase purity of the as-synthesized MOF crystals was ascertained by PXRD analysis **(Figure 7.2a, b)**. The as-synthesized MOF samples were washed several times with DMF and ethanol. MOF samples were dried and the PXRD patterns were recorded in the 2θ range of 5°-40° with a step size of 1° min^{-1}. The PXRD patterns of as-synthesized frameworks matched well with the simulated patterns, thus confirming the bulk purity of the as-synthesized MOF samples. PXRD patterns of both the frameworks exhibited good crystallinity with sharp and intense peaks. The thermal stability of both the frameworks was analyzed under N_2 atmosphere. The frameworks were stable upto 350 °C **(Figure 7.2c, d)**. MOF samples were activated at 90 °C under dynamic vacuum before proceeding to the N_2 adsorption measurements. PXRD patterns were recorded to check the integrity of the framework after activation. The structural integrity was retained for both the frameworks **(Figure 7.2e, f)**.

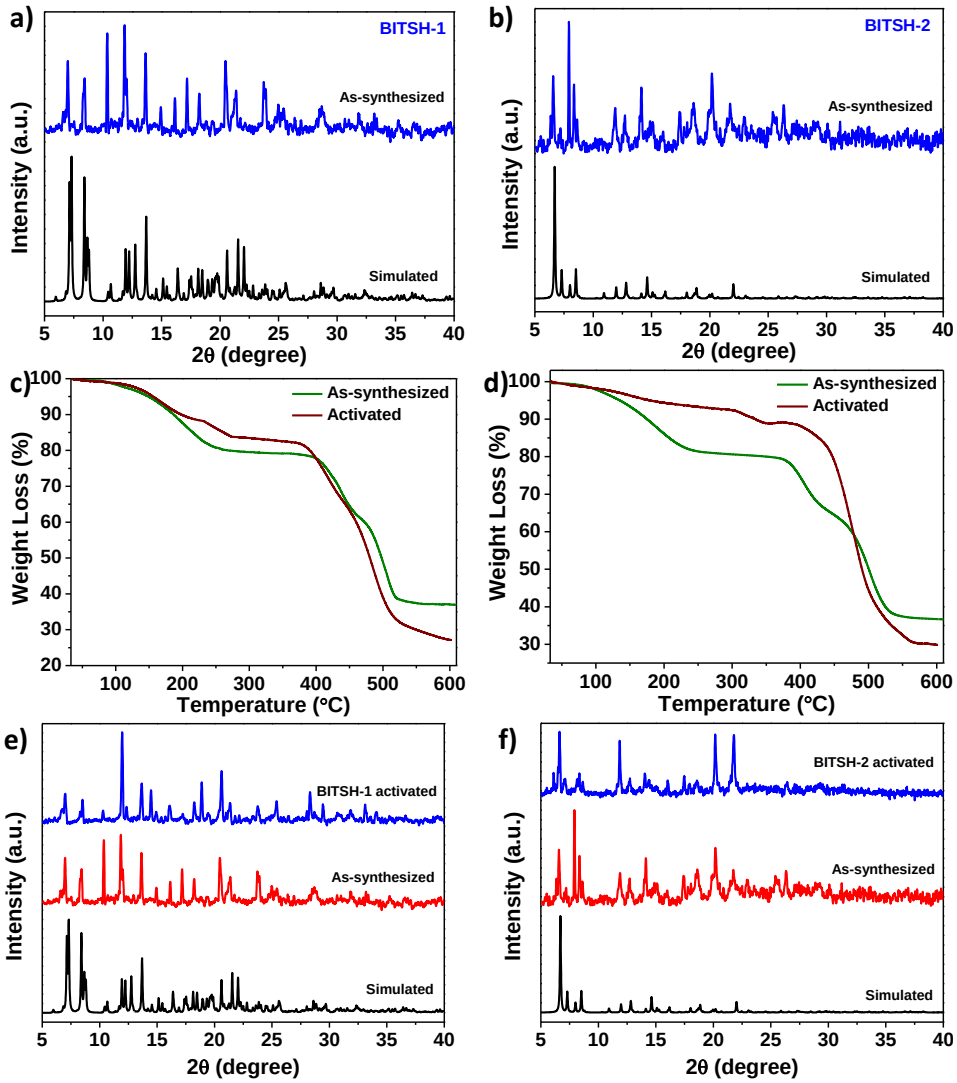

Figure 7.2. PXRD patterns of (a) **BITSH-1** and (b) **BITSH-2**. TGA plot of as-synthesized (c) **BITSH-1** and (d) **BITSH-2**. PXRD patterns of as-synthesized and activated (e) **BITSH-1** and (f) **BITSH-2**.

BITSH-1 and **BITSH-2** exhibited BET surface area of 330 m^2 g^{-1} and 734 m^2 g^{-1} respectively. Both the frameworks displayed pore size of around 8 Å **(Figure 7.3)**. FT-IR analysis revealed the characteristic bands for carboxylate group and Co-O bonding frequencies (Figure S6). SEM analysis, elemental mapping and EDAX analysis were carried out to study the morphology and elemental composition of both the frameworks. SEM analysis of **BITSH-1** and **BITSH-2** showed block shaped crystals. Elemental mapping and EDAX analysis of both the frameworks revealed the presence of Co, C, N, O elements **(Figure 7.4)**.

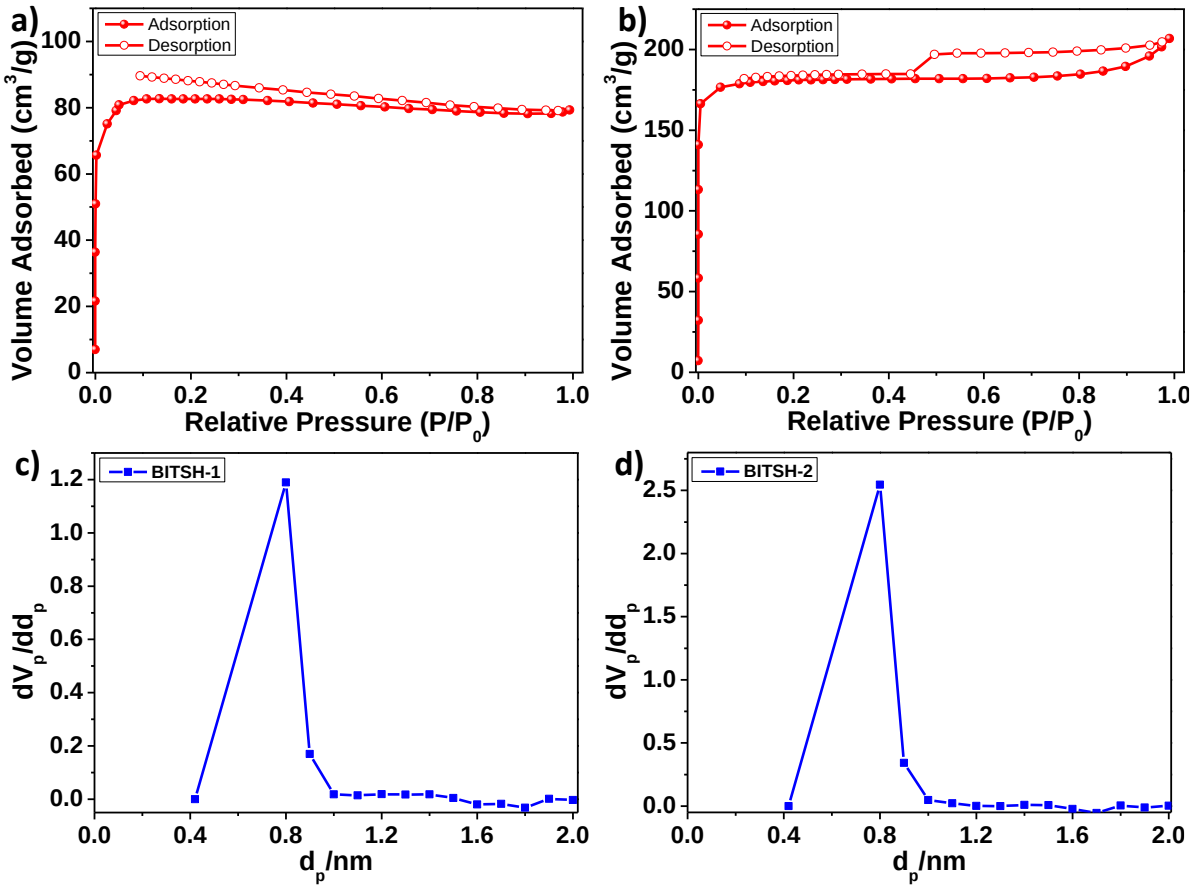

Figure 7.3. N_2 adsorption isotherm of (a) **BITSH-1** and (b) **BITSH-2** and pore diameter of (c) **BITSH-1** and (d) **BITSH-2** MOF samples.

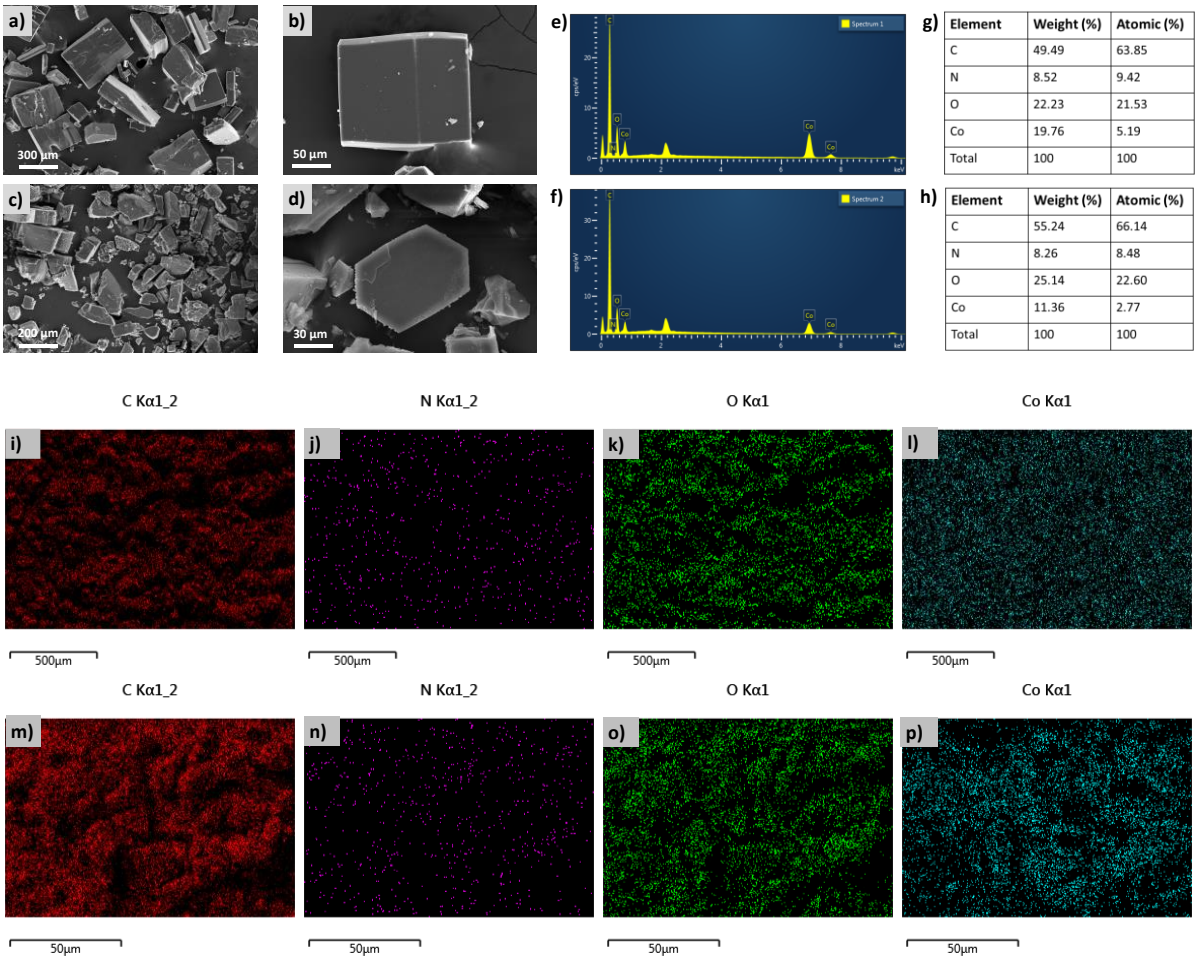

Figure 7.4. SEM images of (a, b) **BITSH-1** and (c, d) **BITSH-2**. Energy-dispersive X-ray spectroscopy (EDAX) spectrum of (e) **BITSH-1** and (f) **BITSH-2**. EDAX analysis of (g) **BITSH-1** and (h) **BITSH-2**. Elemental mapping images of (i-l) **BITSH-1** and (m-p) **BITSH-2**.

7.3.2. Fluorescence sensing studies

The fluorescence-based nicotine sensing ability of **BITSH-1** and **BITSH-2** was studied by first collecting the UV-vis absorption and emission spectra in ethanol. MOF crystals were slightly ground and made a uniform suspension in ethanol (2 mg/mL). **BITSH-1** and **BITSH-2** exhibited strong emission bands with λ_{max} at 331 nm and 336 nm, respectively, upon excitation at 278 nm and 280 nm, due to n-π* transitions of aromatic carboxylic ligands in the MOF frameworks **(Figure 7.5a)**. Incremental additions of 0.1 M nicotine solution in ethanol were added to the well dispersed MOF suspension, and the PL measurements were recorded. Interestingly, both the MOF frameworks could sense nicotine via turn-off fluorescence behavior. Strong PL quenching on increased amounts of nicotine with very high sensitivity was observed **(Figure 7.6)**. The MOFs' stability in nicotine was checked with the help of PXRD.

MOF samples were filtered after nicotine sensing experiments, and the PXRD patterns were recorded to study the framework stability towards nicotine. PXRD patterns of both the frameworks were in good agreement with the as-synthesized and simulated patterns **(Figure 7.5b, c)**.

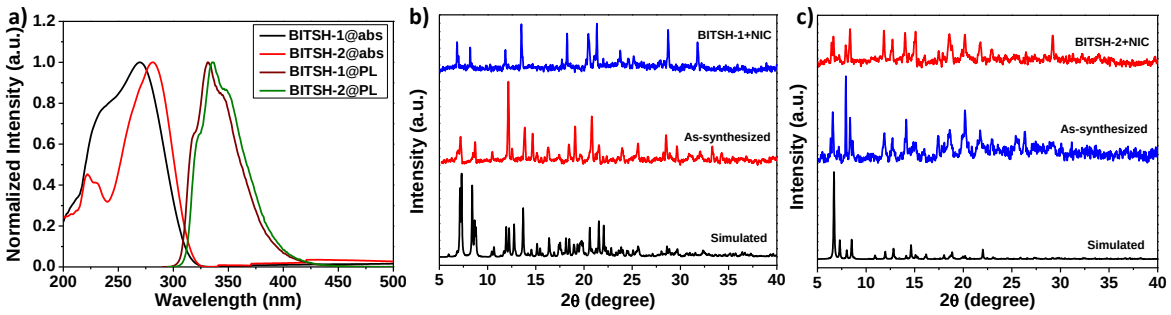

Figure 7.5. (a) UV-vis absorption spectra and PL emission spectra of **BITSH-1** and **BITSH-2**. PXRD patterns of (b) **BITSH-1** and (c) **BITSH-2** recorded after exposure to nicotine.

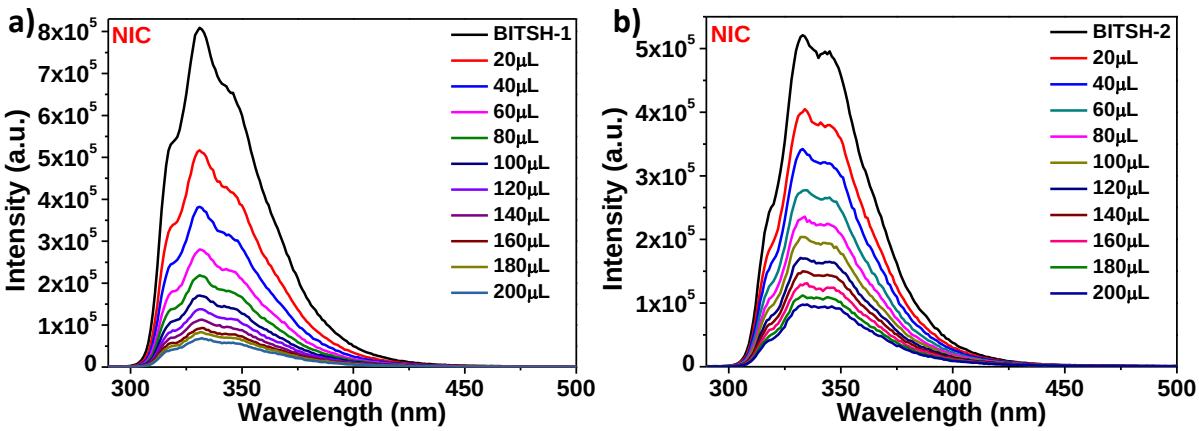

Figure 7.6. Photoluminescence (PL) emission spectra of **BITSH-1** (a) and **BITSH-2** (b) on incremental additions of 0.1 M NIC in ethanol medium.

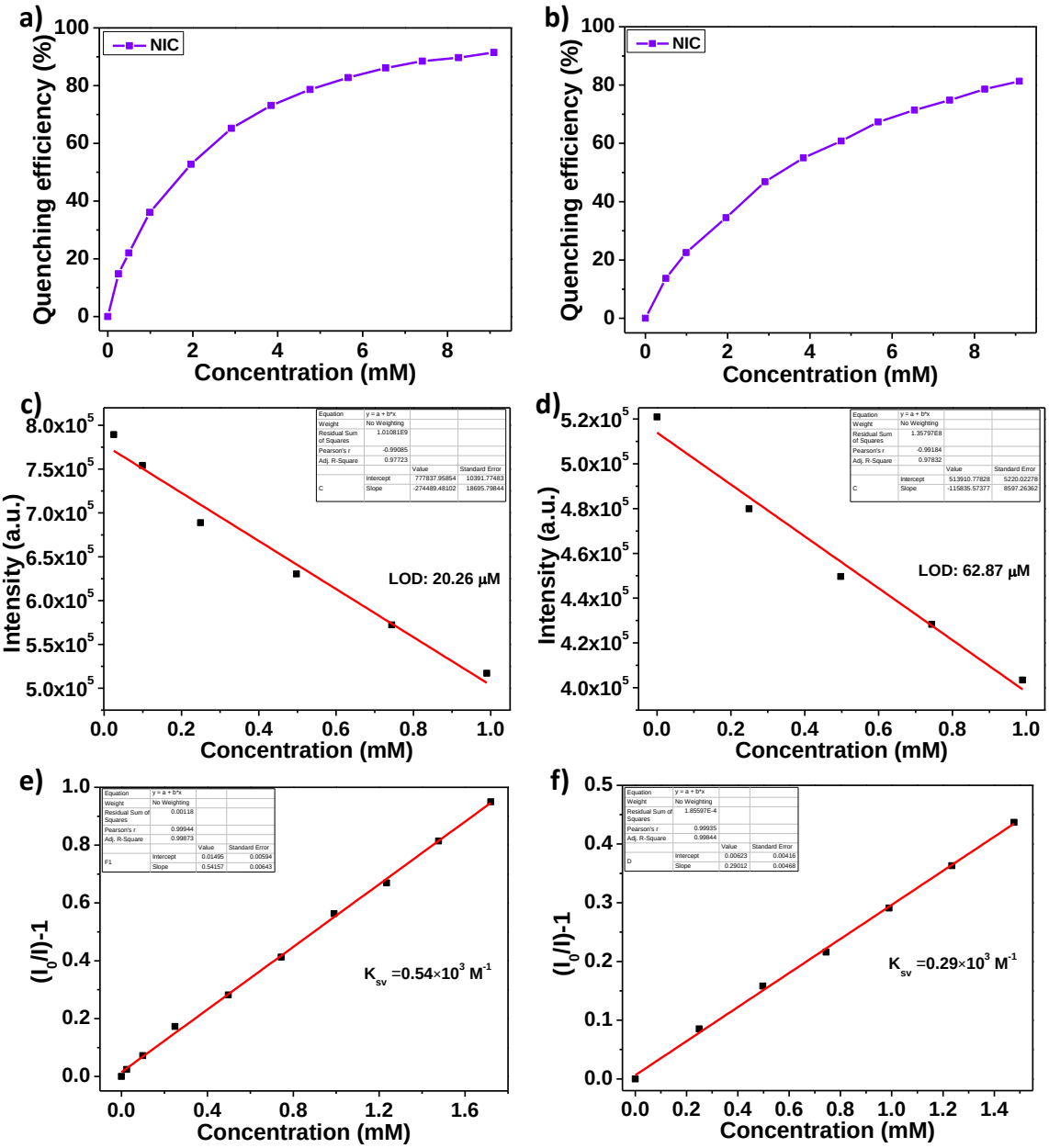

Figure 7.7. Quenching efficiency of nicotine (NIC) obtained from PL measurements of (a) **BITSH-1** and (b) **BITSH-2** on incremental additions of 0.1 M NIC. Detection limit (LOD) of NIC obtained from PL measurements of (a) **BITSH-1** and (b) **BITSH-2**. Linear fit of Stern-Volmer plot of (a) **BITSH-1** and (b) **BITSH-2** in response to NIC.

7.3.3. Selectivity and recyclability studies

The quenching efficiencies (QE) for **BITSH-1** and **BITSH-2** were found to be 91.49 % and 81.52 %, respectively **(Figure 7.7a, b)**. The limit of detection (LOD) for both the frameworks was calculated using equation $3\sigma/k$[34]. The linear fitting of the data obtained by plotting intensity vs. concentration of analyte [Q] gives slope (k) and σ is the standard deviation

obtained from five blank readings of the MOF. The LOD values of 20.26 µM for **BITSH-1** and 62.87 µM for **BITSH-2** were obtained, demonstrating these MOFs' excellent nicotine sensing abilities **(Figure 7.7c, d)**.

Recyclability studies were also carried out to study the reusability of MOF in sensing nicotine. PL intensity of pristine MOF sample was recorded and then 200 µL of 0.1 M nicotine was added and the PL response was recorded. The MOF sample was collected and washed several times with DMF and ethanol. MOF sample was dried prior to reuse for nicotine sensing. The PL intensity of MOF was almost retained to the pristine MOF PL intensity. It showed similar quenching behavior on the addition of nicotine. The MOF sample was again collected and washed before the next cycle, and the same procedure was repeated three times **(Figure 7.8)**.

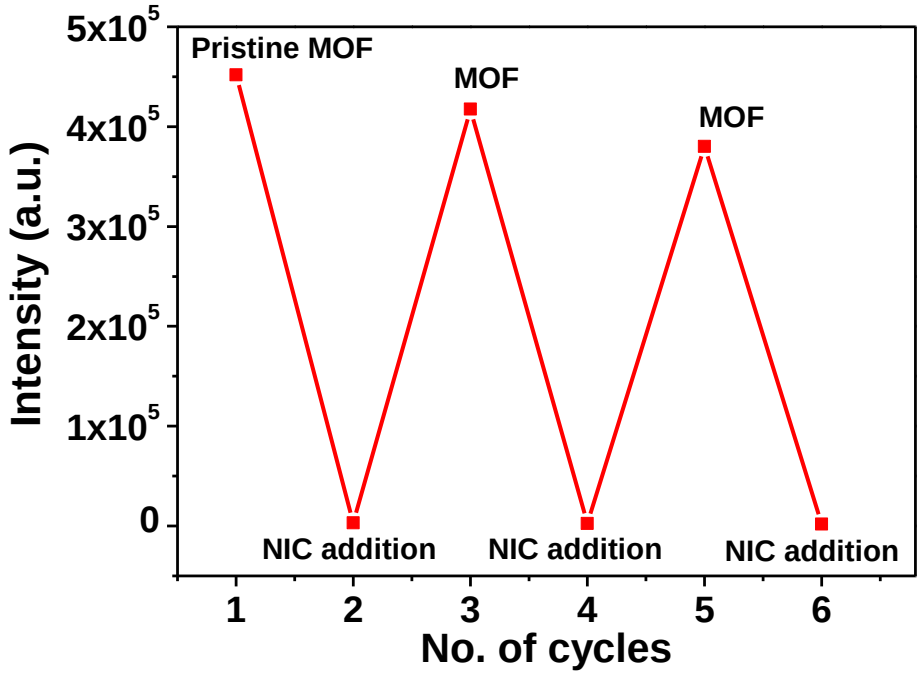

Figure 7.8. Recyclability studies of **BITSH-1.**

Encouraged by the remarkable PL quenching efficiencies of the MOFs, we further checked the selective sensing ability of the MOF towards nicotine. Since both the frameworks are very similar in their structure, only **BITSH-1** has been selected for selectivity studies. Sensitive and selective sensing studies under real conditions will make a chemical sensor more efficient. In this context, detecting nicotine levels in urine sample of smokers will be interesting. Thus, we have chosen NaCl, KCl, NH_4Cl, glucose, dopamine, uric acid as these could be the possible interferents present in the urine sample and carried out selectivity studies. The addition of interferents did not alter the fluorescence intensity of **BITSH-1**, but the addition of nicotine

quenched the fluorescence intensity of **BITSH-1** drastically. Thus, establishing high selectivity of **BITSH-1** in sensing nicotine **(Figure 7.9)**.

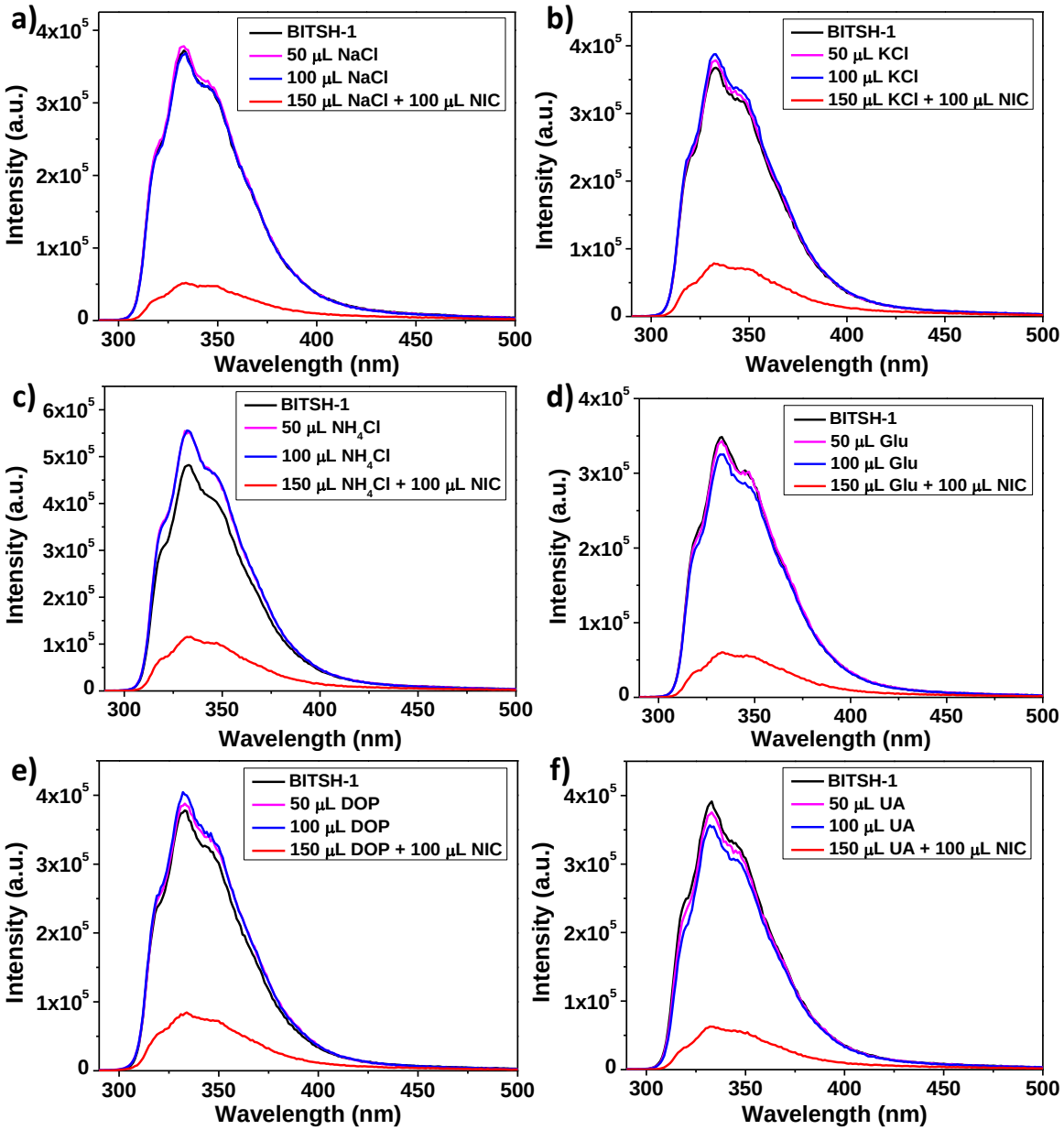

Figure 7.9. Selectivity studies of **BITSH-1** on addition of 0.1 M (a) sodium chloride (NaCl), (b) potassium chloride (KCl), (c) ammonium chloride (NH_4Cl), (d) glucose (Glu), (e) dopamine (DOP) and (f) uric acid (UA).

7.3.4. Studies to support dynamic quenching mechanism

Detailed studies were conducted to analyze the underlying quenching mechanism for detecting nicotine. The concentration of the analyte added incrementally was plotted on the x-axis and the intensity in terms of (I_0/I) was taken on the y-axis, where I_0 is the initial fluorescence intensity of MOF in the absence of analyte, and I is the fluorescence intensity in the presence

of analyte. The linear fitting of the plot $(I_0/I)-1 = K_{SV}[Q]$[35] provided the values for the Stern-Volmer constants (K_{SV}) **(Figure 7.7e, f)**. The K_{SV} value lies in the range of 10^3 M^{-1}, which states that the dynamic quenching process is operating in the present case as $K_q \leq 10^{10}$.[36] To eliminate the possibility of other quenching mechanisms, additional studies were carried out. The other possible quenching mechanism can be energy (electron) transfer between the host and guest. The electron transfer process can be either due to Forster resonance energy transfer (FRET) or Photoinduced energy transfer (PET), usually occurring between the emission spectra of the donor (MOF fluorophore) and absorption spectra of the acceptor (analyte). FRET can be ruled out in the present case as there is no spectral overlap observed between the donor and acceptor **(Figure 7.10)**.

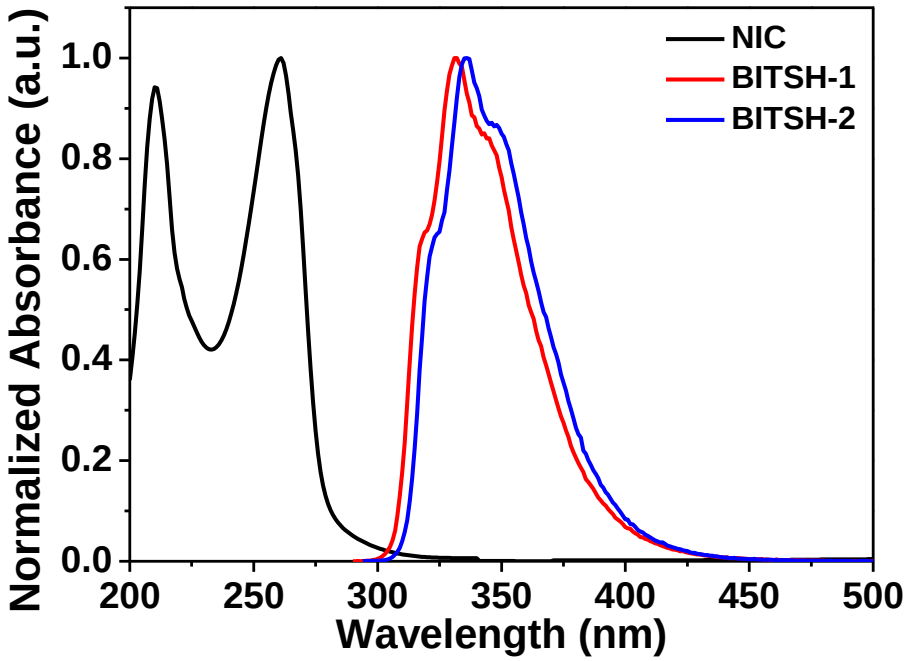

Figure 7.10. Spectral overlap between absorption spectra of NIC and emission spectra of both the MOF systems.

We proceeded further to check the possibility of any ground-state complex formation, the absorption spectra of both the frameworks on incremental additions of nicotine were recorded. It was observed that the MOF peak around 280 nm is retained but with the incremental additions of nicotine, the peak is slightly shifted to 260 nm, which corresponds to the nicotine λ_{max}. Upon further additions of nicotine, the absorption intensity of the MOF peak is reinforced with the nicotine absorption peak. There is no emergence of new peak in this case. This slight blue shift on the addition of nicotine can be due to weak interactions or ground state complex formation between the analyte and MOF resulting to static quenching.[36] **(Figure 7.11a, b)**.

Further, temperature-dependent fluorescence studies were carried out at 288 K, 293 K, and 298 K to check dynamic quenching behavior. It was observed that the K_D value (D stands for the dynamic constant) increased with an increase in temperature following dynamic quenching mechanism[36] **(Figures 7.11-7.12** and **Table 7.1)**. Therefore, the only possible quenching mechanism operating would be Photoinduced energy transfer (PET) via dynamic quenching.

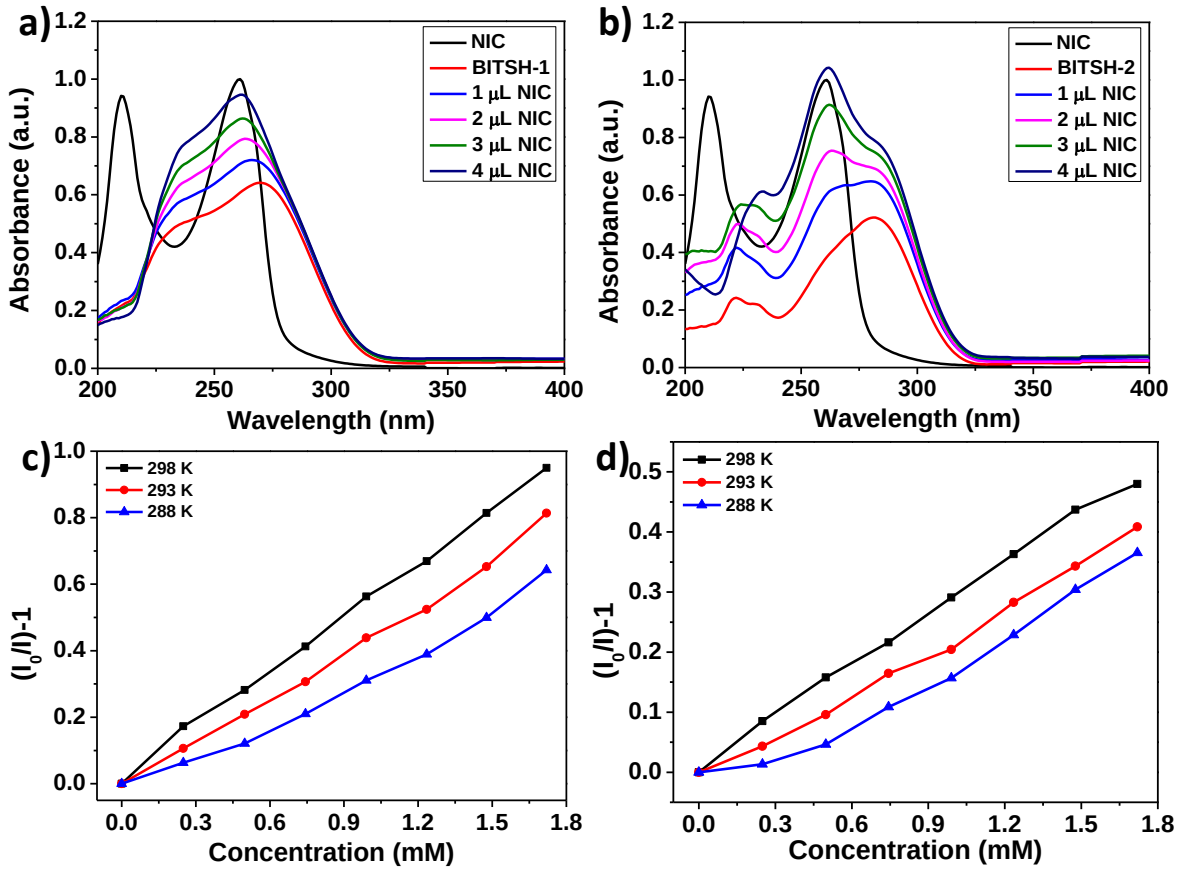

Figure 7.11. UV-vis spectra of (a) **BITSH-1** and (b) **BITSH-2** on addition of NIC in ethanol medium. Stern Volmer plot of (c) **BITSH-1** and (d) **BITSH-2** on incremental additions of NIC recorded at different temperatures.

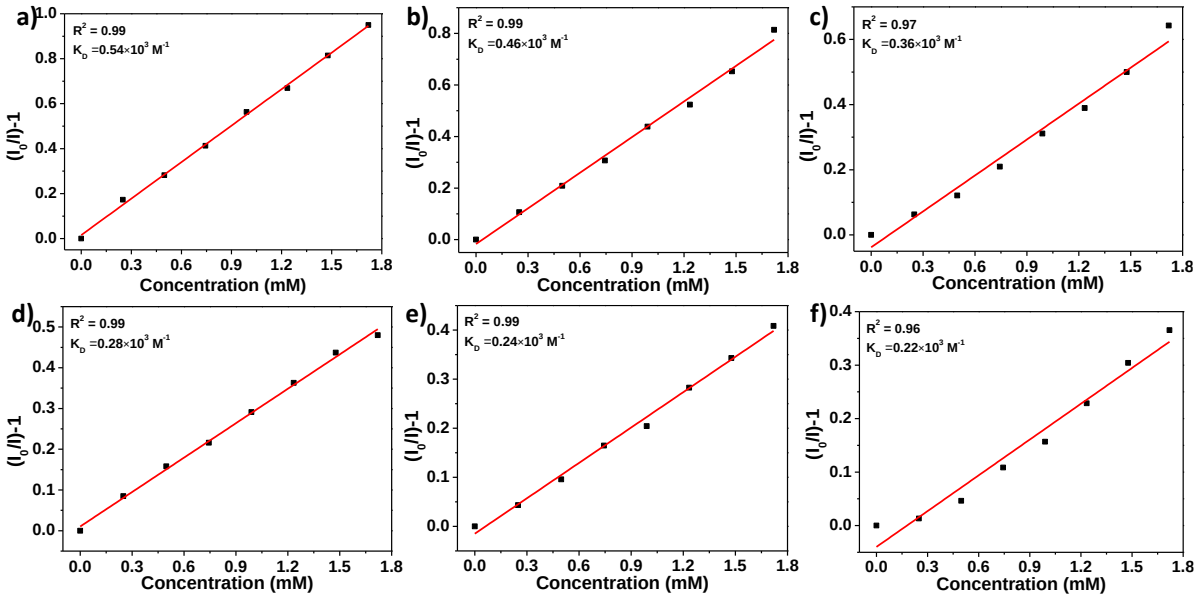

Figure 7.12. Linear fit of Stern-Volmer plot of **BITSH-1** and **BITSH-2** in response to NIC at different temperatures (a, d) 288 K (b, e) 293 K and (c, f) 298 K respectively.

Table 7.1. K_D values of **BITSH-1** and **BITSH-2** in response to NIC at different temperatures.

Temperature (K)	**BITSH-1 K_D (M^{-1})**	**BITSH-2 K_D (M^{-1})**
298 K	0.54×10^3	0.28×10^3
293 K	0.46×10^3	0.24×10^3
288 K	0.36×10^3	0.22×10^3

7.3.5. HOMO-LUMO studies to analyze the sensing mechanism

The values of the HOMO energy levels of MOFs and nicotine were compared to understand further the quenching behavior upon the addition of nicotine. The HOMO energy levels for the MOFs were calculated using the cyclic voltammetry technique **(Figure 7.13)**, by considering their onset oxidation and reduction potentials and by using the following equation, E_{HOMO} = -e [$E_{ox\ onset}$ + 4.741] eV and E_{LUMO} = -e [$E_{red\ onset}$ + 4.741] eV.[33] The HOMO energy levels value for **BITSH-1** and **BITSH-2** were ~ -6.24 eV, and the HOMO energy level of nicotine was considered -6.09 eV, according to the literature.[37] Since the HOMO of nicotine lies above the HOMO of MOF; facile electron transfer occurs from the HOMO energy level of nicotine to the HOMO energy level of **BITSH-1** and **BITSH-2 (Figure 7.14)**. This electron transfer process leads to strong quenching of fluorescence intensities of both the MOFs.

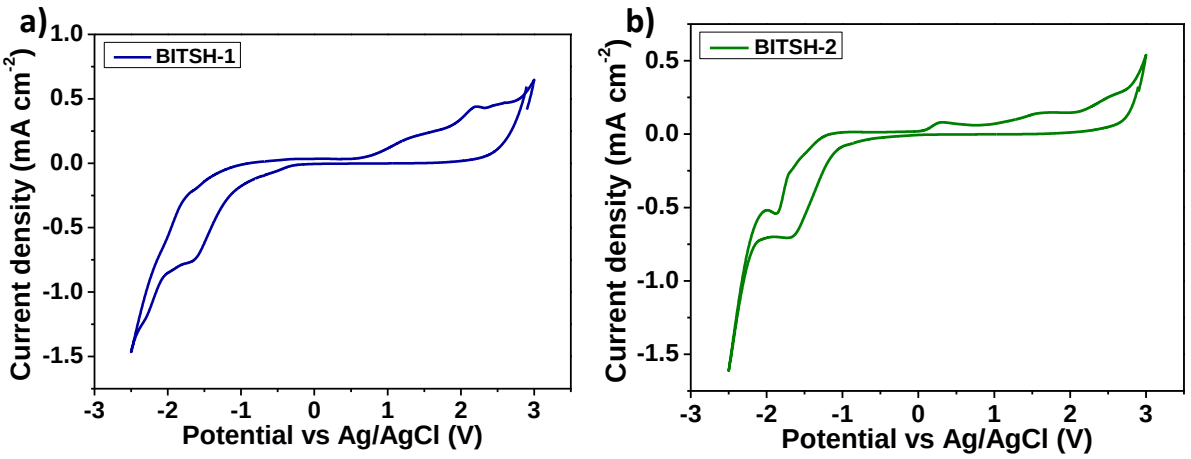

Figure 7.13. Cyclic Voltammogram (CV) of (a) **BITSH-1** and (b) **BITSH-2** recorded in acetonitrile medium.

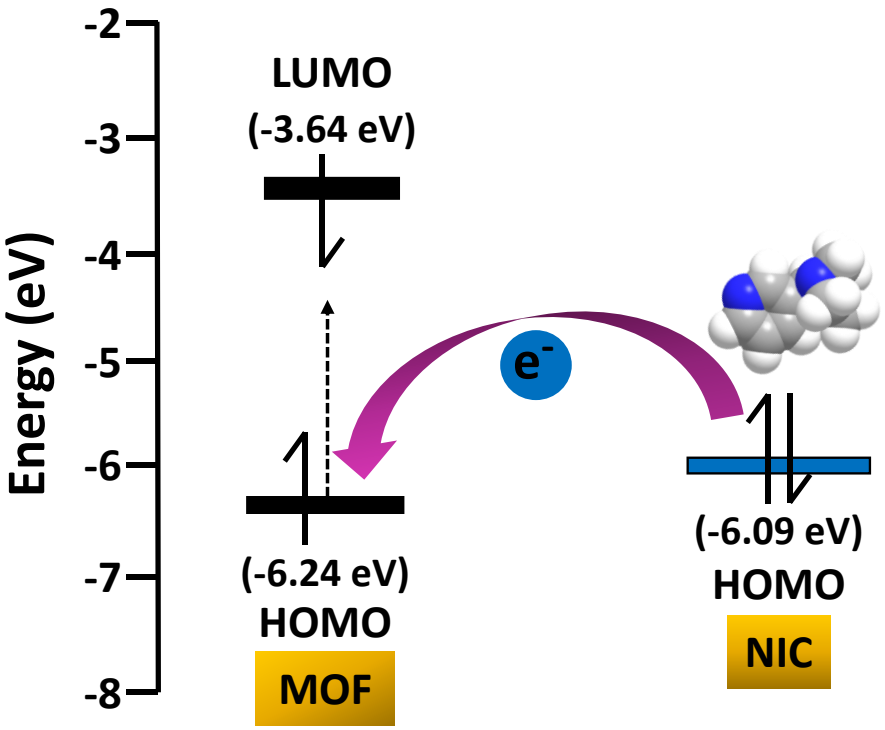

Figure 7.14. Schematic representation of electron transfer between HOMO (π) energy levels of **BITSH-1** and HOMO energy levels of NIC.

7.3.6. X-Ray photoelectron spectroscopy (XPS) studies for the detection of nicotine

XPS analysis was carried out additionally on the MOF crystals before and after fluorescence sensing experiments to confirm the presence of nicotine inside the MOF pores. MOF crystals were filtered after fluorescence experiments and dried at around 100 ℃ to remove excess analyte and solvent molecules that might be present on the surface of the MOF crystals. N 1s

spectra of pristine MOF and MOF after nicotine sensing experiments were analysed for the characteristic C-N peak due to the presence of nicotine. Deconvoluted spectra of both the frameworks after nicotine sensing experiments showed characteristic binding energy peaks of C-N=C bond present in 4,4'-bypridine and C-N bond present in nicotine. Binding energy peak around 400.8 eV attributes to the C-N bond of tertiary N present in the nicotine along with the binding energy peak around 399.5 attributing to C-N=C bond of 4,4'-bypridine present in the MOF framework[38,39] **(Figure 7.15)**.

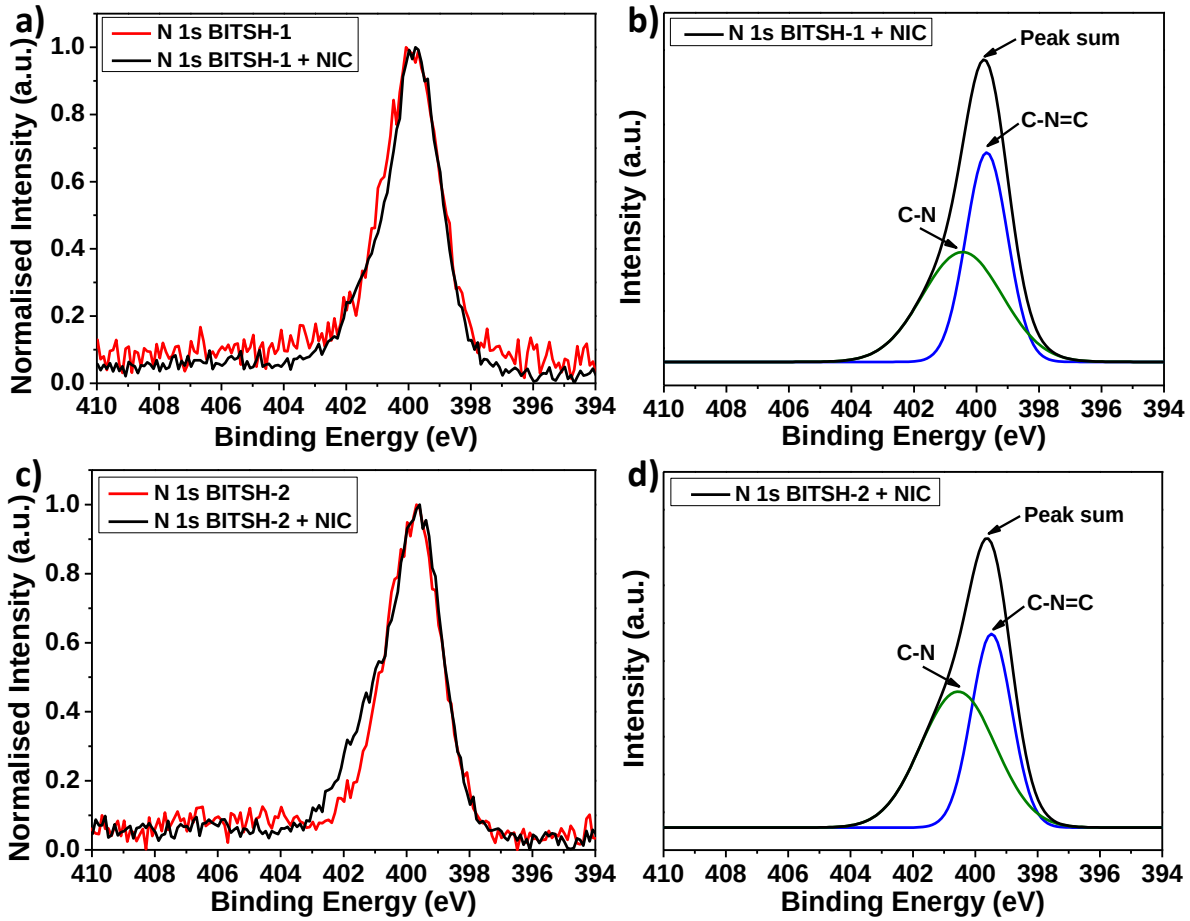

Figure 7.15. N 1s XPS spectrum of (a) **BITSH-1** and (c) **BITSH-2** on addition of NIC. Deconvoluted spectrum of (b) **BITSH-1 + NIC** and (d) **BITSH-2 + NIC**.

7.3.7. Electrochemical sensing studies

To demonstrate the dual-sensing ability of these materials, it was essential to test them using another efficient sensing technique. Accordingly, these MOFs were tested for their electrochemical sensing ability of nicotine. CVs of both the MOFs showed similar oxidation potential due to their structural similarities. Thus, we have chosen only one framework (**BITSH-1**) for the detailed nicotine sensing experiments. For the electrochemical sensing experiments, CVs were obtained with the help of a three-electrode electrochemical set-up using

MOF/GCE as the working electrode, platinum wire as the counter electrode, and Ag/AgCl as the reference electrode using 0.1 M phosphate buffer solution (PBS) electrolyte. MOF crystals were gently ground to prepare a uniform suspension in ethanol (2 mg/mL). MOF suspension was drop casted onto the polished bare GCE and allowed to dry. Then 3 µL of nafion was drop casted onto the GCE and allowed to dry at room temperature. The modified GCE (MOF/GCE) was used for electrochemical measurements. The CVs of bare GCE, MOF/GCE were obtained in 0.1 M PBS (Phosphate buffer) at pH 7.04 in the presence and absence of 1 mM nicotine. The CVs were recorded in the potential window of 0.5 V to 1.2 V with a scan rate of 100 mV/s. No oxidation peak was observed in the case of bare GCE, whereas an oxidation peak at a potential of +0.9 V was observed for MOF/GCE, probably due to the reduction of Co(II)/Co(I) **(Figure 7.16)**. Upon adding 24.4 µM of nicotine, an increase in the oxidation peak current was observed with a shift in the potential to +0.89 V due to the electro-catalytic oxidation of nicotine on the MOF/GCE electrode surface.[10,40]

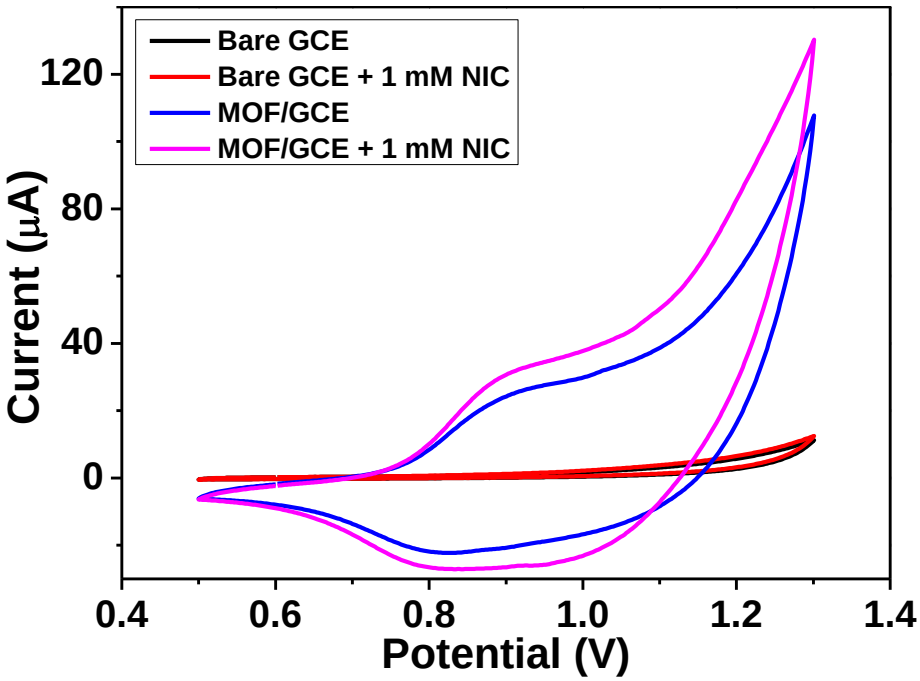

Figure 7.16. Cyclic voltammetry response of MOF/GCE, bare GCE in the absence and presence of nicotine, recorded in 0.1 M PBS (pH 7.04) at a scan rate of 100 mV/s.

To evaluate the effect of scan rate on nicotine oxidation, CVs of MOF/GCE in the presence of 10 µM of nicotine were obtained with different scan rates ranging from 20 to 200 mV/s in 0.1 M PBS buffer at pH 7.04. **Figure 7.17a** shows the relation between anodic peak current and scan rate. An increase in the anodic peak current with increased scan rates was observed, accompanied by a slight shift in anodic peak potentials. **Figure 7.17b** depicts the plot of anodic

peak current (I_{pa}) and scan rate (υ) following a linear relationship with R^2 equal to 0.99. This clearly indicates the (surface) adsorption-controlled mechanism operates, and there is diffusion of nicotine from the bulk aqueous phase to the electrode surface modified with MOF material.[41,42]

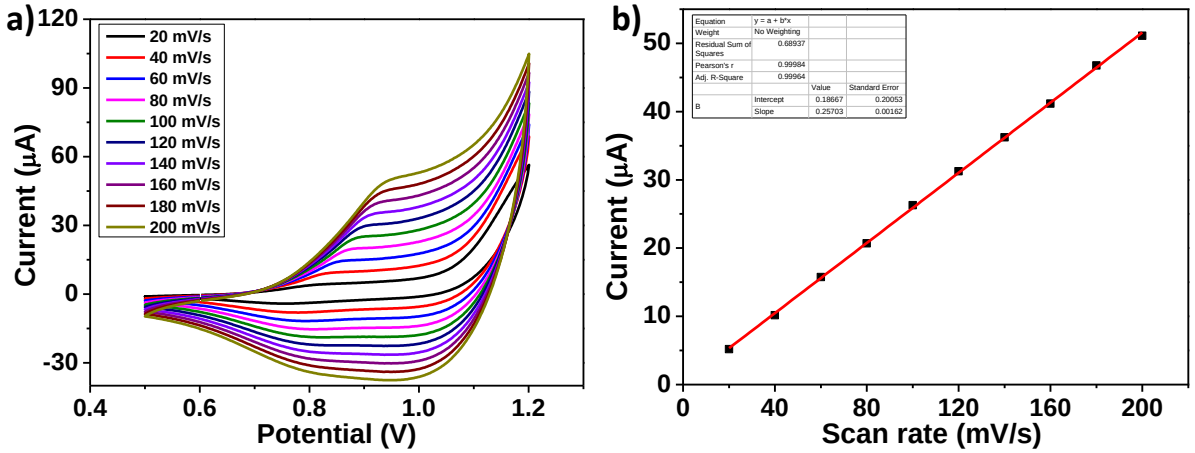

Figure 7.17. (a) Cyclic voltammetry response of MOF/GCE recorded in 0.1 M PBS (pH 7.04) in the presence of 10 µM NIC at different scan rates ranging from 20 mV/s to 200 mV/s, (b) linear relationship between peak current and scan rate.

Square wave voltammetry (SWV) technique was chosen to study the detailed electrochemical response of MOF towards nicotine. SWV technique is more sensitive than CV, which helps to analyze the current responses even at small concentrations. SWV was carried out in the potential range of 0.5 V to 1.0 V with a scan rate of 100 mV/s in 0.1 M PBS at pH 7.04. **Figure 7.18a** shows the SWV response of MOF toward nicotine, the anodic peak current increases with an increase in nicotine concentration ranging from 0 to 2.49 µM of nicotine. The peak current increase can be attributed to the increased nicotine content in the reaction and its migration to the MOF electrode surface. The oxidation peak current response was also recorded in higher concentration ranges, and it was found that the MOF sensor showed a good response in the wide linear range of 0 to 50 µM **(Figure 7.19a)**.

Further, to calculate the limit of detection (LOD), the peak current response was plotted against the concentration ranges of nicotine, as shown in **Figure 7.18b**. The calibration plot was obtained from the linear fitting of the data with R^2 value equal to 0.96. The LOD was calculated using the equation LOD = 3s/m, where s is the standard deviation (n = 3) and m is the slope obtained from the calibration curve.[10] Thus, the LOD calculated was found to be 0.25 µM. It is noteworthy that the MOF sensor shows an excellent sensing response towards nicotine with

high sensitivity and LOD compared to previously known MOF material and other reported materials in the literature **(Table 7.2)**.

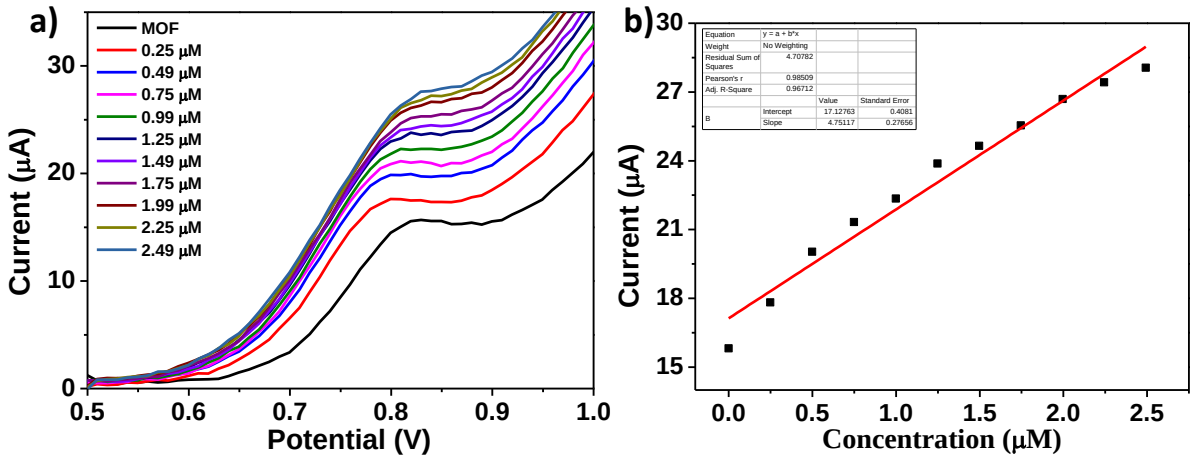

Figure 7.18. (a) Square wave voltammetry response of MOF/GCE recorded in 0.1 M PBS (pH 7.04) on the addition of nicotine in the concentration range of 0.25 µM to 2.49 µM and (b) calibration plot of current response vs. concentration of nicotine.

Table 7.2. Comparison of electrochemical sensors for nicotine determination.

Sensor	Material type	Technique	Linear range	LOD	Dual Sensor	Ref
CuWO4/rGO/ Nf immobilized GCE	rGO nanocomposite	Amperometry	0.1-0.9 µM	0.035 µM	No	**[10]**
Carbon Paste Electrode	Carbon	SWV	50-1000 µM	3.2 µM	No	**[44]**
MWCNTs/Cu NPs	Carbon nanotubes (CNTs)/ Cu nanoparticles (NPs)	CV	1-1000 µM	1.0 µM	No	**[45]**
TiO2/MI-PEDOT	Oxide	Amperometry	0-5000 µM	4.9 µM	No	**[46]**
GO-4-ATP-Au-PT/Au GCE	Au nanoparticles	SWV	1-30 µM	0.17 µM	No	**[47]**

PEDOT/GR/ GCE	Nanocomposite	Amperometry	0.5-1000 µM	0.047 µM	No	**[40]**
Ce NPs	Nanoparticles (NPs)	CV	4500 µM	0.094 µM	No	**[16]**
MONT-1	MOF	EIS	0-60 µM	23.3 µM	No	**[25]**
BITSH-1	**MOF**	**SWV**	**0-50 µM**	**0.25 µM**	**Yes**	**This work**

7.3.8. Real-time sensing studies

BITSH-1 was also explored as a real-time sensor for detecting nicotine levels in cigarette and urine samples. The real samples were prepared by diluting the cigarette sample using 0.1 M PBS buffer and ultrasonicated, followed by filtration to obtain a clear solution of nicotine dissolved in the buffer. Similarly, urine samples were diluted using 0.1 M PBS buffer and ultrasonicated. SWV experiments were then carried out under similar conditions with MOF/GCE as the working electrode in 0.1 M PBS buffer with subsequent additions of actual cigarette and urine samples. The nicotine content present was evaluated using the standard addition method.[43] The nicotine content detected in the cigarette sample without any spike was around 1.24 µM. In addition, we spiked the actual cigarette samples with standard nicotine solutions (0.74 to 1.3 µM), and the nicotine concentration was determined quantitatively using the calibration curve. Correspondingly, the urine samples were spiked with standard nicotine solutions in the concentration range of 0.49 µM to 2.49 µM **(Figure 7.19c, d)**. The selective sensing capability of the MOF towards nicotine was confirmed by studying the nicotine sensing ability of the sensor in the presence of other interfering analytes that can be present in a urine sample. Interferents such as sodium chloride (NaCl), potassium chloride (KCl), ammonium chloride (NH_4Cl), glucose (Glu), dopamine (DOP), and uric acid (UA) were chosen for the selectivity studies. The amperometric current response of MOF for nicotine in the presence of interferents was recorded at an applied potential of +0.85 V. It was observed that the addition of dilute nicotine solution (2 µM) produced a significant change in current intensity. In contrast, no difference was observed in adding a 100-fold excess concentration of interferents **(Figure 7.19b)**. Thus, ascertaining the high selectivity of **BITSH-1** in sensing nicotine and the applicability of the MOF sensor for real-time analysis.

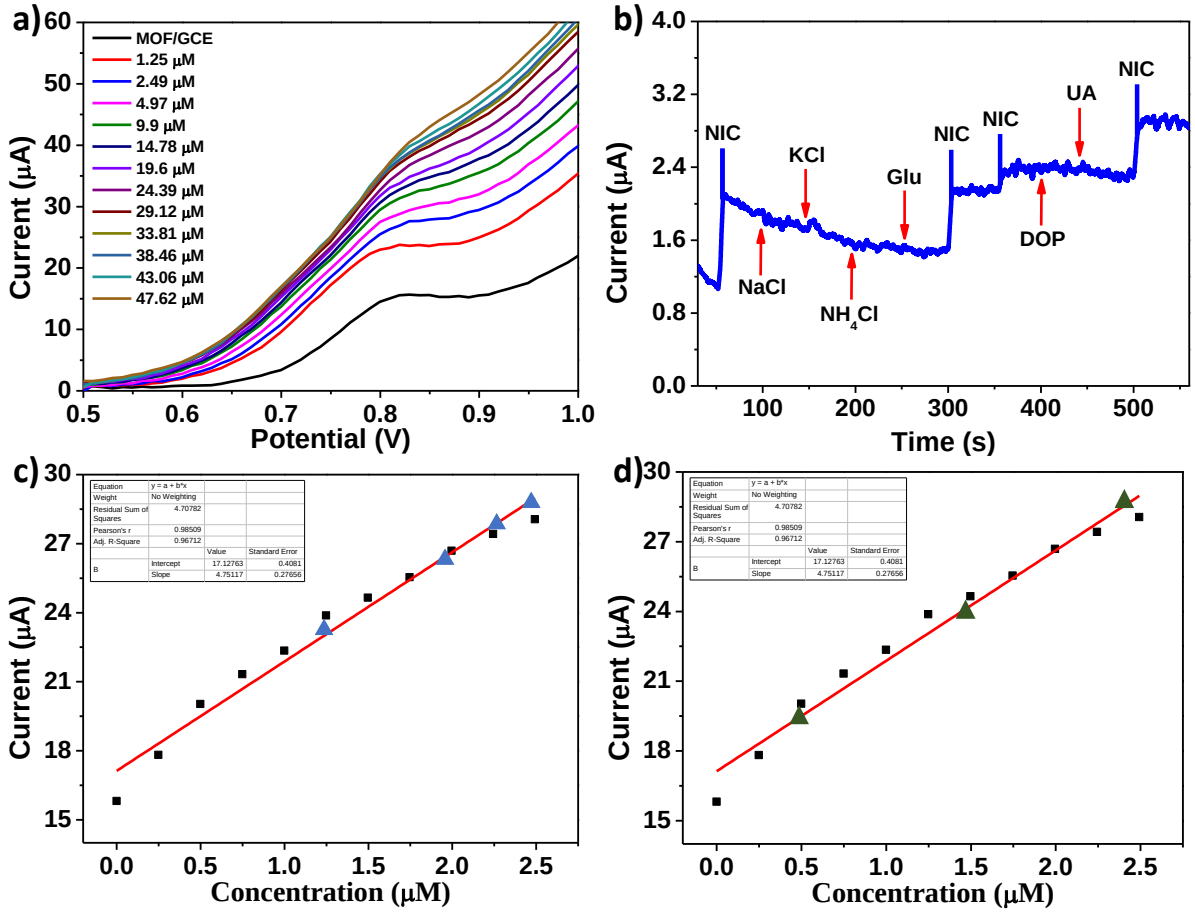

Figure 7.19. (a) Square wave voltammetry response of MOF/GCE recorded in 0.1 M PBS (pH 7.04) on the addition of nicotine in the concentration range of 1.25 µM to 47.62 µM. (b) Amperometric response of MOF/GCE recorded in 0.1 M PBS buffer (pH 7.04) on the addition of nicotine (2 µM) and 100-fold excess concentration of interferents at an applied potential of +0.85 V. Calibration curve of nicotine used for calculating the recovery concentrations of nicotine in (c) cigarette and (d) urine samples.

The nicotine content found after adding known concentration was correlated with the produced current value with the calibration graph (current vs. concentration) obtained using standard nicotine solutions. The relative error in determining the nicotine content in the real samples was not more than 0.2 %. The nicotine recovery values are 98-102 % which confirms the potential of MOF as a real-time sensor in detecting nicotine quantitatively from cigarette and urine samples **(Table 7.3)**.

Table 7.3. Determination of nicotine levels in cigarette and urine samples

Sample	Detected (µM)	Added (µM)	Found (µM)	Recovery (%)	RSD (%)
Cigarette	1.248	-	-	-	0.1
Cigarette + spiked		0.75	1.96	98	0.1
Cigarette + spiked		0.99	2.3	102	0.2
Cigarette + spiked		1.25	2.5	100	0.2
Urine	Not detected	-	-	-	-
Urine + spiked		0.49	0.48	98	0.2
Urine + spiked		1.49	1.48	99	0.1
Urine + spiked		2.49	2.45	98	0.2

7.4. Conclusions

We demonstrated that MOF could be used as an efficient sensor for the detection of nicotine. The rational design and synthesis resulted in a dual-functional sensor that is an equally good fluorescent and electrochemical sensor. The LODs obtained using both techniques are best for any MOF material. The excellent nicotine sensing ability of the MOF in the presence of other analytes and the nicotine recovery from actual cigarette samples confirm that a pure MOF-based nicotine sensor can be a valuable alternative to composite-based sensors prepared with the help of conducting materials. We believe this work will encourage the further development of various other MOF materials for the detection of nicotine and other harmful chemicals.

Conclusions and Future Perspectives

Conclusions

In summary, the results of this research work suggest that the MOFs are promising candidates for sensing applications. It further emphasizes on the potential of MOFs as resilient materials for practical applications in healthcare, industries, and the food processing sectors. The work presented in chapter 3 highlights a significant use of MOF materials in healthcare for monitoring obstructive sleep apnea (OSA) disorders. It also demonstrates the fabrication strategies employed to overcome the insulating nature of MOFs and utilize their excellent water adsorption properties in developing a flexible MOF-based breath sensor. A plausible mechanism has also been proposed to explain the sensing mMior of the MOF in monitoring human breath patterns. Similarly, chapter 4 demonstrated the potential of MOFs in monitoring trace moisture in ppm levels. The work presented in this chapter illustrates the fabrication of an ultra-low humidity sensor with high sensitivity and stability for glove-box related applications. Additionally, the MOF sensor also exhibits the ability to distinguish between polar and non-polar solvents. Detailed mechanistic insights into the exceptional sensing behavior of the MOF device have been thoroughly discussed.

The work presented in chapter 5 provides a detailed account of designing and synthesizing novel MOFs-**BITSH-1** and **BITSH-2**. These frameworks were studied for sensing biogenic amines and food spoilage indicators such as putrescine and cadaverine using fluorescence technique. The remarkable sensing behavior of these frameworks towards biogenic amines in both solution and solid state has been substantiated with comprehensive mechanistic insights. MOF membranes were prepared further to demonstrate the significant potential of these MOF systems for the real-time detection of biogenic amines in protein-rich foods. The work detailed in chapter 6 exhibits the potential of **BITSH-1** and **BITSH-2** to serve as versatile chemical sensors for the detection of ammonia. It also showcases their discriminative sensing behavior towards aliphatic and aromatic amines via "turn-off" and "turn-on" fluorescence behaviors, respectively. This discriminative sensing behavior of the MOF systems towards aliphatic and aromatic amines was further supported by DFT studies. Additionally, MOF pellets and mixed-matrix membranes were prepared to study the vapochromic sensing behavior towards amine vapors and on-site detection of ammonia from a lab-scale chemical reaction.

The findings presented in chapters 5 and 6 unveil opportunities for industrial applications by shaping MOFs into diverse forms, such as membranes, pellets, and thin films. This advancement paves the way for the potential commercialization of MOFs. The work described

in Chapter 7 emphasizes the significance of using fluorescence and electrochemical sensing approaches to analyze the sensing behavior of the MOF system towards nicotine. The MOF sensor exhibited the potential to detect the nicotine content in actual cigarette and urine samples. Nicotine sensing studies were further supported by XPS measurements. This work also demonstrates the sensing capability and selectivity of the MOF system towards nicotine even in the presence of other interfering analytes.

Future perspectives

Metal-Organic Frameworks (MOFs) represents a revolutionary class of materials with enormous potential across many domains. MOF chemistry has the potential to address the global challenges and advance towards a sustainable future. As MOFs continue to captivate scientific interest, ongoing research endeavors will likely contribute to a deeper understanding of their properties and open new avenues for further research. The potential future prospectives can include the following:

- Investigating MOF materials with good conductive properties, exceptional water adsorption capabilities and high pore volumes for breath sensing applications.
- Developing MOF membranes with high reversibility, durability and good stability will offer opportunities for the employment of MOFs as feasible sensors in food processing sectors and industries.
- Designing robust MOF systems specifically tailored for detecting harmful industrial effluents, toxic gases and VOCs.
- Developing flexible frameworks that can undergo structural changes in response to the external stimuli such as temperature, light, guest molecules and pressure. These frameworks can be potent materials for applications such as sensing, and separation.
- Developing MOF-based hybrid materials demonstrates synergistic effects in terms of electrical properties, stability and sensing abilities of MOFs. This approach enhances the feasibility of utilizing MOF materials in wearable sensors, electronic devices, and various industrial applications.
- Commercialization of MOFs is challenging and is limited by various factors such as feasibility, durability, scalability and high manufacturing cost of MOFs. However, these challenges can be addressed by developing highly stable and robust MOF materials with cost-effective starting materials. Additionally, the fabrication of MOF devices addresses challenges related to feasibility and operational aspects.

Bibliography

CHAPTER 1

[1] K. S. W. Sing, D. H. Everett, R. A. W. Haul, L. Moscou, R. A. Pierotti, J. Rouquerol and T. Siemieniewska, *Pure Appl. Chem.*, 1985, **57,** 603.

[2] J. Rouquerol, D. Avnir, C. W. Fairbridge, D. H. Everett, J. H. Haynes, N. Pernicone, J. D. F. Ramsay, K. S. W. Sing and K. K. Unger, *Pure Appl. Chem.,* 1994, **66,** 1739.

[3] D. W. Breck, Zeolite Molecular Sieves: Structure, Chemistry, and Use, *Wiley, New York.,* 1974.

[4] W. M. Meier, D. H. Olsen and C. Baerlocher, Atlas of Zeolite Structure Types, *Elsevier, London.,* 1996.

[5] P. B. Venuto, *Microporous Mater.,* 1994, **2,** 297-411.

[6] S. Sircar, T. C. Golden and M. B. Rao, *Carbon.,* 1996, **34,** 1.

[7] J. L. C. Rowsell and O. M. Yaghi, *Microporous Mesoporous Mater.,* 2004, **73,** 3-14.

[8] H. Furukawa, K. E. Cordova, M. O'Keeffe and O. M. Yaghi, *Science.,* 2013, **341**, 6149.

[9] (a) S. Kitagawa, R. Kitaura and S. I. Noro, *Angew. Chem. Int. Ed.,* 2004, **43,** 2334; (b) S. Kitagawa and R. Matsuda, *Coord. Chem. Rev.,* 2007, **251,** 2490.

[10] Z. X. Kang, L. L. Fan and D. F. Sun, *J. Mater. Chem. A.,* 2017, **5,** 10073-10091.

[11] P. Lama, H. Aggarwal, C. X. Bezuidenhout and L. J. Barbour, *Angew. Chem. Int. Ed.,* 2016, **55,** 13271-13275.

[12] K. Adil, Y. Belmabkhout, R. S. Pillai, A. Cadiau, P. M. Bhatt, A. H. Assen, G. Maurin and M. Eddaoudi, *Chem. Soc. Rev.,* 2017, **46,** 3402-3430.

[13] P. Horcajada, R. Gref, T. Baati, P. K. Allan, G. Maurin, P. Couvreur, G. Ferey, R. E. Morris and C. Serre, *Chem. Rev.,* 2012, **112,** 1232-1268.; P. Garcia Garcia, M. Muller and A. Corma, *Chem. Sci.,* 2014, **5,** 2979-3007.

[14] H. Li, M. Eddaoudi, M. O'Keeffe and O. M. Yaghi, *Nature.,* 1999, **402,** 276.

[15] S. Kitagawa, R. Kitaura and S. I Noro, *Angew. Chem. Int. Ed.,* 2004, **43,** 2334.

[16] (a) G. A. Tompsett, W. C. Conner and K. S. Yngvesson, *Chem.Phys.Chem.,* 2006, **7,** 296; (b) S. H. Jhung, J. W. Yoon, J. S. Hwang, A. K. Cheetham and J. S. Chang, *Chem. Mater.,* 2005, **17,** 4455.

[17] A. N. Khlobystov, A. J. Blake, N. R. Champness, D. A. Leme novskii, A. G. Majouga, N. V. Zyk and M. Schroder, *Coord. Chem.Rev*., 2001, **222,** 155-192.

[18] M. Munakata, *Adv. Inorg. Chem.,* 1998, **46,** 173-303.

[19] S. Kitagawa and M. Munakata, *Trends Inorg. Chem.*, 1993, **3,** 437-462.

[20] L. Pan, K. M. Adams, H. E. Hernandez, X. Wang, C. Zheng, Y. Hattori and K. Kaneko, J. *Am. Chem. Soc.,* 2003, **125,** 3062-3067.

[21] T. M. Reineke, M. Eddaoudi, M. Fehr, D. Kelley and O. M. Yaghi, *J. Am. Chem. Soc.,* 1999, **121,** 1651-1657.

[22] S. R. Batten, B. F. Hoskins and R. Robson, *J. Am. Chem. Soc.,* 1995, **117,** 5385-5386.

[23] W. L. Leong and J. J. Vittal, *Chem. Rev.*, 2011, **111,** 688.

[24] M. C. Brandys and R. J. Puddephatt, *J. Am. Chem. Soc.,* 2001, **123,** 4839.

[25] L. F. Szczepura, C. P. Galloway, Y. Zheng, P. Han, A. L. Rheingold, S. R. Wilson and T. B. Rauchfuss, *Angew. Chem. Int. Ed. Engl.,* 1995, **34,** 1890.

[26] S. Kitagawa and R. Kitaura, *Inorg. Chem.,* 2002, **23,** 101-126.

[27] M. Kondo, T. Okubo, A. Asami, S. Noro, T. Yoshitomi, S. Kitagawa, T. Ishii, H. Matsuzaka and K. Seki, *Angew. Chem.,* 1999, **111,** 190-193.

[28] S. Kitagawa and R. Matsuda, *Coord. Chem. Rev.,* 2007, **251,** 2490-2509.

[29] C. D. Wu and W. Lin, *Inorg. Chem.,* 2005, **44,** 1178.

[30] S. Kitagawa and S. Noro, *Compreh. Coord. Chem.*, 2004, **7,** 231.

[31] A. Y. Robin and K. M. Fromm, *Coord. Chem. Rev.,* 2006, **250,** 2127.

[32] Y. R. Xie, H. Zhao, X. S. Wang, Z. R. Qu, R. G. Xiong, X. Xue, Z. Xue and X. Z. You, *Eur. J. Inorg. Chem*., 2003, 3712.

[33] K. Uemura, S. Kitagawa, K. Fukui and K. Saito. *J. Am. Chem. Soc.*, 2004, **126,** 3817.

[34] Z. Spichal, M. Necas, J. Pinkas and J. Novosad. *Inorg. Chem.*, 2004, **43,** 2776.

[35] X. M. Ouyang, B. L. Fei, T. A. Okamura, H.-W. Bu, W. Y. Sun, W. X. Tang and N. Ueyama, *Eur. J. Inorg. Chem.,* 2003, 618.

[36] E. Q. Gao, Y. X. Xu and C. H. Yan, *Cryst. Eng. Commun.,* 2004, **6,** 298.

[37] M. Du and X. J. Zhao, *Inorg. Chem. Commun.*, 2004, **7,** 1056.

[38] Z. Spichal and M. Necas, J. Pinkas, *Inorg. Chem.,* 2005, **44,** 2074.

[39] Z. F. Chen, R. G. Xiong, B. F. Abrahams, X. Z. You and C. M. Che. *J. Chem. Soc. Dalton Trans.*, 2001, 2453.

[40] S. Noro, S. Kitagawa, M. Kondo and K. Seki. *Angew. Chem. Ed. Engl.*, 2000, **39,** 2082.

[41] J. Tao, M. L. Tong and X. M. Chen, *J. Chem. Soc. Dalton Trans.*, 2000, 3669.

[42] M. Eddaoudi, D. B. Moler, H. Li, B. Chen, T. M. Reineke, M. O'Keefe and O. M. Yaghi, *Acc. Chem. Res.*, 2001, **34,** 319.

[43] W. Lu, Z. Wei, Z. Y. Gu, T. F. Liu, J. Park, J. Park, J. Tian, M. Zhang, Q. Zhang, T. Gentle III, M. Boscha and H. C. Zhou, *Chem. Soc. Rev.*, 2014, **43,** 5561.

[44] M. Eddaoudi, J. Kim, N. Rosi, D. Vodak, J. Wachter, M. O'Keeffe and O. M. Yaghi, *Science.*, 2002, **295,** 469.

[45] H. K. Chae, D. Y. Siberio-Perez, J. Kim, Y. Go, M. Eddaoudi, A. J. Matzger, M. O'Keeffe and O. M. Yaghi, *Nature.*, 2004, **427,** 523.

[46] X. Zhao, B. Xiao, A.J. Fletcher, K.M. Thomas, D. Bradshaw and M. J. Rosseinsky, *Science.*, 2004, **306,** 1012.

[47] M. Dinca, A. F. Yu and J. R. Long, *J. Am. Chem. Soc.*, 2006, **128,** 8904.

[48] K. Uemura, K. Saito, S. Kitagawa and H. Kita, *J. Am. Chem. Soc.*, 2006, **128,** 16122.

[49] S. S. Kaye and J. R. Long, *J. Am. Chem. Soc.*, 2005, **127,** 6506.

[50] S. Kitagawa and M. Kondo, *Bull. Chem. Soc. Jpn.* 1998, **71,** 1739-1753.

[51] G. P. Yang, L. Hou, L. F. Ma and Y. Y. Wang, *Cryst.Eng.Comm.*, 2013, **15,** 2561-2578.

[52] S. Kaushal, G. Kaur, J. Kaur and P. P. Singh, *Mater. Adv.* 2021, **2,** 7308-7335.

[53] C. C. Wang, H. P. Jing, P. Wang and S. J. Gao, *J. Mol. Struct.*, 2015, **1080,** 44-51.

[54] C. W. Huang, V. H. Nguyen, S. R. Zhou, S. Y. Hsu, J. X. Tan, K. C and W. Wu, *Sustain. Energy Fuels.*, 2020, **4,** 504-521.

[55] J. Bedia, V. Muelas Ramos, M. Penas Garzon, A. Gomez Aviles, J. J. Rodriguez and C. Belver, *Catalysts.*, 2019, **9,** 52.

[56] R. I. Walton. *Chem. Soc. Rev.*, 2002, **31,** 230-238.

[57] V. F. Yusuf, N. I. Malek and S. K. Kailasa. *ACS Omega.*, 2022, **7,** 44507-44531.

[58] S. R. Halper, L. Do, J. R. Stork and S. M. Cohen, *J. Am. Chem. Soc.*, 2006, **128,** 15255-15268.

[59] Y. Wu, A. Kobayashi, G. J. Halder, V. K. Peterson, K. W. Chapman, N. Lock, P. D. Southon and C. J. Kepert, *Angew. Chem. Int. Ed.*, 2008, **47,** 8929-8932.

[60] N. A. Khan and S. H. Jhung, *Coord. Chem. Rev.*, 2015, **285,** 11-23.

[61] Z. Ni and R. I. Masel, *J. Am. Chem. Soc.*, 2006, **128,** 12394-12395.

[62] J. H. Bang and K. S. Suslick, *Adv. Mater.*, 2010, **22,** 1039-1059.

[63] S. A. Razavi, M. Y. Masoomi and A. Morsali, *Ultrason. Sonochem.*, 2017, **37,** 502-508.

[64] M. Klimakow, P. Klobes, K. Redemann and F. Emmerling, *Microporous Mesoporous Mater.*, 2012, **154,** 113-118.

[65] H. Li, K. Wang, Y. Sun, C. T. Lollar, J. Li and H. C. Zhou, *Mater. Today.*, 2018, **21,** 108-121.

[66] T. Rodenas, I. Luz, G. Prieto, B. Seoane, H. Miro, A. Corma, F. Kapteijn, F. X. Llabres i Xamena and J. Gascon, *Nat. Mater.*, 2015, **14,** 48-55.

[67] M. Ding, R. W. Flaig, H. L. Jiang and O. M. Yaghi, *Chem. Soc. Rev.*, 2019, **48,** 2783-2828.

[68] B. Li, H. M. Wen, W. Zhou, J. Q. Xu and B. Chen, *Chem.*, 2016, **1,** 557-580.

[69] C. A. Trickett, T. M. Osborn Popp, J. Su, C. Yan, J. Weisberg, A. Huq, P. Urban, J. Jiang, M. J. Kalmutzki, Q. Liu, J. Baek, M. P. Head Gordon, G. A. Somorjai, J. A. Reimer and O. M. Yaghi, *Nat. Chem.*, 2019, **11,** 170-176.

[70] Q. Wang and D. Astruc, *Chem. Rev.*, 2020, **120,** 1438-1511.

[71] A. Dhakshinamoorthy, Z. Li and H. Garcia, *Chem. Soc. Rev.*, 2018, **47,** 8134-8172.

[72] Q. Yang, Q. Xu and H. L. Jiang, *Chem. Soc. Rev.*, 2017, **46,** 4774-4808.

[73] D. Li, M. Kassymova, X. Cai, S. Q. Zang and H. L. Jiang, *Coord. Chem. Rev.*, 2020, **412,** 213262.

[74] V. Stavila, A. A. Talin and M. D. Allendorf, *Chem. Soc. Rev.*, 2014, **43,** 5994-6010.

[75] H. D. Lawson, S. P. Walton and C. Chan, *ACS Appl. Mater. Interfaces.*, 2021, **13,** 7004-7020.

[76] W. P. Lustig and J. Li, *Coord. Chem. Rev.*, 2018, **373,** 116-147.

[77] Y. Cui, J. Zhang, H. He and G. Qian, *Chem. Soc. Rev.*, 2018, **47,** 5740-5785.

[78] Y. Cui, Y. Yue, G. Qian and B. Chen, *Chem. Rev.*, 2012, **112,** 1126-1162.

[79] J. Zhou and B. Wang, *Chem. Soc. Rev.*, 2017, **46,** 6927-6945.

[80] L. Kong, M. Zhong, W. Shuang, Y. Xu and X. H. Bu, *Chem. Soc. Rev.*, 2020, **49,** 2378-2407.

[81] H. Y. Li, S. N. Zhao, S. Q. Zang and J. Li. *Chem. Soc. Rev.*, 2020, **49**, 6364-6401.

[82] S. Yuan, L. Feng, K. Wang, J. Pang, M. Bosch, C. Lollar, Y. Sun, J. Qin, X. Yang, P. Zhang, Q. Wang, L. Zou, Y. Zhang, L. Zhang, Y. Fang, J. Li and H. C. Zhou, *Adv. Mater.*, 2018, **30,** 1704303.

[83] M. Ding, X. Cai and H. L. Jiang, *Chem. Sci.*, 2019, **10,** 10209-10230.

[84] M. K. Smith, K. E. Jensen, P. A. Pivak and K. A. Mirica, *Chem. Mater.*, 2016, **28,** 5264-5268.

[85] M. G. Campbell, D. Sheberla, S. F. Liu, T. M. Swager and M. Dinca, *Angew. Chem. Int. Ed.*, 2015, **54,** 4349-4352.

[86] M. S. Yao, J. J. Zheng, A. Q. Wu, G. Xu, S. S. Nagarkar, G. Zhang, M. Tsujimoto, S. Sakaki, S. Horike, K. Otake and S. Kitagawa, *Angew. Chem., Int. Ed.*, 2020, **59,** 172-176.

[87] V. Rubio Gimenez, N. Almora Barrios, G. Escorcia Ariza, M. Galbiati, M. Sessolo, S. Tatay and C. Marti Gastaldo, *Angew. Chem. Int. Ed.*, 2018, **57,** 15086-15090.

[88] M. G. Campbell, S. F. Liu, T. M. Swager and M. Dinca, *J. Am. Chem. Soc.*, 2015, **137,** 13780-13783.

[89] E. X. Chen, H. Yang and J. Zhang, *Inorg. Chem.*, 2014, **53,** 5411-5413.

[90] M. S. Yao, X. J. Lv, Z. H. Fu, W. H. Li, W. H. Deng, G. D. Wu and G. Xu, *Angew. Chem. Int. Ed.*, 2017, **56,** 16510-16514.

[91] S. V. Patel, T. E. Mlsna, B. Fruhberger, E. Klaassen, S. Cemalovic and D. R. Baselt. *Sens. Actuators B.*, 2003, **96,** 541-553.

[92] E. Zampetti, S. Pantalei, A. Pecora, A. Valletta, L. Maiolo, A. Minotti, A. Macagnano, G. Fortunato and A. Bearzotti, *Sens. Actuators B. Chem.*, 2009, **143,** 302-307.

[93] S. Zeinali, S. Homayoonnia and G. Homayoonnia, *Sens. Actuators B. Chem.*, 2019, **278,** 153-164.

[94] Q. N. Minh, H. D. Tong, A. Kuijk, F. van de Bent, P. Beekman and C. J. M. van Rijn, *RSC Adv.*, 2017, **7,** 50279.

[95] H. Yuan, N. Li, W. Fan, H. Cai and D. Zhao, *Adv. Sci.*, 2022, **9**, 2104374.

[96] O. Yassine, O. Shekhah, A. H. Assen, Y. Belmabkhout, K. N. Salama and M. Eddaoudi, *Angew. Chem., Int. Ed.*, 2016, **55**, 15879.

[97] H. Yuan, J. Tao, N. Li, A. Karmakar, C. Tang, H. Cai, S. J. Pennycook, N. Singh and D. Zhao, *Angew. Chem., Int. Ed.*, 2019, **58**, 14089.

[98] V. Chernikova, O. Yassine, O. Shekhah, M. Eddaoudi and K. N. Salama, *J. Mater. Chem. A.,* 2018, **6**, 5550.

[99] X. Chen, Y. Wang, Y. Zhang, Z. Chen, Y. Liu, Z. Li and J. Li, *Anal. Chem.,* 2014, **86,** 4278-4286.

[100] X. Fang, J. F. Liu, J. Wang, H. Zhao, H. X. Ren and Z. X. Li, *Biosens. Bioelectron.,* 2017, **97,** 218-225.

[101] X. Q. Wu, J. G. Ma, H. Li, D. M. Chen, W. Gu, G. M. Yang and P. Cheng. *Chem. Commun.,* 2015, **51,** 9161-9164.

[102] D. Sheberla, L. Sun, M.A. Blood-Forsythe, S. Er, C. R. Wade, C. K. Brozek, A. Aspuru Guzik and M. Dinca, *J. Am. Chem. Soc.,* 2014, **136,** 8859-8862.

[103] M. G. Campbell, D. Sheberla, S. F. Liu, T. M. Swager and M. Dinca, *Angew. Chem. Int. Ed.,* 2015, **54,** 4349-4352.

[104] Y. Wang, C. Hou, Y. Zhang, F. He, M. Z. Liu and X. L. Li. *J. Mater. Chem. B.,* 2016, **4,** 3695-3702.

[105] C. Zhang, X. R. Wang, M. Hou, X. Y. Li, X. L. Wu and J. Ge, *ACS Appl. Mater. Interfaces.,* 2017, **9,** 13831-13836.

[106] X. Wang, Q. X. Wang, Q. H. Wang, F. Gao, F. Gao, Y. Z. Yang and H. X. Guo, *ACS Appl. Mater. Interfaces.,* 2014, **6,** 11573-11580.

[107] Z. D. Xu, L. Z. Yang and C. L. Xu, *Anal. Chem.,* 2015, **87,** 3438-3444.

[108] S. Kempahanumakkagari, K. Vellingiri, A. Deep, E. E. Kwon, N. Bolan and K. H. Kim, *Coord. Chem. Rev.,* 2018, **357,** 105-129.

[109] T. Ma, H. Li, J. G. Ma and P. Cheng, *Dalton Trans.,* 2020, **49,** 17121-17129.

[110] S. Tajik, H. Beitollahi, F. G. Nejad, K. O. Kirlikovali, Q. Van Le, H. W. Jang, R. S. Varma, O. K. Farha and M. Shokouhimehr, *Cryst. Growth Des.,* 2020, **20,** 7034-7064.

[111] H. X. Guo, D. F. Wang, J. H. Chen, W. Weng, M. Q. Huang and Z. S. Zheng, *Chem. Eng. J.,* 2016, **289,** 479-485.

[112] S. Dong, G. Suo, N. Li, Z. Chen, L. Peng, Y. Fu, Q. Yang and T. Huang, *Sens. Actuators B. Chem.,* 2016, **222,** 972-979.

[113] B. Li, H. T. Fan, S. Q. Zang, H. Y. Li and L. Y. Wang, *Coord. Chem. Rev.,* 2018, **377,** 307-329.

[114] M. Pan, W. M. Liao, S. Y. Yin, S. S. Sun and C. Y. Su, *Chem. Rev.,* 2018, **118,** 8889-8935.

[115] Y. Cui, Y. Yue, G. Qian and B. Chen, *Chem. Rev.,* 2012, **112,** 1126-1162.

[116] Z. Hu, B. J. Deibert and J. Li, *Chem. Soc. Rev.,* 2014, **43,** 5815-5840.

[117] W. P. Lustig, S. Mukherjee, N. D. Rudd, A. V. Desai, J. Li and S. K. Ghosh, *Chem. Soc. Rev.,* 2017, **46,** 3242-3285.

[118] X. D. Wang and O. S. Wolfbeis. *Chem. Soc. Rev.,* 2014, **43,** 3666-3761.

[119] Y. Zhang, S. Yuan, G. Day, X. Wang, X. Yang and H. C. Zhou, *Coord. Chem. Rev.,* 2018, **354,** 28-45.

[120] S. Wu, H. Min, W. Shi and P. Cheng, *Adv. Mater.,* 2020, **32,** 1805871.

[121] W. Sun, M. Li, J. Fan and X. Peng, *Acc. Chem. Res.,* 2019, **52,** 2818.

[122] X. Y. Sun, T. Liu, J. Sun and X. J. Wang, *RSC Adv.,* 2020, **10,** 10826.

[123] G. Yang, X. Jiang, H. Xu and B. Zhao, *Small.,* 2021, **17,** 2005327.

[124] D. Dinda, A. Gupta, B. K. Shaw, S. Sadhu and S. K. Saha, *ACS Appl. Mater. Interfaces.,* 2014, **6,** 10722.

[125] B. F. Hoskins and R. Robson, *J. Am. Chem. Soc.,* 1989, **111,** 5962.

[126] W. Liu, T. Jiao, Y. Li, Q. Liu, M. Tan, H. Wang and L. Wang, *J. Am. Chem. Soc.,* 2004, **126,** 2280.

[127] A. Lan, K. Li, H. Wu, D. H. Olson, T. J. Emge, W. Ki, M. Hong and J. Li, *Angew. Chem. Int. Ed.,* 2009, **48,** 2334.

[128] X. Zheng, L. Zhou, Y. Huang, C. Wang, J. Duan, L. Wen, Z. Tian and D. Li, *J. Mater. Chem. A.,* 2014, **2,** 12413.

[129] S. S. Nagarkar, A. V. Desai and S. K. Ghosh, *Chem. Commun.,* 2014, **50,** 8915.

[130] M. Zhang, G. Feng, Z. Song, Y. P. Zhou, H. Y. Chao, D. Yuan, T. T. Y. Tan, Z. Guo, Z. Hu, B. Z. Tang, B. Liu and D. Zhao, *J. Am. Chem. Soc.,* 2014, **136,** 7241.

[131] W. Liu, Y. Wang, L. Song, M. A. Silver, J. Xie, L. Zhang, L. Chen, J. Diwu, Z. Chai and S. Wang, *Talanta.,* 2019, **196,** 515.

[132] B. Li, X. Chen, P. Hu, A. Kirchon, Y. M. Zhao, J. Pang, T. Zhang and H. C. Zhou, *ACS Appl. Mater. Interfaces.,* 2019, **11,** 8227.

CHAPTER 3

[1] H. Furukawa, K. E. Cordova, M. O'Keeffe and O. M. Yaghi, *Science.,* 2013, **341,** 1230444.

[2] Z. X. Kang, L. L. Fan and D. F. Sun, *J. Mater. Chem. A.,* 2017, **5**, 10073-10091.

[3] P. Lama, H. Aggarwal, C. X. Bezuidenhout and L. J. Barbour, *Angew. Chem. Int. Ed.,* 2016, **55,** 13271-13275.

[4] K. Adil, Y. Belmabkhout, R. S. Pillai, A. Cadiau, P. M. Bhatt, A. H. Assen, G. Maurin and M. Eddaoudi, *Chem. Soc. Rev.*, 2017, **46,** 3402-3430.

[5] P. Horcajada, R. Gref, T. Baati, P. K. Allan, G. Maurin, P. Couvreur, G. Ferey, R. E. Morris and C. Serre, *Chem. Rev.*, 2012, **112,** 1232-1268.; P. Garcia-Garcia, M. Muller and A. Corma, *Chem. Sci.*, 2014, **5**, 2979-3007.

[6] H. Li, M. Eddaoudi, M. O'Keeffe and O. M. Yaghi, *Nature.*, 1999, **402,** 276-279.

[7] M. Bosch, S. Yuan, W. Rutledge and H. C. Zhou, *Acc. of Chem. Res.*, 2017, **50,** 857-865.

[8] P. Samanta, A. V. Desai, S. Let and S. K. Ghosh, *ACS Sustainable Chem. Eng.*, 2019, **7,** 7456-7478.

[9] D. J. Wales, J. Grand, V. P. Ting, R. D. Burke, K. J. Edler, C. R. Bowen, S. Mintova and A.D. Burrows, *Chem. Soc. Rev.*, 2015, **44,** 4290-4321.

[10] A. Mallick, A. M. El-Zohry, O. Shekhah, J. Yin, J. T. Jia, H. Aggarwal, A. H. Emwas, O. F. Mohammed and M. Eddaoudi, *J. Am. Chem. Soc.*, 2019, **141,** 7245-7249.

[11] Z. Hu, B. J. Deibert and J. Li, *Chem. Soc. Rev.,* 2014, **43,** 5815-5840.; R. Goswami, S. C. Mandal, N. Seal, B. Pathak and S. Neogi, *J. Mater. Chem. A.*, 2019, **7**, 19471-19484.

[12] N. R. Jalal, T. Madrakian, A. Afkhami and A. Ghoorchian, *ACS Appl. Mater. Interfaces.,* 2020, **12,** 4859-4869.

[13] H. Yamagiwa, S. Sato, T. Fukawa, T. Ikehara, R. Maeda, T. Mihara and M. Kimura, *Sci. Rep.*, 2015, **4,** 6247.

[14] L. E. Kreno, K. Leong, O. K. Farha, M. Allendorf, R. P. Van Duyne and J. T. Hupp, *Chem. Rev.*, 2012, **112,** 1105-1125.

[15] S. Khatua and P. Biswas, *ACS App. Mater. Interfaces.*, 2020, **12,** 22335-22346.

[16] S. Achmann, G. Hagen, J. Kita, I. M. Malkowsky, C. Kiener and R. Moos, *Sensors.*, 2009, **9,** 1574-1589.

[17] C. H. Chuang and C. W. Kung, *Electroanalysis.*, 2020, **32,** 1885-1895.

[18] N. Hanikel, M.S. Prévot and O.M. Yaghi, *Nat. Nanotechnol.*, 2020, **15,** 348-355.

[19] H. Kim, S. Yang, S. R. Rao, S. Narayanan, E. A. Kapustin, H. Furukawa, A.S. Umans, O. M. Yaghi and E. N. Wang, *Science.*, 2017, **356,** 430-434.

[20] H. Furukawa, F. Gándara, Y. B. Zhang, J. Jiang, W. L. Queen, M.R. Hudson and O.M. Yaghi, *J. Am. Chem. Soc.*, 2014, **136,** 4369-4381.

[21] K. N. Chappanda, O. Shekhah, O. Yassine, S. P. Patole, M. Eddaoudi and K. N. Salama, *Sens. Actuators., B,* 2018, **257,** 609-619.

[22] A. Weiss, N. Reimer, N. Stock, M. Tiemann and T. Wagner, *Microporous Mesoporous Mater.*, 2016, **220,** 39-43.

[23] S. M. Towsif Abtab, D. Alezi, P. M. Bhatt, A. Shkurenko, Y. Belmabkhout, H. Aggarwal, L. J. Weseliński, N. Alsadun, U. Samin, M. N. Hedhili and M. Eddaoudi, *Chem.*, 2018, **4,** 94-105.

[24] Y. Yang, X. Yang, Y. Tan and Q. Yuan, *Nano Res.*, 2017, **10,** 1560-1583.

[25] V. C. De Cock, M. Abouda, S. Leu, D. Oudiette, E. Roze, M. Vidailhet, T. Similowski and I. Arnulf, *Sleep Med.*, 2010, **1,** 247-252.

[26] A. S. Shamsuzzaman, B. J. Gersh and V. K. Somers, *Jama.*, 2003, **290,** 1906-1914.

[27] W. Lee, S. Nagubadi, M. H. Kryger and B. Mokhlesi, *Expert Rev. Respir. Med.*, 2008, **2,** 349-364.

[28] T. Young, P. E. Peppard and S. Taheri, *J. Appl. Physiol.*, 2005, **99,** 1592-1599.

[29] M. Shokoueinejad, C. Fernandez, E. Carroll, F. Wang, J. Levin, S. Rusk and M. Teodorescu, *Physiol. Meas.*, 2017, **38,** R204.

[30] C. Li, V. M. Lubecke, O. Boric-Lubecke and J. Lin, *IEEE Trans. Microw. Theroy Tech.*, 2013, **61,** 2046-2060.

[31] V. Selamneni and P. Sahatiya, *IEEE Sens. J.*, 2019, **20,** 3452-3459.

[32] S. Kanaparthi, *Electroanalysis.*, 2017, **29,** 2680-2684.

[33] J. Canivet, A. Fateeva, Y. Guo, B. Coasne and D. Farrusseng, *Chem. Soc. Rev.*, 2014, **43,** 5594-5617.

[34] S. K. Bhardwaj, N. Bhardwaj, R. Kaur, J. Mehta, A. L. Sharma, K.-H. Kim and A. Deep, *J. Mater. Chem. A.*, 2018, 6, 14992-15009.

[35] K. T. Butler, C. H. Hendon and A. Walsh, *J. Am. Chem. Soc.*, 2014, **136,** 2703-2706.

[36] Z. G. Gu, L. Heinke, C. Woll, T. Neumann, W. Wenzel, Q. Li, K. Fink, O. D. Gordan and D. R. T. Zahn, *Appl. Phys. Lett.*, 2015, **107,** 183301.

[37] J. W. Jiang, *Frontiers of Physics*, 2015, **10,** 287-302.

[38] B. Du, D. Yang, X. She, Y. Yuan, D. Mao, Y. Jiang and F. Lu, *Sensor. Actuat. B-Chem.*, 2017, **251,** 180-184.

[39] T. Li and G. Galli, *J. Phys. Chem., C*, 2007, **111,** 16192-16196.

[40] P. Chowdhury, C. Bikkina, D. Meister, F. Dreisbach and S. Gumma, *Microporous Mesoporous Mater.*, 2009, **117,** 406-413.

[41] P. M. Schoenecker, C. G. Carson, H. Jasuja, C. J. J. Flemming and K. S. Walton, *Ind. Eng. Chem. Res.*, 2012, **51,** 6513-6519.

[42] G. Ananya, N. Pranati and S. Ramaprabhu, *Int. J. Hydrogen Energ.*, 2016, **41,** 3974-3980.

[43] H. Sun, O.A. Zelekew, X. Chen, Y. Guo, D. H. Kuo, Q. Lu and J. Lin, *RSC Adv.*, 2019, **9,** 31828-31839.

[44] A. Gigot, M. Fontana, M. Serrapede, M. Castellino, S. Bianco, M. Armandi, B. Bonelli, C.F. Pirri, E. Tresso and P. Rivolo, *ACS Appl. Mater. Interfaces.*, 2016, **8,** 32842-32852.

[45] J. M. Yun, Y. J. Noh, C. H. Lee, S. I. Na, S. Lee, S. M. Jo and H. I. Joh, D. Y. Kim, *Small.*, 2014, **10,** 2319-2324.

[46] P. Küsgens, M. Rose, I. Senkovska, H. Frode, A. Henschel, S. Siegle and S. Kaskel, *Microporous and Mesoporous Mater.*, 2009, **120,** 325-330.

[47] N. Andre, S. Druart, P. Gerard, R. Pampin, L. Moreno-Hagelseib, T. Kezai, L.A. Francis, D. Flandre and J. Raskin, *IEEE Sens. J.*, 2010, 10, 178-184.

[48] J. Wu, Y-M. Sun, Z. Wu, X. Li, N. Wang, K. Tao, and G. P. Wang, ACS Appl. Mater. Interfaces., 2019, **11,** 4242-4251.

[49] U. Kang and K. D. Wise, *IEEE Trans. Electr. Dev.*, 2000, **47,** 702-710.

[50] J. Dai, H. Zhao, X. Lin, S. Liu, Y. Liu, X. Liu and T. Zhang, *ACS Appl. Mater. Interfaces.*, 2019, **11,** 6483-6490.

[51] Z. Duan, Y. Jiang, M. Yan, S. Wang, Z. Yuan, Q. Zhao, P. Sun, G. Xie, X. Du and H. Tai, Facile, *ACS Appl. Mater. Interfaces.*, 2019, **11,** 21840-21849.

[52] C. Zhou, X. Zhang, N. Tang, Y. Fang, H. Zhang and X. Duan, *Nanotechnology.*, 2020, **31,** 125302.

[53] G. Carotenuto and C. Camerlingo, *6th International Electronic Conference on Sensors and Applications.*, 2019, **42,** 6628.

[54] H. Guo, C. Lan, Z. Zhou, P. Sun, D. Wei and C. Li, *Nanoscale.*, 2017, **9,** 6246-6253.

[55] N. Li, X. D. Chen, X. P. Chen, X. Ding and X. Zhao, *IEEE Electron Device Letters.*, 2017, **38,** 806-809.

[56] J. B. DeCoste, G.W. Peterson, B. J. Schindler, K. L. Killops, M. A. Browe and J. J. Mahle, *J. Mater. Chem. A.*, 2013, **1,** 11922-11932.

[57] N. C. Jeong, B. Samanta, C. Y. Lee, O. K. Farha and J. T. Hupp, *J. Am. Chem. Soc.*, 2012, **134,** 51-54.

[58] M. A. Russo, D. M. Santarelli and D. O'Rourke, *Breathe.*, 2017, **13**, 298-309.

[59] T. Young, P. E. Peppard and D. J. Gottlieb, *Am. J. Respir. Crit. Care Med*., 2002, **165,** 1217-1239.

CHAPTER 4

[1] S. Kolpakov, N. Gordon, C. Mou and K. Zhou, Sensors. 2014, 14, 3986-4013.

[2] D. Zhang, Y. Sun, P. Li and Y. Zhang, ACS Appl. Mater. Interfaces. 2016, 8, 14142-14149.

[3] K. Sharma, N. Alam and S. Islam, Nanoscale Adv. 2020, 2, 2564-2576.

[4] M. Pandey, P. Mishra, D. Saha, K. Sengupta, K. Jain and S. Islam, J. Sol. -Gel Sci. Technol. 2013, 68, 317-323.

[5] L. Kumar, T. Islam and S. C. Mukhopadhyay, Electronics. 2017, 6, 41.

[6] T. Islam, L. Kumar and S. A. Khan, Sens. Actuators, B. 2012, 173, 377-384.

[7] L. Kumar, D. Saha, S. A. Khan, K. Sengupta and T. Islam, IEEE Sens. J. 2011, 12, 1625-1632.

[8] T. Islam, M. R. Mahboob and S. A. Khan, IEEE Sens. J. 2014, 15, 3004-3013.

[9] V. Pascanu, G. González Miera, A. K. Inge and B. Martín-Matute, J. Am. Chem. Soc. 2019, 141, 7223-7234.

[10] T. Leelasree, M. Dixit and H. Aggarwal, Chem. Mater. 2023, 35, 416-423.

[11] T. Leelasree, S. Goel and H. Aggarwal, ACS Appl. Nano Mater. 2022, 5, 16753-16759.

[12] D. P. Van Heerden, V. J. Smith, H. Aggarwal and L. J. Barbour, Angew. Chem. Int. Ed. 2021, 60, 13430-13435.

[13] H. Li, L. Li, R.-B. Lin, W. Zhou, Z. Zhang, S. Xiang and B. Chen, EnergyChem. 2019, 1, 100006.

[14] T. Islam, M. R. Mahboob and S. A. Khan, IEEE Sens. J. 2014, 15, 3004-3013.

[15] T. Islam, A. Nimal, U. Mittal and M. Sharma, Sens. Actuators, B. 2015, 221, 357-364.

[16] C. Lv, C. Hu, J. Luo, S. Liu, Y. Qiao, Z. Zhang, J. Song, Y. Shi, J. Cai and A. Watanabe, Nanomaterials. 2019, 9, 422.

[17] M. R. Mahboob, Z. H. Zargar and T. Islam, Sens. Actuators, B. 2016, 228, 658-664.

[18] R. Liang, A. Luo, Z. Zhang, Z. Li, C. Han and W. Wu, Sensors. 2020, 20, 5601.

[19] K. N. Chappanda, O. Shekhah, O. Yassine, S. P. Patole, M. Eddaoudi and K. N. Salama, Sensors and Actuators B: Chemical. 2018, 257, 609-619.

[20] Y. Liu, L. Yan, H. Cai, H. Zong and L. Chen, MRS Commun. 2021, 11, 504-509.

[21] J. Liu, F. Sun, F. Zhang, Z. Wang, R. Zhang, C. Wang and S. Qiu, J. Mater. Chem. 2011, 21, 3775-3778.

[22] S. Rauf, S. Rauf, M. T. Vijjapu, M. A. Andres, I. Gascon, O. Roubeau and M. Eddaoudi, ACS Appl. Mater. Interfaces. 2020, 12, 29999-30006.

[23] M. A. Andrés, M. T. Vijjapu, S. G. Surya, O. Shekhah, K. N. Salama, C. Serre, M. Eddaoudi, O. Roubeau and I. Gascón, ACS Appl. Mater. Interfaces. 2020, 12, 4155-4162.

[24] M. S. Hosseini and S. Zeinali, J. Mater. Sci. Mater. Electron. 2019, 30, 3701-3710.

[25] K. Wu, T. Fei and T. Zhang, Nanomaterials. 2022, 12, 4208.

[26] N. Takeda, P. Carroll, Y. Tsukahara, S. Beardmore, S. Bell, K. Yamanaka and S. Akao, Meas. Sci. Technol. 2020, 31, 104007.

[27] T. Islam, A. U. Khan, J. Akhtar and M. Z. U. Rahman, IEEE Trans. Ind. Electron. 2014, 61, 5599-5605.

[28] T. Islam, M. R. Mahboob, S. A. Khan and L. Kumar, IEEE Sens. J. 2013, 14, 1148-1153.

[29] J. R. Lakowicz. Principles of Fluorescence Spectroscopy. Springer. 2006, 185-186.

[30] V. G. Machado, R. I. Stock and C. Reichardt, Chem. Rev. 2014, 114, 10429-10475.

[31] B. Chen, Y. Yang, F. Zapata, G. Lin, G. Qian and E. B. Lobkovsky, Adv. Mater. 2007, 19, 1693-1696.

[32] M. Tian, Z. Fu, B. Nath and M. Yao, RSC Adv. 2016, 6, 88991-88995.

[33] Z. Chen and C. Lu, Sens. Lett. 2005, 3, 274-295.

[34] C. Sapsanis, H. Omran, V. Chernikova, O. Shekhah, Y. Belmabkhout, U. Buttner, M. Eddaoudi and K. N. Salama, Sensors. 2015, 15, 18153-18166.

CHAPTER 5

[1] Wunderlichová, L. Buňková, M. Koutný, P. Jančová and F. Buňka, Compr. Rev. Food Sci. Food Saf., 2014, 13, 1012-1030.

[2] B. del Rio, B. Redruello, D. M. Linares, V. Ladero, P. Ruas-Madiedo, M. Fernandez, M. C. Martin and M. A. Alvarez, Sci. Rep., 2019, 9, 120.

[3] C. Izquierdo, J. C. Gómez-Tamayo, J. C. Nebel, L. Pardo and A. Gonzalez, PLoS Comput Biol., 2018, 14 (1), e1005945.

[4] S. Bettini, A. Santino, L. Valli and G. Giancane, RSC Adv., 2015, 5, 18167-18171.

[5] A. R. Shalaby, Food Res. Int., 1997, 29, 675-690.

[6] K. K. Sanjeev, A. Bebin, S. Sudalaimuthu, P. Manickam, G. Krishnan and K. Murugavel, Anal. Methods., 2020, 12, 3438-3453.

[7] L. Elisa, F. Baldini, A. Giannetti, C. Trono and T. Carofiglio, Chem. Commun., 2010, 46, 3678-3680.

[8] F. B. Erim, TrAC, Trends Anal. Chem., 2013, 52, 239-247.

[9] M. S. Steiner, R. Meier, C. Spangler, A. Duerkop and O. Wolfbeis, Microchim. Acta., 2009, 167, 259-266.

[10] J. T. Fletcher and B. S. Bruck, Sens. Actuators, B., 2015, 207, 843-848.

[11] A. H. Malik, S. Hussain and P. K. Iyer, Anal. Chem., 2016, 88, 7358-7364.

[12] M. Nakamura, T. Sanji and M. Tanaka, Chem. Eur. J., 2011, 17, 5344-5349.

[13] K. J. Cash and H. A. Clark, Anal. Chem., 2013, 85, 6312–6318.

[14] S. Chopra, A. Singh, V. N. Singh and N. Kaur, ACS Sustainable Chem. Eng., 2017, 5, 1287-129.

[15] S. Jindal, V. K. Maka and J. N. Moorthy, J. Mater. Chem. C., 2020, 8, 11449.

[16] H. Kim, B. T. Trinh, K. H. Kim, J. Moon, H. Kang, K. Jo, R. Akter, J. Jeong, E. K. Lim, J. Jung, H. S. Choi, H. G. Park, O. S. Kwon, I. Yoon and T. Kang, Biosens. Bioelectron., 2021, 179, 113063.

[17] J. Wang, D. Li, Y. Ye, Y. Qiu, J. Liu, L. Huang, B. Liang and B. Chen, Adv. Mater., 2021, 33, 2008020.

[18] D. Van Heerden, V. Smith, H. Aggarwal and L. Barbour, Angew. Chem. Int. Ed., 2021, 60, 13430.

[19] A. H. Assen, Y. Belmabkhout, K. Adil, A. Lachehab, H. Hassoune and H. Aggarwal, Chemical Engineering Journal., 2021, 419, 129569.

[20] A. Kirchon, L. Feng, H. F. Drake, E. A. Joseph and H.-C. Zhou, Chem. Soc. Rev., 2018, 47, 8611-8638.

[21] H. Aggarwal, R. K. Das, E. R. Engel and L. Barbour, J. Chem. Commun., 2017, 53, 861-864.

[22] P. Samanta, S. Let, W. Mandal, S. Dutta and S. K. Ghosh, Inorg. Chem. Front., 2020, 7, 1801-1821.

[23] G. Radha, T. Leelasree, D. Muthukumar, S. R. Pillai and H. Aggarwal, New J. Chem., 2021, 45, 12931-12937.

[24] H. Y. Li, S. N. Zhao, S. Q. Zang and J. Li, Chem. Soc. Rev., 2020, 49, 6364-6401.

[25] A. Mallick, A. M. El-Zohry, O. Shekhah, J. Yin, J. T. Jia, H. Aggarwal, A. H. Emwas, O. F. Mohammed and M. Eddaoudi, J. Am. Chem. Soc. 2019, 141, 7245-7249.

[26] L. Esrafili, M. Gharib and A. Morsali, New J. Chem., 2019, 43, 18079.

[27] H. D. Lawson, S. P. Walton and C. Chan, ACS Appl. Mater. Interfaces., 2021, 13, 7004-7020.

[28] T. Leelasree, V. Selamneni, T. Akshaya, P. Sahatiya and H. Aggarwal, J. Mater. Chem. B., 2020, 8, 10182-10189.

[29] L. Shi, C. He, D. Zhu, Q. He, Y. Li, Y. Chen, Y. Sun, Y. Fu, D. Wen, H. Cao and J. Cheng, *J. Mater. Chem.*, 2012, **22,** 11629-11635.

[30] S. K. Mostakim and S. Biswas, CrystEngComm., 2016, 18, 3104-3113.

[31] J. R. Lakowicz, Principles of Fluorescence Spectroscopy., Springer., 3rd edn, 2006.

[32] S. Nilanjan, S. Ranadip, M. Singh, S. R. Pillai and S. Neogi, Inorg. Chem. Front., 2021, 8, 296-310.

[33] Y. Fukushima and S. Aikawa, *Tetrahedron Lett.*, 2019, **60,** 151302.

[34] G. Munzi, S. Failla and S. Di Bella, *Analyst.*, 2021, **146**, 2144-2151.

[35] M. S. Steiner, R. J. Meier, C. Spangler, A. Duerkop and O. S. Wolfbeis, *Microchim Acta.*, 2009, **167,** 259.

[36] J. T. Fletcher and B. S. Bruck, *Sens. Actuators B.*, 2015, **207,** 843–848.

[37] H. F. Kung, C. Y. Huang, C. M. Lin, L. H. Liaw, Y. C. Lee and Y. H. Tsai, *J. Food Drug Anal.*, 2015, **23,** 335–342.

[38] M. Y. Khuhawar, A. A. Memon, P. D. Jaipal, M. I. Bhanger, *J Chromatogr B Biomed Sci Appl.*, 1999, **723,** 17-24.

[39] D. Telsnig, K. Kalcher, A. Leitner and A. Ortner, *Electroanalysis.*, 2013, **25,** 47-50.

[40] H. Kim, B. T. Trinh, K. H. Kim, J. Moon, H. Kang, K. Jo, R. Akter, J. Jeong, E. K. Lim, J. Jung, H. S. Choi, H. G. Park, O. S. Kwon, I. Yoon and T. Kang, *Biosens. Bioelectron.*, 2021, **179,** 113063.

[41] S. Jindal, V. K. Maka and J. N. Moorthy, *J. Mater. Chem. C.*, 2020, **8,** 11449.

[42] J. Tu, S. Sun and Y. Xu, *Chem. Commun.*, 2016, **52,** 1040-1043.

[43] H. J. Yan, Y. Chen and S. M. Xu, Int. J. Hydrogen Energy., 2012, 37, 125-133.

CHAPTER 6

[1] B. Bao, L. Yuwen, X. Zheng, L. Weng, X. Zhu, X. Zhan and L. Wang, *J. Mater. Chem.* 2010, **20,** 9628-9634.

[2] M. A. Medina, J. L. Urdiales, C. Rodríguez-Caso, F. J. Ramírez and F. Sanchez-Jimenez, *Crit. Rev. Biochem. Mol. Biol.* 2003, **38,** 23-59.

[3] M. R. Ajayakumar and P. Mukhopadhyay, *Chem. Commun.* 2009, **25,** 3702-3704.

[4] M. Mon, J. Ferrando Soria, T. Grancha, F. R. Fortea-Perez, J. Gascon, A. Leyva Perez, D. Armentano and E. Pardo, *J. Am. Chem. Soc.* 2016, **138,** 7864-7867.

[5] F. Wang, C. Dong, Z. Wang, Y. Cui, C. Wang, Y. Zhao and G. Li, *Eur. J. Inorg. Chem.* 2014, 6239-6245.

[6] Z. M. Merchant, S. G. G. Cheng and A. G. Gaonkar, *Elsevier Science, New York.* 1995, chapter **15**.

[7] B. Timmer, W. Olthuis and A. Van den Berg, *Sens. Actuators, B.* 2005, **107,** 666-677.

[8] Z. Quan, G. Xie, Q. Peng, J. Shan, W. Xing, J. Zhang, S. Li, Z. Chan, C. Chou and H. Zou, *Pol. J. Environ. Stud.* 2016, **25,** 1669-1673.

[9] A. Mallick, B. Garai, M. A. Addicoat, P. St. Petkov, T. Heine and R. Banerjee, *Chem. Sci*. 2015, **6,** 1420-1425.

[10] A. Mallick, A. M. El-Zohry, O. Shekhah, J. Yin, J. Jia, H. Aggarwal, A. H. Emwas, O. F. Mohammed and M. Eddaoudi, *J. Am. Chem. Soc*. 2019, **141,** 7245-7249.

[11] E. Mertz and S. C. Zimmerman, *J. Am. Chem. Soc*. 2003, **125,** 3424-3425.

[12] N. T. Greene, S. L. Morgan and K. D. Shimizu, *Chem. Commun*. 2004, 1172-1173.

[13] M. Comes, M. D. Marcos, R. Martinez-Manez, F. Sancenon, J. Soto, L. A. Villaescusa, P. Amorós and D. Beltran, *Adv. Mater*. 2004, **16,** 1783-1786.

[14] J. Yu and C. Zhang *J. Mater. Chem. C*. 2020, **8,** 16463-16469.

[15] D. Van Heerden, V. Smith, H. Aggarwal and L. Barbour *Angew. Chem. Int. Ed*. 2021, **60,** 13430-13435.

[16] A. H. Assen, Y. Belmabkhout, K. Adil, A. Lachehab, H. Hassoune and H. Aggarwal, *Chem. Eng. J.* 2021, **419,** 129569.

[17] H. Aggarwal, R. K. Das, E. R. Engel and L. Barbour, *Chem. Commun*. 2017, **53,** 861-864.

[18] T. Leelasree, V. Selamneni, T. Akshaya, P. Sahatiya and H. Aggarwal, *J. Mater. Chem. B*. 2020, **8,** 10182-10189.

[19] T. Leelasree and H. Aggarwal, *J. Mater. Chem. C*. 2022, **10,** 2121-2127.

[20] G. Radha, T. Leelasree, D. Muthukumar, S. R. Pillai and H. Aggarwal, *New J. Chem.* 2021, **45,** 12931-12937.

[21] J. J. Liu, Y. B. Shan, C. R. Fan, M. J. Lin, C. C. Huang and W. X. Dai, *Inorg. Chem.* 2016, **55,** 3680-3684.

[22] P. Mani, A. A. Ojha, V. S. Reddy and S. Mandal, *Inorg. Chem*. 2017, **56,** 6772-6775.

[23] J. R. Stetter, W. R. Penrose and S. Yao, *J. Electrochem. Soc*. 2003, **150,** S11-S16.

[24] T. Hinoue, M. Miyata, I. Hisaki and N. Tohnai, *Angew. Chem., Int. Ed*. 2012, **51,** 155-158.

[25] A. Hulanicki, S. Glab and F. Ingman, *Pure Appl. Chem*. 1991, **63,** 1247-1250.

[26] a) J. P. Perdew, K. Burke, M. Ernzerhof, *Physical Review Letters.*, 1996, **77,** 3865-3868. b) Y. Zhang and W. Yang, *Physical Review Letters.* 1998, **80,** 890-890.

[27] J. Vande Vondele, M. Krack, F. Mohamed, M. Parrinello, T. Chassaing and J. Hutter, *Computer Physics Communications.* 2005, **167,** 103-128.

[28] S. Grimme, J. Antony, S. Ehrlich and H. Krieg, *The Journal of Chemical Physics.* 2010, **132,** 154104.

[29] S. K. Mostakim and S. Biswas, *CrystEngComm*. 2016, **18,** 3104-3113.

[30] J. R. Lakowicz, Principles of Fluorescence Spectroscopy. *Springer*, 3rd edn. 2006.

[31] J. Yu and C. Zhang, *J. Mater. Chem. C.* 2020, **8,** 16463-16469.

[32] Y. J. Zhao, K. Miao, Z. Zhu and L. J. Fan, *ACS Sens.,* 2017, **2,** 842-847.

[33] N. Seal, R. Goswami, M. Singh, R. S. Pillai and S. Neogi, *Inorg. Chem. Front.* 2021, **8,** 296-310.

[34] J. Zhang, D. Yue, T. Xia, Y. Cui, Y. Yang and G. Qian, *Microporous Mesoporous Mater*. 2017, **253,** 146-150.

[35] Y. P. Li, S. N. Li, Y. C. Jiang, M. C. Hua and Q. G. Zhai, *Chem. Commun.* 2018, **54,** 9789.

[36] W. P. Ma and B. Yan, *Dalton Trans.* 2020, **49,** 15663.

[37] N. B. Shustova, A. F. Cozzolino, S. Reineke, M. Baldo and M. Dinca, *J. Am. Chem. Soc.* 2013, **135,** 13326- 13329.

[38] D. Wong, A. Phani, S. Homayoonnia, S. S. Park, S. Kim and O. Abuzalat, *Adv. Mater. Interfaces.* 2022, **9,** 2102086.

[39] D. I. Pavlov, T. S. Sukhikh, A. A. Ryadun, V. V. Matveevskaya, K. A. Kovalenko, E. Benassi, V. P. Fedina and A. S. Potapov, *J. Mater. Chem. C.* 2022, **10,** 5567-5575.

[40] H. J. Yan, Y. Chen and S. M. Xu, *Int. J. Hydrogen Energy.* 2012, **37,** 125-133.

[41] S. C. Yan, Z. S. Li and Z. G. Zou, *Langmuir,* 2010, **26,** 3894-3901.

[42] L. Shi, C. He, D. Zhu, Q. He, Y. Li, Y. Chen, Y. Sun, Y. Fu, D. Wen, H. Cao and J. Cheng, *J. Mater. Chem.* 2012, **22,** 11629-11635.

CHAPTER 7

[1] A. Mishra, P. Chaturvedi, S. Datta, S. Sinukumar, P. Joshi and A. Garg, *J. Med. Paediatr. Oncol.,* 2015, **36,** 24-31.

[2] P. A. Newhouse, A. Potter, M. Kelton and J. Corwin, *J. Biol. Psychiatry.*, 2001, **49,** 268-278.

[3] H. O. Vargas, S. O. V. Nunes, M. R. P. de Castro, M. M. Vargas, D. S. Barbosa, C. C. Bortolasci, K. Venugopal, S. Dodd and M. Berk, *Neurosci. Lett.,* 2013, **136,** 544.

[4] U.S. Department of Health and Human Services. The Health Consequences of Involuntary Exposure to Tobacco Smoke: A Report of the Surgeon General. Atlanta, GA: U.S. Department of Health and Human Services, Centers for Disease Control and Prevention, Coordinating Center for Health Promotion, National Center for Chronic Disease Prevention and Health Promotion, Office on Smoking and Health, 2006.

[5] M. L. Chin Chen, M. Rambla Alegre, A. Durgavanshi, D. Bose and J. Esteve Romero, *J. Chromatogr. B.,* 2010, **878,** 2397-2402.

[6] J. M. Garrigues, A. Perez Ponce, S. Garrigues and M. de la Guardia, *Chim. Acta.,* 1998, **373,** 63-71.

[7] K. R. Tambwekar, R. B. Kakariya and S. Garg, *J. Pharm. Biomed. Anal.,* 2003, **32,** 441.

[8] A. M. Hossain and S. M. Salehuddin, *Arab. J. Chem.,* 2013, **6,** 275.

[9] A. Marsh, B. J. Clark and K. D. Altria, *Electrophores.,* 2004, **25,** 1270.

[10] A. Karthika, P. Karuppasamy, S. Selvarajan, A. Suganthi and M. Rajarajan, *Ultrasonics Sonochemistry.,* 2019, **55,** 196-206.

[11] J. Rajendran, A. N. Reshetilov and A. K. Sundramoorthy, *Mater. Adv.,* 2021, **2,** 3336-3345.

[12] H. Kassa, A. Geto and S. Admassie, *Bull. Chem. Soc. Ethiop.,* 2013, **27,** 321-328.

[13] X. Li, H. Zhao, L. Shi, X. Zhu, M. Lan, Q. Zhang and Z. H. Fan, *J. Electroanal. Chem.,* 2017, **784,** 77-84.

[14] H. Chen, M. B. Muller, K. J. Gilmore, G. G. Wallace and D. Li, *Adv. Mater.,* 2008, **20,** 3557-3561.

[15] B. Yu, Y. Liu, J. Zhang, T. Hai, B. Li, P. Lu, H. Li, Y. Zhang, J. Yu, Z. Ye and Y. Jing, *Int. J. Electrochem. Sci.,* 2016, **11,** 4979-4987.

[16] A. M. Fekrya, S. M. Azabb, M. Shehataa and M. A. Ameera, *RSC Adv.,* 2015, **5,** 51662-51671.

[17] L. Svorc, D. M. Stankovic and K. Kalche, *Diamond Relat. Mater.,* 2014, **42,** 1-7.

[18] G. A. M. Mersal, N. Y. Mostafa and A. E. H. Omar, *Mater. Res. Express.,* 2017, **4,** 085031.

[19] Y. Jing, X. Yuan, Q. Yuan, K. He, Y. Liu, P. Lu, H. Li, B. Li, H. Zhan and G. Li, *Sci. Rep.,* 2016, **6,** 29230.

[20] H. Aggarwal, R. Das, K. E. R. Engel and L. Barbour, *J. Chem. Commun.,* 2017, **53,** 861-864.

[21] D. Van Heerden, V. Smith, H. Aggarwal and L. Barbour, *Angew. Chem. Int. Ed.,* 2021, **60,** 13430.

[22] A. Sharma, D. Kim, J. H. Park, S. Rakshit, J. Seong, G. H. Jeong, O. H. Kwon and M. S. Lah, *Commun. Chem.,* 2019, **2,** 39.

[23] N. R. Jalal, T. Madrakian, A. Afkhami and A. Ghoorchian, *ACS Appl. Mater. Interfaces.,* 2020, **12,** 4859-4869.

[24] G. Radha, T. Leelasree, D. Muthukumar, S. R. Pillai and H. Aggarwal, *New J. Chem.,* 2021, **45,** 12931-12937.

[25] D. Rani, K. K. Bhasin and M. Singh, *ACS Materials Letters.,* 2020, **2,** 9-14.

[26] M. A. Ataur Rahman, L. Cai, S. A. Tawfik, S. Tucker, A. Burton, G. Perera, M. J. S. Spencer, S. Walia, S. Sriram, P. Gutruf and M. Bhaskaran. *ACS Sensors.,* 2022, **7,** 82-88.

[27] D. Yan, Y. Lou, Y. Yang, Z. Chen, Y. Cai, Z. Guo, H. Zhan and B. Chen, *ACS Appl. Mater. Interfaces.,* 2019, **11,** 50, 47253-47258.

[28] T. Leelasree, V. Selamneni, T. Akshaya, P. Sahatiya and H. Aggarwal, *J. Mater. Chem. B.,* 2020, **8,** 10182-10189.

[29] T. Leelasree and H. Aggarwal, *J. Mater. Chem. C.,* 2022, **10,** 2121-2127.

[30] Y. Ma, G. Xu, F. Wei, Y. Cen, Y. Ma, Y. Song, X. Xu, M. Shi, S. Muhammad and Q. Hu, *J. Mater. Chem. C.,* 2017, **5,** 8566-8571.

[31] N. Elgiddawy, S. Ren, W. Ghattas, W. M. A. E. Rouby, A. O. El Gendy, A. A. Farghali, A. Yassar and H. Korri Youssoufi, *Sensors (Basel).,* 2021, **21,** 1715.

[32] L. Zhang, Y. Han, J. Zhu, Y. Zhai and S. Dong, *Anal. Chem.,* 2015, **87,** 2033-2036.

[33] L. Shi, C. He, D. Zhu, Q. He, Y. Li, Y. Chen, Y. Sun, Y. Fu, D. Wen, H. Cao and J. Cheng, *J. Mater. Chem.,* 2012, **22,** 11629-11635.

[34] S. Nilanjan, S. Ranadip, M. Singh, S. R. Pillai and S. Neogi, *Inorg. Chem. Front.,* 2021, **8,** 296-310.

[35] S. K. Mostakim and S. Biswas, *CrystEngComm.,* 2016, **18,** 3104-3113.

[36] J. R. Lakowicz, Principles of Fluorescence Spectroscopy. *Springer.,* 3rd edn. 2006.

[37] G. P. Becerra, F. Rojas Rodriguez, D. Ramirez, A. E. Loaiza, F. Tobar Tosse, S. M. Mejia and J. Gonzalez, *Comput Biol Chem.,* 2020, **86,** 107266.

[38] H. J. Yan, Y. Chen and S. M. Xu, *Int. J. Hydrogen Energy.,* 2012, **37,** 125-133.

[39] S. C. Yan, Z. S. Li and Z. G. Zou, *Langmuir.,* 2010, **26,** 3894-3901.

[40] J. Rajendran, A. N. Reshetilov and A. K. Sundramoorthy, *Mater. Adv.,* 2021, **2,** 3336-3345.

[41] M. B. Nguyen, V. T. H. Nhung, V. T. Thu, D. T. N. Nga, T. N. P. Truong, H. Y. Giang, P. T. H. Yen, P. H. Phong, T. A. Vu and V. T. T. Ha, *RSC Adv.,* 2020, **10,** 42212-42220.

[42] S. Dong, G. Suo, N. Li, Z. Chen, L. Peng, Y. Fu, Q. Yang, T. Huang, *Sens. Actuators B. Chem.,* 2016, **222,** 972-979.

[43] K. Cinkova, L. Dianova, M. Vojs, M. Marton and L. Svorc, *Acta Chim. Slovaca.,* 2015, **8,** 166-171.

[44] M. Stoces and I. Svancara, *Electro Anal.,* 2014, **26,** 2655-2663.

[45] T. W. Lo, L. Aldous and R. G. Compton, *Sens. Actuators B. Chem.,* 2012, **162,** 361-368.

[46] C. T. Wu, P. Y. Chen, J. G. Chen, V. Suryanarayanan and K. C. Ho, *Anal. Chim. Acta.,* 2009, **633,** 119-126.

[47] A. Saljooqi, T. Shamspur and A. Mostafavi, *J. Mater Sci: Mater Electron.,* 2020, **31,** 5471-5477.

List of Publications and Conferences

Publications included in the thesis

- **T. Leelasree,** V. Selamneni, T. Akshaya, P. Sahatiya and Himanshu Aggarwal.* MOF based flexible, low-cost chemiresistive device as a respiration sensor for sleep apnea diagnosis. ***Journal of Materials Chemistry B.*** 2020, 8, 10182-10189. **(Selected as top 50 articles published in Journal of Materials Chemistry B in 2020)**
- **T. Leelasree** and Himanshu Aggarwal.* MOF sensors for food safety: ultralow detection of putrescine and cadaverine in protein rich foods. ***Journal of Materials Chemistry C.*** 2022, 10, 2121-2127.
- **T. Leelasree,** M. Dixit and Himanshu Aggarwal.* Cobalt-based metal-organic frameworks and its mixed-matrix membranes for discriminative sensing of amines and on-site detection of ammonia. ***Chemistry of Materials.*** 2023, 35, 416-423.
- **T. Leelasree,** S. Goel and Himanshu Aggarwal.* MOF-based dual sensor for the electrochemical and fluorescence detection of nicotine. ***ACS Applied Nano Materials.*** 2022, 5, 16753-16759.
- **T. Leelasree,** P. N. Sidhartha, Manav Tathacharya, Karumbaiah N. Chappanda and Himanshu Aggarwal.* A Low-cost, Swift Response, Highly Sensitive MOF-based Dual Sensing Device Enables Detection of Ultralow Humidity Levels and Solvent Polarity Changes. ***Journal of Materials Chemistry C.*** 2024, 12, 7295-7305.

Other publications by the author

- **T. Leelasree** and Himanshu Aggarwal.* Design and Investigation of a Novel Two-Dimensional Cobalt Metal-Organic Framework for the Highly Sensitive Electrochemical Detection of Nitrofurazone Drug in Food and Biological Samples. (Manuscript submitted)
- G. Radha, T. **Leelasree,** D. Muthukumar, S. R. Pillai and Himanshu Aggarwal.* Highly selective detection of TNP over other nitro compounds in water: the role of selective host-guest interactions in Zr-NDI MOF. ***New Journal of Chemistry.*** 2021, 45, 12931-12937.

- M. Christina Nilavu, **T. Leelasree,** Himanshu Aggarwal* and N. Rajesh.* Cobalt-based Metal-Organic Framework for Desulfurization of Thiophene as a Model Fuel. ***Sustainable Energy Fuels*.** 2024, 8, 1679-1690.

List of Conferences

- Current Trends in Analytical Chemistry (CTAC-2021), Second DAE Symposium, BARC, Mumbai.
- 9th DAE-BRNS Interdisciplinary Symposium on Materials Chemistry, (ISMC-2022) BARC, Mumbai.
- National Symposium on Convergence of Chemistry and Materials (CCM-2023), Department of Chemistry, BITS PILANI, Hyderabad campus.
- CESC- 2023 (Crystal Engineering and Solid-State Chemistry), IISER Thiruvananthapuram.
- Indo-German conference, titled 'Catalysis for Circular Economy towards Sustainable Energy (CatCE2), BITS PILANI, Hyderabad campus.

Awards, Recognitions and Patents

- Dr. K. V. Rao Scientific Society (KVRSS) **Research Award** 2021-22.
- **Best poster award**- National Symposium on Convergence of Chemistry and Materials (CCM-2023).
- **RSC Poster prize award** from Journal of Materials Chemistry A at the National Symposium on Convergence of Chemistry and Materials (CCM-2023).
- **ACS Best Poster Award** at CESC- 2023 (Crystal Engineering and Solid-State Chemistry), IISER Thiruvananthapuram.
- The paper "MOF based flexible, low-cost chemiresistive device as a respiration sensor for sleep apnea diagnosis," J. Mater. Chem. B., has been selected as **top 50 articles** published in Journal of Materials Chemistry B in 2020 and is a part of **2020 Journal of Materials Chemistry B most popular articles**.
- My work on MOF based breath sensor was recognized and highlighted in the **"Times of India newspaper"** (Hyderabad, Feb 22, 2021).

Patents

- Patent application has been filed for the invention titled **"A mixed-linker fluorescent metal-organic framework (MOF) and process for preparing a sensor comprising the MOF"** and the application number is **IN Application: 202111051661. (Granted- Patent No. 542203).**

Biography of the Candidate

Ms. T. Leelasree received the Bachelor of Science (B.Sc.) degree in Chemistry from Ethiraj college for women affiliated to Madras University, Chennai, Tamil Nadu, India, and the Master of Science (M.Sc.) degree in Chemistry from Women's Christian college affiliated to Madras University, Chennai, Tamil Nadu, India. She is currently pursuing the Ph.D. degree in Chemistry at Birla Institute of Technology and Science, Pilani, Hyderabad, Telangana, India. She has published 8 Journal articles in high impact journals including *Chemistry of Materials, J. Mater. Chem. B., J. Mater. Chem. C*. She has also acquired an Indian patent. She also received prestigious Dr. K. V. Rao Scientific Society (KVRSS) Research Award and other awards include RSC Poster prize award and ACS Poster prize award. Her research interests include design of novel Metal-organic frameworks (MOFs) for sensing applications, develop novel strategies to fabricate MOF devices and explore the potential of MOFs to address challenges across various industries.

Biography of the Supervisor

Dr. Himanshu Aggarwal is a materials' chemist with over 10 years of experience in the design, synthesis, characterization and applications of porous materials, in particular, metal-organic frameworks (MOFs). He completed his Ph.D. degree in Supramolecular Chemistry from Stellenbosch University, South Africa. After his Ph.D., he worked as a postdoctoral fellow in KAUST, Saudi Arabia where he designed novel porous materials for carbon capture, humidity control, and separation of alkane mixtures. He joined BITS-Pilani, Hyderabad Campus as an Assistant Professor in 2019. He has keen interests in designing porous materials for sensing, separation, carbon capture, and catalysis. He has published several results in high impact journals including *J. Am. Chem. Soc*., *Angew. Chemie. Int. Ed*., *Chem*, *Chemical Science*, *Chem. Eng. Journal, Chemistry of Materials, and J. Mater. Chem. C*. He was recently awarded the SMC Bronze medal and also elected as the associate fellow of Telangana Academy of Sciences. His group recently designed new series of MOF materials named after BITS-Hyderabad Campus, for the sensing of food spoilage indicators from protein rich foods like fish and cheese, and evaluation of nicotine from urine samples. In addition to that, his group also designed the first MOF-based breath sensor for the diagnosis of sleep apnoea. *This work was selected among the top 50 articles published in J. Mater. Chem. B in the year 2020 and the Times of India newspaper*.